TUM School
of Natural Sciences

Forschungs-Neutronenquelle
Heinz Maier-Leibnitz (FRM II)

TECHNISCHE UNIVERSITÄT MÜNCHEN

PhD Thesis

Towards FRM II LEU Conversion: Viable Barriers to Prevent Excessive Radiation-Induced Interdiffusion in Monolithic U-Mo Fuel Plates

Christian Schwarz

May 2023

Supervised by
Prof. Dr. Winfried Petry

Technische Universität München
TUM School of Natural Sciences

Towards FRM II LEU Conversion:

Viable Barriers to Prevent Excessive Radiation-Induced Interdiffusion in Monolithic U-Mo Fuel Plates

Christian Schwarz

Vollständiger Abdruck der von der TUM School of Natural Sciences der Technischen Universität München zur Erlangung eines

Doktors der Naturwissenschaften (Dr. rer. nat.)

genehmigten Dissertation.

Vorsitz: apl. Prof. Dr. Norbert Kaiser

Prüfer der Dissertation:

1. Prof. Dr. Winfried Petry
2. Prof. Dr. Bastian Märkisch

Die Dissertation wurde am 17.05.2023 bei der Technischen Universität München eingereicht und durch die TUM School of Natural Sciences am 17.07.2023 angenommen.

Abstract

TUM takes part in the global efforts to develop new nuclear fuels for research and test reactors with the goal to convert those using highly-enriched uranium (HEU) to a lower enrichment in order to reduce proliferation risks. The focus of TUM's research lies on a monolithic fuel based on a uranium-molybdenum (U-Mo) alloy. This fuel type provides a high uranium density, which makes it possible to convert the FRM II research reactor to an enrichment below 20 %.

Several aspects have to be considered to qualify such a new fuel of low-enriched uranium, including its performance in irradiation tests and the establishment of a specification-conform manufacturing process. This thesis' main focus lies on the application of a diffusion barrier layer between the U-Mo fuel foils and the Al cladding with physical vapor deposition (PVD). Without such a layer, the radiation-driven diffusion between fuel and cladding forms an interaction layer that is detrimental to fuel performance.

Zirconium is most commonly used so far as a diffusion barrier material in this context. The application of the Zr via PVD has been used for the first time in the EMPIrE test, where small-scale fuel plates were irradiated in a material test reactor. These samples were investigated by destructive examinations within this thesis together with unirradiated plates as a comparison. Stable and predictable behavior was found hereby in general. Cracks in the Zr layer caused by a combination of the PVD parameters and the cladding process were found to be of no adverse impact. A novel observation, however, was the formation of porosities by the accumulation of fission gases in the Zr layer close to the U-Mo.

As a step towards industrialization of the coating process, the PVD device had been already scaled up to produce Zr-coated foils in full-size geometry. With this pilot device and the gained knowledge from the irradiation test, several batches of U-Mo foils were coated to investigate the influence of parameters like substrate biasing, Zr purity, coating thickness, and foil surface quality. Destructive characterizations of the final plates after cladding application found substantial amounts of cracks in the coating and oxidized U-Mo below. However, it was shown that the PVD process was not the primary cause of this. The surface texture of the procured U-Mo foils, on the other hand, was identified as a main driver for the formation of cracks and oxidation during the cladding process. Nevertheless, with an adjustment of the PVD parameters, the issue was successively reduced with each sample batch by generating a more ductile Zr layer that better withstands the mechanical stress introduced by the cladding process. In the course of these adjustments, the substrate holder of the PVD device was also significantly improved regarding handling, reliability, and substrate fixation.

Parallel to this, the more versatile mini-size PVD device was used for investigations on the alternative diffusion barrier materials molybdenum and tungsten, which may present certain advantages over the commonly used Zr. First tests with Mo coatings displayed oxidation that caused debonding of the cladding. This was resolved by the application of a protective Al coating via PVD. However, the used parameters resulted in significant thermal diffusion between Mo and Al, and the formation of an inhomogeneous intermixing zone consisting of several intermetallic phases. W diffusion barriers displayed very promising results in heavy-ion irradiations, where coating thicknesses of about 1 µm acted already as an effective diffusion barrier. However, the extreme brittleness of W causes severe cracking of the coating when combined with the cladding process.

Zusammenfassung

Als Teil der weltweiten Bemühungen zur Reduzierung von Proliferationsrisiken beteiligt sich die TUM an der Entwicklung neuer Kernbrennstoffe für Forschungs- und Testreaktoren mit dem Ziel, bestehende Reaktoren, die mit hochangereichertem Uran (HEU) betrieben werden, auf eine geringere Anreicherung umzurüsten. Der Forschungsschwerpunkt der TUM liegt hierbei auf einem monolithischen Brennstoff auf Basis einer Uran-Molybdän-Legierung (U-Mo). Dieser Brennstofftyp bietet eine hohe Urandichte, welche es ermöglicht, den Forschungsreaktor FRM II auf eine Anreicherung unter 20 % umzurüsten.

Zur Qualifizierung eines solchen neuen Brennstoffs aus niedrig angereichertem Uran müssen verschiedene Aspekte, wie das Verhalten in Bestrahlungstests und die Etablierung eines spezifikationskonformen Herstellungsprozesses, berücksichtigt werden. Das Hauptaugenmerk der vorliegenden Arbeit liegt auf der Herstellung einer Schicht mittels PVD-Verfahren, die als Diffusionsbarriere zwischen der U-Mo Brennstofffolie und der umgebenden Al-Hülle (Cladding) wirkt. Ohne eine solche Barriereschicht bildet sich durch strahlungsgetriebene Diffusion eine Wechselwirkungsschicht zwischen U-Mo und Al aus, welche sich nachteilig auf das Verhalten des Brennstoffs auswirkt.

Als Material für solch eine Diffusionsbarriere wird in diesem Zusammenhang bisher meist Zirkonium verwendet. Im EMPIrE-Test, bei welchem kleinskalige Brennstoffplatten in einem Materialtestreaktor bestrahlt wurden, ist zum ersten Mal die Aufbringung des Zr mittels PVD erprobt worden. Durch zerstörende Prüfung wurden die resultierenden Proben im Rahmen dieser Arbeit zusammen mit unbestrahlten Platten als Vergleich untersucht. Dabei wurde ein stabiles und vorhersagbares Verhalten festgestellt. Risse in der Zr-Schicht, verursacht durch eine Kombination aus PVD-Parametern und Cladding-Prozess, hatten keine negative Auswirkung. Eine neue Beobachtung hingegen war die Bildung von Porositäten in der Zr-Schicht nahe des U-Mo durch die Ansammlung von Spaltgasen.

Die PVD-Anlage wurde bereits zur Produktion von Zr-beschichteten Folien in sogenannter "Full-size"-Geometrie hochskaliert. Mit dieser Pilotanlage und den gewonnenen Erkenntnissen aus dem Bestrahlungstest wurden nun mehrere Chargen von U-Mo-Folien beschichtet, um den Einfluss von Parametern wie Substratspannung, Zr-Reinheit, Schichtdicke und Oberflächenqualität der Folien zu untersuchen. Zerstörende Prüfung der fertigen Platten zeigten ein beträchtliches Ausmaß an Rissen in der Beschichtung und damit einhergehende Oxidation des darunterliegenden U-Mo. Es zeigte sich jedoch, dass nicht der PVD-Prozess dafür die primäre Ursache ist, sondern die Oberflächenbeschaffenheit der U-Mo-Folien ein Haupttreiber für Rissbildung und Oxidation während des Cladding-Prozesses sind. Durch eine Anpassung der PVD-Parameter wurde das Problem jedoch mit jeder Probencharge sukzessive reduziert, indem duktilere Zr-Schichten erzeugt wurden, die den Belastungen durch den Cladding-Prozess besser standhalten. Im Zuge dessen wurde auch der Substrathalter der PVD-Anlage hinsichtlich Handhabung, Zuverlässigkeit und Substratfixierung deutlich verbessert.

Parallel dazu wurde die kleinskaligere PVD-Anlage für Untersuchungen zu Diffusionsbarrieren mit den alternativen Materialien Molybdän und Wolfram eingesetzt. Erste Tests mit Mo-Beschichtungen zeigten starke Oxidation, die zum Ablösen des Claddings führte. Dies konnte durch das Aufbringen einer schützenden Al-Schicht mittels PVD behoben werden. Die verwendeten Parameter führten jedoch zu einer erheblichen thermischen Diffusion zwischen Mo und Al, was zur Bildung einer inhomogenen Reaktionszone aus mehreren intermetallischen Verbindungen führte. W-Diffusionsbarrieren zeigten sehr vielversprechende Ergebnisse bei Schwerionenbestrahlungen, wobei bereits Schichtdicken von 1 µm als effektive Diffusionsbarriere wirkten. Die extreme Sprödigkeit von W führt jedoch in Kombination mit dem Cladding-Prozess zu einer starken Rissbildung der Beschichtung.

Contents

Chapter 1

Motivation

click

cli-click

...

With just the steadily increasing rate of clicks of the neutron counter, it would have been a rather tedious experience for an unknowing spectator when Enrico Fermi set one of the cornerstones that led into the nuclear age by finally announcing "*The curve is exponential*". There, on a squash court under the stands of the University of Chicago's football stadium, Fermi and his team achieved the first artificial self-sustaining chain reaction on the 2nd of December 1942 by building an operational nuclear reactor.

This experiment, illustrated in Figure 1.1, was conducted within the framework of a scientific and technical endeavor unprecedented in history – the Manhattan project. In less than seven years after the discovery of nuclear fission by Otto Hahn, its developments ultimately culminated in the infamous events that ended World War II.

Figure 1.1: Artist's rendering of the first artificial self-sustaining chain reaction achieved with the reactor Chicago Pile-1 on the right.

Soon after that, the nuclear technology progressed from its military use into the civilian sector. With President Eisenhower's "Atoms for Peace" speech in 1953, the formerly top-secret topic was introduced to the public. A program of the same name was launched to share nuclear technology with other nations committed to the peaceful use of nuclear power. In the wake of this, numerous reactors were purchased all over the world, including the first German research reactor, the *Forschungsreaktor München* (FRM), which went critical four years later. Many of these research and test reactors including the FRM soon upgraded their fuel using highly enriched uranium (HEU) to meet the demands for higher neutron fluxes. This resulted in an annual export of about 700 kg of HEU from the US by the late 1970s to fuel foreign reactors [144], which started to raise concerns regarding proliferation risks concerning the Treaty on the Non-Proliferation of Nuclear Weapons. Thereupon, the US Department of Energy (DOE) initiated the Reduced Enrichment for Research and Test Reactors (RERTR) Program in 1978, which aims to develop technologies in order to convert reactors to use low enriched uranium (LEU) and therefore reduce the amount of fissile material in the civilian sector [135]. Since then, over 70 reactors have been successfully converted [108]. As of 2016, 74 research reactors around the world still have to undergo conversion [16], one of which is the successor of the FRM.

1.1 The FRM II

When the scientific demand for neutrons further increased, the operator of the FRM, the *Technische Universität München* (TUM), decided not to upgrade the FRM but to build a new reactor instead. After more than 20 years of conceptual planning and construction, the swimming pool-type reactor named Forschungs-Neutronenquelle Heinz Maier-Leibnitz (FRM II) reached criticality on March 2nd, 2004. The ensemble of FRM and FRM II with the neutron guide hall in between is depicted in Figure 1.2. By providing a maximum undisturbed thermal neutron flux of $8{\cdot}10^{14}$ per cm^2 and second at only 20 MW of thermal power, FRM II is one of the most advanced neutron sources in the world with a wide application range from fundamental research to material science for the industry to medical purposes like radioisotope production and cancer treatment.

Figure 1.2: The FRM II (middle) with the dome of its predecessor FRM on the right.

The neutron beams of high brilliance for the experimental setups are achieved by a compact core of one single fuel element. The cylindrical geometry is 24 cm in diameter and has an active zone of 70 cm height. This design was based on other *high-performance research reactors* (HPRRs) like the *High Flux Reactor* (HFR) at the *Institut Laue-Langevin* (ILL) in Grenoble, France, and the *High Flux Isotope Reactor* (HFIR) at the *Oak Rich National Laboratory* (ORNL) in Tennessee, US [4, 30, 85]. It features 113 fuel plates of involute shape, as depicted in Figure 1.3. The plates are arranged around the inner tube through which the Hf control rod is inserted. In total, the fuel element has a uranium inventory of 8.1 kg with an enrichment of 93 %, which denotes the atomic percentage of the isotope ^{235}U that is fissile with thermal neutrons. With this fuel loading, the FRM II is capable to run a cycle of 60 days. Four such cycles are conducted per year with maintenance breaks in between.

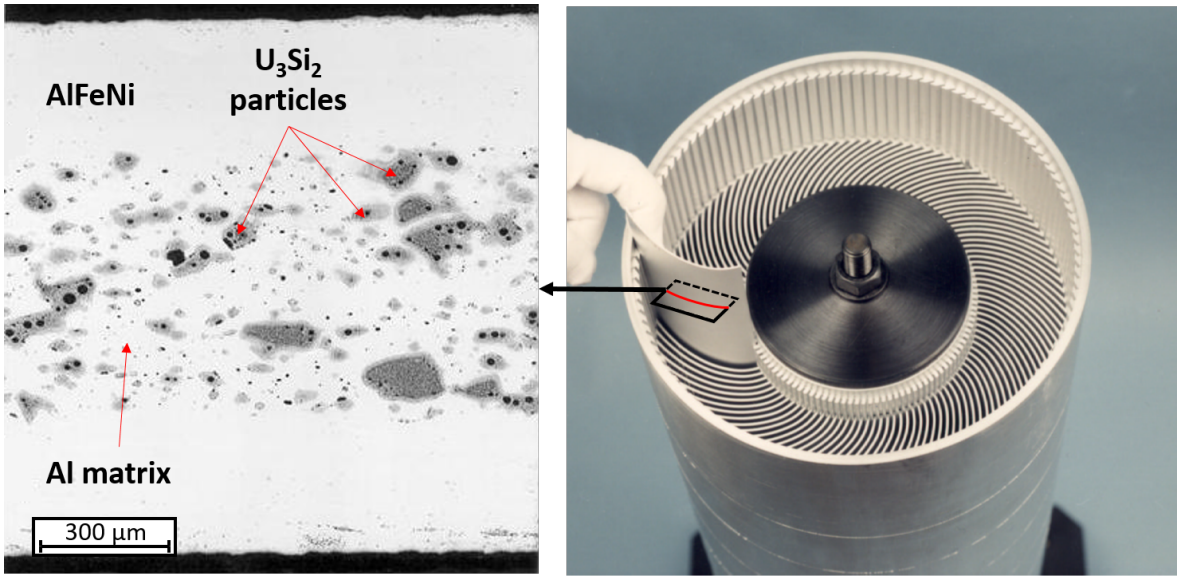

Figure 1.3: Cross section of the current FRM II fuel plate in the fuel zone with $3\,g/cm^3$ uranium content (left). Arrangement of the involute fuel plates between the inner and outer tube of a fuel element during manufacturing (right). Based on [4].

The uranium in the fuel plate consists of ground powder of uranium silicide (U_3Si_2) in an Al matrix. This so-called *fuel meat* is encased in a cladding made out of an AlFeNi alloy (see Figure 1.3). Fuel types like that with particles of uranium dispersed inside another material are called *dispersion fuels*. To reach the designated uranium content of $3.0\,g/cm^3$ in the meat, the U_3Si_2 is mixed with Al power to make up 27 vol.% [117]. However, the outer region of the fuel plates facing the moderator tank is prepared with a zone of only $1.5\,g/cm^3$ uranium content to avoid power peaks [30]. Manufacturing of these plates and the whole fuel element for FRM II is performed at CERCA, a division of the Framatome Fuel Business Unit [19].

The design of FRM II's core was optimized for the *cold source*, a container filled with liquid deuterium (D_2) at a temperature of 25 K, which is a key component of the reactor and supplies more than half of all experimental setups with cold neutrons of about 2 meV. To achieve a high cold flux, the source has to be placed close to the fuel element, while still being able to maintain its low temperature. Hence, the compact core is designed to only generate 20 MW of thermal power, which makes it possible to operate the cold source in the thermal flux maximum, while its coolability is still given. However, at the time the FRM II was designed and constructed, no LEU fuel was qualified to operate such a compact core [45, 55, 115]. Hence, the FRM II was configured to run with the HEU fuel described above. In line with the international agreements to minimize the use of HEU, FRM II aims to convert its fuel core to a lower enriched one with $< 50\,\%$ ^{235}U. However, a conversion is only viable if several criteria are met:

- Outer core dimensions are maintained
- Only marginal losses ($< 10\,\%$) of neutron flux
- Cycle length of 60 days must be achieved
- Economic feasibility of the new core, i.e. no significant increase of operation costs
- No degradation of safety in every aspect

Especially the dimensional restrictions only leave the option to use a fuel with higher uranium density, when the enrichment is reduced while maintaining the neutron flux. In doing so, the total inventory of fissile ^{235}U per fuel element even has to be increased to compensate for the increased absorption of neutrons by the higher content of ^{238}U. Hence, high-performance research reactors require a significantly higher uranium density for conversion. Such a high-density fuel is not available yet and has still to be qualified. Three promising candidates are currently under investigation:

- Dispersed U_3Si_2 with higher U density
- Dispersed U-Mo in Al matrix
- Monolithic U-Mo

The dispersed silicide fuels are currently qualified for low and medium neutron flux reactors up to a uranium density of $4.8\,\mathrm{g/cm^3}$ [83]. Dispersed U-Mo fuel can reach higher U densities up to $8\,\mathrm{g/cm^3}$ [137], however, the higher neutron capture cross section of Mo (2.5 barn) compared to Si (0.166 barn) [84] requires additional fuel loading to compensate for the higher neutron absorption. Finally, the option of *monolithic* fuel is defined by a single foil of U-Mo alloy that makes up the fuel meat. This type with a uranium loading of $> 15\,\mathrm{g/cm^3}$ is the only current option to achieve an LEU core. With this in mind, this thesis focuses on U-Mo monolithic fuel for the conversion of FRM II.

TUMs efforts to develop high density uranium fuels for the purpose of conversion to lower enrichment are embedded in European and international cooperations. For Europe this is the HERACLES Consortium [10, 39], an association of European fuel developers and nuclear research centers that operate reactors including CEA (Commissariat à l'énergie atomique et aux énergies alternatives), Framatome CERCA, ILL, and SCK CEN (Studiecentrum voor Kernenergie). The fuel development at TUM is accompanied by core design for a lower enriched core. This comprises neutronic and thermohydraulic calculations. Both efforts are strongly interconnected to similar endeavors in the US by the NNSA (National Nuclear Security Administration), a federal agency that is part of the DOE. As an outcome of these international cooperations, TUM and the US partners recently published a study on a monolithic U-Mo core design for the FRM II [105].

1.2 Fuel Development & Qualification

In general, a fuel type is *qualified* when a regulatory body agrees to its use within specified limits of uranium density and operating conditions in one or more of its licensed research reactors. Further, it is agreed upon that it can be reliably and consistently manufactured to the required specifications by at least one manufacturer. To achieve this, a certain fuel undergoes a thorough procedure of data acquisition and testing. Guidelines for this process are for example defined by the *International Atomic Energy Agency* (IAEA) [33] or in the US by the *Nuclear Regulatory Commission* (NRC) [83].

Until a reactor conversion to a new fuel is successfully realized, multiple aspects have to be considered, which can be categorized and divided into working groups on *fuel qualification*, *fuel fabrication*, and *reactor conversion*. These separate entities focus on their specific topic while receiving feedback and sharing data to adjust the possible parameter space. In a first phase, the generic specifications of a fuel are set, including the conceptual design, the development of the manufacturing process, out-of-pile testing of fresh fuel, and finally irradiation testing with post-irradiation examinations (PIE). If successful, the reactor-specific geometry is then further developed in the second phase. Knowledge of critical physical properties is gradually established in the process: first for the material itself (chemical and phase composition, heat capacity, thermal conductivity, mechanical properties, geometry, grain size distribution, thermal expansion coefficient,...), then for a fuel plate (fission density distribution, plate swelling, blister formation, cladding corrosion, fission product release,...), and finally for the whole fuel assembly (neutronics, hydraulic and mechanical behavior,...). A detailed fuel qualification plan exemplarily for monolithic U-10Mo fuel for US HPRRs can be found in [17].

Irradiation experiments are the central touchstone to evaluate the performance of a fuel. In the early phase of a fuel qualification program, the first irradiation tests are performed on mini-plates, which are at least a magnitude smaller in size than the designated final size. This allows for a larger number of individual test plates in the limited reactor space available. Accordingly, this is used as a scoping procedure to select a fuel design by investigating multiple variables and generating a high statistical confidence. For monolithic U-Mo fuel, such a down-selection process has been conducted with several irradiation campaigns at the ATR that included parameters like the Mo content, diffusion barrier application, and techniques for bonding of fuel and cladding [112]. To identify scale-up effects, selected designs are consequently tested in full-size irradiation tests for prototypic-scale geometries that provide a more representative power profile under HPRR operating conditions.

For monolithic U-Mo fuels, the interface between fuel and cladding turned out to be a major issue. The formation of an amorphous interaction layer – also known as interdiffusion layer (IDL) – at this interface displays many porosities by the accumulation of fission gases (see Figure 1.4). This substantially affects the fuel performance because of decreased thermal conductivity and by the accumulation of fission gases in the pores of the IDL, which promotes plate swelling and debonding of fuel meat and cladding. Similar issues with the formation of detrimental interaction layers have been encountered before at other fuel types.

A way to tackle this is the application of protective layers between the diffusing components [46]. Plates with such diffusion barriers were fabricated and showed a significantly improved performance in irradiation tests (see Figure 1.4).

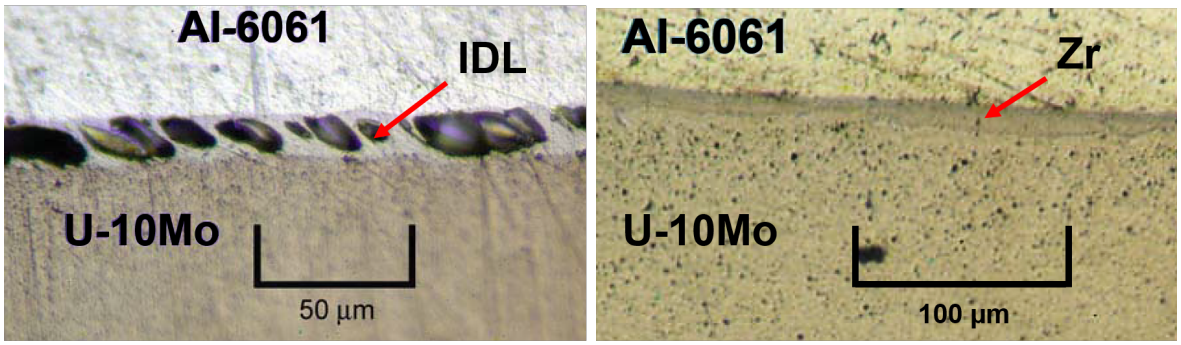

Figure 1.4: Micrographs of irradiated fuel plates with monolithic U-10Mo and Al-6061 cladding. A porous IDL that accumulates fission gases formed on the interface of fuel and cladding (left) at fission densities of up to $7{\cdot}10^{21}$ fissions per cm^3. A diffusion barrier of Zr applied in between inhibits this effect at similar fission densities (right). Based on [112].

1.3 Plate Fabrication

Before a fuel plate of monolithic U-Mo is ready for its use in a reactor, it has undergone various production steps. The following describes the process developed in the US:

First, the fuel foil is produced, which is schematically depicted in Figure 1.5. It starts with the alloying of the U-Mo, which is usually done in two steps: production of a master alloy composed of depleted uranium (DU) and Mo followed by a blending with HEU to cast the final ingot. After that, the ingots are annealed to homogenize the Mo content (see Figure 1.6(left)). For the rolling step, the ingots are canned into a welded steel assembly together with a Zr foil as diffusion barrier. The following hot co-rolling step targets a thickness reduction of about 75 % and is followed by thermal annealing to decrease the mechanical stresses introduced by the rolling. After that, these so-called *master foils* are de-canned (see Figure 1.6) and subsequently undergo the cold-rolling step to smooth out fuel meat thickness variations and to precisely establish the designated final foil thickness. A second annealing step is performed before the foils get their final dimension by shearing. A more detailed description of this fabrication process can be found in [42, 48, 80].

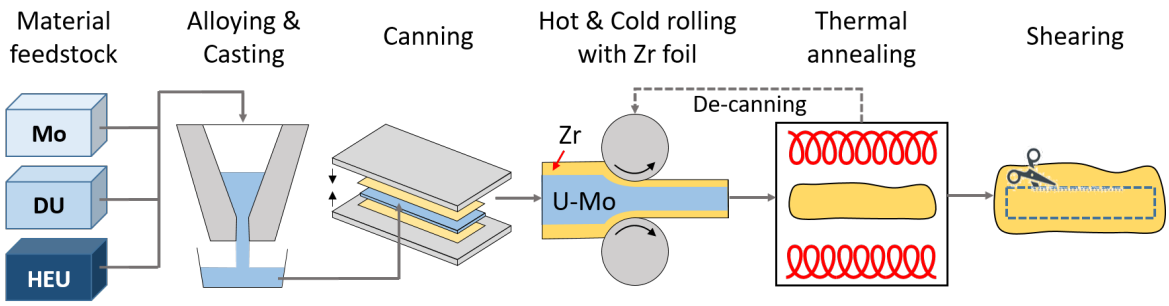

Figure 1.5: Schematic of the fabrication process for monolithic U-Mo foils with Zr diffusion barrier.

This fabrication process was established in the framework of the US fuel development program, which investigated multiple manufacturing options for the different production steps. They finally settled for hot co-rolling instead of plasma spraying and electroplating to apply a diffusion barrier, and for hot isostatic pressing (HIP) instead of friction stir welding and transient liquid phase bonding to subsequently apply the Al6061 cladding [50, 110]. Zr became the standard diffusion barrier material as it combines satisfying irradiation behavior with practicable producibility.

Figure 1.6: Exemplary images from the foils fabrication process. As-cast ingots prepared for homogenization (left) and a master foils after de-canning (right). From [42].

The European fuel development program [136], however, chose to investigate another approach for monolithic fuel which includes physical vapor deposition (PVD) for the application of the diffusion barrier and AlFeNi as a cladding material, which is applied by the C2TWP process proprietary to Framatome-CERCA [130]. Especially the PVD process shows great potential due to its versatility to influence the mechanical properties of the barrier coating and the production of arbitrary layer thicknesses [8, 119, 132]. However, this is an additional production step when compared with the co-rolling, where the application of the diffusion barrier is simply included in the production of the fuel foil. For PVD coating with a diffusion barrier, the above-described foil fabrication process stays the same in principle. By just leaving out the Zr foil before the hot-rolling step, a so-called bare foil is produced in the end.

1.4 The Aim of this Thesis - from EMPIrE to FUTURE-MONO-1

The PVD process for its application in the fabrication of monolithic U-Mo fuel plates was investigated and refined at TUM for mini-size foils by Steyer [132]. This led to the first irradiation test that included foils of this type – the EMPIrE campaign [37]. The plates were put into the ATR reactor alongside plates produced with a co-rolled Zr diffusion barrier layer of the same thickness for a direct comparison. They were successfully irradiated and showed stable and predictable swelling behavior in non-destructive examinations [113]. After several years of cool-down, these foils are ready for destructive examination, which is performed in the framework of this thesis. Additionally, unirradiated fuel plates that were produced in preparation for the EMPIrE test are also characterized as a comparison.

In the meantime, Baumeister advanced the capabilities at TUM and constructed a PVD device to coat full-size foils [8]. After parametrization and preliminary tests with stainless steel foils, the device is now ready for parameter studies with U-Mo foils in preparation for the upcoming full-size irradiation experiment FUTURE-MONO-1 planned in 2023. Figure 1.7 shows schematically the development steps towards this irradiation test. The LEU foils for irradiation will be produced at Framatome. TUM performs the coating with the Zr diffusion barrier and sends the foil to Framatome, where the cladding is applied and thereafter the final fuel plate is produced. The irradiation will finally be conducted at the BR2 reactor at SCK CEN. Each production step is carried out multiple times with subsequent characterizations, testing different production parameters and using the gained knowledge for previous steps. This feedback loop ensures to gradually approach suitable fuel plate quality for a successful irradiation test.

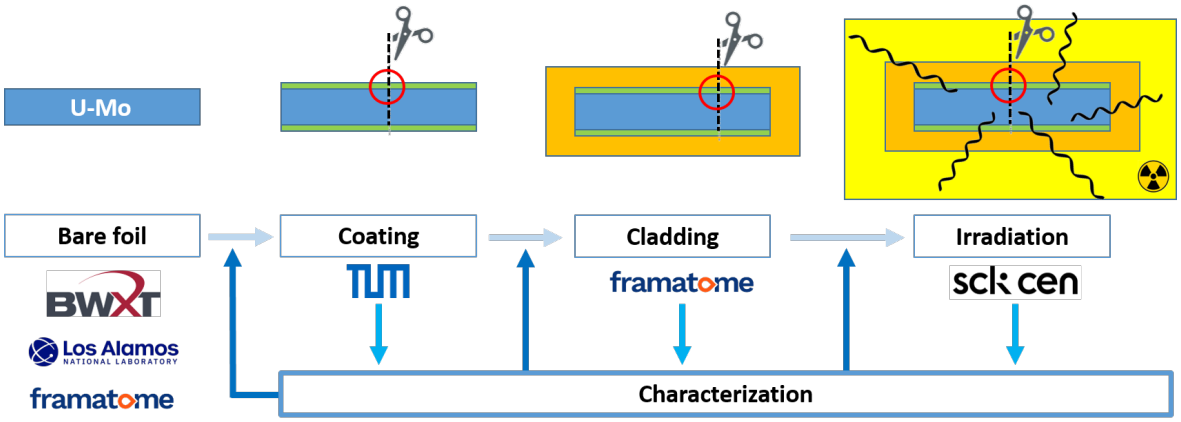

Figure 1.7: Scheme showing the iteration loops of characterization for different steps of fuel development.

The versatility of the PVD coating process provides the opportunity to look into potential alternative diffusion barrier materials that may otherwise not be feasible to produce with other techniques. Correspondingly, this thesis also investigates certain aspects of molybdenum and tungsten coatings concerning layer properties and diffusion behavior.

Chapter 2

Theoretical Background

This chapter lays the theoretical foundation for the experimental content dealt with in this thesis. It features relevant material properties of the different components of nuclear fuel plates, which includes fuel, cladding, and diffusion barrier materials. Then, diffusion in solids in general is treated from a mathematical and atomistic point of view. Finally, for the proper application of diffusion barrier layers, the theory of sputtering and layer growth is described in detail.

2.1 Material Properties

Nuclear materials are subject to strict requirements, especially due to high standards for safety. This calls for a fine tuning of multiple material properties in each component of a nuclear fuel plate. The following section gives an overview of the most important properties for monolithic U-Mo fuel plates, which includes the U-Mo fuel meat, the Al-based cladding, and possible diffusion barrier materials.

2.1.1 U-Mo Fuels

The fission of uranium is the central process of most nuclear reactors. Especially the fissile isotope ^{235}U contributes most to maintain the chain reaction, which makes the enrichment a crucial parameter. However, for the purpose of studying the material properties of a fuel candidate, the enrichment of uranium is of minor importance for investigating common material properties as the isotopic effects are minuscule. Therefore, most experiments for fuel qualification – except in-pile irradiations – are carried out with natural uranium (0.72 % ^{235}U) or depleted uranium and available data on material properties does usually not include information regarding enrichment.

Metallic uranium comes in three allotropic forms: Orthorhombic α-U is stable up to 668 °C, tetragonal β-U is stable from 668 °C to 770 °C, and cubic γ-U from 770 °C up to its melting point at 1135 °C. Based on this, one would think that at reactor conditions uranium fuel is naturally in its α-form. However, many of its properties are not desirable in reactor operation. Apart from its rapid oxidation [5], the biggest problem is the anisotropic behavior under irradiation, which is due to the orthorhombic crystal structure [75]. The lattice constants of α-U have different thermal expansion coefficients – one direction even shrinking, while the other two expand at increasing temperature – which results in microstructural strains that cause cracks or cavitation in the fuel during thermal cycling. This dimensional instability can be avoided by using γ-U, which displays isotropic expansion due to its body-centered cubic (bcc) crystal structure and is also the most malleable and ductile form.

This phase, however, is only stable at higher temperatures. For low temperatures, it decays into the thermodynamically favored α-phase. In order to stabilize the γ-phase, the uranium is alloyed with molybdenum forming the metastable γ-U-Mo. Other transition metals from group V to VIII also have this stabilization ability like zirconium and niobium, which also feature a high melting point and thermal conductivity as well as a good corrosion resistance. Molybdenum was chosen because it combines these relevant properties with a comparatively high density (10.22 g/cm^3). A disadvantage is the thermal neutron absorption cross section of 2.5 barn compared to 1.11 barn for Nb and 0.19 barn for Zr [84].

Figure 2.1 shows the U-Mo equilibrium phase diagram illustrating the different areas of composition and temperature in which a certain phase is stable. Some areas consist only of a single phase, while others contain two separate phases in varying ratios. Phases in brackets indicate a phase that is not pure but mixed with some other component. For example, (γ-U) is a γ-U-rich phase in which a certain amount of Mo is dissolved. If the composition of this

phase is changed by adding more and more Mo, the solubility limit of Mo in γ-U is reached at some point entering a two-phase region, where the undissolved (Mo) and the (γ-U) form separate phases dissolving some amount of the other one. At certain concentrations it might happen that so-called *intermetallic phases* with a very small region of concentration variation are formed, that often (but not necessarily) have a stoichiometric composition. U and Mo form the intermetallic U_2Mo phase, which is also known as the γ′-phase. It can have slight stoichiometric variations (otherwise it would be just a vertical line in the phase diagram and not an area), but it is always a pure phase and does not dissolve other phases of U and Mo (therefore it is not in brackets in the adjacent two-phase regions).

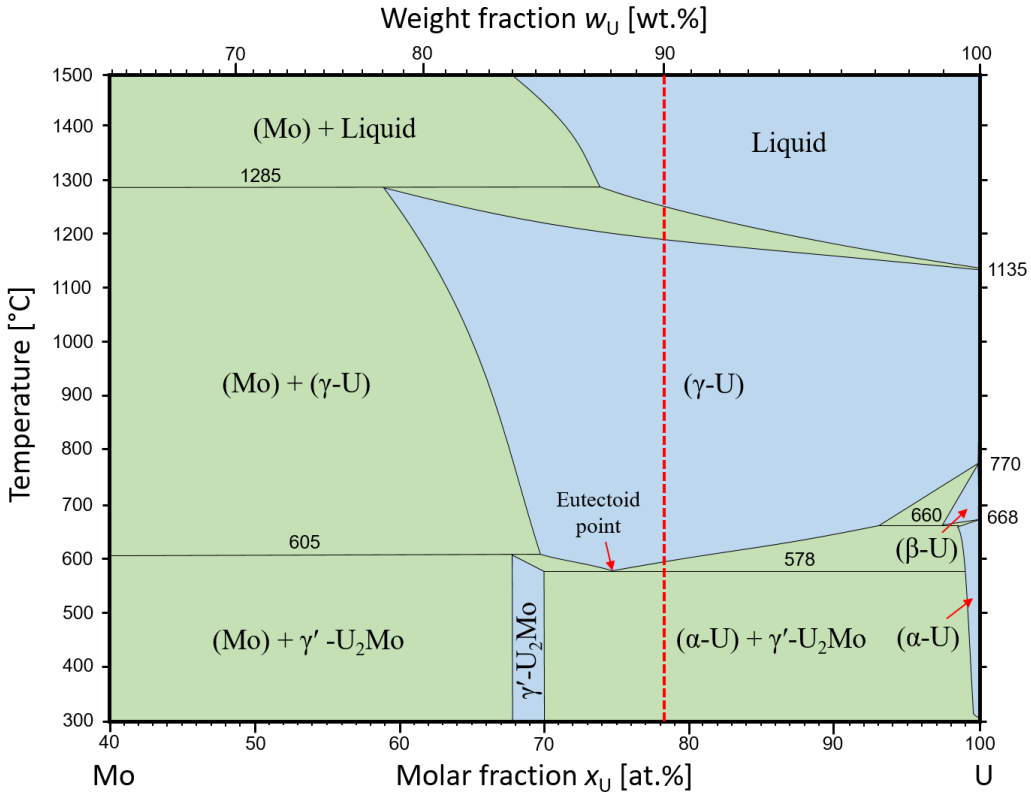

Figure 2.1: Binary phase diagram of the U-Mo system. Single phases are colored in blue, while double-phase areas are green.The dashed line indicates the position of U-10wt.%Mo. Data from [139].

The desired phase for nuclear fuels is the γ-U with dissolved Mo. This material is produced by alloying the desired amounts of U and Mo at an adequate temperature conform with the corresponding region in the phase diagram. The lowest temperature at which this phase is stable is 578 °C at the eutectoid point. Subsequent quenching creates the final γ-(U-Mo) at room temperature with its stability depending on the amount of dissolved Mo. In general, more Mo content corresponds to a higher stability [99]. However, the higher the amount of molybdenum, the lower the effective uranium density in the fuel, and the more thermal neutrons are absorbed by the Mo. As a result of the tradeoff between these effects, 12 wt.%

of Mo is considered the maximum practical content for research reactor fuels [43]. This thesis deals exclusively with U-Mo alloys of 10 wt.% Mo, which corresponds to a molar fraction of 78.4 at.% U. Accordingly, any "U-Mo" in the following text means "U-10wt%Mo" if not specified otherwise.

Although the γ-phase is stabilized with the Mo content, it is still metastable at low temperatures and ultimately decays into the α- and γ′-phase. The rate of this decay depends on the temperature and can be visualized by a time-temperature-transformation (TTT) diagram. Figure 2.2 presents the corresponding diagram for U-10wt.%Mo. At room temperatures, the γ-phase is basically stable. The higher the temperature gets, the faster the diffusion-driven decay is. The maximum decay rate is reached at just under 500 °C, where the cellular reaction forming α-U starts already after about 5 hours. Above this, the decay rate is slower again as the temperature gets closer to the stable regime of the γ-phase. This stable region is a few degrees above the eutectoid temperature as U 10wt.%Mo is slightly right to the eutectoid point (see U-Mo phase diagram, Figure 2.1).

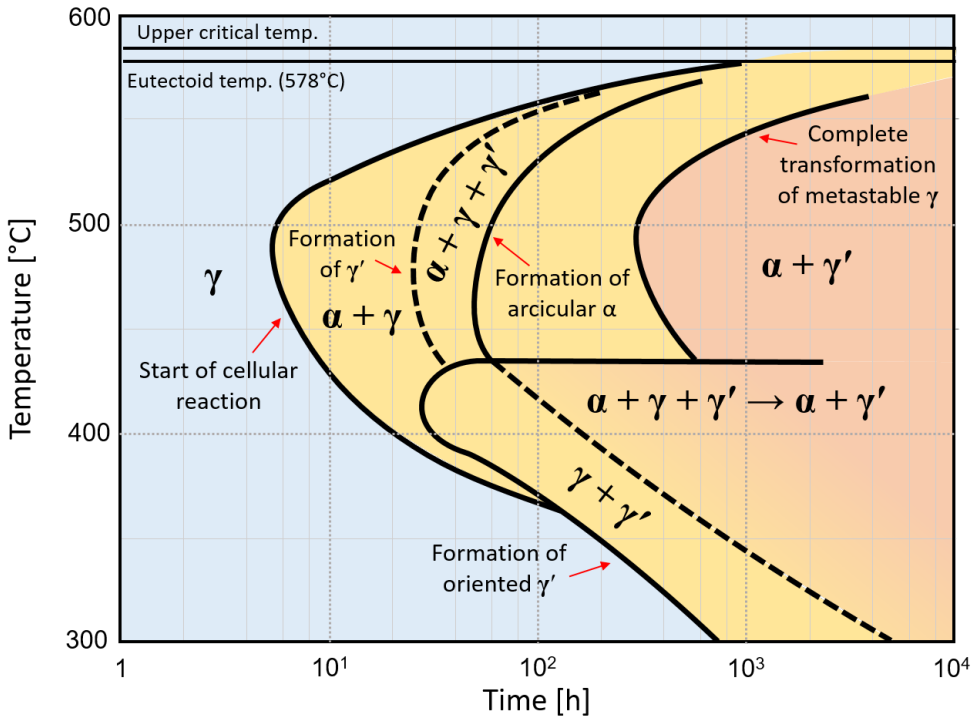

Figure 2.2: TTT diagram of the U-10wt.%Mo alloy. Regions of pure γ phase are colored blue, regions of partial decay into other phases yellow and complete decay red. Based on [107].

The TTT diagram gives an overview of to what extent post-alloying processes are compatible with the γ-phase integrity of the fuel. These processes may include hot-rolling and cold-rolling of the cast ingots to fabricate foils [42], annealing steps [47], PVD coating, and cladding application techniques like hot isostatic pressing (HIP) [92]. It must be ensured that no significant amounts of undesired phases are produced that way.

2.1.2 Cladding Material

The cladding is the outer layer of a fuel plate that separates the fuel from the cooling water, and therefore retains the fission products. Material requirements on the cladding are a low thermal neutron absorption cross section, a high corrosion resistance and a high thermal conductivity. Power reactors usually use zirconium alloys, but for research reactors, which have a higher power density, a material with better thermal conductivity is needed to ensure the coolability, which is one of the key safety aspects. For this purpose, Al with a thermal conductivity of 220 W/m·K is used as base material. Although it reacts with oxygen/water, corrosion resistance is still given as it forms a thin passivation layer of Al_2O_3, which prevents further oxidation. However, hardness and tensile strength of pure Al need to be enhanced to serve as a structural material. This is done by alloying small quantities – to keep the absorption cross section low and the corrosion resistance high – of other elements into the Al in order to tune the desired mechanical properties. While the United States use Al 6061, an alloy of various constituents (Fe, Cu, Mn, Cr, Zn, Ti) with < 1 wt.% each, European high-flux reactors utilize AlFeNi (about 1 wt.% of Fe, Ni and Mg) with a better corrosion resistance at higher temperatures [43].

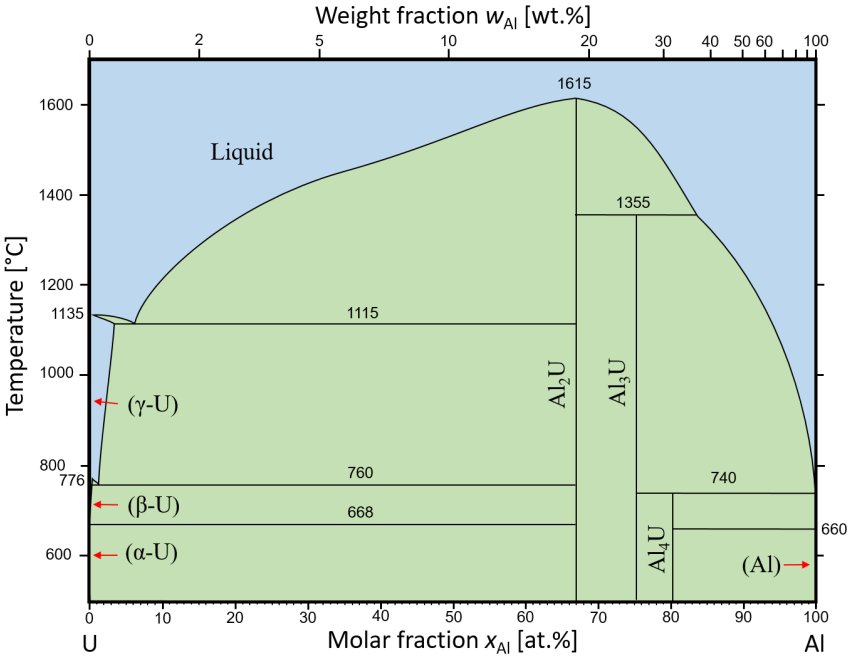

Figure 2.3: Binary phase diagram of the U-Al system. Single phases are colored in blue, while double-phase areas are green. Based on [89].

A major issue of Al-based claddings is the chemical interaction with the U-Mo fuel. Uranium and aluminium display a strong affinity to interdiffusion, especially of U diffusing into Al [58]. Correspondingly, an interdiffusion layer forms at the interface of U-Mo fuel and Al cladding, which mostly consists of the intermetallic compounds Al_2U, Al_3U, and Al_4U [98] (see phase diagram in Figure 2.3). These phases cause multiple issues like mismatch in thermal expansion, reduced heat transport, formation of porosities that accumulate fission

gases, and deterioration of the fuel/cladding bonding. In dispersion fuels, the interdiffusion can be reduced by alloying Si into the Al matrix [43]. However, doing this with the cladding of monolithic fuels is not an option as its composition is already designed to fulfill the mechanical requirements. The solution is here to introduce a thin layer of another material between fuel and cladding that acts as a diffusion barrier.

2.1.3 Diffusion Barrier Materials

In order to reduce the intermixing of fuel and cladding a third component has to be introduced at the interface. To act as such a diffusion barrier, the material foremost should display a low diffusion tendency with all involved components forming no or only insignificant amounts of intermetallic phases, that are stable under irradiation. Especially refractory metals are promising candidates for this purpose. A finer selection is achieved when other properties related to reactor operation are taken into account. This involves a high melting point, high thermal conductivity, low absorption cross section for thermal neutrons, and a good corrosion resistance. Furthermore, linear expansion coefficients of the diffusion barrier materials should be close to U-Mo ($11.7{\cdot}10^{-6}\,\mathrm{K}^{-1}$ [102]) to avoid mechanical stress and debonding at the interfaces. Various studies have been performed to investigate suitable elements or compounds [13, 40]. The candidates relevant for this work are presented in the following.

Zirconium

Zirconium is a refractory metal with a density of $6.5\,\mathrm{g/cm^3}$ and a low absorption cross section of 0.19 barn. It comes in two phases before it melts at 1855 °C. The hexagonal-close-packed (hcp) α-Zr transforms into the bcc β-Zr at 863 °C. As mentioned before, its thermal conductivity of $24\,\mathrm{W/m{\cdot}K}$ is too low to be considered as a cladding material for research reactors, however, for a thin diffusion barrier in the order of 10 to 30 µm this is sufficient. Like Al, it quickly forms a passivation layer of its oxide ZrO_2 and is therefore strongly resistant to corrosion. Commercially available Zr contains up to 4 at.% hafnium (Hf) due to their close chemical resemblance. This poses a problem as Hf is known as a strong neutron absorber usually used for control rods with its absorption cross section of 106 barn. Because of this, Zr used in nuclear reactors has to be additionally separated from Hf. This product is known as reactor-grade Zr.

Figures 2.4, 2.5 and 2.6 show the binary phase diagrams of Zr with the fuel and cladding materials U, Mo, and Al, respectively, to give an overview of possible reactions. Especially the intermetallic phases UZr_2 (hcp) and Mo_2Zr (fcc) are to be mentioned, as well as a wide variety of possible intermetallic Al-Zr compounds with different stoichiometric ratios at the interface of the cladding. Empirical diffusion results on these material combinations in form of diffusion couples and actual fuel plates with Al6061 cladding are described by [40] and [97]. In general, it was observed that no interdiffusion is visible for temperatures up to 600 °C and times of more than a month. This means that Zr is a suitable diffusion barrier for reactor conditions. For fuel fabrication processes like hot isostatic pressing, however, higher temperatures can be reached, which start to trigger diffusion processes.

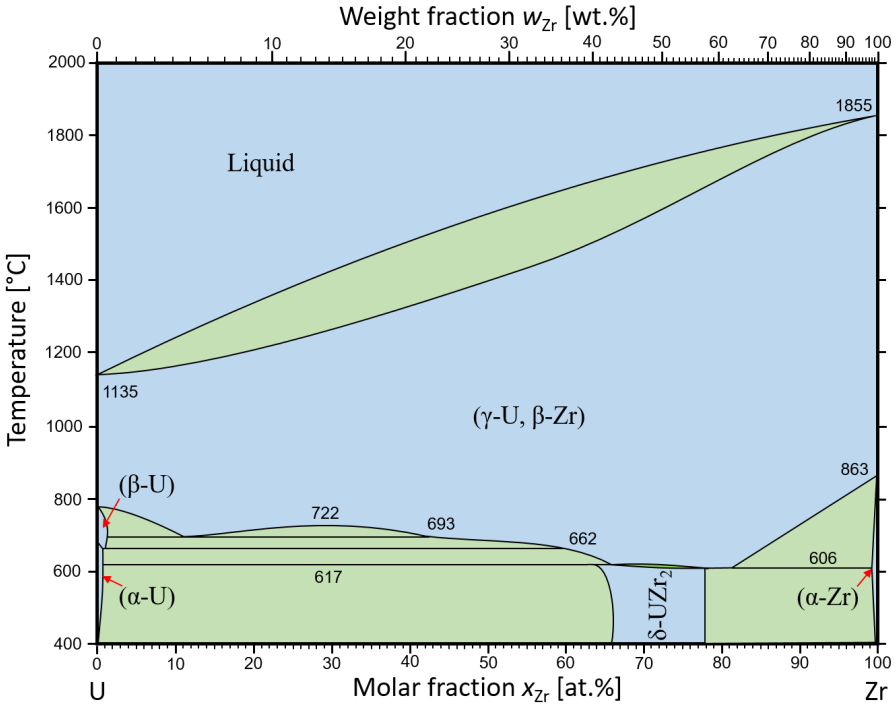

Figure 2.4: Binary phase diagram of the U-Zr system. Single phases are colored in blue, while double-phase areas are green. Based on [87].

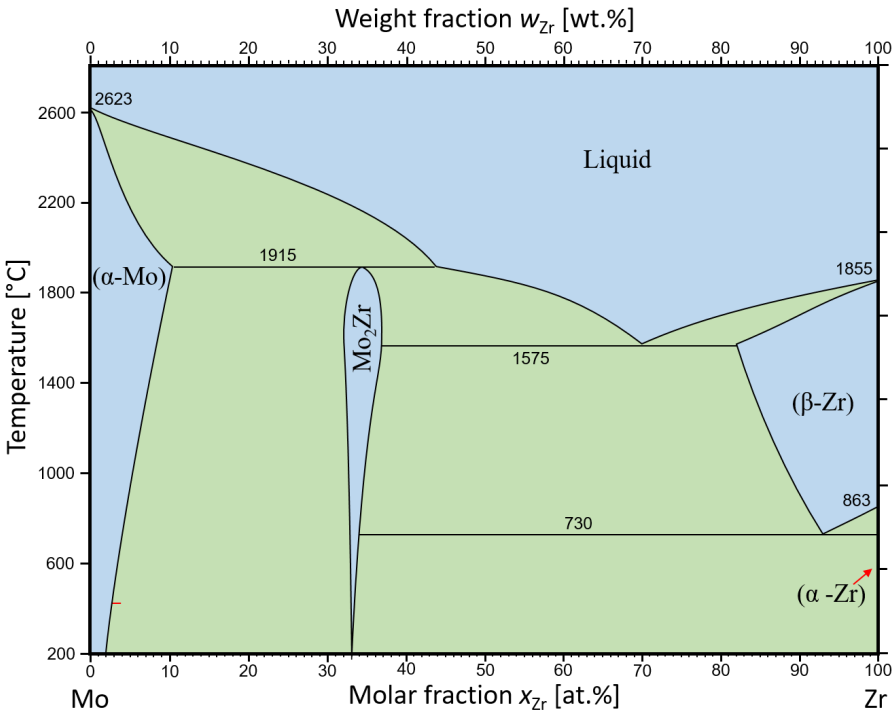

Figure 2.5: Binary phase diagram of the Mo-Zr system. Single phases are colored in blue, while double-phase areas are green. Based on [141].

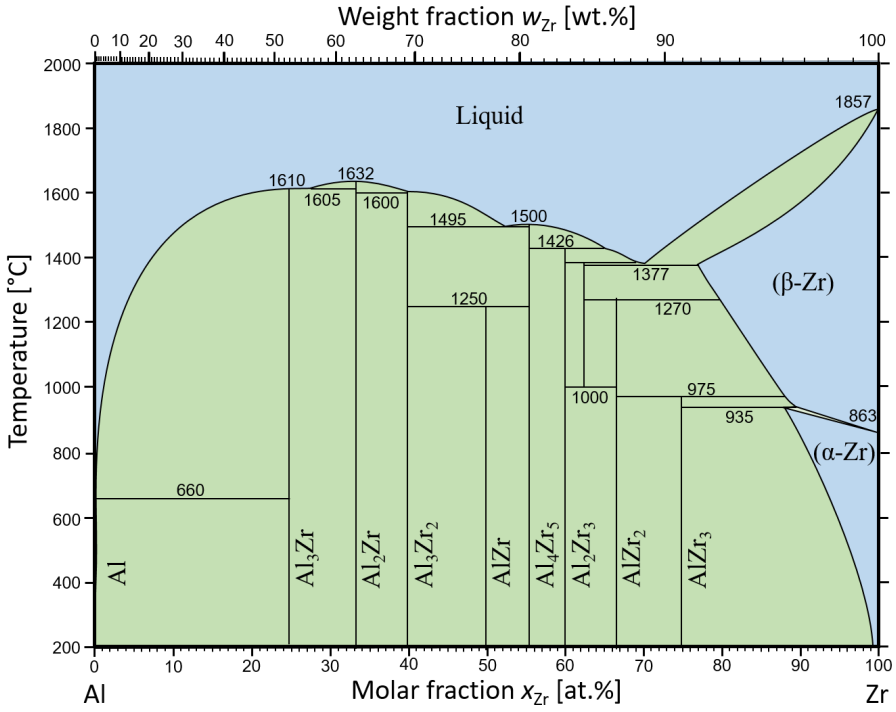

Figure 2.6: Binary phase diagram of the Al-Zr system. Single phases are colored in blue, while double-phase areas are green. Based on [60].

In case of temperatures of 700 °C and above, it is shown that the diffusion process at the fuel interface proceeds as follows: β-Zr starts to form, which is – supported by the same crystal structure – completely soluble in the γ-U. A layer of γ-U and β-Zr forms accordingly, as well as UZr_2 (see phase diagram in Figure 2.4), while the Mo has a lower solubility in the Zr-phases and starts to enrich in the U-Mo until precipitates of Mo_2Zr start to form. This, on the other hand, depletes the Mo in the U-Mo and destabilizes the γ-phase, which decays forming α-U as described in Section 2.1.1. Furthermore, other intermetallic phases of all three components like U_4MoZr_5 can form, which is visible when the three binary phase diagrams of U, Mo, and Zr are combined to form the ternary U-Mo-Zr phase diagram depicted in Figure 2.7. Phases like this, however, are of minor importance for the diffusion process [21]. It is also observed that all intermetallic products formed by this interdiffusion process appear to be stable under irradiation [114].

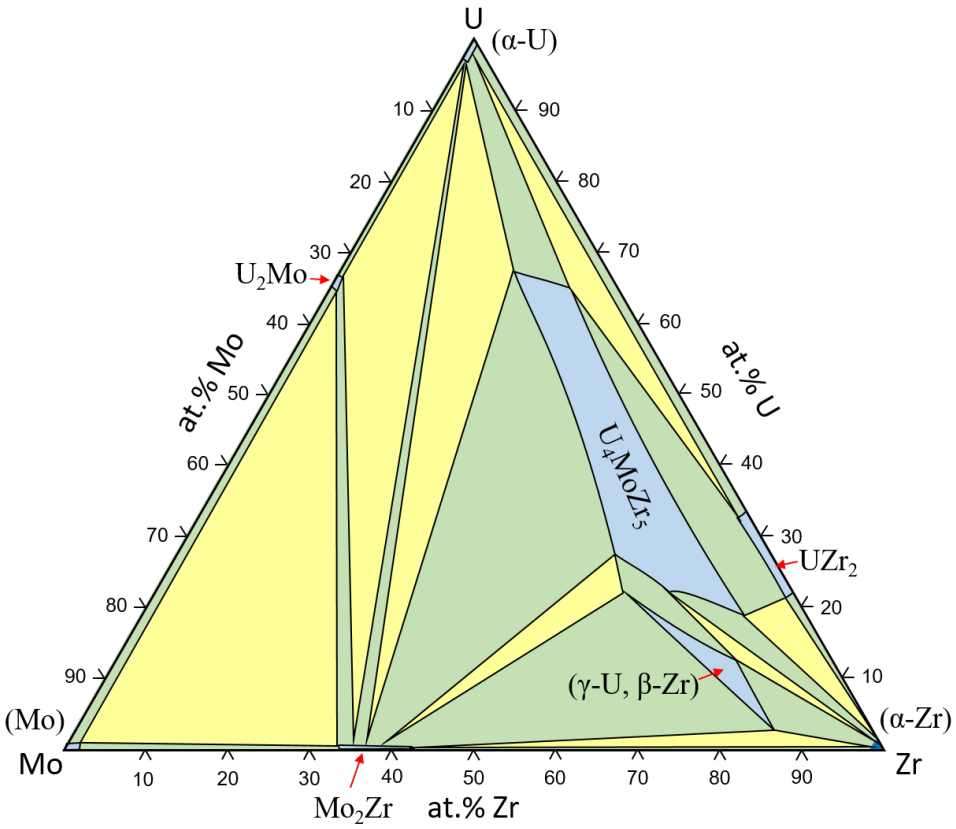

Figure 2.7: Ternary phase diagram of the U-Mo-Zr system at 500 °C. Single phases are colored in blue, double-phase areas are green, and triple-phases are yellow. Based on [140].

The same holds true for the Zr/Al interface. Of the many possible intermetallic line phases (see Figure 2.6) mostly Al_3Zr forms at temperatures of about 600 °C and small amounts of Zr_2Al_3 for temperatures above that.

Molybdenum

Molybdenum offers the opportunity to reduce interdiffusion without introducing another element into the fuel plate as it is already part of the U-Mo fuel meat. This is an advantage for reprocessing of the fuel, which is more complex the more different materials are involved. The crucial material properties for its use as material in nuclear fuels are already described in Section 2.1.1. It is clear that diffusion of Mo into the U-Mo fuel does not significantly compromise the fuel, since the solubility of Mo is limited in the γ-U (see Figure 2.1) [40].

Figure 2.8 shows the binary phase diagram of the Mo-Al system. It is immediately apparent that multiple intermetallic phases like Mo_3Al, $MoAl$, Mo_3Al_2, Mo_3Al_8, and $MoAl_5$ form. Especially in the Al-rich region many additional compounds are reported that are not included in the depicted phase diagram, like $MoAl_3$, $MoAl_4$, Mo_5Al_{22}, and $MoAl_{12}$ [118].

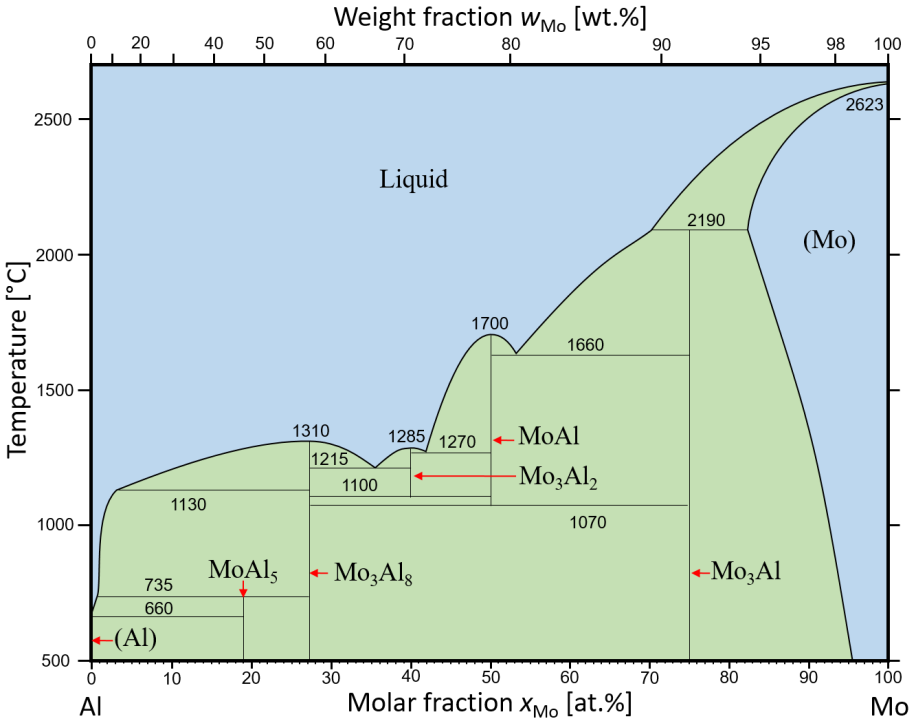

Figure 2.8: Binary phase diagram of the Al-Mo system. Single phases are colored in blue, while double-phase areas are green. Based on [120].

Tungsten

Tungsten is a heavy metal with a high density (19.25 g/cm^3) and an excellent corrosion resistance as well as a high thermal conductivity of 164 W/m·K. In thermal equilibrium, only one (body-centered cubic) structure is present till it melts at 3422 °C, which is the highest melting point of all metallic elements.

W and U are barely soluble into each other and form no intermetallic phases (see Figure 2.9). In combination with Al, phases like WAl_4, WAl_5, and WAl_{12} are known at temperatures below 700 °C and more than 10 wt.% of Al can be dissolved in α-W (see Figure 2.10).

A disadvantage compared to the other candidates is the high neutron absorption of 18 barn [84], which may be able to be partly compensated by using thinner diffusion barrier layers, as theoretical models suggest that tungsten is a more effective diffusion barrier than other candidates (see Section 2.2.5). Furthermore, tungsten is known to be very brittle, which can pose a problem for the integrity of the barrier layer after processes where mechanical stresses occur. Especially impurities can significantly worsen its ductility [106].

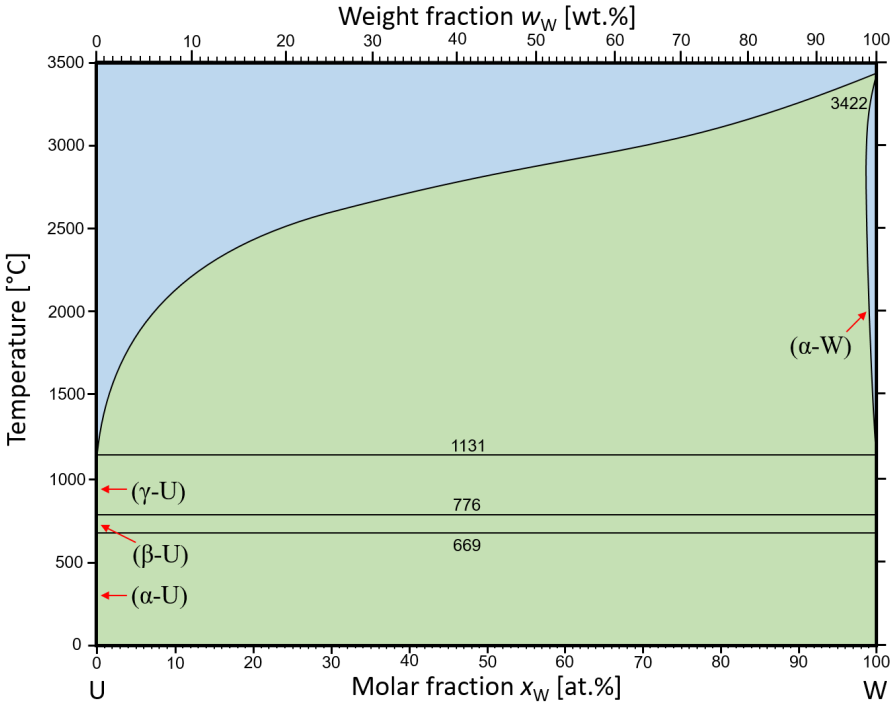

Figure 2.9: Binary phase diagram of the U-W system. Single phases are colored in blue, while double-phase areas are green. Based on [142].

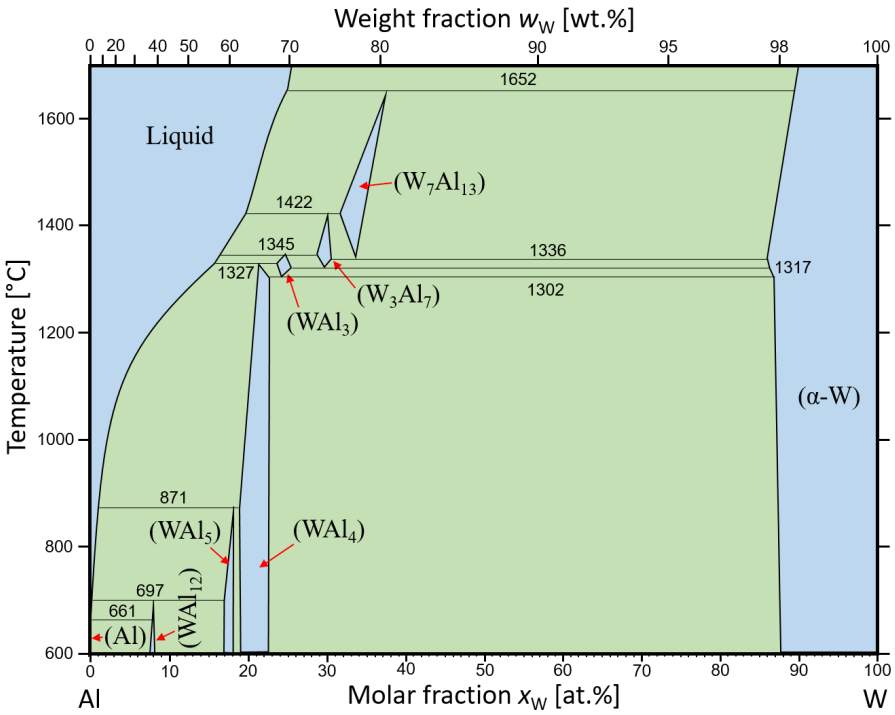

Figure 2.10: Binary phase diagram of the Al-W system. Single phases are colored in blue, while double-phase areas are green. Based on [138].

2.2 Diffusion in Solids

The following sections deal with the topic of diffusion. First, from a general point of view that introduces the mathematical description, followed by an examination of the underlying phenomena in solids on an atomic level. The formation of solid phases is exemplarily shown using hypothetical diffusion couples while introducing the Gibbs free energy and the chemical potential as driving forces. The picture is then expanded towards polycrystalline materials as the enhanced diffusion along grain boundaries has a significant impact. Finally, the semi-empirical Miedema model is presented as a way to estimate the magnitude of interdiffusion between material combinations, which can serve as an informative basis for the choice of potential diffusion barrier materials.

2.2.1 Fick's Law & Diffusivity

On a large scale, nature shows a general trend towards disorder as a statistical consequence of random motion. The measurable state function of this disorder is called the *entropy S*. Subsequently, separated sets of particles intermix over time to form a homogeneous system if no other separating forces are involved. This net movement of particles is known as *diffusion*. A phenomenological continuum description of these processes is given by *Fick's laws*, which were postulated as empirical observation by Adolf Fick in 1855.

Fick's first law says that the *diffusion particle flux* $\boldsymbol{j}$ is caused by the negative gradient of particle number concentration C with a proportionality constant D, the *diffusion coefficient* or *diffusivity* [73]:

$$\boldsymbol{j} = -D \cdot \nabla C(\boldsymbol{x}, t) \tag{2.1}$$

The flux in turn changes the concentration. This co-dependency together with the conservation law that particles are neither destroyed nor created results in the *diffusion equation*, known as Fick's second law, that describes the temporal evolution of the scalar concentration field *C(x,y,z,t)*:

$$\frac{\partial C}{\partial t} = \nabla \cdot (D \nabla C) = D \Delta C \tag{2.2}$$

Analytical solutions of this equation, giving the concentration as a function of time and position, are known for several common geometries and can be found in textbooks like [73] and [96]. This will not be further elaborated here. While Fick's laws are valid in general, their phenomenological approach does not include the underlying physical processes that are necessary to describe the behavior of diffusion processes more realistically. Especially the diffusivity D is in reality anything but a constant. In anisotropic media, it is a second-rank symmetrical tensor $\overline{\boldsymbol{D}}$, which can be transformed to its three orthogonal principal axes to the form

$$\overline{\boldsymbol{D}} = \begin{pmatrix} D_1 & 0 & 0 \\ 0 & D_2 & 0 \\ 0 & 0 & D_3 \end{pmatrix}, \tag{2.3}$$

where D_1, D_2 and D_3 are called the *principal diffusivities*. In solids, the crystal system defines the degree of anisotropy. While, for example, cubic systems are isotropic ($D_1 = D_2 = D_3$), hexagonal systems are not ($D_1 = D_2 \neq D_3$) and as a result the diffusion flux $\boldsymbol{j}$ and the concentration gradient ∇C usually do not point in the same direction anymore. This modification of the diffusivity is still covered by the diffusion equation, but at the point where (principle) diffusivities are temperature-dependent or finally even dependent on the local concentration, a more fundamental view of the underlying phenomena is needed.

2.2.2 Random Walk Theory & Atomic Jumps

In order to get a more realistic view on diffusion, a change of perspective is needed from a continuous distribution of matter to an atomistic one with discrete particles. For solids this means that a certain tracer atom is displaced within a lattice structure that restricts the movement (except for amorphous materials). The most common mechanisms of such a displacement are depicted in Figure 2.11.

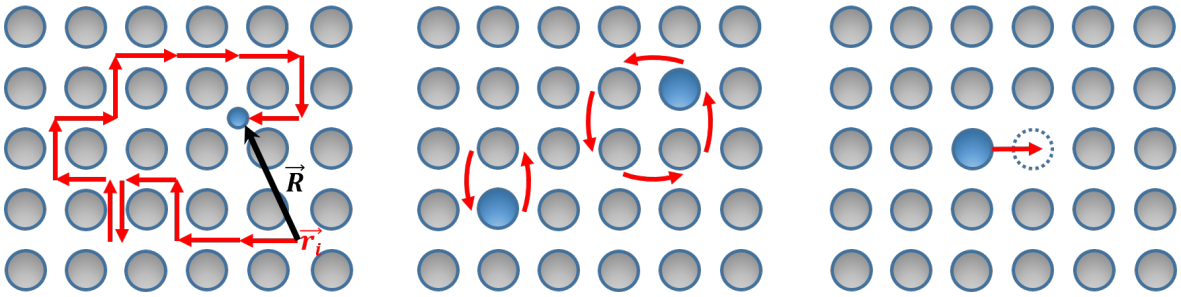

Figure 2.11: Diffusion mechanisms of tracer atoms (blue) in a crystal lattice (grey): Interstitial diffusion (left), direct exchange and the ring mechanism (middle), and vacancy diffusion (right).

The *interstitial mechanism* describes smaller particles moving between the interstitial sites of the solvent's host lattice. If the tracer particles are of similar size as the lattice atoms, they can diffuse by pushing a lattice atom into an interstitial site taking its place; a process which is called *interstitialcy mechanism*. Collective mechanisms summarize the exchange of a group of particles; either a direct exchange of two particles or a circular exchange of many atoms known as the *ring mechanism*. Finally, the *vacancy mechanism* is considered the most dominant process for the diffusion of matrix atoms [73]. Here, an atom moves by jumping into an unoccupied lattice spot, called *vacancy*, creating a new vacancy in its former position. Or – from a different point of view – the vacancy moves through the material causing intermixing.

Each position change of an atom to a neighboring lattice or interstitial site is called a *jump*. In crystals, the jumps usually have fixed length(s) d related to the lattice parameter a of a given crystal system. The rate of jumps Γ is promoted by thermal activation and follows an Arrhenius law [73]:

$$\Gamma = \nu^0 \cdot \exp\left(-\frac{\Delta G}{k_B T}\right) \tag{2.4}$$

The factor ν_0 denotes the *attempt frequency* of jumps, k_B the Boltzmann constant, T the temperature, and ΔG is the *Gibbs free energy* of activation, an energy barrier to overcome for a jump. Thus, the larger the thermal energy of the system, the higher the probability that a jump attempt is successful. Subsequently, the diffusivity can be expressed as the product of jump rate and distance per jump squared: $D = \Gamma \cdot d^2$. At this point, the temperature dependence of the diffusivity $D(T)$ becomes obvious and the maximum theoretical diffusivity at an infinite temperature D^0 is defined as a reference point.

When viewing the diffusion as *Brownian motion* in a lattice, i.e. as a series of single jumps, where every jump can also be reversed, it can be mathematically treated as a random-walk problem. Of special interest is here the evolution of the *total displacement* $\boldsymbol{R}$ of a diffusing particle, which is composed of all the *individual displacements* $\boldsymbol{r}_i$ of the single jumps (as depicted for the interstitial mechanism in Figure 2.11). Einstein [20] and Smoluchowski [127] analyzed the behavior of such a system and found the relation named after them

$$\langle R^2 \rangle = 2n \cdot D \cdot t \,, \tag{2.5}$$

which links the mean square displacement $\langle R^2 \rangle$ of an n-dimensional system to diffusivity and time t. This is also known as the *parabolic law*, which is visualized in Figure 2.12 showing the intermixing of two materials – a so-called *diffusion couple* – with a constant and uniform diffusivity.

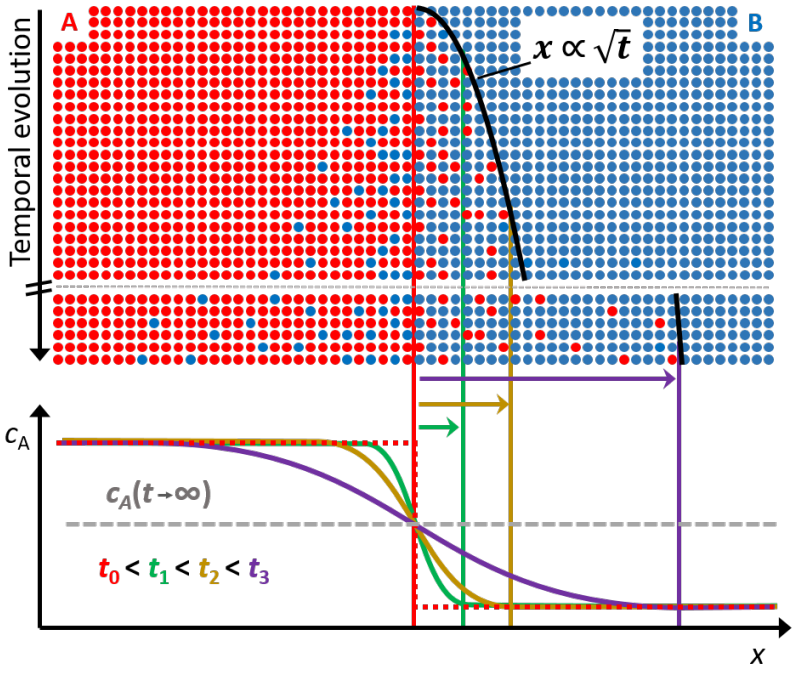

Figure 2.12: Schematic interdiffusion process of a diffusion couple of hypothetical materials A (red) and B (blue). The black line shows the parabolic law that the plane of constant concentration shifts with the square root of the time. Below is the evolution of the concentration profile over time.

In reality, however, the jumps may not always be completely random. Memory effects, where one jump influences the following ones, happen necessarily when vacancies are involved: If a vacancy jump is performed, the vacancy is now opposite to the tracer atom, thus increasing the probability of a back jump of the tracer atom. As a result, the diffusion efficiency is reduced with respect to a true random walk, and a lattice- and diffusion mechanism-dependent correlation factor is introduced that quantifies this effect.

2.2.3 Gibbs Free Energy, the Chemical Potential & Diffusion Couples

So far it has been assumed that the maximization of entropy is the sole cause for diffusive material flow. In reality, there is a range of external and internal driving forces that have an additional effect on the rate and direction of the particle flow. External forces can be the gravitation or an electric field; internal ones are properties of the material itself like stress gradients or chemical forces. Especially the latter are worth a closer look, as chemical behavior plays a major role in multi-element systems. For example, the idealized diffusion couple in Figure 2.12 assums an infinite solubility of the materials into each other, which is not the general behavior. Typical systems have a *miscibility gap*, a region of concentration where the limit of solubility is exceeded. As a result, the respective diffusion couples do not evolve towards a perfect mixture with equal concentrations on both sides of the initial interface but saturate instead at a certain level.

In general, for systems with multiple particle species i and corresponding particle numbers N_i, chemical effects come into play that shift the thermodynamic equilibrium. Instead of solely maximizing the entropy, a system more generally tends to minimize the so-called *Gibbs free energy* G (as already mentioned in equation 2.4), which includes the entropy S and the temperature T, as well as the *inner energy* U, the pressure p and volume V of the system:

$$G = U + pV - TS = H - TS \tag{2.6}$$

Inner energy, pressure, and volume can be combined to form the *enthalpy* H. The generalized driving force, which includes the concentration, is now the change of the Gibbs free energy with respect to the change of particle number of a given species N_i at constant pressure, temperature, and amount of particles of all other species. This *partial molar Gibbs free energy* is referred to as the *chemical potential* μ_i of species i:

$$\mu_i = \left(\frac{\partial G}{\partial N_i}\right)_{T,P,N_{j\neq i}} \tag{2.7}$$

In thermodynamic equilibrium at a constant temperature and pressure, the Gibbs free energy is at its minimum and does not change anymore, thus, the total sum of the products of each species' chemical potential with the respective stoichiometric amount is zero.

$$\mathrm{d}G = \sum_{i=1}^{n} \mu_i \, \mathrm{d}N_i = 0 \tag{2.8}$$

In summary, it can be said that diffusive flow is driven by a gradient of the chemical potential, of which material concentration is just one aspect. This includes the observed effect of diffusion towards higher concentrations, which is possible if chemical forces favor this direction.

With this knowledge, the hypothetical A-B diffusion couple with the miscibility gap already discussed above is examined again with the addition of an intermediate phase β between the A-rich solid solution phase α and the B-rich solid solution phase γ. Figure 2.13 depicts this scenario with the corresponding phase diagram shown in (A). A certain temperature T (dashed line) is chosen at which the three phases α, β, and γ are present as well as the two-face regions α+β and β+γ in between.

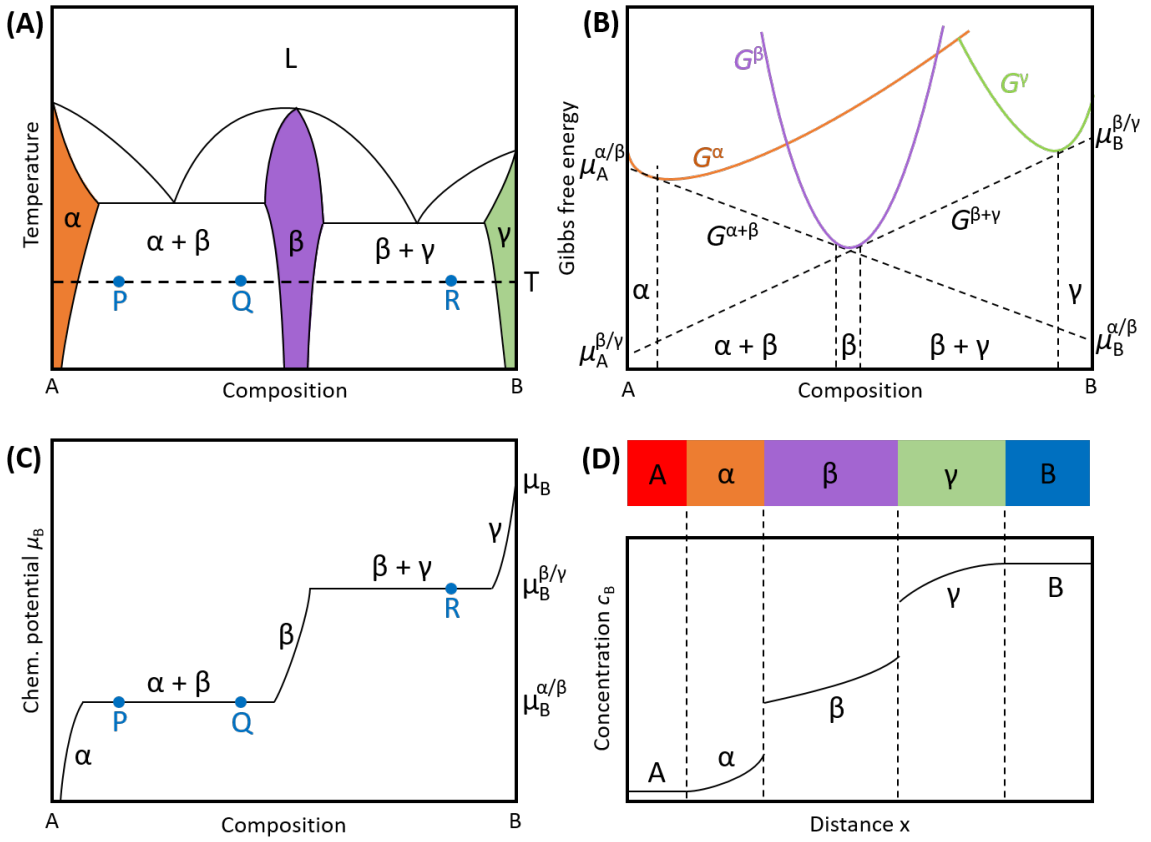

Figure 2.13: Behavior of a hypothetical A-B diffusion couple with the corresponding phase diagram (A), Gibbs free energy diagram (B), chemical potential variation of component B (C) and resulting concentration profile of component B (D). Based on [95].

To analyze the behavior of this system, Figures 2.13(B) and 2.13(C) show the Gibbs free energy diagram and the variation of the chemical potential μ_B (μ_A is just a similar behavior in reverse). The three stable phases can be seen as local minima of their respective Gibbs free energy curve. In the two-phase regions, the respective phases are separated from each other at their local minimum of G and thus, each component is in equilibrium. When their local composition is varied, the combined free energies $G^{\alpha+\beta}$ and $G^{\beta+\gamma}$ just change linearly

between the respective minima of the pure phases. As a result, the chemical potential stays constant in the two-phase region, while it continuously changes within a single phase. This local equilibrium of the two phases is just established at their interface. A phase mixture like α+β cannot grow in a binary interdiffusion zone; if it existed, the chemical potential would be constant throughout it, and thus, intermixing would stop as there is no driving force for diffusion anymore. To emphasize this, we form diffusion couples out of the alloys P, Q, and R as shown in Figures 2.13(A) and 2.13(C). Despite the fact that P and Q have different volume fractions of the phases α and β, no diffusion would happen as both alloys have the same chemical potential. For the coupling of alloys Q and R, on the other hand, a chemical potential difference is given, which would result in diffusion and growth of phase β. However, while this is true for any binary system, it's not valid anymore for ternary systems. Here, two-phase mixtures – but no three-phase mixtures – are possible due to an extra degree of freedom [94].

Figure 2.13(D) shows the resulting diffusion zone of the binary A-B couple with the phases that formed and a concentration profile of component B. When A and B diffuse into each other driven by μ_A and μ_B, the α- and γ-phases form. Then, the β-phase forms on the interface of α and γ driven by $\mu^{\alpha/\beta}$ and $\mu^{\beta/\gamma}$. The concentration at these interfaces can experience jumps due to the missing phase mixture.

Diffusion couple experiments are in practice a simple and versatile tool to study phase diagrams and determine diffusion characteristics in general. Likewise, investigations on diffusion behavior of monolithic U-Mo fuel plates are nothing but diffusion couple analysis – in this case, the considered couples are either fuel-cladding, fuel-diffusion barrier, or cladding-diffusion barrier. As the fuel (U-Mo) is already a compound of two elements, there are at least three components involved. Thus, in order to further expand the examples of Figures 2.12 and 2.13, a diffusion couple of a ternary system will now be considered in Figure 2.14.

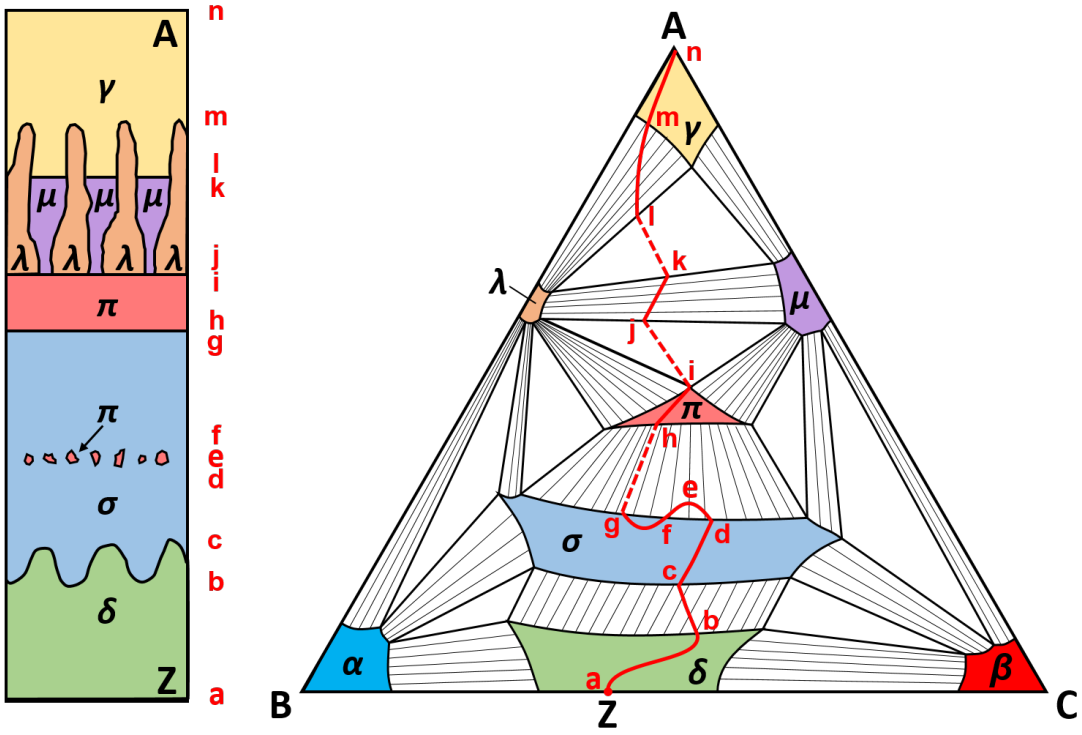

Figure 2.14: Isothermal section of a hypothetical ternary phase diagram of the components A, B and C with multiple phases distinguished by different colors. On the left is a reaction zone formed by the diffusion path in the phase diagram between the diffusion couple A-Z, where Z is within the δ phase consisting of B and C. Based on [95].

This diffusion couple consists of the pure component A and Z, a phase of B and C. As mentioned before, the diffusion zone for ternary systems can now show a more complex morphology with two phases present in the same area. Yet, unlike in binary systems, the phases formed and their exact morphology can generally not be deduced unambiguously from a given phase diagram. Conversely, however, the microstructure of the reaction zone can be visualized in the phase diagram by the so-called *diffusion path*. It represents the average composition of the reaction zone within planes parallel to the initial interface as points in the phase diagram. In Figure 2.14, various individual points of the path are highlighted by the letters a - n to show different zones. For example, a line crossing a single phase like (a-b) corresponds to an existing layer of phase δ in the reaction zone, while two-phase regions like (j-k) are located in the miscibility gap that connects the two phases λ and μ. Still, planar interfaces with a local equilibrium between two phases (i-j) can form as seen before in binary systems. As a result, there is, again, a discontinuity in the concentration and, consequently, the diffusion path is also not continuous and is represented as a dashed line. There are cases where regions of supersaturation near interfaces disturb local equilibria to from thermodynamically unstable structures that result in wavy interfaces (b-c) or precipitates (d-e-f).

2.2.4 Grain Boundary Diffusion

Some general mechanisms of diffusion as depicted in Figure 2.11 have been outlined above, and it was already mentioned that these mechanisms result in different diffusivities. However, for this picture, it has been assumed that the processes take place in the lattice of a perfect defect-free (except for the necessary vacancies) single crystal, which is commonly not the case. Most macroscopic materials with an intrinsic order are polycrystalline, which means that they consist of many microscopic *crystallites* or *grains* of different sizes that are perfect crystals on their own. These grains display a more or less random crystallographic orientation (see also Section 2.3.3 about crystal growth) within the material and as a result, neighboring grains share an interface, which is called the *grain boundary*. Depending on the tilt angle between them, visualized in Figure 2.15, grain boundaries display lattice distortions and open bonds. Low-angle boundaries (smaller than about 15 degrees) show discrete dislocations with a regular pattern, while for high-angle boundaries a regular structure is no longer given. These defects cause a higher energy of the grain boundaries than within the undistorted lattice, which gives rise to an increased diffusion along the grain boundaries. Compared to a free surface, at which the diffusion is also increased, high-angle boundaries have about a third of their energy [73].

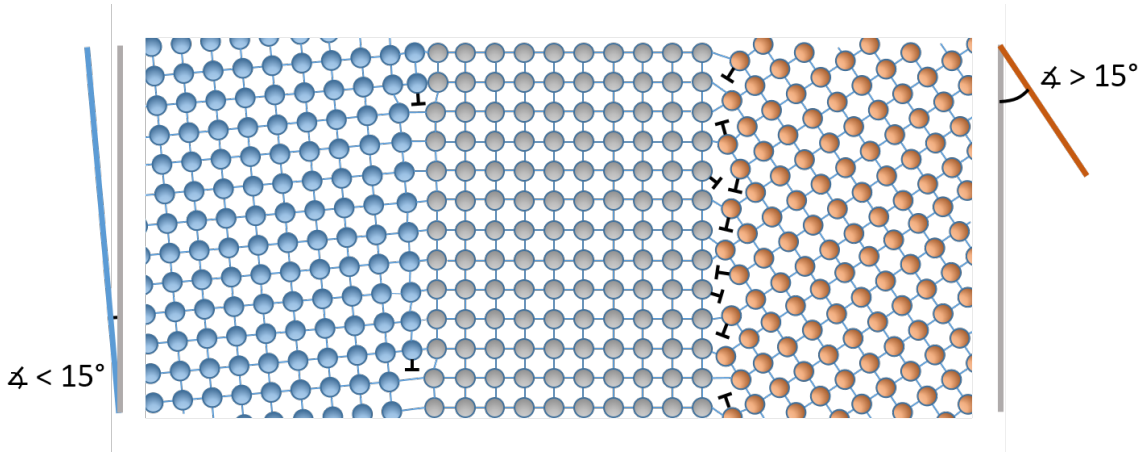

Figure 2.15: Schematic representation of 2-dimensional grain boundaries between three grains (blue, grey, red). The left boundary (blue-grey) has a low-angle misorientation resulting in slight distortions and occasional open bonds, while the high-angle boundary (grey-red) shows a lot more defects.

For the description of grain boundary diffusion, Fisher [24] developed a model (visualized as part of Figure 2.16) that treats the boundaries as semi-finite, isotropic slabs of thickness δ with a diffusivity D_{gb} embedded in grains of the lattice diffusivity D (usually $\ll D_{gb}$). The distance d between the slabs is a measure for the average grain size. Diffusion of tracer atoms into this model structure starting at the surface is now considered regarding a constant annealing temperature T and for a certain time t. Apart from the two obvious processes – diffusion from the source either directly into the lattice or along the grain boundary – leakage of the tracer atoms from the grain boundary into the lattice has to be considered as well. Depending on the relative impact of these effects, different diffusion regimes can

be categorized, that prevail in certain domains of annealing temperature (see also equation 2.4 – the activation energy for D is larger than that of D_{gb}), annealing times, grain sizes, lattice, and grain-boundary parameters. A typical classification into the regimes A, B, and C established by Harrison [38] is shown in Figure 2.16.

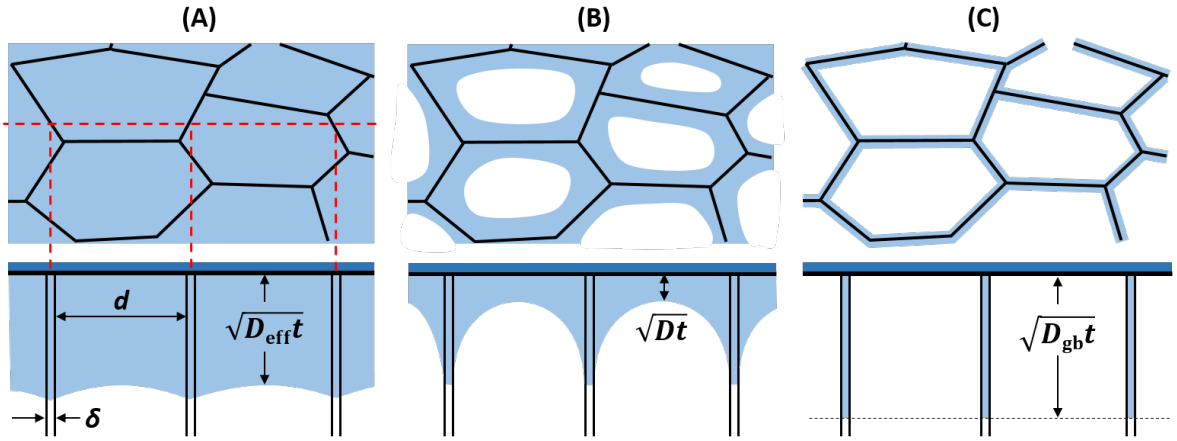

Figure 2.16: Different regimes of grain boundary diffusion. A source of diffusing particles (dark blue) is put onto the surface of a medium with a certain grain structure. The top row shows a surface-near section of the material parallel to the surface, the bottom row a vertical section based on Fisher's model. The penetration profile of the diffusant (light blue) depends on the relative magnitude of lattice and grain boundary diffusivity.

The type-A regime is observed when the lattice *diffusion length* $\sqrt{Dt}$ is a little larger than the spacing d between grain boundaries. This is the case if at least one of the following conditions is given: high temperatures, long annealing times, or small grain sizes. This results in an almost planar diffusion front that propagates with an effective diffusion coefficient D_{eff}, a weighted average of lattice diffusivity D and grain-boundary diffusivity D_{gb} [73]:

$$D_{eff} = gD_{gb} + (1-g)D \tag{2.9}$$

where $g = q\delta/d$ is the fraction of atomic sites in the grain boundary of the polycrystal and q a numerical factor depending on the grain shape (i.e. $q = 1$ for parallel grain boundaries and $q = 3$ for cubic grains).

For type-B kinetics, the condition $\delta \ll \sqrt{Dt} \ll d$ applies, which is met for lower temperatures, or/and relatively short annealing times, or/and sufficiently large grains. Significant diffusion out from the grain boundaries into the lattice happens, but in contrast to regime A, the developing fringes do not substantially overlap.

Short annealing times and low temperatures, at which lattice diffusion $\sqrt{Dt} \ll \delta$ is strongly suppressed, induce type-C diffusion. Here, grain boundary diffusion dominates almost exclusively without any essential leakage into adjacent grains.

2.2.5 Diffusion Barriers & the Miedema Model

In many industrial applications – most famously semiconductors for integrated circuits – it is necessary to inhibit the intermixing of tangent materials, while other properties, like i.e. the electrical conductivity, remain mostly unchanged. In the case of nuclear fuel development, it should be prevented that the fuel meat and cladding material mix without deteriorating the thermal conductivity, which is important for effective cooling. This is achieved by inserting a thin (usually in the order of a few micrometers) layer between the materials to be separated, which is called a *diffusion barrier*. In order to act as such, the material of this layer should have a very low tendency of interdiffusion with any of the materials in contact. Besides, other properties unrelated to diffusion may be required due to a specific application, as described above.

Finding a suitable diffusion barrier material is achieved at first by theoretical considerations to narrow the materials down to a set of promising candidates. Subsequently, experimental testing is performed to investigate the real behavior, which cannot be completely reproduced by theoretical models. A way to quantify the trend of a certain composition of elements toward intermixing or separation is by the *formation enthalpy* ΔH^{f} (in kJ/mol). The sign of ΔH^{f} gives the general direction of development; negative formation enthalpy indicates a preference for intermixing, while a positive value means that separation is energetically favorable. Logically, the formation enthalpy for a pure element is always zero.

A semi-empirical model to calculate formation enthalpies for a wide variety of alloy systems was developed by Miedema [76]. It combines physical quantities like electronegativity, electron densities, and atom sizes with empirical constants that describe the behavior of alloy systems taking different crystal structures into account. After various refinements of the Miedema model, like the introduction of chemical short-range order by López and Alonso [66], a calculator was created by Zhang [149] that combines a large database of empirical parameters with the refined models. This easy tool allows the computation of *standard* formation enthalpies for binary and ternary compounds as well as for solid solutions. Here, standard conditions are defined as atmospheric pressure (1 atm = 101.325 kPa) and a temperature of 298 K. This has to be considered if the relevant process is not at these standard conditions. Furthermore, it has to be pointed out that the Miedema model like any other thermodynamic approach is only valid in equilibrium, which is for example not given for the irradiation-driven diffusion in the fuel of a nuclear reactor.

Nevertheless, Miedema's model still serves as a good reference point for possible diffusion barrier materials. Accordingly, the standard formation enthalpies have been calculated for the intermixing of promising elements (Zr, W, Mo) with the main components of fuel (U) and cladding (Al). Figure 2.17 shows the resulting total formation enthalpies.[1]

[1] Exact results may vary for the choice of different data bases in the Miedema calculator. For the displayed plots, the values are calculated with the database "ZSL07" under consideration of the refined Miedema model by Alonso [66].

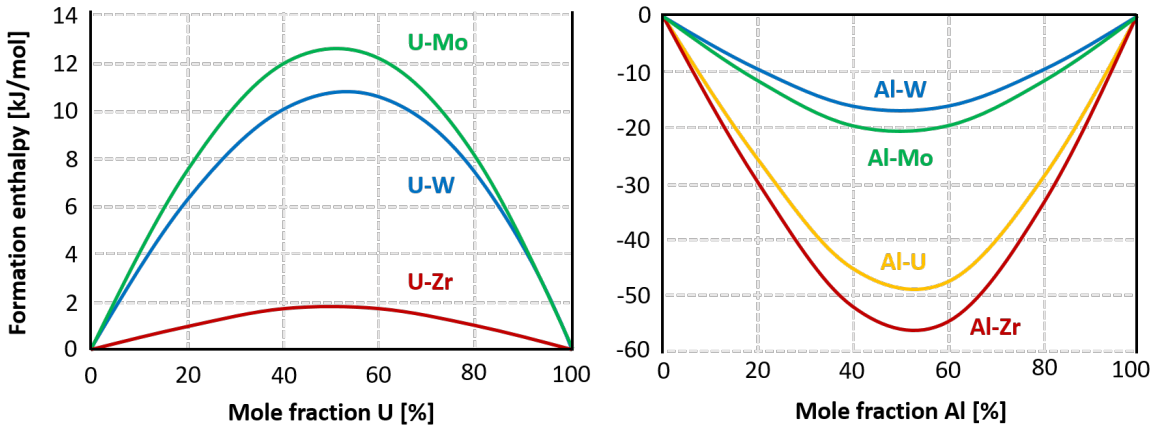

Figure 2.17: Standard formation enthalpies calculated for mixtures of possible diffusion barrier materials (Zr, W, Mo) with uranium fuel (left) and aluminium cladding (right) respectively. The diffusion couple U-Al is shown as a reference.

Standard formation enthalpies of mixtures of the selected elements with uranium are all positive, which indicates a trend for separation instead of mixing (older databases for fitting parameters for Miedema's model actually show negative values for Zr). As a qualitative statement, it can be stated that W and Mo seem to show a slightly better separation with U than Zr. However, the nuclear fuel under consideration is not pure U, but U-Mo with 10 wt.% Mo (which is roughly 20 at.% Mo). Calculating the formation enthalpy of a ternary mixture with atomic composition of 4 parts U, 1 part Mo and 5 parts of the respective other elements results in -54 kJ/mol for Al, -3.9 kJ/mol for Zr, 1.4 kJ/mol for W and 2.5 kJ/mol for Mo.

Similar behavior can be seen for the mixtures with the Al cladding, except for the fact that all formation enthalpies are negative here, thus the systems rather prefer intermixing. Zr performs significantly worse compared to Mo and W, and even worse than uranium which was calculated as a reference curve. This would suggest that Zr is actually worse than no diffusion barrier at all, which does not agree with experimental findings [112]. This discrepancy can be the product of various factors. First of all, the fitting parameters of Miedema's model are not as reliable when combining transition metals (U, Mo, W, Zr) with non-transition metals (Al). Furthermore, the formation of possible intermediate phases like intermetallic compounds and their diffusion behavior is not included.

Finally, it has to be pointed out that the model considered here only deals with bulk diffusion without the effects of grain boundaries discussed above. Different types of possible grain structures in a diffusion barrier can have a huge impact on its performance as such. Fine-granular layers result in a higher diffusivity as the increased volume fraction of grain interfaces enhances diffusion. The orientation of the grain boundaries also plays an important role. Grain boundaries that directly connect the to-be-separated materials act as short-circuits for the barrier, while boundaries parallel to the barrier layer's interface can even have a favorable effect when the particle flux is transversally diverted.

2.3 Sputter Deposition & Film Growth

Sputter deposition is a vacuum deposition method to apply thin films and coatings. It belongs to the wider range of Physical Vapor Deposition (PVD) techniques, which includes all methods where a material in condensed phase gets vaporized and then condenses back as a thin film. This vaporization can be achieved for example by heating of the material – in this case, the method is called *evaporation* – or by pulsed laser ablation, to name a few common ones. For sputter deposition, vaporization is accomplished by a bombardment of the material with particles generated by a glow discharge plasma. This effect is called *sputtering*, while the term is also used synonymously for the whole technique of sputter deposition.

This chapter covers the various aspects of sputter deposition from the generation of glow discharge plasmas over particle ejection to condensation and film growth. Additionally, it features the description of possible operation modes as well as auxiliary techniques for the control of the resulting coating properties.

2.3.1 Electric Discharge in Gases

Widely known for their use as neon lights to brightly illuminate larger cities, glow discharge plasmas also serve as a means for analytical spectroscopy as well as they form the basis of sputter applications considered in this thesis.

A starting point for the description of glow discharge plasmas is the electrical conduction in low-pressure gases. For this purpose, one images a glass tube filled with a gas at pressures in the order of one millibar, while a direct-current (DC) voltage can be applied between two electrodes inside the tube. Charge carriers, either electrons or ions, are needed for the conduction. These are created in pairs by ionization of the gas atoms/molecules, which can be caused by different processes resulting in the multiple discharge regimes visualized in the corresponding voltage-current characteristics (see Figure 2.18).

The regimes (A-D) at low voltages are called *dark discharges* as they produce no light visible to the human eye. An exception to this are *corona discharges* that can form near sharp points or edges where the electric field is locally increased. These regimes are not relevant for the following description of sputtering itself, however, processes that happen here are important for plasma ignition. For example, the creation of new charge carriers by electrons ionizing the gas atoms. This is quantified by α, the *primary ionization coefficient*, which is defined by the number of ionization events caused by an electron per unit length along the electric field. If $\alpha > 1$, the electrons can multiply fast within the distance to the anode d causing an avalanche.

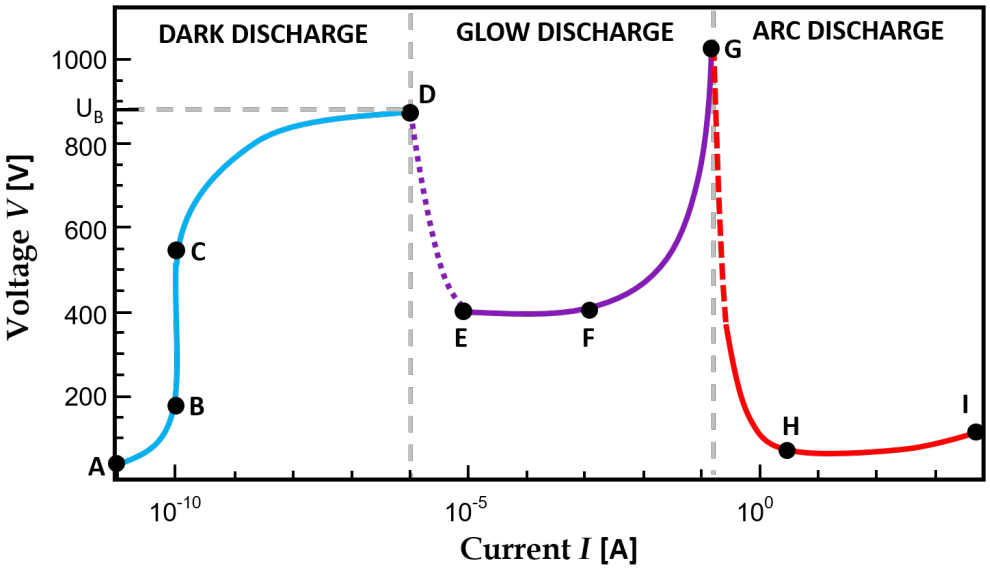

Figure 2.18: Voltage-current characteristics showing the different regimes of electrical discharges in gases. The current is scaled logarithmically. The values are not from a specific measurement but intend to show the order of magnitude of the described phenomena.

The transition to the visible *glow discharge* region is reached with the electrical breakdown, corresponded with the *breakdown voltage* U_B (point D in Figure 2.18), when the discharge is self-sustaining. This means that no external ionization source is needed anymore and the present charge carriers produce sufficient new ones on their own. For this, a mechanism is needed that produces new seed electrons that generate successor avalanches. The main driver for this is the impact of ions at the cathode, which releases secondary electrons. Other minor contributions exist also, like secondary electrons generated by the photoelectric effect. These are summarized in the γ-process, where the γ is the *secondary ionization coefficient* defined as the number of secondary electrons produced per ion of the primary avalanche. When each electron of the avalanche triggers at least one secondary electron, the *Townsend criterion* for breakdown is reached.

$$\gamma\left(e^{\alpha d}-1\right)=1 \tag{2.10}$$

The result is a significant increase of the current over several magnitudes (depending on the internal resistance of the power supply that connects the electrodes). The voltage on the other hand drops, because charge separation between fast-moving electrons and slow-moving ions distorts the initial electric field in a way so that it can not be considered uniform anymore. The low ion mobility causes a positive space charge near the cathode resulting in a potential drop that enhances the α-process, which is dependent on the local electric field strength. This predominates the simultaneous decrease of ionization events at the anode side. The breakdown criterion for this has to be rewritten in integral form where the local differences are taken into account [27].

$$\int_0^{d_0} \alpha\left(E(x)\right)\,\mathrm{d}x = \ln\frac{1}{\gamma} \tag{2.11}$$

After the breakdown, the gas enters the *normal glow* regime (E-F), where the voltage and number of charge carriers are almost constant across the tube (except near the electrodes). This is the regime where neon tubes are operated. Depicted in Figure 2.19 are the several regions that form across the discharge tube, composed of *glows*, that emit significant light from de-excitations or recombinations, and *dark spaces* (also called *sheaths*). The *positive column*, where electrons cause excitation of atoms, is the actual plasma in the sense of its definition as being quasineutral, i.e. the total charge is zero on a macroscopic scale. While this positive column is important for applications in illumination, the *negative glow* is crucial for sputtering. Here, the secondary electrons from the cathode gained enough energy to generate new electron-ion pairs creating a bright glow as many of the electrons in this region of high charge density are still slow and therefore can recombine. The remaining ions on the other hand are accelerated towards the cathode where they are able to sputter off material. However, this regime is not where sputtering applications for thin-film deposition operate yet. In normal glow regime, the current density at the cathode is fixed, and increasing the total current is associated with the growth of the so-called *cathode spot*, the area through which the current flows. So when the current is further increased, at some point the cathode spot occupies the entire surface of the cathode. Still further increase of current again requires an increase in voltage. The maximum current density is proportional to $V^{3/2}$, which is known as Child's law [15]. This comes from the limitation by the space charge regions, where the electric fields are strongest and most of the voltage drop – the so-called *cathode fall* – happens. In contrast to normal glow, this regime of discharge is called *abnormal glow* (F-G). This is where sputtering is usually performed, as the electric field gradient near the cathode becomes high enough for accelerated ions to efficiently sputter material off the cathode when striking it.

Finally, another electrical breakdown is reached when the growing current heats the cathode to a point where thermionic emission – electrons being released due to their high thermal energy - comes into play. This breakdown produces a high-current plasma arc at a comparatively low voltage. Consequently, this set of regimes is called arc discharges. At the breakdown, a discontinuous *glow-to-arc transition* zone (dashed red line in Figure 2.18) is crossed before the discharge reaches the arc region, where high currents at low voltages can cause damages on samples and device components in a sputtering process.

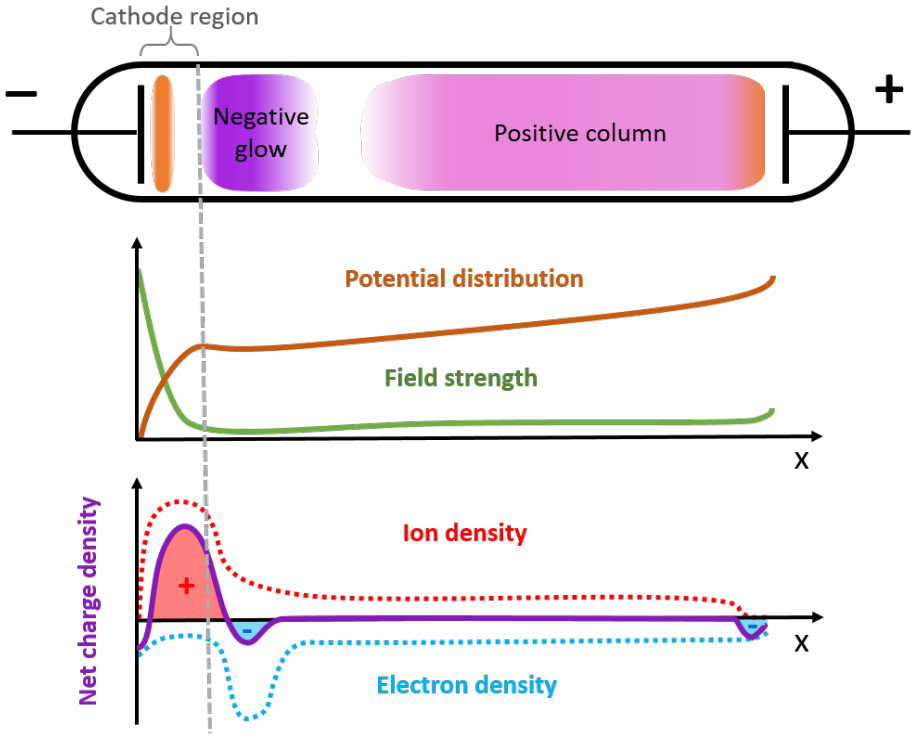

Figure 2.19: Scheme of a glow discharge tube with the different glow regions and dark spaces between the cathode (left) and anode (right). Below is the spatial dependence of certain parameters related to the discharge as a general trend without units. Based on [64].

Describing all these regimes may look a bit exaggerated as only the abnormal glow regime seems relevant for the sputtering. But real sputtering devices are not ideal machines, hence several subtleties are better understood if the whole range of discharge in gases is taken into account. Although the V-I diagram already serves as a good foundation, the breakdowns are worth a closer look.

The breakdown voltage is an important parameter not only for the ignition of plasmas generated for certain applications, but especially for the overall design of devices with energized and grounded parts, avoiding parasitic plasmas or discharges resulting in short circuits. This requires an optimization of geometries in terms of the electrode or gap distance d at a certain range of working pressures p. To obtain a model for the behavior of the breakdown voltage depending on these parameters, the primary ionization coefficient α is expressed in terms of pressure p and electric field E, which is composed of the voltage over the distance V/d.

$$\alpha = A \cdot p \cdot \exp\left(-\frac{B}{p/E}\right) \tag{2.12}$$

A detailed derivation of this can be found in [116] and considers the ionization probabilities of electrons involving their mean free paths - which introduces the pressure of the gas. A and B are gas-dependent constants that have to be determined empirically. A is the

saturation ionization in ion pairs per meter and pascal of a gas, while B is related to the excitation and ionization energies. It has to be mentioned that A, and consequently also B, is actually a parameter and dependent on E/p, but it is usually approximated as constant. This approximation is considered valid for $B/2 \leq E/p \leq 3B$ [116]. If this expression for α is now put into the Townsend criterion (see Equation 2.10) and solved for the breakdown voltage, one gets *Paschen's law*:

$$U_{\mathrm{B}} = \frac{B \cdot pd}{\ln\left(A \cdot pd\right) - \ln\left[\ln\left(1 + \frac{1}{\gamma}\right)\right]} \tag{2.13}$$

The resulting Paschen curves for different gases as shown in Figure 2.20. As pressure and gap distance are the two main drivers of this behavior independent of the gas type, they are combined into one parameter as the product pd. By setting the derivative of Equation 2.13 with respect to pd equal to zero, one can obtain the pd value at which the minimum breakdown voltage occurs. Putting this value back into Paschen's law gives the value of the minimum breakdown voltage $U_{\mathrm{B,min}}$, also called *minimum sparking potential*.

$$U_{\mathrm{B,min}} = \mathrm{e} \cdot \frac{B}{A} \ln\left(1 + \frac{1}{\gamma}\right) \tag{2.14}$$

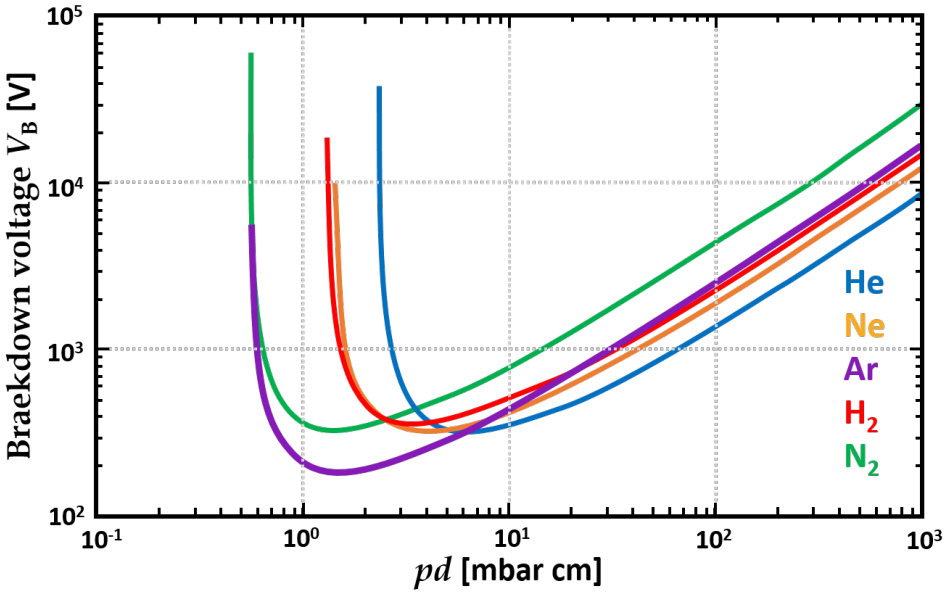

Figure 2.20: Paschen curves for a selection of common gases. Data from [62].

This gives a good approximation for the voltage up to which no discharges occur. But one has to keep in mind that the Paschen curves are semi-empirical fits that hold for planar geometries, homogeneous electric fields, and pure gases as well as the range of E/p mentioned above. In real devices, stronger deviations from this behavior are to be expected especially at sharp edges, where the electric field line density is locally increased. However, the described basic phenomena of gas discharges serve as a good framework for the following description of the sputtering technique.

2.3.2 Sputtering

The field of sputtering techniques is wide and diverse. The following considers basic ideas of sputtering and then focuses on the methods relevant for this thesis – direct current magnetron sputtering with auxiliary techniques like substrate biasing.

General Principle & Main Components

The most simple sputtering configuration is a planar direct current (DC) device as schematically depicted in Figure 2.21. In principle, this is basically what has been shown in the previous section as a discharge tube operated in the abnormal glow regime.

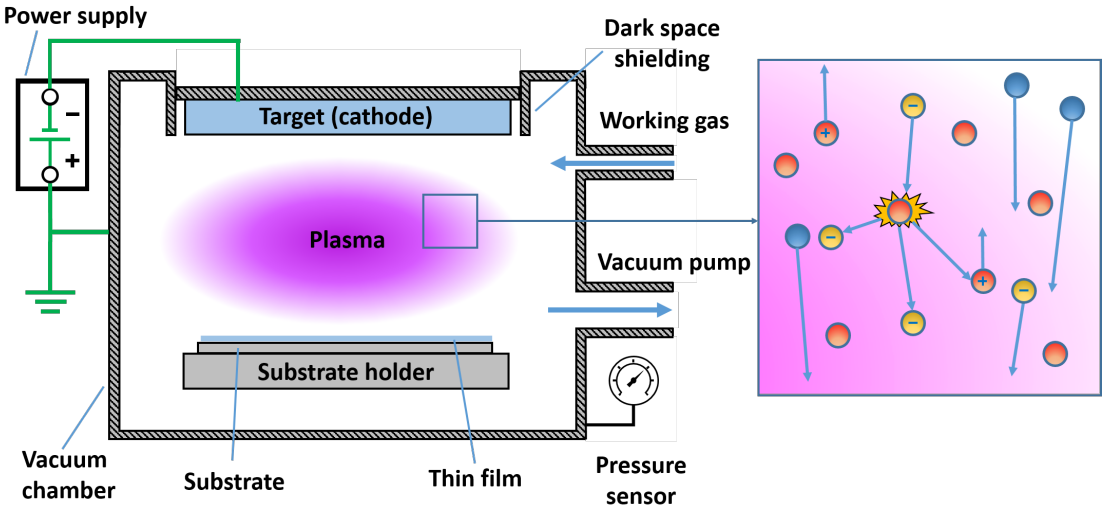

Figure 2.21: Scheme of a DC sputtering device including the most important components. A section of the plasma region is shown on the right with sputtered particles (blue), working gas atoms and ions (red), and electrons (yellow) causing ionizing collisions.

A vacuum chamber serves as the "tube" now. It is evacuated by a system of pumps to a certain base pressure p_B in order to remove as many impurities in the atmosphere as possible. When the working gas – usually argon - is introduced, its pressure p_W is measured by pressure sensors, and gas flow adjusted accordingly via mass flow controllers (MFC).

The planar cathode, called *target*, is made out of the material designated to be sputtered. It is connected to a power supply that applies the required voltage for plasma ignition. The similarities with the discharge tube end regarding the anode. There is no single anode as such; the applied voltage at the cathode is with reference to ground, so the grounded vacuum chamber can be considered the anode. Dark-space shields are grounded screens that are installed in the proximity of components that should not be exposed to plasma, like the backing plate of the target, which would get sputtered otherwise and contaminate the growing thin film. The shields are constructed in a way that no plasma can ignite at designated spots based on Paschen's law (see Equation 2.13).

The last main component is the substrate holder on which the specimen to be coated is put. It can be as simple as a mere platform, but generally, it offers the opportunity to introduce a wide range of parameters to control the properties of the growing coating layer. This can be done e.g. by controlled heating/cooling of the substrate or by applying a defined electrical potential to it. Furthermore, it can be used for spatial changes like the substrate-to-target distance or to move the substrate in any way during the coating.

Physical Sputtering - from a Particle Point of View

Interactions of energetic particles from the plasma – here usually argon ions - with the target surface are described by momentum transfer theory and can cause a wide range of resulting effects, which are schematically depicted in Figure 2.22.

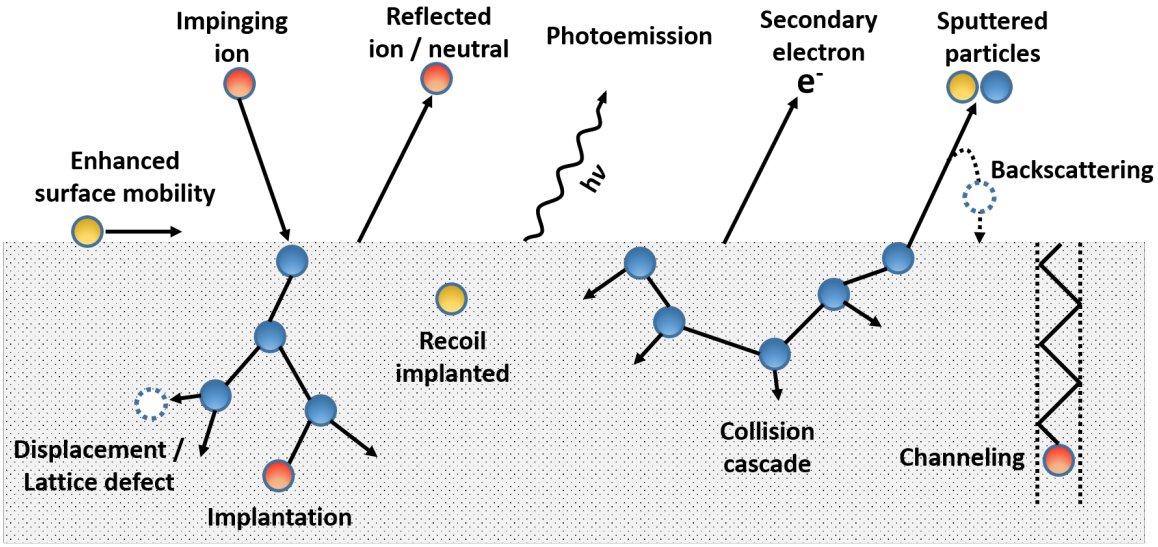

Figure 2.22: Scheme of interactions of impinging particles of the working gas (red) with target atoms (blue) and potential impurities (yellow). Based on [70] and [26].

The most simple effect is when the impinging ion is reflected off the target surface. This creates high-energetic neutrals by a charge-transfer reaction, which in turn can cross the plasma – given that the pressure is low enough to avoid thermalization through collisions – and bombard the growing film on the substrate, thus affecting the film formation process.

Particles transfer energy to the surface, whether they are reflected or penetrate the material. This can enhance the mobility of adsorbed surface species and trigger chemical reactions at the surface (more important for reactive sputtering) or even implant surface particles into the material by recoil. Furthermore, photons and secondary electrons are ejected, which is only a minor effect compared to the sputtering [70], but especially the electrons are a crucial contribution to maintain the plasma discharge.

When the impinging particles enter the target material, they deposit their energy triggering collision cascades. Eventually, the particle is implanted into the surface region of the target,

while the deposited energy causes preferential diffusion and lattice defects that can even completely destroy the crystallographic structure of the surface region, which is called *amorphization*. If the ion hits the surface in a certain angular range with regard to the crystallographic plane, it can penetrate the material even deeper; an effect called *channeling*. The important effect for sputtering is when such a collision cascade recoils back to the surface with enough energy left to overcome the surface binding energy E_{sb} and eject particles. However, there is a possibility that these sputtered particles will be scattered back to the target, where they move across the surface finding a new spot in the lattice to settle.

The effectiveness of the sputtering process is quantified by the sputtering yield Y, which is defined as the mean number of sputtered atoms from the target per incident ion. As this is dependent not only on the target material properties like atomic mass and surface binding energy (see an example for the dependence on the elements of the periodic system in Figure 2.23) but also on the mass, energy (distribution), and incident angle (distribution) of the impinging ions, a specific formula for Y would turn out rather complex. This is why sputter yields are usually given as empirically measured values with regard to specific configurations / parameter ranges. Nevertheless, certain general correlations can be derived.

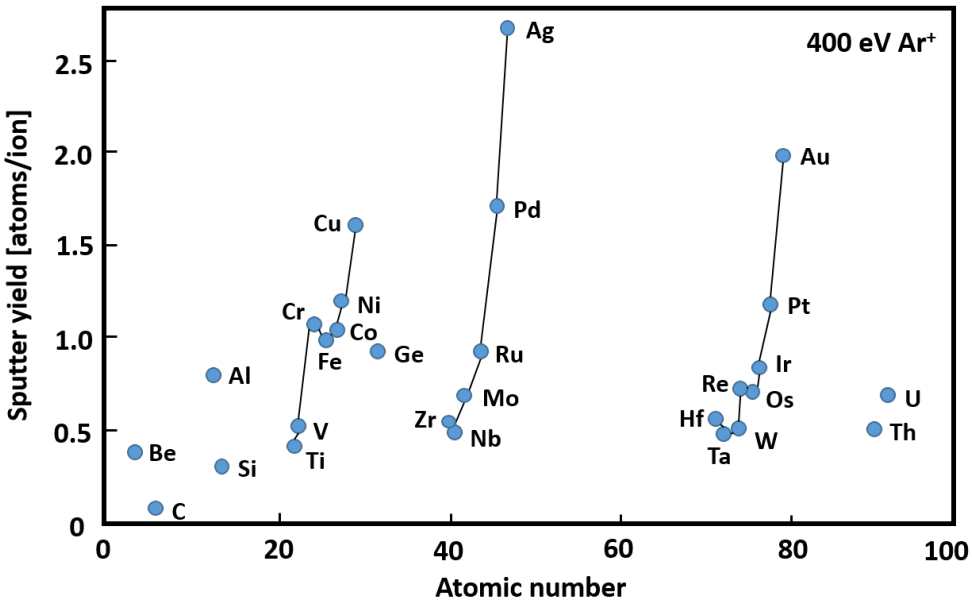

Figure 2.23: Sputtering yield of 28 elements for 400 eV argon ions. Based on [56].

For effective particle ejection, the maximum energy transfer from incident to target particle is desired. Considering the laws of conservation of momentum and energy for elastic collisions, the relative energy transfer is described by

$$\frac{\Delta E}{E} = \frac{4 m_\mathrm{i} m_\mathrm{t}}{(m_\mathrm{i} + m_\mathrm{t})^2} \cdot \cos^2 \theta_\mathrm{i} \tag{2.15}$$

with the masses $m_{\mathrm{i,t}}$ of the incident and target particle as well as the angle of incidence θ_i measured with regard to the line joining the centers of mass upon impact. Regarding

the masses, this term is maximized when incident and target particle have the same mass $m_i = m_t$. From this follows that regarding an optimized sputtering yield one should choose a working gas with an atomic mass close to that of the to-be-sputtered material. For example when sputtering Ti ($A \approx 48$), Zr ($A \approx 91$), or Sn ($A \approx 119$), one should use Ar ($A \approx 40$), Kr ($A \approx 84$), and Xe ($A \approx 131$) as working gas respectively. In reality, this is rarely implemented as the high natural abundance of argon makes it so much cheaper than any other noble gas. Hence, argon as working gas is used almost exclusively.

Regarding the incidence angle, the energy transfer has a maximum when the centers of mass are hit directly ($\theta_i = 0°$). This is at least what follows from Equation 2.15, but applying this directly to the sputter yield would be naïve as a maximum moment transfer deeper into the material is not what is desired. As stated before, the recoil of the collision cascade to the surface is needed for sputtering. Therefore, an incidence that is not orthogonal to the surface will have a reduced energy transfer, but the momentum vector points already more back to the surface. So even if less energy is transferred, this energy is introduced close to the surface and recoiling particles have a higher probability to escape. At some point, on the other hand, the angles with regard to the surface get too shallow and reflection of the incident particles gets dominant, so the optimum incident angle is somewhere in between (see Figure 2.24). Although this consideration brings some insights, it is difficult to integrate in practice as the exact distribution of incident angles is hardly adjustable in a controlled way without significantly changing other crucial parameters of the plasma. As the trajectories of impinging ions are directed by the electric field lines, which in turn are normal on the surface, most incidence angles are close to normal.

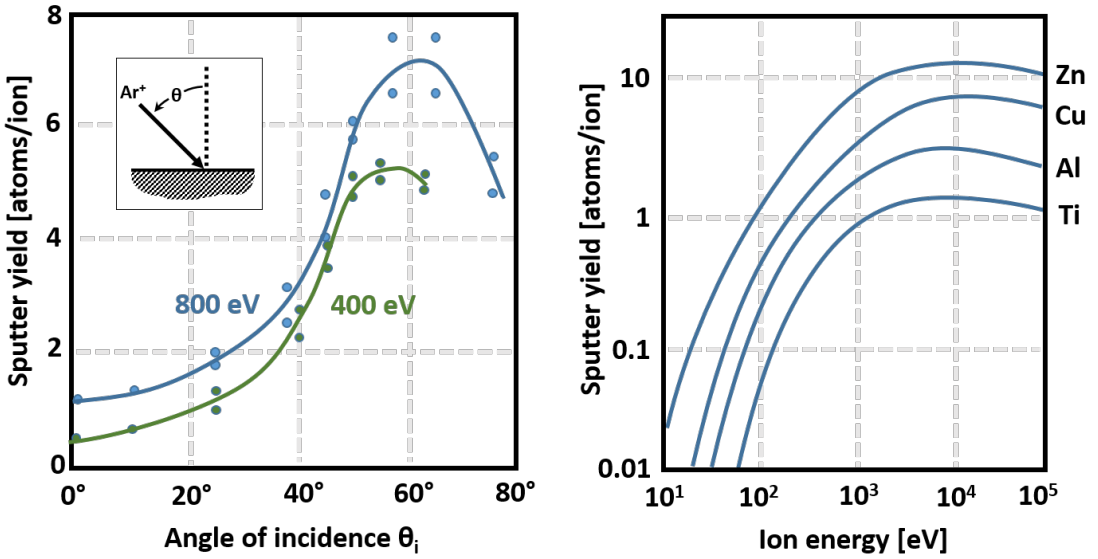

Figure 2.24: Dependence of sputter yields on incidence angles (left; using Hg^+ ions on Fe target) and energy (right; using argon ions) of impinging ions. Data from [145] and [69].

Finally, there is the energy of the impinging ions to consider (see Figure 2.24). Low energies up to about 25 eV do not cause sputtering of a solid as a certain threshold energy has to be exceeded for the displacement of atoms in a lattice and to overcome the surface binding energy. For higher energies up to about 1 keV, the sputter yield increases roughly linearly in the so-called *knock-on regime*, where surface or surface-near atoms get dislodged. For higher energies, multiple atoms can be dislodged triggering cascades with a non-linear behavior. At energies of about 50 keV, deep-ion implantation causes a reduction of the sputter yield.

When exiting the target, sputtered particles display a certain energy $Y(E_s)$ as well as an angular distribution $Y(\theta_s)$, which are in turn again dependent on the energy and incident angle of the impinging ion as well as the orientation of crystallographic planes and surface roughness of the target. Simple models for normal incidence describe the distributions as $Y(E_s) \approx E_s/(E_s+E_{sb})^m$ and $Y(\theta_s) \approx \cos^n \theta_s$, where the energy-dependent fit parameters are in a range of about $m = 2\text{-}3$ and $n = 0.5\text{-}1.5$. This behavior is graphically depicted in Figure 2.25. For a more detailed examination, reference is made to the works of Stepanova [129] and Yamamura [147]. This is omitted here as the focus of this work is on the layer formed by the sputtered particles after condensation, which may have different properties than after ejection due to interactions (mostly collisions) with the working gas and plasma.

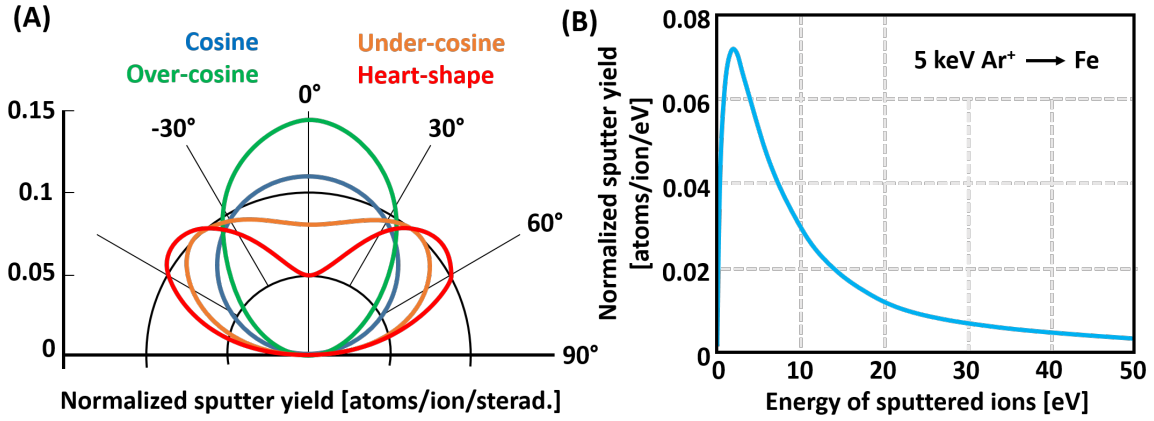

Figure 2.25: Angular and energy distribution of sputtered particles. (A) The angular distribution is described by a cosine to the power of the fitting parameter n, which depends on the energy of the incident ions. This comes from the type of collission cascade triggered. Low-energy ions ($n < 1$, under cosine) trigger surface-near recoils that scatter more, while higher energies ($n > 1$) cause ejections from deeper layers that travel more along the surface normal. (B) General trend of the energy distribution of sputtered particles exemplary of Fe sputtered by argon ions of 5 keV. Based on [18].

The Collisional Plasma

Ionizing collisions, as indicated in Section 2.3.1, are a key factor for igniting and maintaining a glow discharge plasma and the Paschen curves show the dependence of such breakdowns on the macroscopic quantities pressure p and gap size d. While pressure values themselves are something very intuitive, the pressure as a plasma parameter is not as tangible, and difficult to put in an intuitive quantitative relation to the resulting effects. Hence, for the underlying plasma phenomena for single particles on the microscopic scale, the mean free path λ is introduced.

$$\lambda = \frac{1}{n \cdot \sigma} \tag{2.16}$$

Here, n is a particle number density and σ is a cross section. For a certain gas at a fixed temperature the pressure can be converted into the particle number density using the ideal gas law $p = nk_\mathrm{B}T$. In general, the mean free path gives the average distance a particle moves till something happens. This representation is very general on purpose as there are hundreds of different mean free paths depending on what that "something" is.

The most simple case describes the average distance thermalized identical gas particles travel between two elastic collisions. This perspective requires an additional factor of $\sqrt{2}$ in the denominator of Equation 2.16, which only describes a beam of particles hitting stationary particles. Assuming the atoms as hard spheres, this collisional cross section σ is equivalent to the geometrical cross section of the considered gas atom $\sigma = \pi(2r_\mathrm{g})^2$ with the atomic radius r_g of the gas atom.[2] In the case of argon ($r_\mathrm{g} = 182\,\mathrm{pm}$) at room temperature (293 K), this results in a pressure-dependent mean free path of

$$\lambda_\mathrm{Ar} = \frac{6.9 \cdot 10^{-2}}{p}\,\mathrm{mbar\ mm}. \tag{2.17}$$

Concerning the sputtering process, an important question is now what the mean free path is for a beam of sputtered particles with atomic radius r_s and mass m_s crossing the working gas/plasma. For this, the collisional cross section has to be adjusted for the new geometric conditions as well as for the motion of the background gas with mass m_g. Assuming a gas with a Maxwell-Boltzmann energy distribution, the kinetic gas theory gives [72]:

$$\lambda = \frac{k_\mathrm{B} \cdot T}{\pi(r_\mathrm{s} + r_\mathrm{g})^2 \sqrt{1 + \frac{m_\mathrm{s}}{m_\mathrm{g}}}} \cdot \frac{1}{p} \tag{2.18}$$

One further step and the geometrical interpretation of the cross section is finally overthrown when also including the observed particle energy dependence of the cross sections $\sigma(E)$, which can be empirically fitted in the range of 1 - 200 eV [128]:

$$\sigma(E) = \sigma(E_0) \cdot \left(\frac{E}{E_0}\right)^{0.29} \quad \text{with } E_0 = 1\,\mathrm{eV} \tag{2.19}$$

[2] There are multiple definitions of atomic radii as atoms by nature are not hard spheres. Here, the van der Waals radius is used for r_g, which in turn is actually defined by the closest approach of two particles. Data for van der Waals radii of elements was extracted from [1].

There are multiple considerations possible to refine this model of the mean free path further, like using the energy distribution of the sputtered particles, accounting for the energy change of a particle after a first collision, and so on, or actually looking at the distance traveled normal to the target till the particle gets thermalized. Furthermore, the pressure in real sputtering devices is not completely homogeneous. Especially near the target, the background gas is heated by the plasma, which results in a decreased local density and subsequently an increased mean free path. The effect is called gas rarefaction [18].

At this point, however, there is no need to take the increasing complexity of the mentioned effects into account, as the results of the simplified model above are already sufficient to get the right order of magnitude for an estimation. Hence, applying this behavior to a sputtering process of zirconium ($r_s = 252\,\text{pm}$) in an argon atmosphere, the pressure-dependent mean free paths for different energies can be calculated and are plotted in Figure 2.26.

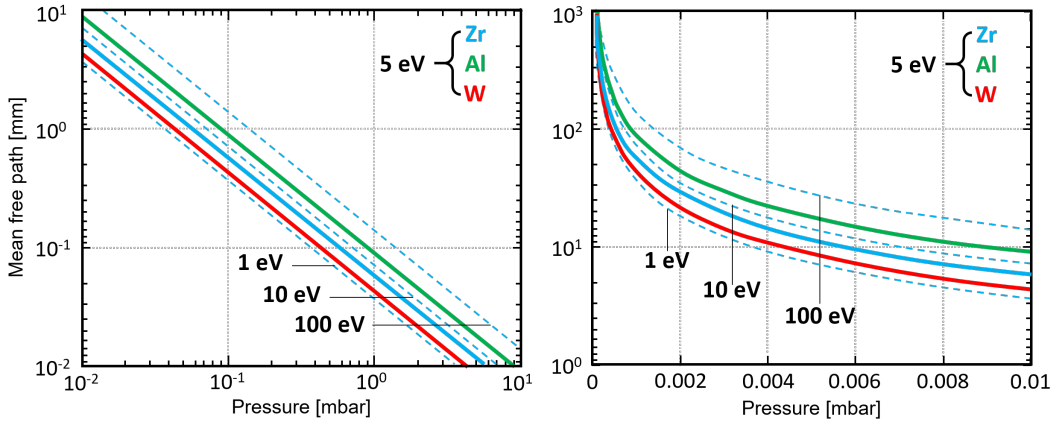

Figure 2.26: Dependence of mean free paths on argon pressure for particles of the elements Zr (blue), Al (green), and W (red) with an energy of 5 eV (solid lines). To illustrate the energy dependence, curves for Zr are also shown with 1 ev, 10 eV, and 100 eV (dashed lines). On the left, a logarithmic pressure range of 0.01 – 10 mbar is shown, while the right side shows the narrower range 0 – 0.01 mbar linearly. In both cases, the mean free path is plotted logarithmically.

This translation of the pressure to a mean free path is a more intuitive tool when it comes to evaluating how likely something is to happen within a certain geometry. In the given case, λ can be directly compared to the target-to-substrate distance d for an estimation if most sputtered particles reach the substrate unscattered (if $d < \lambda$). Now if the pressure is increased, the mean free path gets shorter accordingly, and more and more collisions happen that scatter the sputtered particles off their initial trajectories towards the substrate. As a result, less particles reach the designated surfaces and coat more of the other components inside the vacuum chamber instead. This reduced efficiency of the coating rate is unfortunate but can be compensated for, i.e. with increased sputter power, if it wouldn't be for the energy loss of the particles by the collisions that may have an even bigger impact on the coating (see Section 2.3.3).

This may tempt the simple – but ultimately misleading – solution to just reduce the pressure as far as necessary for line-of-sight deposition. The restriction is that the working gas cannot be arbitrarily thin; not just because fewer gas molecules would also result in fewer sputtered particles, but ultimately because the plasma itself cannot be sustained at pressures too low as necessary ionizing collisions getting rarer (see left side of the Paschen curves in Figure 2.20).

Hence, the goal of designing a DC sputtering device would be to find a geometry at which a desired mean free path can be achieved with regard to the substrate-to-target distance, while still being able to maintain the plasma. Considering the typical pressure range for a DC discharge of 0.1 - 10 mbar, the mean free path would be less than 1 mm. This would be impossible to implement as this distance is below the gap size that allows for the plasma to ignite in between.

Magnetron Sputtering

The issue of short mean free paths can be resolved by introducing a static magnetic field $\boldsymbol{B}$ into the DC discharge. This is easily achieved by attaching permanent magnets behind the target in an appropriate manner to orientate the magnetic field lines perpendicular to the electric field $\boldsymbol{E}$. This technique called magnetron sputtering is schematically depicted in Figure 2.27. The arrangement of the fields forces particles with charge q and a velocity vector $\boldsymbol{v}$ to gyrate around the magnetic field lines caused by the Lorentz force $\boldsymbol{F} = q(\boldsymbol{E} + \boldsymbol{v} \times \boldsymbol{B})$. From the vector product can be deduced that the velocity component perpendicular to the magnetic field $v_\perp$ is important for this behavior. Hence, secondary electrons ejected from the target are mainly affected and get confined in the vicinity of the target. The edge of the cathode sheath acts as a magnetic mirror, so the electrons bounce back and forth on helical paths along the magnetic field lines until a collision knocks them off.

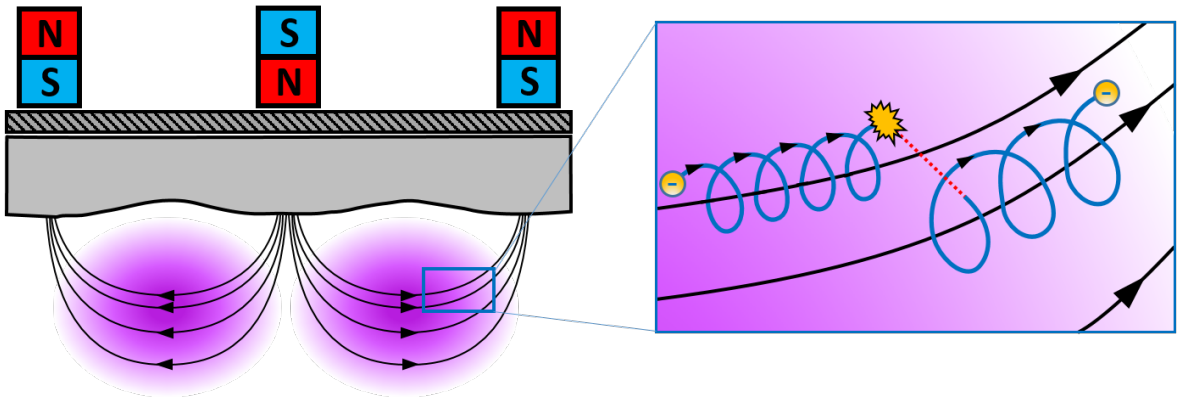

Figure 2.27: Scheme of a magnetron configuration for sputtering. The magnetic field causes the electrons to gyrate along the field lines. The resulting increase of path lengths enhances the probability of ionizing collisions. The section on the right shows a collision of an electron and scattering to a different field line including energy loss noticeable by an increased gyration radius.

An important aspect of this setup is the distinction that the electrons and ions behave differently. This causes a crucial separation between ions and electrons that is understood best with the gyration radius R of a moving charge at a given magnitude of the magnetic flux B:

$$R = \frac{m \cdot v_{\perp}}{|q| \cdot B} \tag{2.20}$$

The masses of the ions m_{i} are several orders of magnitude larger than the electron masses m_{e} and following this, the gyration radius behaves accordingly – the fact that the (secondary) electrons are also significantly faster than the ions is, however, not enough to compensate for that. For typical magnetic flux densities of 20 - 50 mT the electrons gyrate in the order of millimeters, while ions have a gyration radius of up to 1 meter. Consequently, the ions are almost undisturbed on the characteristic dimensions of the magnetron system and therefore continue to impinge on the target and sputter off particles. The electrons, on the other hand, gyrate with radii smaller than the system and are therefore called *magnetized*. A more detailed treatment of the influences of electric and magnetic fields on the plasma can be found in [79].

The electron confinement close to the target results in an increased probability of ionizing collisions with the working gas generating more ions to bombard the target surface, which in turn also generates new additional secondary electrons. This positive feedback loop significantly enhances the ionization in the discharge, which not only increases the sputtering rate but also reduces the voltage and pressure needed to ignite the plasma. Especially with the working pressure reduced by several orders of magnitude to a range of $10^{-3} - 10^{-2}$ mbar, the mean free paths are also drastically increased into the centimeter range (see Figure 2.26).

In summary, the upgrade from a common planar DC device to a magnetron system brings a significant performance boost on multiple levels with only slight changes of the general design. Furthermore, one additional adjustment can be made with the choice of the magnetic field configuration [146]. In the conventional version of a magnetron, all magnetic field lines begin and end in the poles of the magnets forming closed loops to confine the plasma. This configuration is called a *balanced* magnetron. However, with regard to layer growth (see Section 2.3.3) it may be beneficial to weaken the confinement of the plasma more or less in order to use electrons or ions to bombard the substrate. This is implemented by strengthening the outer magnets of the assembly relative to the inner ones, allowing some field lines to end at the substrate and therefore, extending the plasma towards it. The reversed configuration with field lines extending towards the chamber walls, although rarely used, is also possible and results in a further reduction of ion current density on the substrate. This is called a *type-1 unbalanced* magnetron, while the one mentioned before is called *type-2*. All three described configurations are schematically depicted in Figure 2.28.

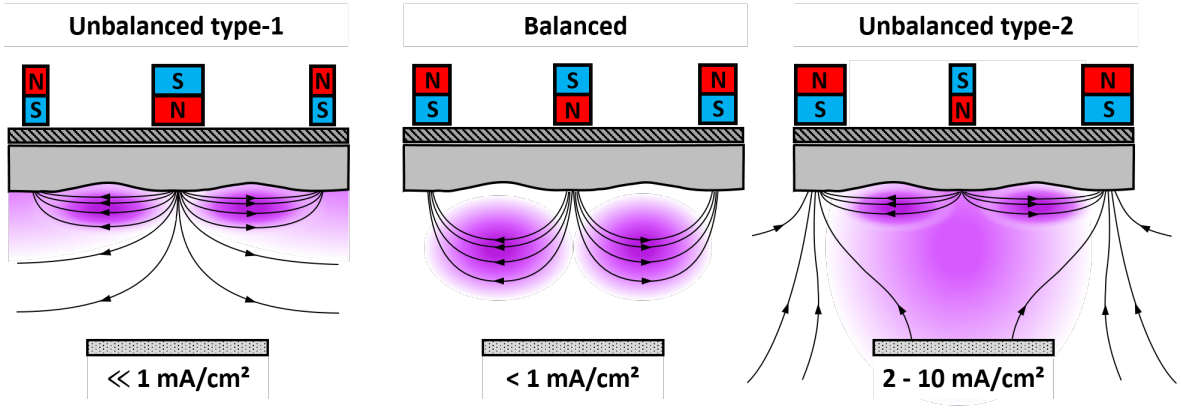

Figure 2.28: Scheme of different magnetic configurations for planar magnetron sources. By varying the relative strength of the permanent magnets, the confinement of the plasma can be controlled to bombard the substrate with charged particles of a certain current density. Based on [36] and [52].

2.3.3 Film Growth

Upon reaching the substrate, the sputtered particles are able to form a thin film, which is the main objective of sputtering as a deposition technique. But for most applications, the mere creation of this thin film of the right material is not enough. Layer adhesion, density, phase composition, crystal structure and orientation – just to name a few examples – can vary greatly resulting in different mechanical, electrical, or optical properties. To get an understanding of the underlying effects, one has to analyze the layer growth process on an atomic scale and, hence, derive which parameters are to be controlled to affect a certain property in a desirable way.

Adsorption and Surface Diffusion

The first process that happens when a particle hits the substrate's surface is *adsorption* (otherwise it will get reflected off the surface). The weak intermolecular bonds responsible for this are caused by the van der Waals force. The resulting so-called *adatom* is loosely bound; it can migrate over the surface or be desorbed again. The first effect is known as *surface diffusion* and plays an important role for layer growth. In order to find a suitable position in the lattice, meaning a site where the energy is minimized, the adatoms first need a certain activation energy E_{diff} (typically in the order of 0.1 eV and about 5 - 20 % of the energy needed for desorption [90]) to be able to overcome the differences of surface potentials.

A more intuitive perspective on the growth dynamics is the concept of *nearest neighbors*, instead of looking at potential energy and minimization thereof. Thus, for a strong bond the adatom attempts to get as many neighboring atoms as possible. A simple visualization of this is the *Terrace-Step-Kink* model (TSK) for a primitive cubic system depicted in Figure 2.29. Adatoms diffusing across the surface have a higher probability to get caught at sites with a larger number of nearest neighbors. This principle also applies to other crystal lattices,

but the growth of other lattice planes is more difficult to visualize. In fact, a simple cubic crystal (with maximum possible nearest neighbors of 6) of the TSK model is rarely observed in nature. Face-centered cubic, body-centered cubic, or hexagonal close-packed with 12, 8, and 12 nearest neighbors respectively are way more common.

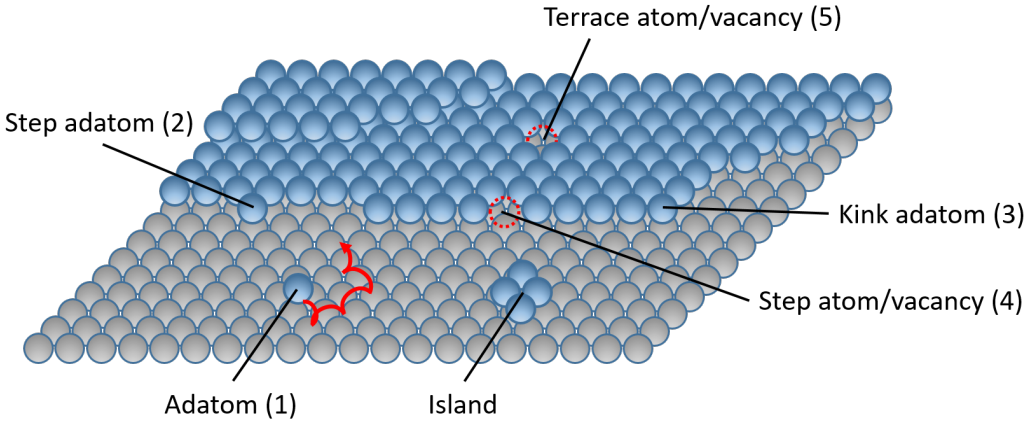

Figure 2.29: TSK model for a primitive cubic system. A deposited material (blue) grows onto a substrate (grey). Adatoms migrate by surface diffusion to find sites where the number of nearest neighbors (in brackets) are increased.

Naturally, adatoms are not exclusively deposited onto the lowest terrace, so in order to fill the energetically advantageous positions at the lower layer, the simplest process is to jump the steps. This usually comes with an energy barrier E_{ES}, known as the *Ehrlich-Schwoebel barrier*, as the number of nearest neighbors is temporarily reduced during the jump. Figure 2.30 schematically shows the surface potential of a one-dimensional terrace with a step. In order to increase the probability $\exp[-E_{\mathrm{ES}}/k_{\mathrm{B}}T]$ to cross the Ehrlich-Schwoebel barrier, the kinetic energy $E_{\mathrm{kin}} = k_{\mathrm{B}}T$ of the adatom has to be increased. The same applies for the general surface diffusion with the corresponding surface potential E_{diff} mentioned above.

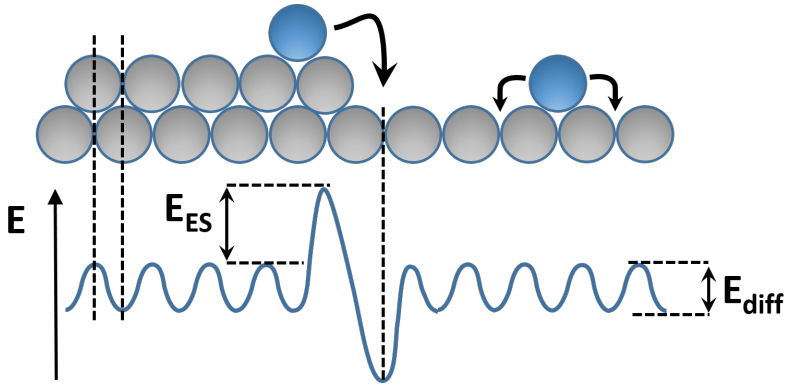

Figure 2.30: Scheme of a one-dimensional surface potential with a step as seen by the adatoms (blue). For adatom diffusion over the surface, the surface potential E_{diff} has to be overcome, while jumping steps needs to cross the Ehrlich-Schwoebel barrier E_{ES}. Based on [104].

For an ideally high adatom mobility, the particles always find the spot where the energy is minimized before new particles arrive, which means a monolayer of particles is completed before the next one starts to grow. This layer-by-layer growth regime is called *Frank-Van der Merwe* growth, but due to the ideal conditions needed it is rarely observed in its pure form.

Nucleation and Crystal Growth

More common growth regimes can be described when interactions of adatoms with each other, which have been omitted so far, are taken into account. Considering a steady flux of arriving particles that create a population of adatoms diffusing over the surface, there is a chance that some of those adatoms meet and combine to increase their nearest neighbors with this bond. This process is called *nucleation*. As the particles of this small nucleus still have kinetic energy it is possible that it disintegrates again, which is mostly the case for very small nuclei. On the other hand, the nucleus can capture more adatoms to form bigger *clusters* or *islands*. The stability of such clusters is dependent on the size; larger clusters have more nearest neighbor bounds and offer more surfaces to capture further adatoms as a gain mechanism. On the other hand, a bigger surface also enhances the possible loss of particles. In total, the net growth rate depends on a volume-related term for increased stability versus a surface term causing the reduction thereof. For small radii of the cluster, the surface term predominates and, therefore, the probability for decay is greater than further growth. As soon as a certain critical radius is exceeded, the volume term takes over and the cluster is considered stable and can grow further. Figure 2.31 depicts the described processes schematically.

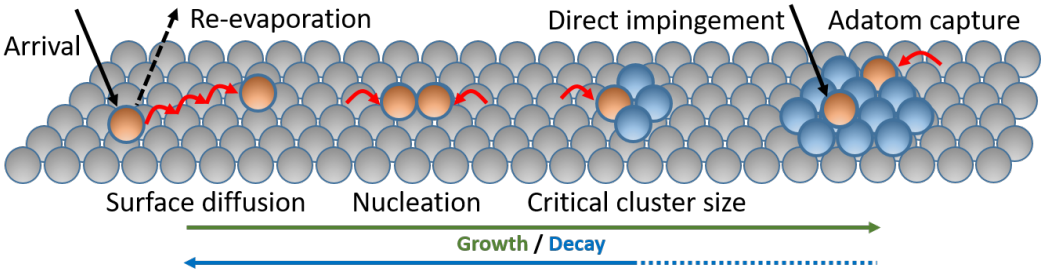

Figure 2.31: Scheme of processes involved in nucleation of adatoms (red) to clusters (blue) on a substrate (grey).

If the sputtered atoms are, contrary to the Frank-Van der Merwe growth, more strongly bound to each other than to the substrate layer, the island growth dominates. This regime is called *Volmer-Weber* growth. The intermediate case between those two, layer-plus-island growth, is called *Stranski-Krastanov* growth, where a layer of a certain thickness, depending on the strains and chemical potentials, forms first followed by island growth. From an adatom energy point-of-view, higher energies favor layer growth as islands are more likely to decay. The other way around, low particle energy (low surface diffusion length) in combination with a high sputtering rate (leaving no time to find suitable lattice spots before the next layer is deposited) causes a high nucleation rate for island growth.

So far, the growing nuclei have been assumed to be without any inner structure. When treated as the crystals they are, the *orientation* of their lattice planes has to be taken into account. Depending on the crystal system of the growing substance, many possible crystal orientations can form with respect to the substrate's surface. The substrate material in turn also has a certain crystal structure and orientation as well as surface conditions (roughness, impurities), which influence the growth of deposited material. As a result, the population of islands forming on the substrate has a random orientation distribution at first but can be shifted towards certain energetically preferred orientations depending on various parameters.

Figure 2.32 illustrates this behavior with two selected crystal orientations, one of which tends to island growth and the other to layer growth. Varying the energy of the system in form of temperature changes the equilibrium and leads to preferential growth of one or the other orientation. Furthermore, the influence of temperature on the initial nucleation rate can also be seen, as higher kinetic energies increases the probability that nuclei decay before reaching the critical radius.

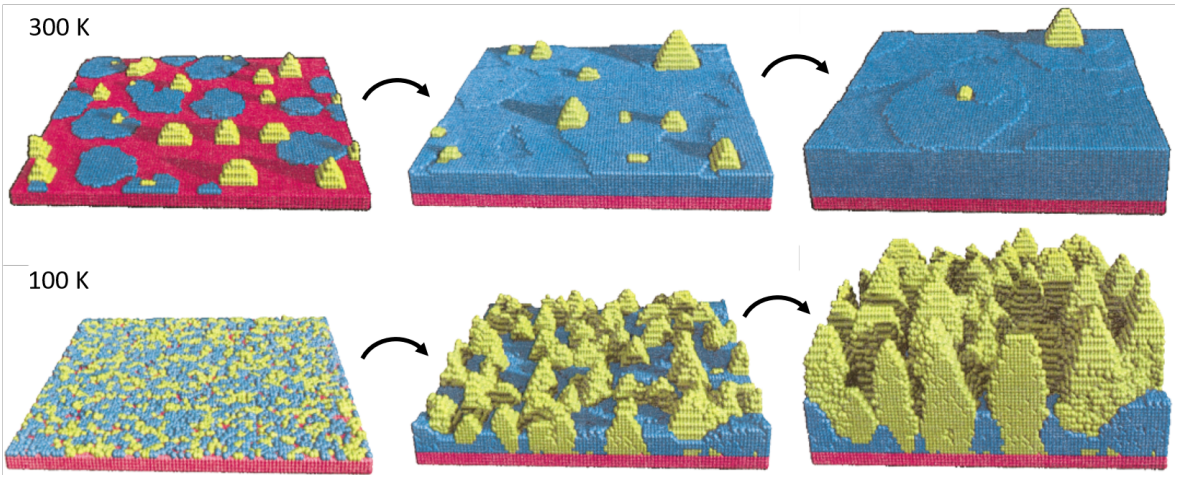

Figure 2.32: Simulation of Al deposited onto a substrate (red) at different temperatures. The development over time can be seen from left to right. Two crystal orientations parallel to the substrate's surface are implemented: The (001) orientation in yellow has a lower adatom potential energy than the (111) orientation in blue, which makes the former grow faster in height. At temperatures of 300 K (top row), the enhanced diffusion mobility causes a net flux to the (111) grains, while the (001) grains dominate at lower temperatures of 100 K (bottom row). From [7].

Grain Structures

At some point in the growth of a thin film, the randomly orientated islands get so big that they start to touch each other and, thus, interfere and inhibit their undisturbed growth. From this point on, the individual crystals are usually referred to as *grains*, with distinct *grain boundaries* between them. Depending on the conditions during growth, the grains display various morphologies and by this can be classified into different categories, so called *structure zones*.

It has to be mentioned right at the outset that structure zones are not areas with well-defined delimitations, but phenomenological regions with certain common appearances or properties. Although there are of course (usually energy-dependent) mechanisms that cause the transitions between the zones, those processes are not triggered by hard thresholds, but by changing probabilities (for like crossing the Ehrlich-Schwoebel barrier as shown before) which cause more of a continuous transition of some degree. Consequently, a variety of classification schemes have been developed over the years. For sputter deposition, a common division is into the 4 zones I, T, II, and III, illustrated in Figure 2.33.

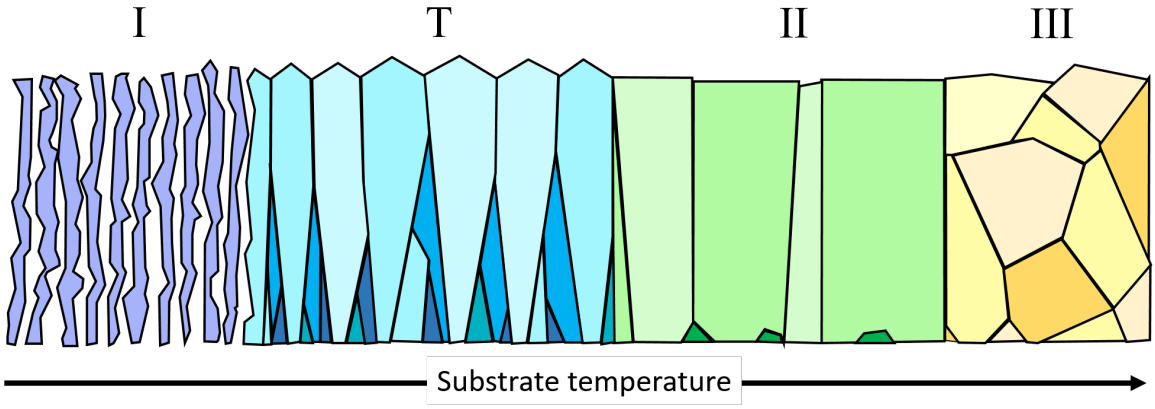

Figure 2.33: Scheme of 4 structure zones for sputter deposition formed with increasing substrate temperature. Different shades of each color represent different crystal orientations. Based on [6] and [31].

Zone I is defined by a negligible adatom mobility. Condensing particles do not have enough energy to overcome the surface diffusion potential and stay at the site of impingement, making this also known as the *hit-and-stick* regime. High deposition rates can be another cause for this zone when surface diffusion is given, but the next layer of particles forms already on top before an adatom can find a favorable spot. As a consequence, the growing islands are mostly non-crystalline. This type of growth leads to a film consisting of fibrous columns with overhanging structures that cause shadowing of the lower parts. Thus, the angular distribution of impinging particles has a significant impact on the film, as the shadowing gets more pronounced when particles deviate from a normal incidence angle, causing bigger and bigger voids in the already porous structure.

Zone T is caused by the conditions described in the previous section about nucleation. The surface diffusion of adatoms results in the formation of randomly orientated clusters that turn into grains as they grow. A characteristic feature is the V-shaped columns with faceted tops. This is caused by the different growth rates perpendicular to the substrate. This way, some of the initial randomly orientated grains are overgrown by others leading to a more preferential out-of-plane orientation with increasing layer thickness. The remaining grains form the depicted V-shape at the base. The spikey surface structure of the deposited films results from the edges between two facets that grow on top as the surviving orientations.

Zone II is reached when energy allows restructuring of the grains. This already happens at the stage of nucleation, when the randomly-orientated islands diffuse into each other and combine to form a favorable bigger cluster – a process known as *coalescence*. Of these two initial islands, one has a more preferential orientation that minimizes the surface energy with respect to the substrate. The elevated energy in the system makes the restructuring process possible and the energetically-favorable cluster consumes the other one by transfer of atoms at the grain boundary. This causes a selection of orientations already at an early stage of film growth and reduces the overall amount – and, therefore, increases the size – of grains.

Zone III is defined by *recrystallization* of the grain structure. Here, the energy of the particles is high enough for particles not only to diffuse on grain boundaries but through them. This *bulk diffusion* is leading to a restructuration of the whole material with big, randomly-orientated grains.

In summary, it can be said that a material can be deposited in various structures and, thus, it is obvious that the structure should be adapted to the purpose of the thin film. In case of diffusion barriers e.g., the grain structure should be rather coarse in order to minimize grain boundary diffusion. Furthermore, mechanical properties resulting from the structure, like the ductility of the film, should be taken into account.

Structure Zone Diagrams

The position of the described zones in a given parameter space can differ strongly as soon as a new parameter, like the amount of impurities in a thin film [6], is introduced. A way to visualize the obtainable structures of a deposition process is a structure zone diagram (SZD). This is done by reducing or summarizing the numerous coating parameters in a suitable way to illustrate their influence on the growth structure. Initially, the idea of SZDs was introduced for evaporation sources with respect to the substrate temperature dependence [81], but the concept is applicable to multiple other techniques and parameters. Thornton eventually used it for sputter depositions and also introduced the working pressure as a parameter that has a kinetic effect on the growing surface by particle bombardment [134]. Especially the atom-to-ion ratio and the ion energy have a significant impact and different structures are observed when comparing low ion energy and high flux versus high ion energy but low flux [100]. Hence, techniques to modify ion bombardment like substrate biasing (see Section 2.3.4) or unbalanced magnetrons (see Section 2.3.2) were developed.

Thornton's approach of separating thermal and kinetic effects on the respective axes in the SZD can be generalized by adding the effects of the ions. This is implemented in the SZD by Anders [2], displayed in Figure 2.34. Here, the thermal axis, with the substrate temperature normalized by the melting temperature of the material, received an additional term related to the temperature shift caused by the potential energy of impinging particles. This sum is called the *generalized temperature* T^*. The linear pressure axis, on the other hand, is replaced by a logarithmic one with the *normalized energy* E^* that describes the displacement and heating effects from the bombarding particles' kinetic energy. Additionally, Anders made use of the vertical axis to include the effects of these parameters on the *net film thickness* t^*, which is reduced by film densification and sputtering – especially for high particle bombardments, the zone of *ion etching* is reached, where more material is removed than deposited.

This SZD can now act as a valuable reference point for the diffusion barrier coatings produced in the framework of this thesis. However, this representation can only serve as a rough orientation as Anders does not fail to emphasize that, "*each combination of substrate, film material, and deposition conditions represent a unique system that is not adequately described by a SZD*" [2].

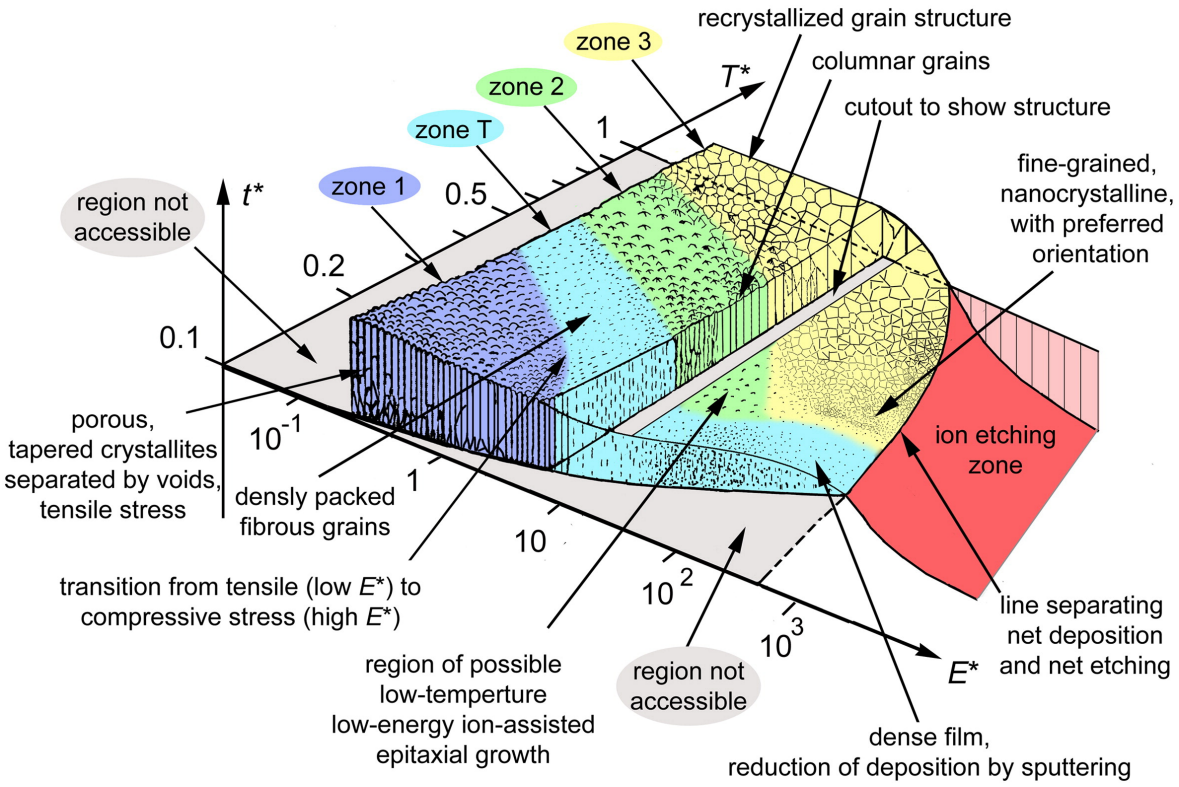

Figure 2.34: Structure zone diagram by Anders showing different regions of crystal structure and growth rates depending on the normalized energy E^* and the generalized temperature T^*. From [2]

2.3.4 Auxiliary Techniques for Sputtering

Apart from temperature, the SZD of Anders indicates that particle bombardment of a growing film has a crucial effect on the resulting properties, thus, the various components of this particle flux and ways to control them have to be addressed. Furthermore, the effects of the substrate like surface texture and contaminations have been mentioned shortly.

In order to achieve better results by applying the knowledge of these effects, a wide range of auxiliary techniques has been developed to modify or complement the basic sputter deposition process shown before in Figure 2.21.

Substrate Biasing

Substrate biasing is a method to control the bombardment of the growing layer with charged particles by varying the substrate's electric potential [67]. The *biasing voltage* U_{bias} that accelerates the particles is the difference in potentials of plasma and substrate. However, depending on its implementation type, the substrate can be at different potentials. To understand the different types of potentials, we will first take a closer look at the plasma:

With the electron temperature being some orders of magnitudes larger than the ion temperature, the electrons are leaving the plasma faster. This results in the *plasma potential* V_{p} being slightly positive with respect to ground potential V_{g}, which is also the anode in the case of DC sputtering. The sheaths close to the electrodes, like the anode fall region, are a consequence of this loss of electrons. In general, the same happens to any object (e.g. the substrate) that is introduced into the plasma; it will get charged negatively with respect to the plasma as the initial electron flux is higher than the ion flux. In this case the object is *floating*, meaning that it has no connection to something that removes charges. Hence, the buildup of negative charges continues till the object repels enough electrons that the negative and positive fluxes are balanced, i.e. the net current on the substrate is zero. In this state, the substrate is on the so-called *floating potential* V_{f}. As a consequence, ions from the plasma are accelerated towards the substrate by the difference in potentials $V_{\text{f}} - V_{\text{p}}$, which is the biasing voltage in this case. However, there are other configurations for the substrate that result in corresponding biasing voltages U_{bias}. The most simple one for example is grounding the substrate together with the vacuum chamber and the anode. This way, a net substrate current I_{s} is retained by constantly removing the negative charges.

While plasma and floating potentials can be just slightly changed with geometry and sputter parameters like pressure or power, the resulting biasing voltages are still basically reduced to the two described configurations, which leave not much margin of control for the particle bombardment. A more sophisticated way to independently put the substrate on a dedicated potential V_{s} (even positive ones with respect to ground) is by equipping it with its own power supply.

Figure 2.35 schematically depicts these three configurations. Bombardment with particles from the plasma is naturally driven by the potential difference between the bombarded object and the plasma. In the case of cathode sputtering, it is the voltage $U_{\text{c}} = V_{\text{c}} - V_{\text{p}}$,

where V_c is the potential of the cathode. The same goes for the different biasing voltages. However, as the plasma potential is not necessarily known in practical applications, ground potential usually serves as a reference point, which is logically also the reference point for the grounded power supplies that display target voltage U_t and substrate voltage U_s. This is justified as the plasma potential in DC magnetron discharges is usually in the range of 2 – 20 V [36, 101], and therefore small compared to applied voltages.

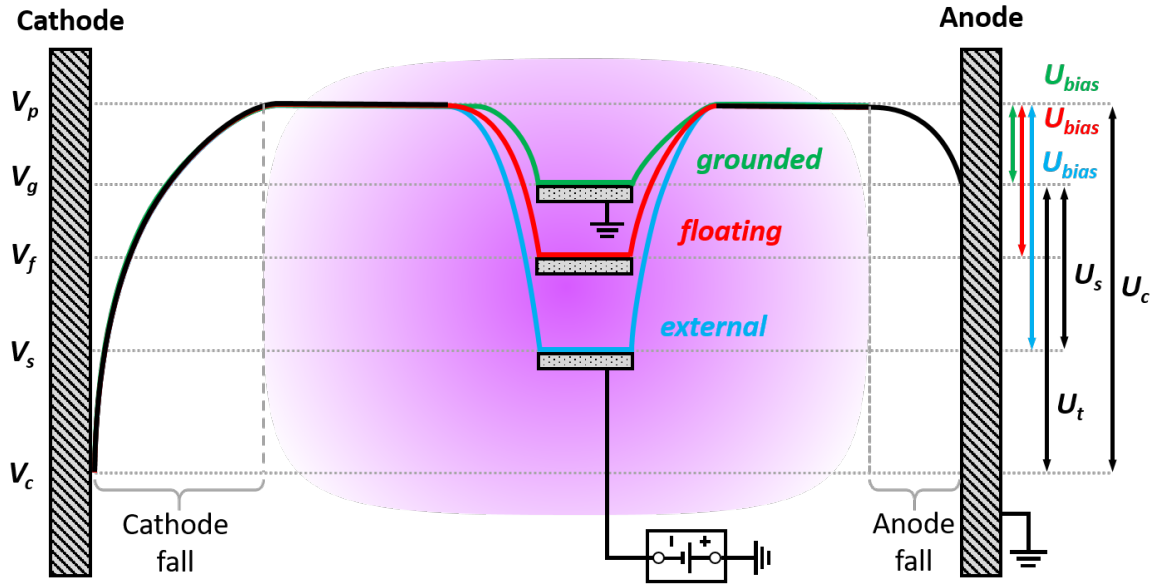

Figure 2.35: Schematic representation of the course of the electric potential between cathode and anode of a sputtering plasma including different substrate potentials. The bias voltages U_{bias} are responsible for accelerating ions towards the grounded (green), floating (red) or externally applied (blue) potentials respectively. Based on [132].

The substrate voltage U_s is now used as a tool to obtain different regimes of particle bombardment. Figure 2.36 shows a typical plot of the substrate current, which is composed of an ion and electron component, $I_s = I_s^i + I_s^e$. This resembles the behavior of a Langmuir probe [54], with the difference that the substrate is comparatively big and therefore disturbs the plasma to some degree.

The different individual behavior of ion and electron current is due to their different masses and the respective energy distribution functions. As the ions have a comparatively low kinetic energy of around 50 meV, they can be considered approximately monoenergetic. The electrons, on the other hand, with energies in the range of several eV have a much broader energy distribution. As a result, ions will be almost immediately repelled as soon as the substrate voltage is above the plasma potential, while electron current drops more gradually when the substrate voltage is lowered, repelling low-energetic electrons first. Similarly, the saturation currents – at which all of the corresponding particle species reach the substrate – are attained respectively fast/slowly.

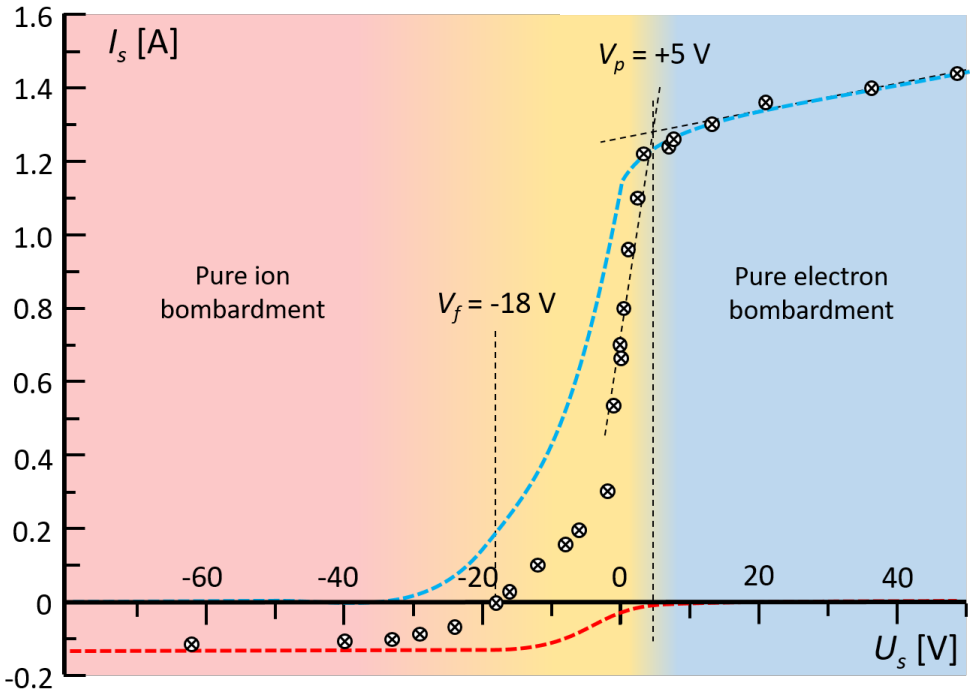

Figure 2.36: Substrate current depending on substrate voltage based on exemplary data from [82]. The ion (red) and electron (blue) components of the current are not part of the data, but the principal behavior is illustrated as dashed lines.

Electrons are useful for introducing thermal energy to the substrate. Ion bombardment also heats the substrate, but most importantly the ions are able to sputter off unwanted structures. Especially, in the island growth regime shadowing effects can be mitigated by eroding prominent structures with ion bombardment. However, the ion energy has to be tuned accordingly with the biasing voltage. When the ion saturation current is reached and the negative voltage is increased further, the individual kinetic energy of the ions is increased, but not their number. Hence, the defects (e.g. lattice defects, stresses, argon ion implantation,...) introduced by the high ion energy predominate the positive effects of the ion bombardment at a certain point.

Plasma Cleaning

Power supplies that are used for applying a biasing voltage to the substrate can usually also be utilized for pre-deposition cleaning of the substrate's surface by particle bombardment. Basically this is just sputtering but with the electrodes reversed. The impinging ions remove surface films and can also erode the surface layers of the substrate up to some micrometers, depending on process parameters and time. This is highly beneficial for the adhesion of the subsequent coating as it roughens the surface and creates open chemical bonds.

However, it must be considered that the sputtered material from the substrate condensates somewhere in the vacuum chamber and possibly contaminates the target. This contam-

ination in turn can then be redeposited onto the substrate during the regular coating. Consequently, a target cleaning step has to be introduced, which is done by regular sputter operation, while preventing deposition of the substrate. This can be implemented with a shutter between target and substrate, but can also be achieved for cylindrical targets by moving the magnetic field – and thus the sputter direction – away from the substrate.

Substrate Heating

The temperature of the substrate plays an important role in the growth of the thin-film (as described in Section 2.3.3). In general, higher temperatures are favored regarding the growth of dense and ductile layers with well-defined grains. On the other hand, the enhanced diffusion at higher temperatures (see Equation 2.4), which causes a more suitable grain structure, also results in intermixing of coating and substrate material. On a small scale, this can be favorable for a good layer adhesion, but higher degrees of interdiffusion are naturally undesired for a material that is supposed to act as a diffusion barrier. Furthermore, elevated temperatures can generate unwanted phases or destroy desired ones. Accordingly, the phase diagrams of the involved materials should be checked beforehand. In the case of U-Mo fuel foils as substrate, in which the γ-phase is to be preserved, the TTT diagram (see Figure 2.2) has to be examined in order to adjust temperature and process time in a way to minimize decomposition.

Substrate heating can be also used as a post-deposition annealing step to remove high residual film stresses, which can cause microcracks, flaking, or blistering of the film from the surface. This practice, however, has to be used with caution as it can result in more damage than it is supposed to prevent. Especially for coating and substrate materials with significantly different thermal expansion coefficients, the interface is heavily strained which can introduce even more macroscopic defects during heating and cooling cycles [70].

Apart from improving the layer growth during the process, preheating the substrate before the coating can have positive effects, especially on the layer adhesion as adsorbed impurities get evaporated at a higher degree off the surface. This mainly concerns a thin film of a few atomic layers of water, which condenses out of the humidity and is adsorbed onto the substrate's surface, where it prevents an adequate substrate bonding of the first atoms arriving from the sputter target. A detailed description of the adsorption and desorption processes of vapor-phase molecules on plane surfaces is given by Langmuir [57].

Given the above examples, it is already evident that some auxiliary processes like preheating and post-deposition annealing need an additional external – meaning it is not related to the PVD process itself – heating source that can be controlled independently without interfering with the sputtering process by changing plasma parameters during the coating. This can be achieved using various methods. Most commonly a heating element is integrated into the substrate holder, consisting of a coil for resistive heating. Heat transfer to the substrate is either achieved by conduction in an appropriate way or by radiative heating, as convection is negligible in the low-pressure environment. Under certain conditions, direct resistive heating of the substrate may be possible. Apart from a suitable electric resistance of the

substrate's material, other components of the substrate holder should not be affected by the required currents, especially power supplies for biasing voltage, if this technique is used simultaneously.

Apart from the active external heating, the particle bombardment and radiation from the plasma as well as condensation of sputtered material are additional sources of heat. Summarizing these contributions, one may use the term *passive heating* as their combined effect is a byproduct of the process conditions that are usually set in a way to optimize the sputtering process with little consideration regarding substrate temperature control. Besides, many different process parameters contribute to the heat flux onto the substrate – like sputtering power, pressure, substrate-target distance, and biasing voltage – some of which influence each other to different degrees. Thus, the external heating described above is usually the method of choice, if a wide range of temperature control is needed.

Regarding the mentioned negative effects of heating, it may be necessary in some cases to install also some cooling resources, if the process parameters alone generate too much heat. This is usually implemented in form of cooling channels integrated into the substrate holder with temperature or flow-rate control of the inlet water.

If no means of temperature measurement, which can disturb the coating process, are installed at the substrate, parameter studies with temperature measurements have to be performed separately to derive the approximate substrate temperature of the process at a certain parameter set in retrospect.

Miscellaneous Techniques Related to Sputtering

A few other techniques of the wide range of PVD methods are shortly mentioned in the following. Especially, different types of power supplies and their possible operation modes offer a wide range of applications. Sputtering of insulating targets for example is achieved by switching the sign of the cathode voltage at a high rate with a special radiofrequency (RF) power supply – calling the method ***RF sputtering*** accordingly. This avoids charge buildup at the target that would otherwise extinguish the plasma discharge.

A similar goal of dealing with insulators is pursued by ***reactive sputtering***. Here, a ceramic compound is deposited by a chemical reaction of the conductive target material with a reactive gas (usually nitrogen or oxygen) added to the argon atmosphere, forming a metal oxide or nitride. However, this also needs a power supply capable of temporary voltage reversal (but not of such a high frequency as the RF), a so-called ***pulsed mode***. The reason for this is *target poisoning* which happens inevitably as the reactive gas component also reacts at the target surface forming a thin insulating layer there.
In general, target poisoning or insulating impurities on energized parts are inextricably linked to the phenomenon of *arcing*, which is common in reactive sputtering but also occurs in DC sputtering of metals. An arc is a local high-current discharge (see Section 2.3.1) that is initiated by breakdown of dielectric layers and inclusion, which cause charge buildup and usually also have a higher secondary electron emission. For a more detailed description

see [3]. As a result of the high local current, material is liquefied and ejected as droplets or macroparticles that degrade the quality of the deposited layer, while the generated craters remain as surface defects on the target or substrate.
To suppress these arcing events, sputtering and biasing power supplies are equipped with an ***arc management system*** that detects forming arcs within microseconds based on the changing current/voltage characteristics and immediately interrupts the energy supply or even reverses the voltage to shut down the arc as quickly as possible.

Chapter 3

Instrumentation & Methods

This chapter describes the technical systems and process steps used for the production and analysis of suitable samples. The instrumentation consists of the sputtering devices for mini-size and full-size foil geometries as well as the enhancement of the substrate holder for the latter one. Detailed steps for the fabrication of U-Mo plates are described followed by the sample preparation for subsequent materialographic investigations on coated foils and finished plates with cladding. Optical and electron microscopy and their use as fundamental methods for sample examination are explained.

3.1 Instrumentation

Instrumentation includes the PVD devices, which are the central pieces for the production of diffusion barrier coatings with suitable properties. For this, the substrate holder, which has been continuously improved, also plays a decisive role.

3.1.1 Mini-size PVD Device

This coating device is named after the geometry of foils (82.5 mm x 19 mm) that are used as a substrate. It was designed and constructed as a highly versatile system with a broad parameter space to study and control the layer adhesion and coating properties, which are crucial for its performance as a diffusion barrier [132]. This expansion of the parameter space turned out to be necessary, as the first effort of TUM building a coating device [119] with a substrate geometry of up to 700 mm $\times$ 62.4 mm had flaws regarding the long-term adhesion of the Zr coating on the U-Mo.

Glovebox System

Requirements for chemical cleaning of the to-be-coated U-Mo foils and prevention of re-oxidation resulted in a system that is more extensive than just a process chamber with a sputtering source. Two gloveboxes connected by a transfer lock ensure that all processes including cleaning, coating, and packaging of a U-Mo foil are performed in an inert atmosphere of argon. Each of the gloveboxes has a small transfer lock for loading and unloading of samples or tools. A gas purification system for each glovebox keeps the O_2 and H_2O content in the atmosphere below 1 ppm (parts per million). To contain radioactive material in case of a leak, the gloveboxes are operated at about 2 mbar below the ambient pressure in the lab. This whole system is depicted in Figure 3.1.

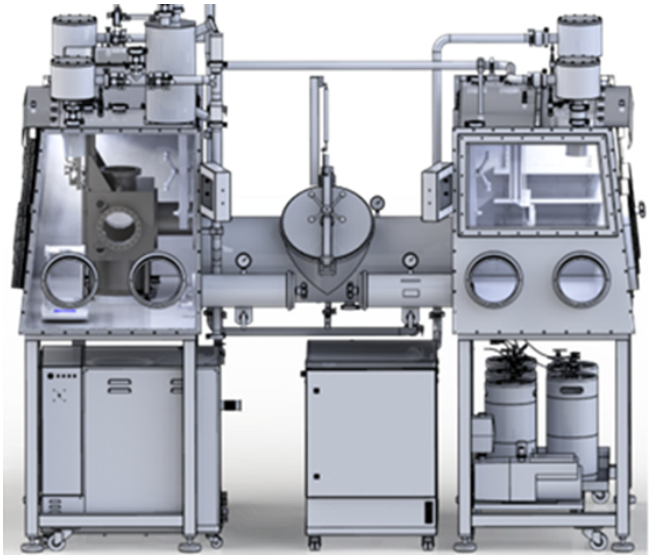

Figure 3.1: Model of the complete glovebox system consisting of a glovebox with the actual PVD device (left) and a glovebox designated for chemical preparations (right) connected by a transfer lock. From [131].

One glovebox is designated for chemical cleaning of the U-Mo foils and is equipped accordingly with an activated carbon filter to remove acid or solvent vapors. For the supply of various chemicals, a dispensing system is integrated to avoid using the transfer locks. The second glovebox contains the actual sputtering system as well as a precision scale for weighing of samples, and a pair of heat sealing pliers for leak-tight packaging of samples in aluminum composite bags.

Vacuum Chamber & Gas Supply

Central part of the device is the vacuum chamber that contains the sputtering source and the substrate holder. A view of the inside is shown in Figure 3.2. The interior dimensions are 40 cm in width, 30 cm in height, and 32 cm in depth, which results in a volume of about 40 liters. The front door of the chamber can be removed completely by a wire rope hoist to get maximum accessibility to all components inside. Evacuation is performed by a fore pump (rotary vane pump *TRIVAC D 65 B* by Leybold) in series with a turbomolecular pump (*TURBOVAC MAG W 1300 iP* by Leybold), reaching a base pressure below 10^{-7} mbar for a low-impurity atmosphere. The first stage of the pumping process is done solely by the fore pump, as the turbomolecular pump is not designed to operate in the ambient pressure regime. For this, a bypass is implemented that features a butterfly valve, which is opened slowly to restrict the initial flow rate. This is done to avoid whirling up loose particles in the chamber with the first pressure surge of the pump. These particles can settle on the substrate and degrade the coating or can cause short circuits between energized and grounded components.

Figure 3.2: Vacuum chamber with removed front door showing the sputtering source and the substrate holder.

Argon with a purity grade of 4.8 (corresponding to 99.998 %) is used as process gas. Process pressures for sputtering and plasma cleaning in the range of $10^{-3} - 10^{-1}$ mbar are set by adjusting the gas inlet with mass flow controllers (type: *F-201CS* by Bronkhorst). For the low-pressure regime, a gate valve in front of the turbomolecular pump can be set to an

intermediate position between open and closed to reduce the throughput of the pump and therefore the amount of argon flow to set the designated pressure. In case of the higher pressures needed for plasma cleaning, only the fore pump is used by bypassing the turbomolecular pump. A second mass flow controller with a gas supply of nitrogen makes the device also capable of reactive sputtering. Pressure is measured by two pressure gauges: a wide-range sensor (*Ceravac CTR 100 N* by Leybold) that covers twelve orders of magnitude in mbar, and a precision gauge (*Penningvac PTR 90* by Leybold) that allows an accurate adjustment over three magnitudes in the region of the working pressure. Venting of the chamber is manually performed by a small venting valve installed at a flange of the chamber.

Sputtering Source

The source type is a planar DC magnetron run by a power supply (*TruPlasma DC 3002* by TRUMPF Hüttinger) with an integrated arc management system and a maximum output of 2000 W.
As a target serves a simple cuboid of the desired material with a base area of 122 mm × 54 mm and a thickness of up to 10 mm. The target is attached to a copper backing plate by a single screw. This easily removable assembly is fixed at the sputter source by magnetic force using the permanent magnets of the magnetron. It is able to hold a target of U-Mo with a density of 17.2 g/cm^3 and a thickness of 10 mm. Thermal conductance paste is applied on both sides of the backing plate (in contact with the target and the heat sink) for effective heat dissipation. A grounded metal housing is mounted around the target to serve as a dark space shielding that allows plasma ignition only at the target. Figure 3.3 depicts the mentioned components.

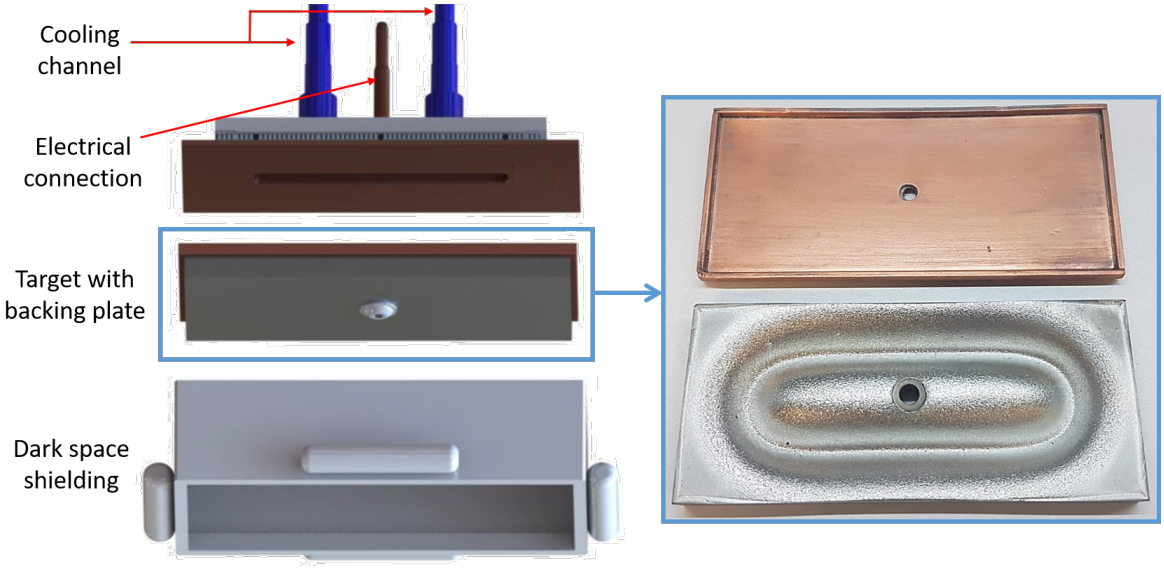

Figure 3.3: Model of the sputtering source separated in parts that can be removed manually without tools (left). On the right is a picture of a used target removed from its backing plate. Based on [12].

Figure 3.4 shows the interior layout with the magnetic system and the resulting field lines. The fixed permanent magnets provide a reliable constant field. However, this stationary planar geometry naturally results in an inhomogeneous erosion (a so-called *racetrack profile* as seen in Figure 3.3) of the target as the ion bombardment is increased at positions of stronger magnetic field. Consequently, a target utilization of only about 25 % can be achieved as the target has to be changed when the depth of the racetrack groove starts to reach the copper backing plate.
Good electrical insulation is crucial to separate high-voltage parts from grounded parts, especially from the cooling water. This is achieved by an aluminum nitride plate, which serves as an electrical insulator, but is a good heat conductor at the same time.

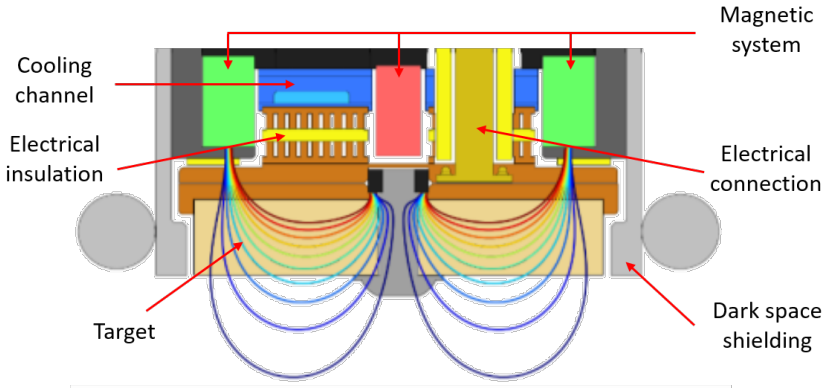

Figure 3.4: Sectional view of the sputtering source showing the magnetic field lines of the magnetron. Based on [132].

Substrate Holder

The substrate holder is the component that introduces new control parameters compared to the previous device, in which the substrates were just placed onto a plate with integrated water-cooling. For a broader study of effects on the coating, the advanced substrate holder depicted in Figure 3.5 is capable of substrate heating, application of a biasing voltage, and a variable target-to-substrate distance. A theoretical treatment of the influence of these parameters on layer growth can be found in Chapter 2.3.3.

Substrates are simply placed on a plate of 100 mm diameter with no means of clamping for fixation whatsoever to ensure a complete surface coverage of the substrate with coating. The plate is made out of molybdenum due to its high melting point and its resistance to hydrofluoric acid, which is used to dissolve residues of zirconium. However, to reduce zirconium deposition on the Mo plate, an aperture ring is placed above it. Three versions of the Mo plate are used for different operation modes: for biasing or heating of the substrate, the respective plate has either a good or a weak thermal contact with the copper heat sink. For a high-temperature mode that achieves substrate temperatures of up to 1000 °C, the Mo plate has rectangular cutouts below to substrate to allow direct line-of-sight with the radiative heater.

A shutter between the Mo plate and the target can be opened and closed pneumatically. It serves as a protection for the substrate from falling flakes of coating material that peel off the chamber walls or the target. Additionally, the shutter can be closed at the beginning of a sputtering process to remove impurities from the target's surface without depositing them on the substrate. As mentioned above, heating of the substrate is achieved by radiative heating with a module that utilizes resistive heating of a graphite element. This heating element is controlled by an external power supply. Several thermocouples are installed at various components of the substrate holder to monitor the temperature. To link the heating powers (as well as sputtering powers) with the resulting substrate temperatures, a study has been performed by lo Muzio [63].

For the application of biasing voltage an appropriate DC power supply (*TruPlasma Bias 3003* by TRUMPF Hüttinger) with an integrated arc management system is used that reaches a maximum voltage of 1200 V. This voltage is just applied to the Mo plate and the ring that holds it; all other components are grounded and thoroughly separated by electric insulators to avoid the ignition of parasitic plasmas. Especially the power supply lines inside the vacuum chamber were designed in a way to achieve this. For the top part of the substrate holder, a grounded mantle serves as a dark space shield and protection against coating of the inner parts.

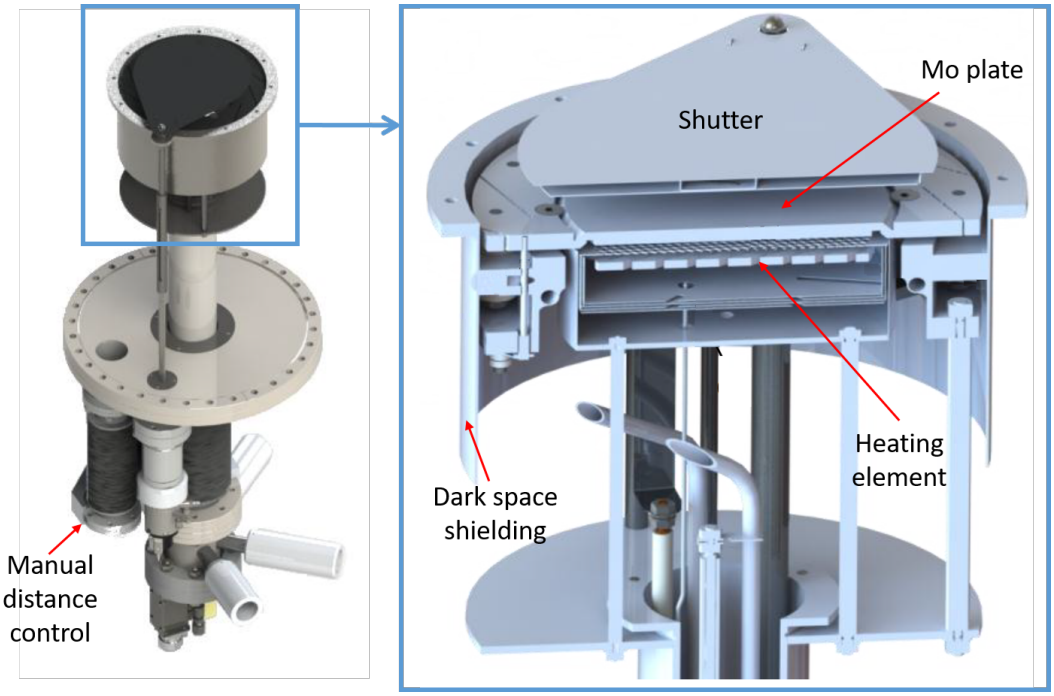

Figure 3.5: Model of the complete substrate holder unit (left) integrated into the flange that is installed at the bottom of the vacuum chamber. The different connectors for cooling water, heating power, and biasing power are easily accessible outside of the glovebox together with the manual distance control between substrate and target. On the right is a sectional view of the part inside the vacuum chamber showing the inner structure with the heating element. Based on [12].

3.1.2 Full-size PVD Device

The full-size device was developed as a follow-up of the mini-size device with the primary goal of scaling up the geometry to coat U-Mo foils of the dimensions intended for monolithic research reactor fuel plates. The so-called *full-size* geometry of 762 mm × 45 mm is defined as a reference size here. As a step towards industrialization, the full-size device serves as a pilot system to demonstrate the feasible production of coated full-size foils. The experience gained from studies with the mini-size device [34, 132] was used to decide which features to control the parameter space were to be retained and which omitted [8, 124].

Glovebox System

The complete device is contained in the frame of a single glovebox shown in Figure 3.6. A separate glovebox for chemical cleaning or even cleaning in the same glovebox as the coating device was shown to be unnecessary, as the re-oxidation of U-Mo on air after cleaning is not severe enough to degrade the layer adhesion significantly. It is sufficient to introduce the foils into the glovebox within 30 minutes after cleaning. For this, the glovebox is equipped with a main transfer lock of 1000 mm in length and 400 mm in diameter. Small samples and tools can be introduced by a transfer lock of 440 mm in length and 150 mm in diameter. The argon atmosphere is retained by a gas purification system that keeps the oxygen content as well as water vapor below 1 ppm (parts per million). To contain radioactive material in case of a leak, the glovebox is operated at about 2 mbar of negative pressure with regard to ambient pressure in the lab.

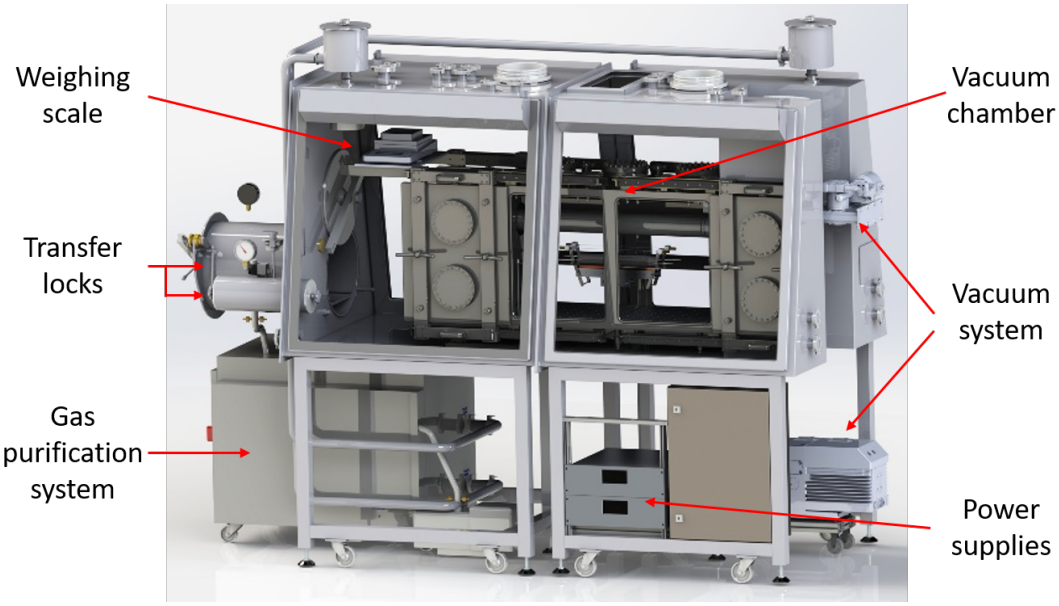

Figure 3.6: Model of the complete full-size device.

Apart from the vacuum chamber with the actual sputtering system, the glovebox is further equipped with a pair of heat sealing pliers for leak-tight packaging of samples in aluminum composite bags as well as a weighing scale. This scale is placed on top of the guide rails of the vacuum chamber doors to weigh large substrate foils hanging by a special adapter at the bottom of the scale.

Vacuum Chamber & Gas Supply

Figure 3.7 shows a model of the vacuum chamber with the sputter source and substrate holder installed. The interior dimensions are 100 cm in width, 56 cm in height, and 40 cm in depth, which results in a volume of about 220 liters. Four sliding doors give access to the inside of the chamber. Evacuation is performed by a fore pump (rotary vane pump *TRIVAC D 65 B* by Leybold) in series with a turbomolecular pump (*TURBOVAC MAG W 1300 iP* by Leybold), reaching a base pressure below 10^{-6} mbar for a low-impurity atmosphere. The evacuation process is similar to the one of the mini-size device: The first stage of the pumping process is done solely by the fore pump, as the turbomolecular pump is not designed to operate in the ambient pressure regime. For this, a bypass is implemented that features a manual butterfly valve, which is opened slowly to restrict the initial flow rate. This is done to avoid whirling up loose particles in the chamber with the first pressure surge of the pump. These particles can settle on the substrate and degrade the coating or can cause short circuits between energized and grounded components.

Except for two manual venting valves installed at the top of the vacuum chamber, the other installations are equal to the ones from the mini-size device. This includes the argon supply, mass flow controllers, and pressure sensors.

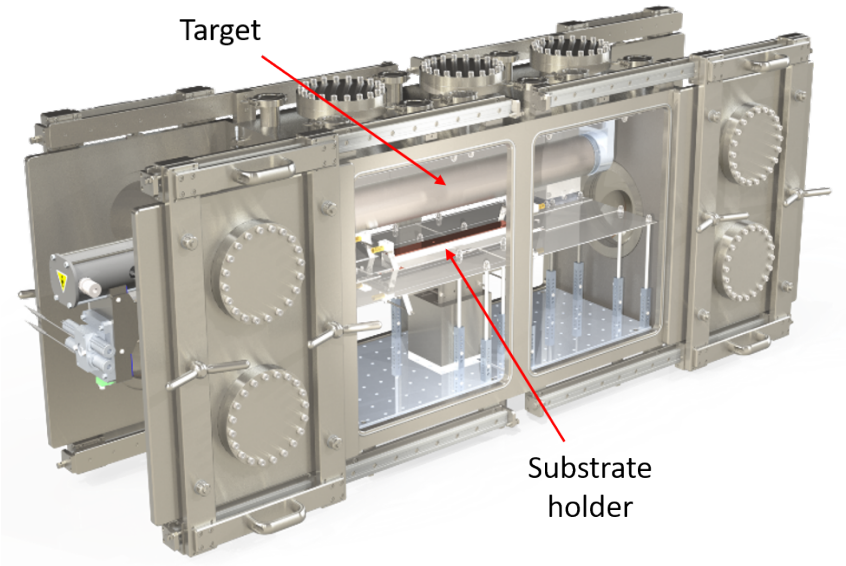

Figure 3.7: Model of the vacuum chamber of the full-size device with installed sputtering source and an early version of the substrate holder.

Sputtering Source

The full-size device is designed as pilot equipment to demonstrate the feasibility of the sputter coating process for industrialization. To achieve this, the mini-size device was not just enlarged to full size geometry but the general design was optimized. The most noticeable difference to the previously used device for mini-size foils is the use of an industrial rotary magnetron shown in Figure 3.8. Apart from a few minor technical adjustments to fit the chamber geometry is this a standardized industrial product by the commercial supplier *Sputtering Components*. Here the rotating target has the geometry of a hollow cylinder through which the cooling water flows. This technique is a well-proven industrial standard and features several advantages. The target utilization is in the order of 80 - 90 % [35], significantly higher compared to stationary planar targets that have utilization of around 25 %. This is due to the more homogeneous erosion of the cylindrical target that comes with the additional advantage of more stable plasma parameters during long-term operation. During its operation, the geometry changes much less compared to the distinctive racetrack formation induced by the magnetic field on planar targets.

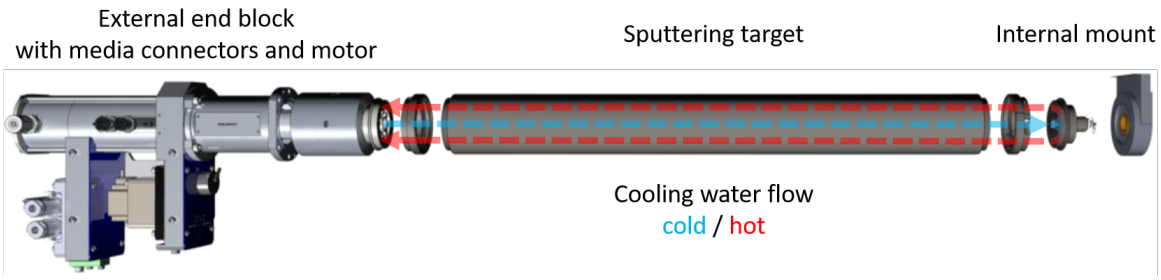

Figure 3.8: Model of the rotary sputtering source. The end block with the motor for target rotation is mounted outside of the vacuum chamber. It features media connectors for cooling water, sputtering power, and pressurized argon for swiveling the magnet bar. A vacuum flange connects the end block with the target inside the chamber. An internal mount carries the weight of the target. Based on [8].

This focus on long-term operation comes at the expense of flexibility. The target, for example, is not so easily changeable anymore, especially when considering that this has to be executed inside the glovebox. Furthermore, the target has to be flushed with pressurized argon to remove the cooling water. The disassembly of the target also allows the exchange of the magnetic system, which consists of a single magnet bar inside the target. Two magnet bars have been purchased: a standard magnet bar (*SRM80* by Sputtering Components) with a balanced field configuration and a custom designed magnet bar (*uTRM80* by Sputtering Components) that delivers a type-2 unbalanced magnetic field for increased charged particle bombardment of the substrate (see Chapter 2.3.2 Figure 2.28). In addition, the magnet bar inside the target is swivel-mounted and can be turned by 135°. This allows operation in a distinct cleaning position where the target is sputtered free from possible impurities without depositing those onto the substrate. This way, no additional shutter mechanism is needed between target and substrate. This swivel mechanism and the magnetic field resulting from the unbalanced magnet bar are schematically depicted in Figure 3.9.

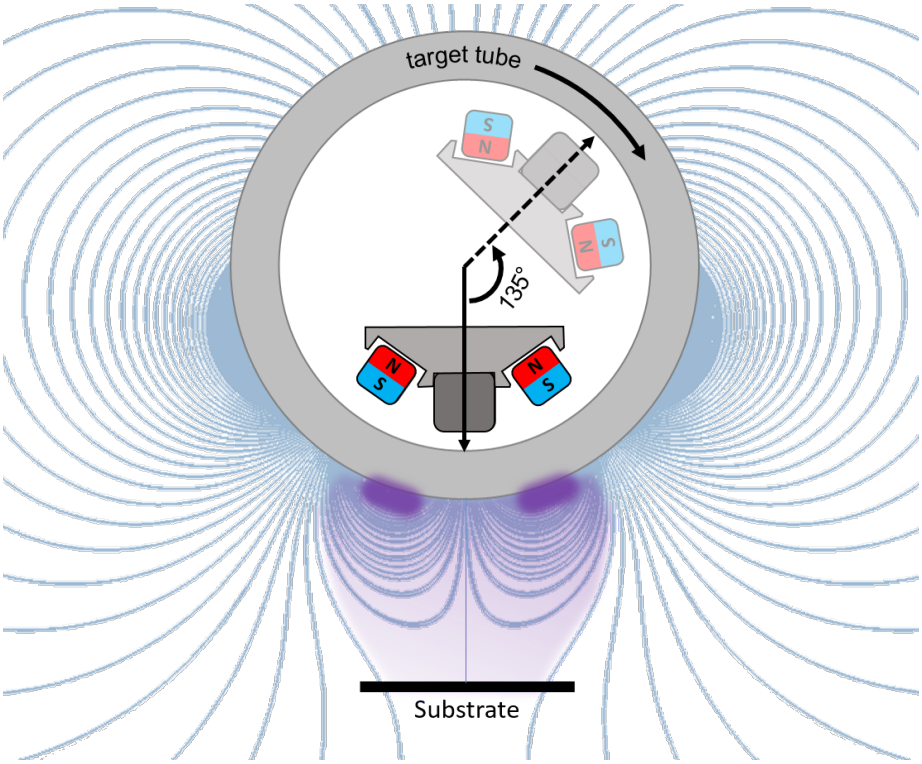

Figure 3.9: Schematical true-to-scale cross section of the target with the unbalanced magnet bar and the resulting magnetic field in coating position. The plasma (purple) is concentrated at the two erosion zones on the target, but some ions can escape to the substrate. The cleaning position of the magnet bar is indicated in dimmed colors. Based on [8].

The source is run by a DC power supply (*TruPlasma DC 3020 G2* by TRUMPF Hüttinger) with an integrated arc management system and a maximum output of 20 kW.

The cylindrical target has an outer diameter of 100 mm and a length of 870 mm with an effective erosion zone of 850 mm. With a wall thickness of 10 mm, the total weight of such a target made out of zirconium is slightly above 16 kg. Two zirconium targets have been used with different quality regarding impurities. One being a common industrial-grade zirconium (type: Zr 702) and the other a purified reactor-grade Zr. Data on the content of impurities in both targets can be found in Tables 3.1 and 3.2.

Table 3.1: Impurity content of the Zr 702 sputtering target.

Element	Hf	O	Fe	C	H	Cr	Ti	N
Content [ppm]	12900	1200	720	150	100	75	56	45

Table 3.2: Impurity content of the reactor-grade Zr sputtering target.

Element	O	Fe	Hf	C	Sn	Cr	Al	H	Nb	Ta	Zn	Nb	Pb	Ca
Content [ppm]	369	157	46	39	32	26	25	5	<50	<50	<50	<40	<20	<10

Element	Cu	Mg	Mn	Mo	N	Ni	Ti	V	W	Co	U	B	Cd
Content [ppm]	<10	<10	<10	<10	<10	<10	<10	<10	<10	<5	<0.5	<0.4	<0.4

3.1.3 Substrate Holder Development

In the course of this thesis, the substrate holder for the full-size device went through several adjustments and design changes like the implementation of various features, elimination of issues, and improved handling. This development is presented in the following.

1st Generation

The first design was developed by Grimm [34] and is depicted in Figure 3.10. It was an experimental setup for half-size substrates to test features like electron heating and several types of thermal conductance foils. Application of biasing voltage was implemented as well as water cooling with no external heating mechanism. Like at the mini-size device, the substrate foil is placed loosely on the holder without any fixation. For continuous adjustment of substrate-to-target distance, the whole assembly was mounted on a manual laboratory scissor jack.

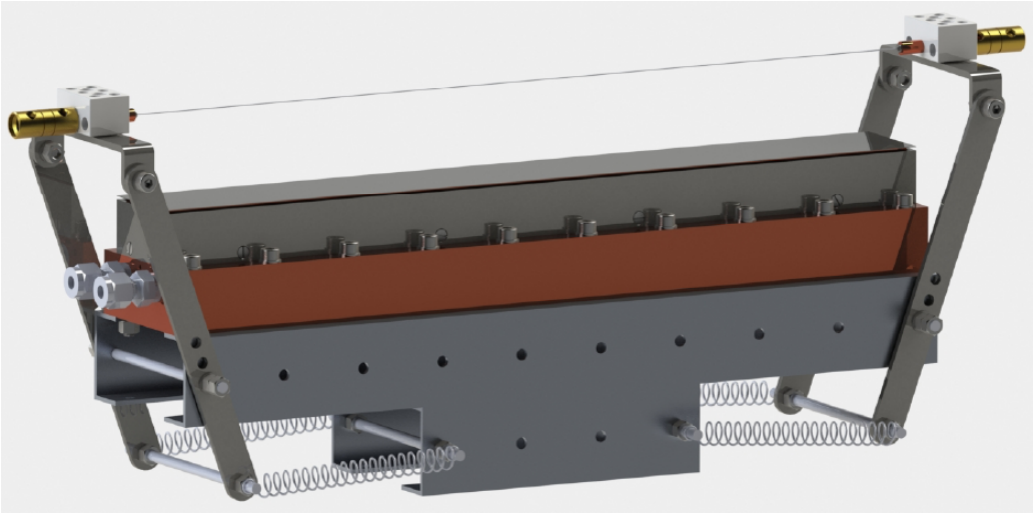

Figure 3.10: Model of the first substrate holder (for half-size geometry) used in the full-size device. From [34].

This substrate holder was used for initial parametrization tests of the full-size sputtering device [103]. The biggest issue, which has already been observed with the mini-size device, is the bending of the foils during sputtering. This is caused by a combination of inner stresses of the growing layer and different thermal expansion coefficients of coating and substrate material. Correspondingly, the bending is more pronounced, the thicker the coating is. Figure 3.11 illustrates an example of such a bent foil. After coating of the back side, the foils are effectively flat again. However, some issues arise from this still. The bending during sputtering increases the inhomogeneity of the coating as the middle part of the foil is significantly closer to the target. This inhomogeneity mainly concerns the layer thickness, but the bending could also affect other layer properties caused by the different ion bombardment. In severe cases, the bent foil could touch the target during sputtering causing a short circuit to the substrate holder. This could destroy one or both of the power supply units.

Fixing the substrate foils with adhesive thermally conductive foil or by an electrostatic chuck was unsuccessful. As a result, the concept of the design for the upscaled full-size substrate holder was fundamentally changed.

Figure 3.11: Bent half-size (380 mm length) stainless steel substrate foil after coating of one side.

2nd Generation

The necessity to keep the substrate straight during the sputtering process resulted in the design of the first full-size substrate holder depicted in Figure 3.12. This is achieved by clamping the ends of the foils into two blocks that move freely on two guiding rods. After the foil is mounted, it gets tensioned by a spring on a threaded rod that presses against the clamping block. This even continuously adapts to the thermal expansion and contraction of the foil and keeps it flat during the whole sputtering process. An additional advantage of this design is that substrates of any length up to full-size geometry (762 mm) can be processed by simply sliding the clamping blocks to a different initial position.
The two pedestals that carry the construction have a mechanism to adjust the height of the clamping blocks and therefore the substrate-to-target distance. However, this is not continuous anymore but fixed to a couple of discreet distances between 30 mm and 70 mm. Temperature measurements on the foil were performed to record the state of the substrate at different process steps and sputter parameters [28]. Like in the first version of the substrate holder, no means of external heating is installed and the design does not allow for cooling.

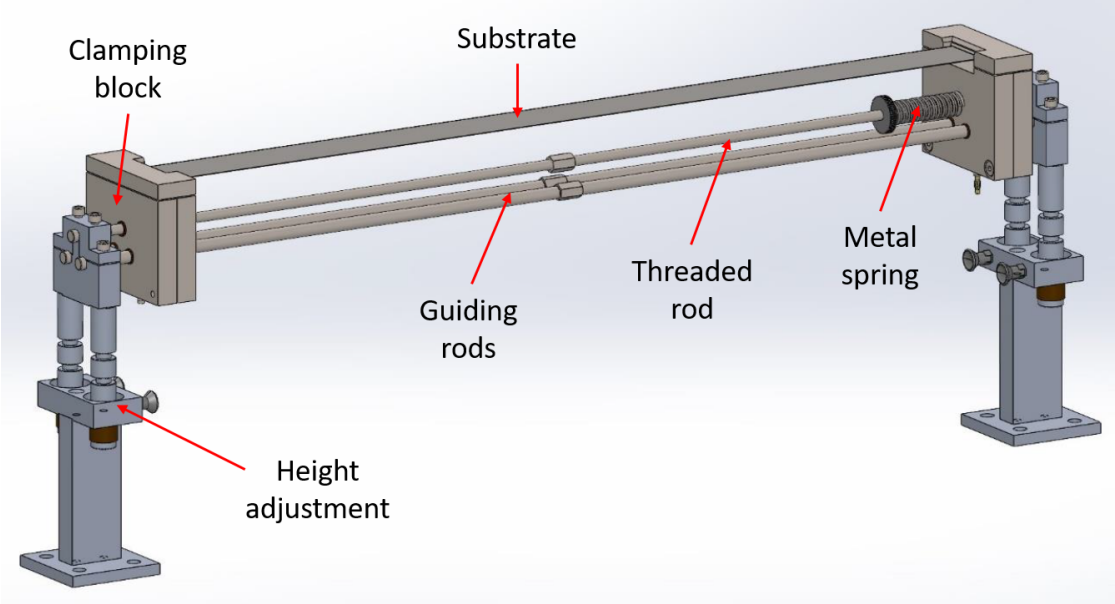

Figure 3.12: Model of the second-generation substrate holder. Based on [25].

The challenge of this design is the implementation of the biasing voltage. For this, live parts have to be shielded except for the substrate itself. This is why the clamping blocks have an inner structure that is not only responsible for the clamping but also for the electric connection, while the outer housing is on ground potential to act as a dark space shielding. Figure 3.13 shows a model of this. Live and grounded parts have to be separated thoroughly by ceramic plates or sufficient distance. Insulating bushings are used for the holes in the central block through which the guiding rods and the threaded rod pass. Clamping of the substrate alone with a designated yoke was shown to be not sufficient. Thus, an additional fixation mechanism is implemented by drilling two holes at each end of the substrate and clipping it into pins on the inner block. The live parts of the block are shielded from sputter coating by a cover plate. The downside of this whole concept is that a part of the two foil's ends does not get coated and has to be cut after the process.

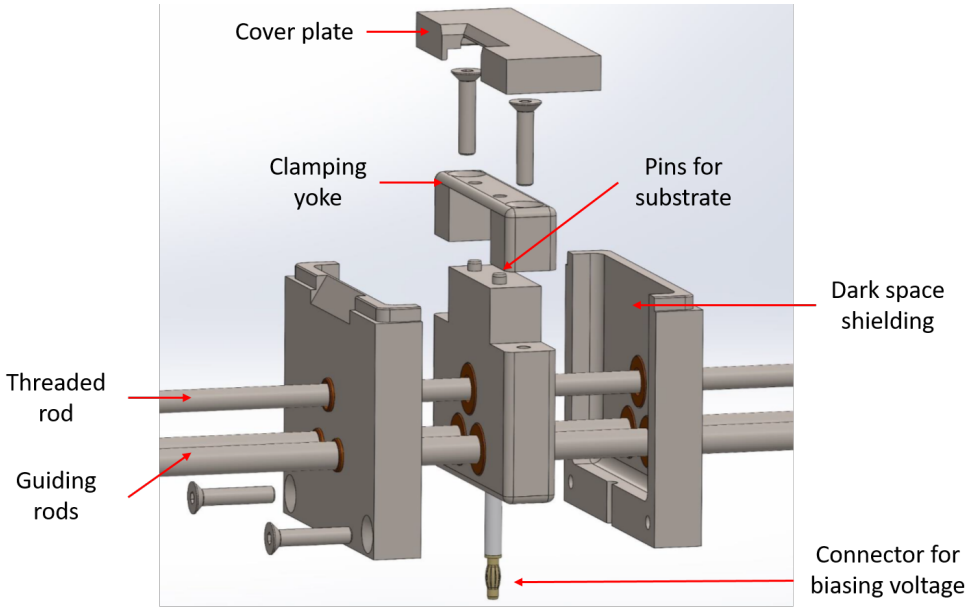

Figure 3.13: Exploded view drawing of a clamping block used in the second-generation substrate holder. Based on [25].

Albeit in principle successful, the design exhibited some flaws that degraded the long-term performance and are not acceptable for an industrialized process:

Short circuits are a major issue of the substrate holder as they appeared multiple times at various spots. The problem arises from an adverse combination of requirements on the sputtering device. For biasing and plasma cleaning, it must be possible to apply a voltage to the substrate and thus also to certain parts of the substrate holder that connect the power supply with the substrate. To prevent the ignition of parasitic plasmas on these parts, they must be protected with grounded parts that act as a dark space shielding. For effective shielding during plasma cleaning (800 V at pressures of up to 0.1 mbar), the gaps between live and grounded parts should be smaller than a few millimeters (see Paschen curves in Figure 2.20). However, at some edges of the live parts, the electric field is locally enhanced, which can cause corona discharges as mentioned in Chapter 2.3.1. This was slightly improved by rounding the edges but was not sufficient to solve the issue completely. In addition, the small gap sizes are disadvantageous concerning loose zirconium flakes that can short circuit the live and grounded parts. Furthermore, particles of conductive zirconium diffuse through the chamber during sputtering and can coat parts of the substrate holder to slowly form a permanent short circuit.In summary, the problem is that, the smaller the gap size, the lower the probability of parasitic plasmas to form, but on the other hand, the easier the formation of short circuits caused by zirconium particles.
Another design flaw is that the force of the contracting substrate acts almost tangential on the clamping block. As a result, the block slightly tilts and gets stuck on the guiding rods. This issue even worsens over time as zirconium dust from the sputtering gathers on the guiding rods and increases the friction.

3rd Generation

The experience with the first clamping substrate holder led to an improved version that was designed to resolve the flaws encountered before. The design, as depicted in Figure 3.14, is based on the same principle as the previous model, using a spring for tensioning the foils. Apart from this, additional features were implemented like a rotatable suspension for the foil and the possibility of resistive heating.

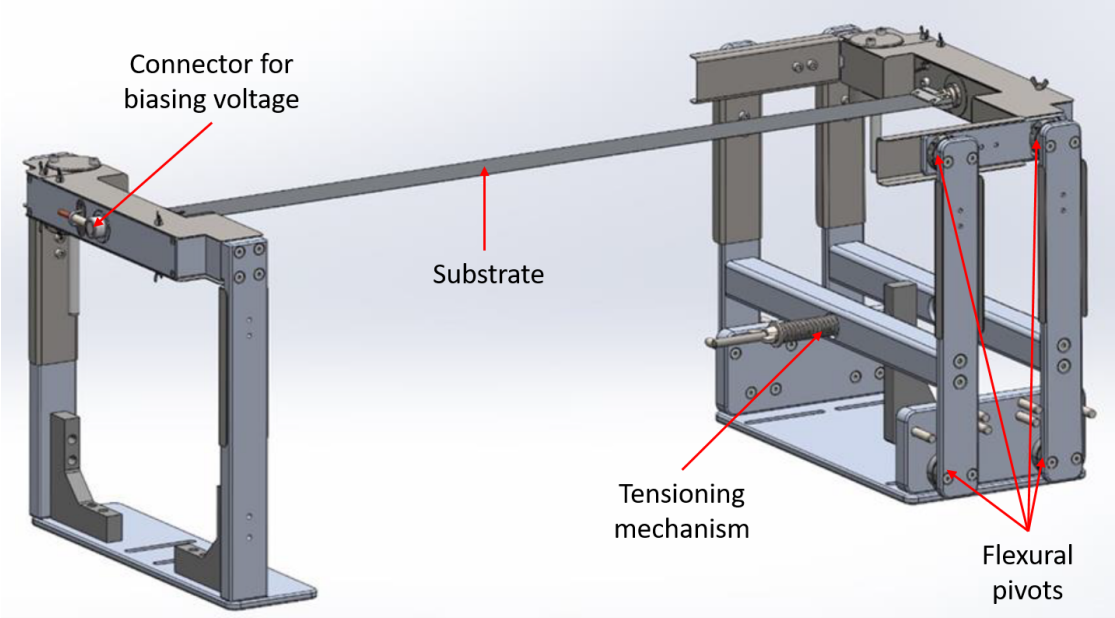

Figure 3.14: Model of the third-generation substrate holder. Based on [25].

Instead of direct linear motion, like with a guiding rod in the previous version, the travel of the clamping unit necessary for keeping the foil tensioned is achieved by slight angular motion. While one of the clamping units is stationary, the other is carried by four vertical axes that can be tilted using flexural pivots. Figure 3.15 shows such a pivot and illustrates its application. The force for tensioning is still applied by a metal spring that acts on the cross-beams that stabilize the vertical axes. The major advantage of the flexural pivots is the frictionless movement without wearing, which makes them completely resistant to pollution. Furthermore, they require no lubrication or maintenance in general. With these features, this component is ideal for long-term use inside the vacuum chamber. A theoretical disadvantage of the described working principle is that the height of the clamping block – and therefore the substrate-to-target distance – changes with the rotation of the vertical axes. However, the flexural pivots only allow for rotations of a maximum of 7.5°, which is further restricted to 3.5° in the design of the substrate holder by the use of stopping pins. Accordingly, the change in substrate-to-target distance is less than 1 mm. If no external force by the spring is applied, the restoring force of the flexural pivots returns the clamping block to its position of rest.

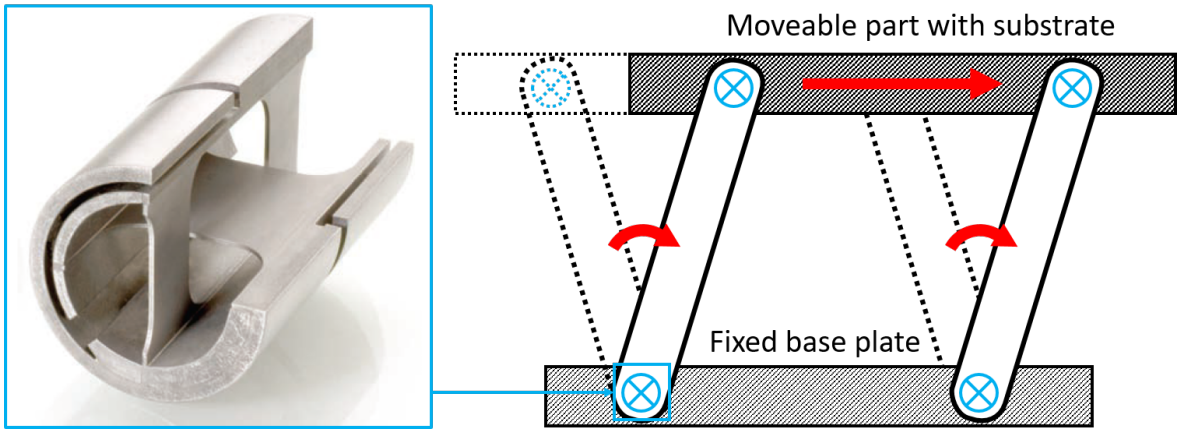

Figure 3.15: Cutaway of a flexural pivot (left) and its application principle: an angular motion using the flexural pivot bearings (blue) mediates the linear translation of the movable upper part at which the substrate is clamped. Based on [111].

The substrate foils are mounted on two pins of each clamping block. The two drill holes needed for this on each side of the foil are of the same dimension and position as for the previous substrate holder. The foils then get fixed by a yoke, which is tightened by a screw (see Figure 3.16).

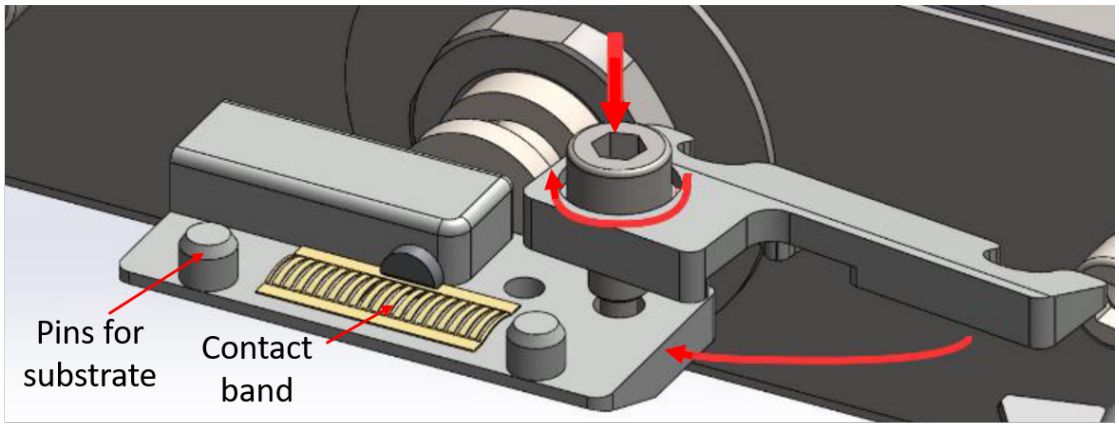

Figure 3.16: Model of the component for substrate mounting showing the mechanism for clamping of the substrate. Based on [25].

The application of voltage to the substrate is achieved by a conductive central axle made out of the copper alloy CuCr1Zr, which has good electric conductivity and sufficiently high yield strength of 470 MPa. At the end of the axle is a contact band of gold-coated beryllium-copper for a good electrical connection with the substrate foil. To reduce the complexity, no additional dark-space shielding, which is prone to short circuits, is implemented at the clamp. As a negative consequence, the clamping body is exposed to the plasma. However, this is acceptable as the mounting body is robust and easily exchangeable. Furthermore, possible material eroded by the plasma cannot contaminate the substrate as

the mounting body is quickly covered by a protective layer of zirconium. Ceramic bushings and washers made of alumina are used to insulate the live axle from the grounded parts in the inside of the clamping body. This is done in a way, that zirconium coating cannot cause short circuits. Figure 3.17 illustrates the internal insulation. The two concentric bushings separated by a gap play an important role to avoid short circuits caused by zirconium coating. For a short-circuit, the two bushings have to be connected by conductive coating, which is only possible in the remote inside of the clamping body that is not in line-of-sight with the sputter source and also hard to reach by diffusion of sputtered particles.

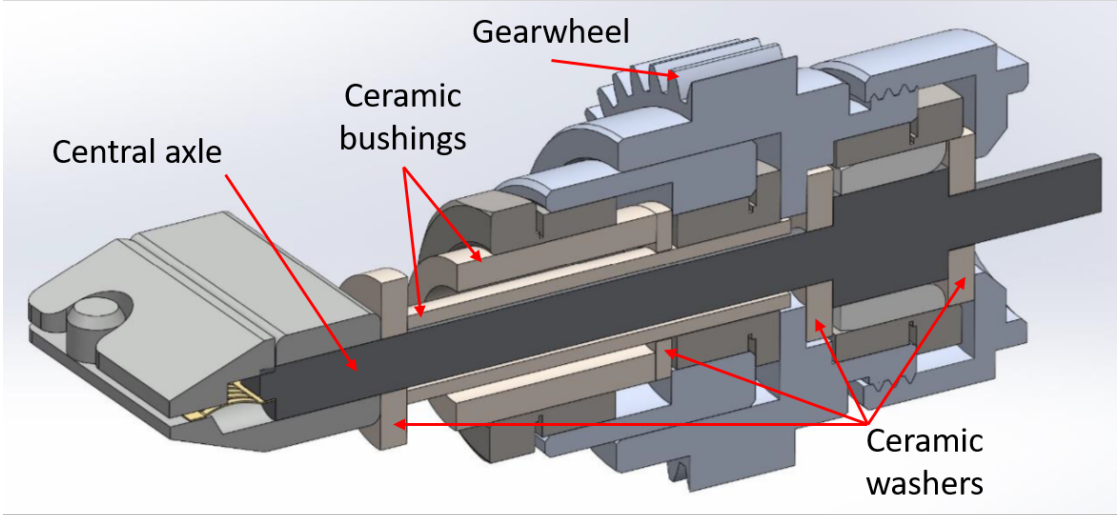

Figure 3.17: Cross section of the clamping body showing the central axle for electric connection and the different insulation ceramics. Based on [25].

An additional feature that has been implemented is the possibility of turning the substrate while still being mounted on the clamping body. Figure 3.18 shows the gear train inside the clamping block by which the mounted foil is rotatable. This already safes time, as the foils do not have to be removed from the clamping body anymore for processing of the second side. If equipped with a remote controlled tool for turning, a huge advancement towards a more time-efficient process necessary for industrialization can be made. Coating both sides of the foil in one sputtering session would eliminate time-consuming steps like venting and re-evacuation of the vacuum chamber.

Finally, the possibility of resistive heating of the foil for experimental purposes is implemented. This is done by connecting the central axle to a heating power supply instead of the power supply for biasing voltage. The choice of materials for the central axle and the contact band allows for a maximum current of 120 A without affecting the resilience of the components.

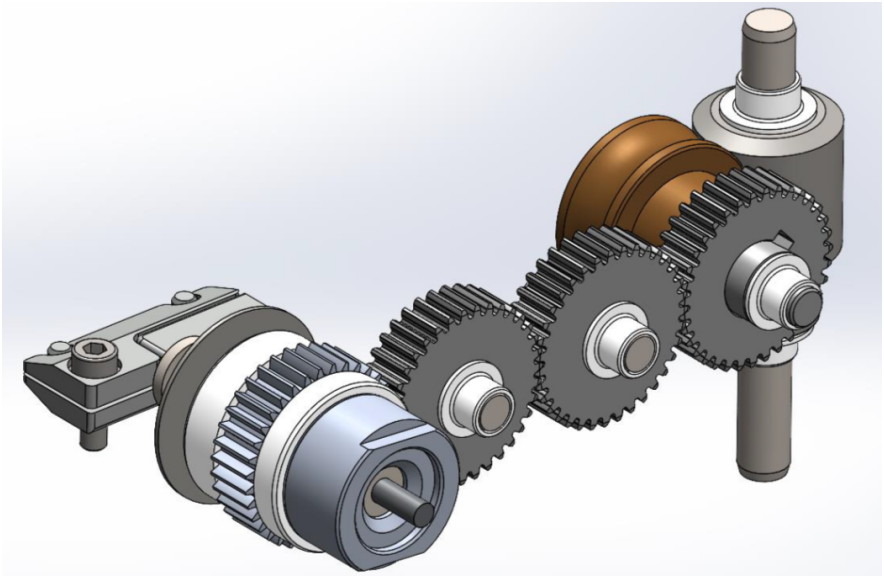

Figure 3.18: Model of the gear train for rotation of the clamping body. From [25].

3.2 Plate Fabrication

Bare foils of U-Mo undergo several preparation and processing steps. After quality control and documentation, the foils are cut, measured, drilled, and chemically cleaned before processing them into a U-Mo fuel plate by coating and cladding.

3.2.1 Cutting

In some cases, it is necessary to remove damages from bare U-Mo foils that could affect the processing and therefore the final quality of the plate. Especially edge dents and cracks that do not extend too far into the foil can be removed without much loss of material. This is done with a hand-operated workshop guillotine (type: *Dahle 580*) equipped with a blade suitable for metal sheets as depicted in Figure 3.19.

Some foils are bent in a way that the sides are not straight anymore, giving the foil a slight banana shape. These distortions may be due to inner stresses caused by the co-rolling, which are slowly released during storage. Hence, these foils are trimmed to get a rectangular shape again. In some cases, it is beneficial to cut and trim a deformed full-size foil in a way to produce two half-size foils as schematically shown in Figure 3.20. This reduces the amount of scraps and increases the number of foils for parameter tests (first coating batches were performed on half-size foils).

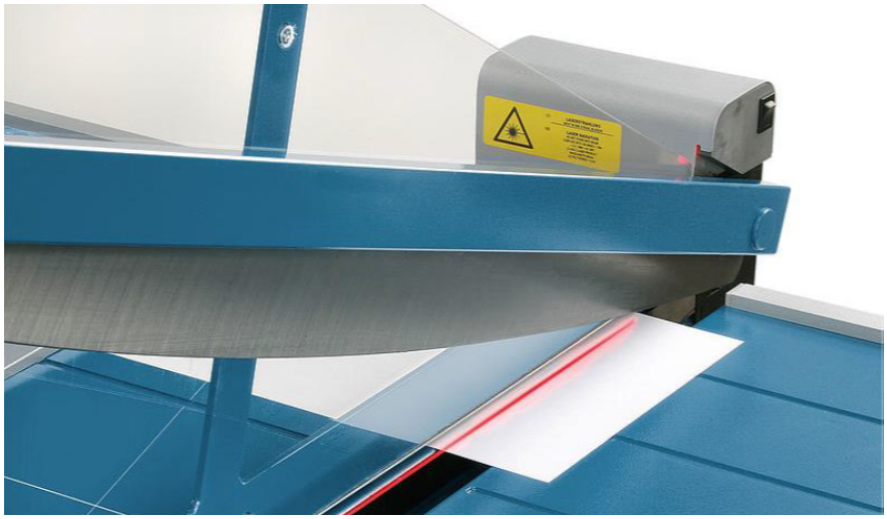

Figure 3.19: Cutting of a foil with the workshop guillotine. The red laser indicates the cutting line.

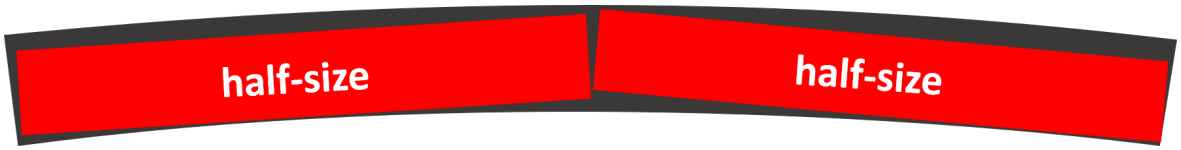

Figure 3.20: Cutting scheme of a deformed full-size foil (black) into two half-size foils (red).

3.2.2 Geometry Measurement

After the final cut, the dimensions of the foils are measured precisely. This is especially important for the later cladding process where the parameters are adjusted to every foil. Figure 3.21 displays the measuring scheme.

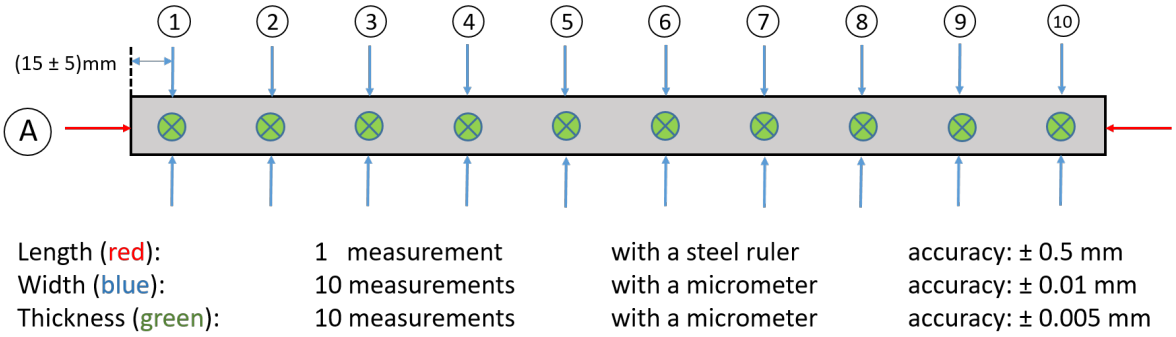

Figure 3.21: Geometry measurement scheme for a full-size foil with one length measurement and ten equidistant points of width and thickness measurement. The measurements are numbered starting from the side referenced with (A).

The length of every foil is measured with a steel ruler and then equidistant width and thickness measurements are performed with an appropriate micrometer. One side of the foil is chosen as a reference point to number the measurements. This reference point has to be tracked throughout all following process steps until the preparation for cladding. LEU foils that will be later used for in-pile irradiations have to undergo a similar procedure, but with a finer grid of measurement points. Especially regarding the foil's thickness distribution, which has to be precisely known for calculations of fuel swelling.

3.2.3 Drilling

Each substrate foil needs two drill holes on each end for mounting at the substrate holder. This is done with a portable electric drill. With a customized drilling jig, depicted in Figure 3.22, the foils can be aligned and fixed to consistently achieve a uniform result. The foil is put between the two pieces of the jig and then fixed with a screw clamp.

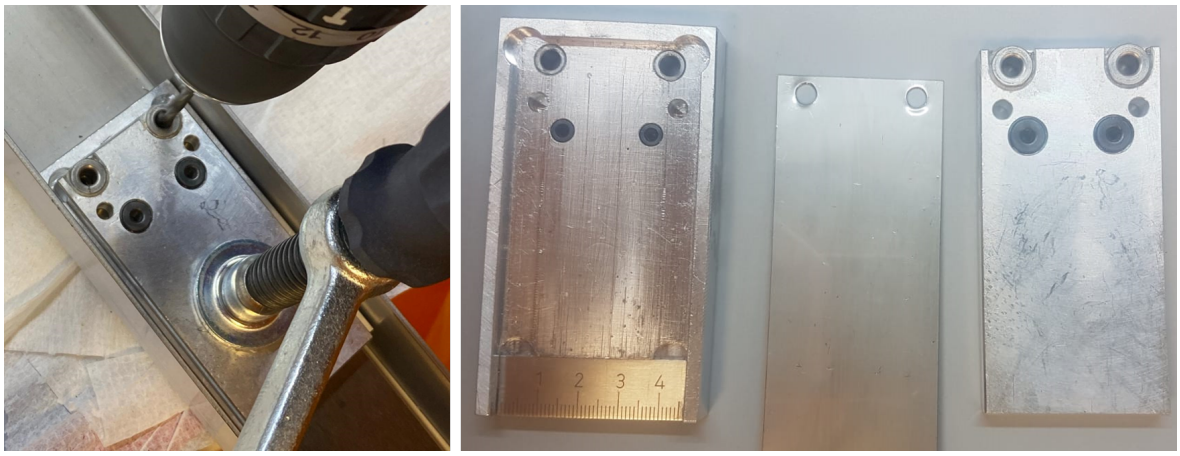

Figure 3.22: The process of drilling a stainless steel substrate foil (left) and the finished foil between the bottom and top piece of the drilling jig (right).

3.2.4 Chemical Cleaning

Uranium is a base metal that easily oxidizes in air. Correspondingly, U-Mo foils form an oxide layer after prolonged storage. This poses a problem for the sputter coating as the layer of brittle oxide causes delamination of the diffusion barrier. To avoid this, the oxide is removed chemically before the coating process. This can be done using HNO_3 (nitric acid) as a reagent, but it was shown that H_2O_2 (hydrogen peroxide) in an alkaline solution is a more selective cleaning agent. It does not attack the U-Mo as much as the acid, and therefore introduces fewer surface damages to the foil [9, 123]. The reaction is based on the further oxidation of the uranium oxides to form the uranyl cation UO_2^{2-}:

$$UO_2 + H_2O_2 \longrightarrow UO_2^{2+} + 2\,OH^-$$

In neutral and acidic media, further oxidation takes place to form uranyl peroxide UO_4 with a low solubility [29]. In an alkaline environment, however, the uranyl cations form soluble hydroxo and peroxo complexes instead [68, 150]:

$$UO_2^{2+} + 3\,O_2^{2-} \longrightarrow [UO_2(O_2)_3]^{4-}$$

The alkalinity for the used cleaning solution is achieved with *SurTec 138*, an industrial builder based on KOH (potassium hydroxide) with additives of phosphates and fatty acids for an effective removal of contaminants [133]. The final cleaning solution consists of 15 vol.% SurTec 138 and 10 vol.% H_2O_2 (with a concentration of 30 vol.%) in deionized water.

For mini-size foils, the cleaning was performed in a measuring cylinder inside the designated chemistry glovebox. A similar procedure was not feasible for the full-size geometry. However, it was observed that cleaning outside of the glovebox is sufficient if the foils are transferred into the argon atmosphere of the glovebox within 30 minutes. The oxidation in this short time frame is not severe enough to lower the coating adhesion on the U-Mo surface significantly. An additional advantage is that this makes the handling way easier and does not degrade the glovebox atmosphere by introducing several liters of liquid which partly evaporates.

Figure 3.23 shows the according setup that was built for chemical cleaning of full-size foils. It is composed of a custom-made stainless steel cage and a basin made of acrylic glass that holds about 3 liters. The foil to be cleaned is put into the cage which then can be immersed in the cleaning solution. A circulation pump keeps the liquid in motion to achieve a more efficient cleaning. An outlet with a manual valve is implemented for easy drainage of the radioactive liquid. This assembly is realized twice, one filled with the cleaning solution for the deoxidation step and one as a rinsing step with deionized water. As a final step, each foil is dried using pressurized argon.

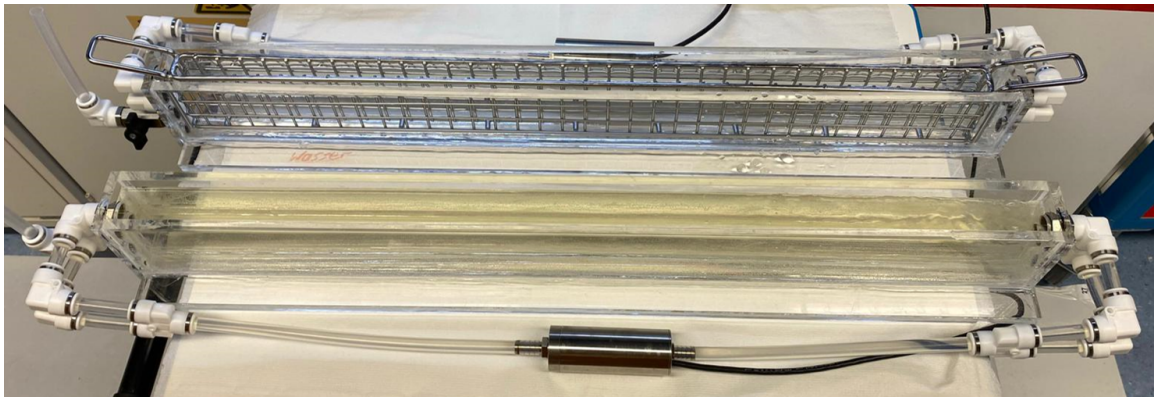

Figure 3.23: Cleaning containers for full-size foils with circulation pumps.

3.2.5 Coating

The general procedure of the coating process is independent of the used device. The substrates are placed or fixed on the substrate holder, then the chamber is closed and evacuated to a base pressure of about 10^{-7} mbar for the mini-size device and about 10^{-6} mbar for the full-size device. A plasma cleaning step with a negative substrate voltage of 800 V is

performed for 5 minutes at an argon pressure of about $5{\cdot}10^{-2}$ mbar to remove impurities for better coating adhesion. Subsequently, the target is sputter-cleaned for 2 minutes to remove impurities from the target's surface. Re-deposition of these impurities onto the substrate is prevented either with a shutter for the mini-size device (see Section 3.1.1) or by swiveling the magnet bar for the full-size device (see Section 3.1.2). After that, the substrates are coated at an argon pressure of about $5{\cdot}10^{-3}$ mbar with a sputtering power of either 300 W (mini-size device) or 5000 W (full-size device; see Figure 3.24). Auxiliary techniques like external heating and biasing voltage are applied individually for each sample. With the constant deposition rate known, the coating thickness is controlled by the process time. After cooling down for at least 30 minutes, the chamber can be vented and the coated samples unclamped.

Figure 3.24: Coating process of a foil in the full-size device.

The final cutting of the foils to remove the drilled and uncoated ends is either performed with the workshop guillotine at TUM or after shipping with the laser-cutting equipment at Framatome.

3.2.6 Packaging

While still in the argon atmosphere of the glovebox, each coated foil is packed into an oxygen-tight bag made out of aluminum barrier film [65], and sealed with a heat sealer. This bag is put into a slightly bigger bag of the same material together with an oxygen indicator pill and an oxygen absorber. This way, potential leaks in the outer bag can be detected and mitigated. After transferring the packed foils out of the glovebox, they are taped to a backing plate to prevent bending during shipping.

3.2.7 Cladding

Application of the AlFeNi cladding to the foils is performed at Framatome in Romans-sur-Isère, France. The used method, the so-called *C2TWP* process, is proprietary to Framatome, and therefore cannot be described here. However, a recently published patent gives some insight into this process [130]. Subsequently, the fuel plates are finished after a thinning of

the AlFeNi cladding to the final thickness. This is done either by machining or chemical etching. An example of a final plate is shown in Figure 3.25.

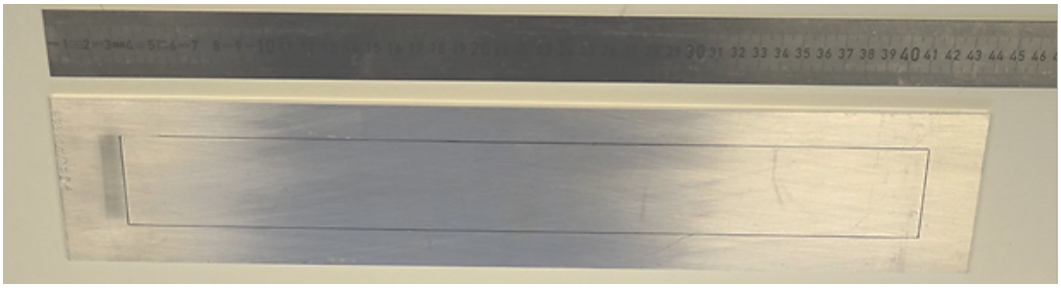

Figure 3.25: A fuel plate of half-size geometry. The approximate position of the U-Mo foil inside is marked in the surface.

3.3 Sample Preparation & Examination

The final plates are first non-destructively examined with ultrasound transmission scanning before destructive methods are used to prepare the fuel plates for metallographic examination with various microscopy techniques. This includes sectioning of the plates to create sample pieces from chosen positions, mounting of the sample pieces in epoxy resin and final preparation of the specimens by grinding and polishing.

3.3.1 UT Scanning

As a means of non-destructive examination, *ultrasound transmission* (UT) scans are performed on each plate. For this, an emitting transducer couples a high-frequency ultrasound signal into the material that is detected with a second transducer at the backside of the plate. The transmitted intensity is dependent on the local damping in different materials and reflection on interfaces. Scanning the whole area of the plate with the transducer couple creates a color-coded image of transmission intensity that makes defects of a certain size visible. Especially defects like debonding of interfaces and other voids that cause strong damping of the signal, like end gaps at the short edges of the foils, are sensitive to this method.

3.3.2 Cutting

Positions of interest are chosen from the plate to cut out sample pieces for further preparation and examination. Of importance here is the orientation of the chosen cross sections with respect to the foil's ends, which is explained in Figure 3.26.

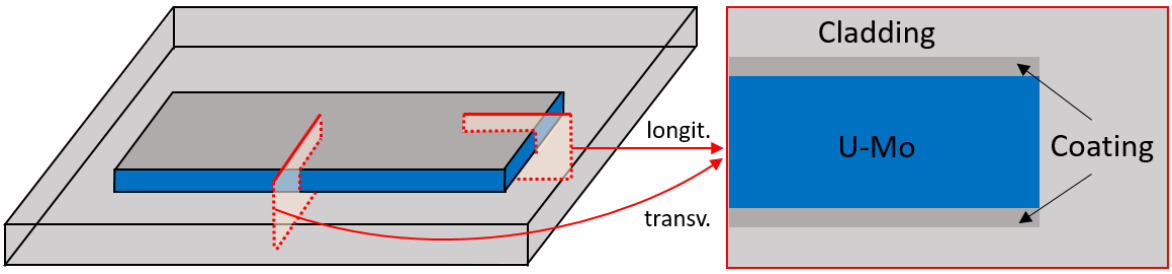

Figure 3.26: Scheme depicting the orientation of cross sections of a coated U-Mo foil with cladding. The red rectangles show the planes of a cross section, which are either longitudinally (cut through the short side of the foil) or transversally (cut through the long side) orientated. The resulting cross sections (right) look the same and therefore always need additional information about the displayed orientation.

At first, the cutting was performed with a precision sectioning saw (type: *IsoMet 1000* by Buehler) as depicted in Figure 3.27. Sufficient cooling and a slow feed rate ensure that introduced structural damages are minimized. Later, the sectioning was performed with the laser cutting equipment at Framatome, which is much more time-efficient.

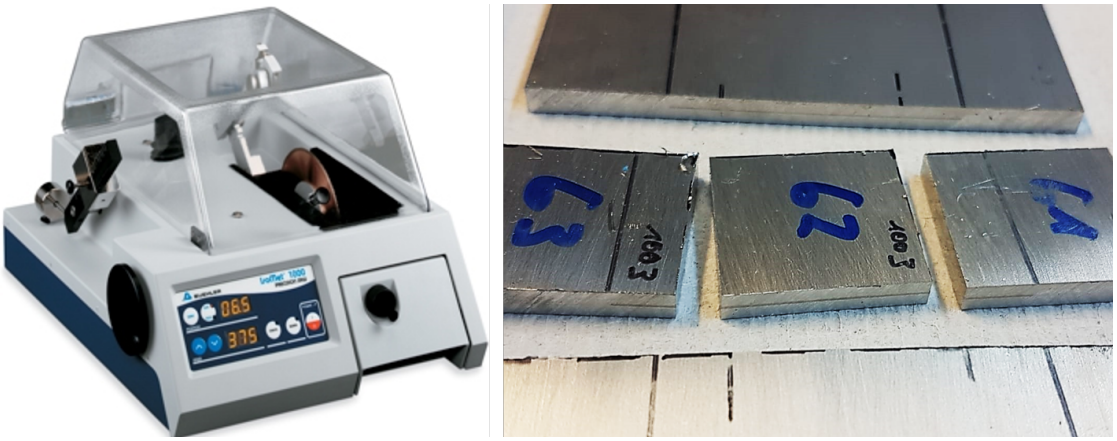

Figure 3.27: Precision sectioning saw used for plate cutting (left; from [11]) with an example of a sectioned plate showing the clean cutting edge that makes the foil in the inside visible.

3.3.3 Mounting

Sample pieces are then cold-mounted in epoxy resin. Usually, *EpoFix* by Struers is used, which is a low viscosity, slow curing transparent epoxy that does not shrink during the 12-hour curing time. This is important, as shrinkage can cause the epoxy to detach from the sample piece while curing. The resulting gaps are usually just a few micrometers wide but still pose a problem for the following polishing of the samples, when debris gathers in the gaps and is washed out in every polishing step, causing scratches.

The sample pieces are placed in polypropylene mounting cups of either 30 or 40 mm diameter with the to-be polished surface faced downwards. Special plastic clips or double-

sided tapes are used to keep the samples in position. To further minimize the risk of gap formation, most samples are mounted using a vacuum impregnation unit (*CitoVac* by Struers) as illustrated in Figure 3.28. The mounting cups with the samples are placed in the chamber and then filled with the epoxy under vacuum. This results in better adhesion of the epoxy, especially on porous surfaces. Furthermore, this destroys air bubbles, which can form during stirring of the epoxy and the hardener, and avoids the formation of new bubbles while pouring the epoxy into the mounting cups.

Figure 3.28: Mounting cups with sample pieces inside the vacuum impregnation unit ready to be filled with epoxy.

3.3.4 Grinding & Polishing

After the curing of the epoxy, the mounted samples can be removed from the cups and engraved with a sample identifier. Grinding and polishing is performed to reveal the true materialographic structure of the samples using semi-automatic grinding and polishing machines (type: *Saphir 520* by ATM and *Tegramin-25* by Struers). The first grinding step removes the most material, which is important to reach the bulk material that was not altered by the previous cutting step. After that, the abrasion rate is gradually reduced. Selecting the right recipe is crucial for a good surface finish without scratches. This involves the right choice of grinding discs, polishing cloths, lubricants, and suspensions, as well as process time, pressing force, and rotation speed of each step. Cross sections of coated fuel plates can be particularly demanding due to the sandwich of materials with strongly different properties: while U-Mo is comparatively hard, the Al of the cladding is soft and ductile, which can cause smearing. Including the coating as a third material with different properties (e.g. ductile zirconium compared to hard and brittle tungsten) makes the preparation even more sophisticated. Different wear rates of the material can cause edge rounding at the interfaces, which makes it impossible to focus a complete image in microscopy. Table 3.3 shows exemplary a recommended recipe for the preparation of a U-Mo fuel plate with Zr coating. However, this serves just as a guidance and may be altered during the preparation of a specific sample set.

Table 3.3: Grinding and polishing recipe for a U-Mo fuel plate with Zr coating. The values are valid for mounting cup diameters of 30 mm. Names of discs and suspensions relate to products of Struers.

Step	Disk	Lubricant / Suspension	Time [min]	Force [N]	Rotational Speed [rpm]
1	Piano-80	Water	"until flat"	25	300
2	Molto-220	Water	10 - 15	25	300
3	Largo	Largo-9	10	30	150
4	Largo	Largo-3	5	15	150
5	Dur	Dur-1	5	15	150
6	Chem	OP-U NonDry	2	7 – 13	150

Voids in the plate that are not filled with epoxy can cause problems with the polishing. Figure 3.29 shows a big stain on the cross section which was formed by liquid that was pressed into the void at the foil's end during polishing and leaked out afterward. This, however, alters the polishing quality only subjectively. A more severe issue is when abrasive material from previous polishing steps is released from a void and causes scratches. To minimize this risk, the specimens have to be rinsed thoroughly between every polishing step to flush the debris out of the gaps and voids.

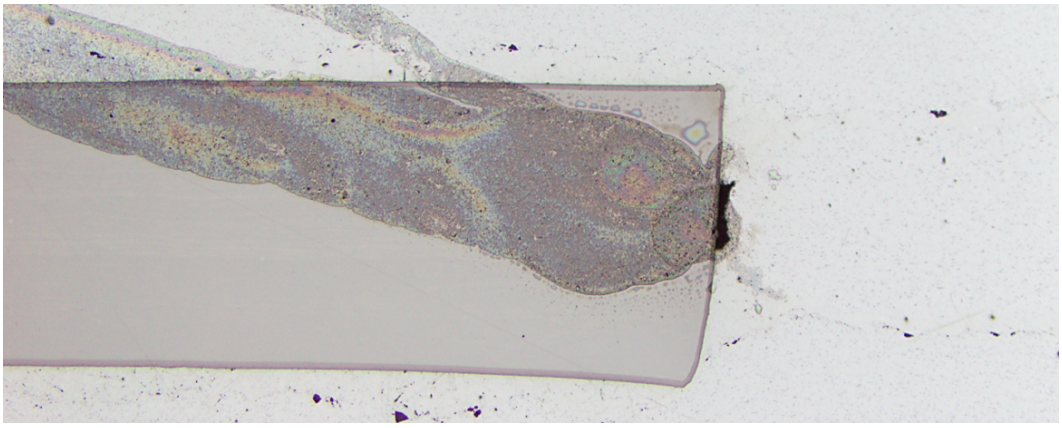

Figure 3.29: Cross section of a sample after polishing with a stain caused by debris that gathered in the gap.

Finished cross sections, as depicted in Figure 3.30, are ready for microscopy. They show a good finish across the whole surface without tarnished spots, stains, or scratches. The foils and the cladding can be already distinguished with the eye.

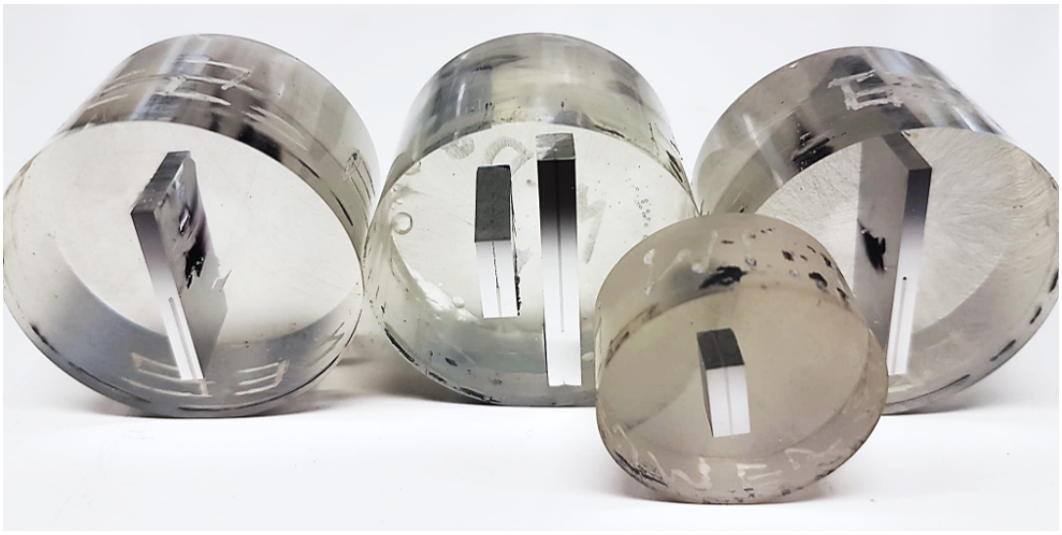

Figure 3.30: Selection of mounted plate sections after grinding and polishing.

3.3.5 Optical Microscopy

An optical microscope is the most fundamental tool to observe the nature of a sample. With an objective lens for a 100× magnification, resolutions of approximately one micrometer are usually reached. This can be done on prepared cross sections or to investigate surface structures like a bare U-Mo foil or the topography of a coating.

Different modes of illumination and light detection are used to highlight specific properties for a better contrast:
Bright-field reflection mode corresponds to human vision; the sample is illuminated by white light and contrast is caused by the attenuation of different areas. In dark-field mode, only the light that got scattered on the surface of the sample is gathered, which results in better contrast for textures like scratches or pores. Using polarized light as illumination together with a polarization filter can be used to reveal the microstructure of the sample; e.g. differently orientated grains of the same material phase may result in different contrasts by polarized light. Figure 3.31 illustrated the mentioned examples.

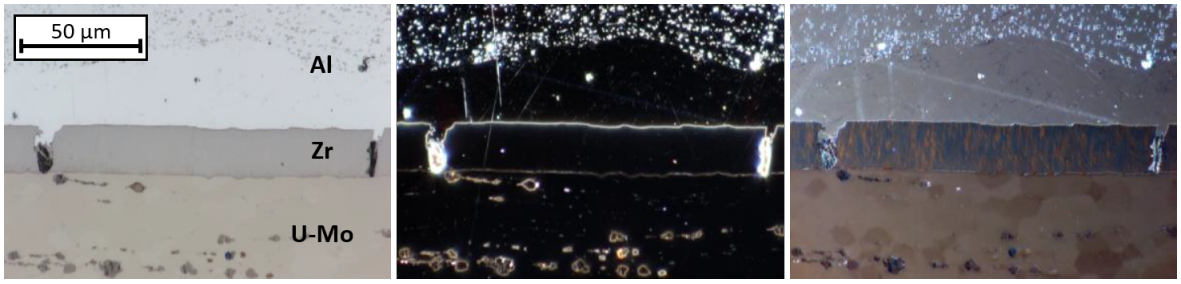

Figure 3.31: Exemplary cross section of a Zr-coated U-Mo foil with Al cladding. The same sample area is shown in bright-field mode (left), dark-field mode (middle), and in polarized light. Based on [23].

3.3.6 Electron Microscopy

At a few hundred nanometers, the resolution limit of an optical microscope is reached. This limit is surpassed by using electrons with a significantly shorter wavelength than visible light as a source of illumination. An electron gun produces, accelerates, and focuses the electrons. Coils deflect the electron beam in the x and y direction to scan a chosen area of the sample surface, giving the method its name *scanning electron microscopy* (SEM). The manifold elastic and inelastic interactions of the electron beam with the specimen generate a variation of detectable signals that provide comprehensive information regarding topography and composition. The signal is processed as a local intensity, represented as grayscale brightness in the scanned image. When interpreting this measured intensity, one has to consider that each type of signal is not from an arbitrarily small spot but from a certain *interaction volume* in which this corresponding signal was generated. The size of this interaction volume is dependent on the energy of the electron beam and the local material density and composition.

Backscattered Electrons

When the electrons from the beam enter a material, they are scattered and deposit their energy. Hereby, some of these electrons reverse their initial direction, reach the surface again and escape the sample. These *backscattered electrons* (BSE), which usually still have more than 50 % of their initial energy, are then detected by a designated BSE detector. Figure 3.32 compares the simulations of electron trajectories in materials with a low and high atomic number Z to illustrate the measurement principle.

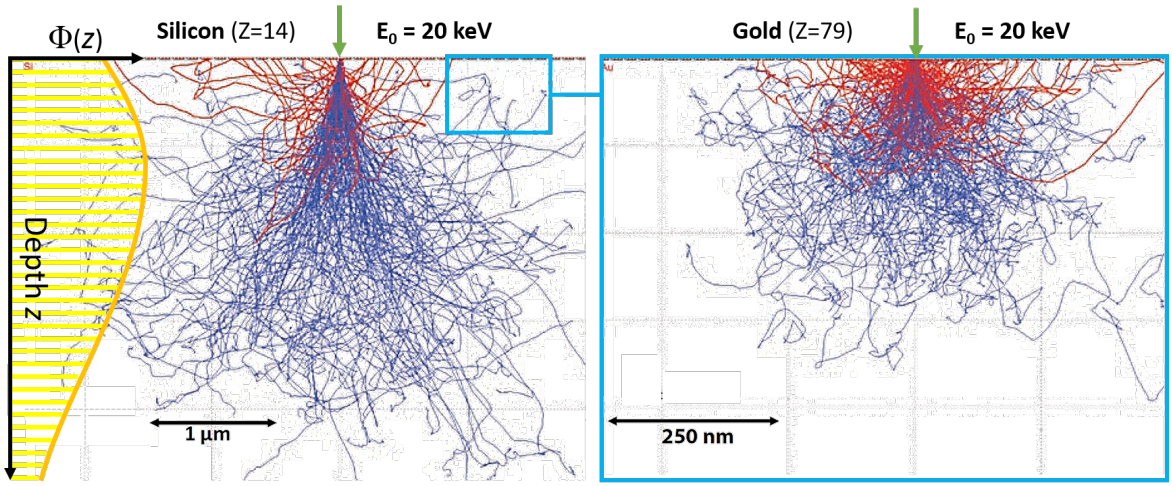

Figure 3.32: Monte Carlo simulation of electron trajectories in silicon (left) and gold (right) for an 20 keV incident beam perpendicular to the surface. The interaction volume is smaller for high-Z materials and the ratio of backscattered electrons (red) is larger. The yellow plot shows the distribution function $\Phi(z)$ in depth of X-rays generated in silicon. Based on [32].

Low-Z materials scatter the electrons much less, which means that they can penetrate much deeper into the sample. Materials with a higher electron density, on the other hand, already scatter the beam electrons strongly near the surface and therefore increase the probability of electrons being ejected from the surface again. The resulting change in signal intensity is a powerful tool to investigate the compositional microstructure of a sample by the atomic number contrast. However, one has to keep in mind that the penetration depth (typically in the order of 100 nm to a few μm) is different for different materials, and thus the information gained from a certain "spot" always corresponds to an interaction volume of different size depending on local composition. The backscattered electrons furthermore carry topographical and crystallographic information of a specimen as their intensity also partly depends on the incident angle and crystal orientation.

Secondary Electrons

The detection of secondary electrons (SE) is an ideal tool for the investigation of fine surface structures. They are produced by inelastic collisions of the beam with electrons of the conduction or valence band of the sample material, which are then ejected. This occurs along the whole path of a beam electron (see trajectories in Figure 3.32) until it is absorbed. However, the energy transfer to the secondary electrons is so low that their propagation in matter is strongly limited. As a result, only surface-near secondary electrons have sufficient kinetic energy left to exceed the surface energy and escape to the detector with a few eV remaining. The typical escape depth of a secondary electron is in the order of a few nanometers, which means that the gained intensity image of a scan shows only information from a very thin slice below the surface of a sample. This means that, unlike the backscattered electron image, the major part of the brightness variation is due to the surface texture. This is illustrated in Figure 3.33. The incoming beam of electrons has a certain penetration depth into the material, but the closed point on the surface for generated secondary electrons to escape is less depending on the local inclination of the surface. As a result, more electrons escape on average at steep faces and consequently producing the topographical contrast to reveal the shapes of objects on the surface.

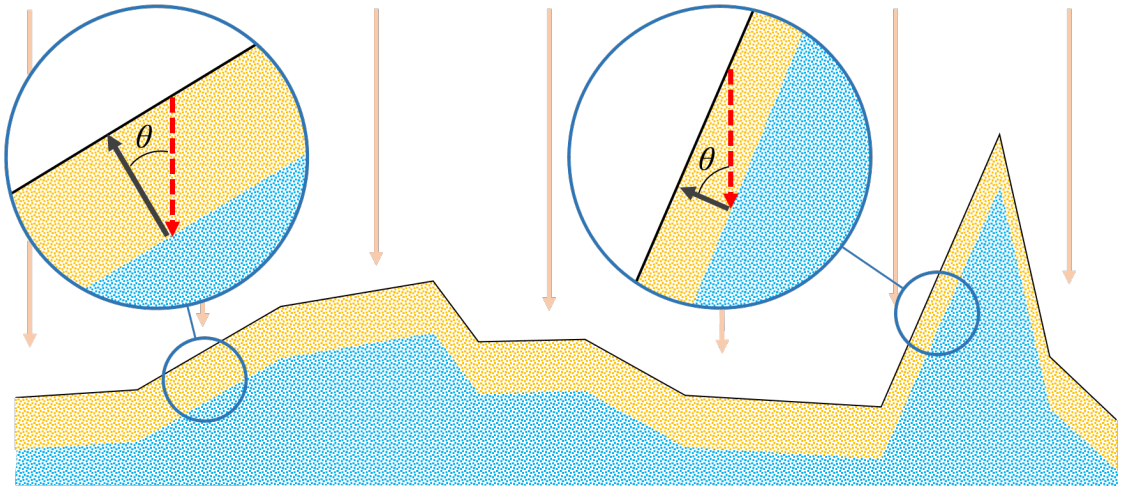

Figure 3.33: Geometric argument explaining the different secondary electron signal depending on the topography. The electron beam scanning the surface (orange arrows) has a certain penetration depth (red arrow) in which secondary electrons are produced. At higher surface inclination θ, the electrons are closer to the surface and have a higher probability to escape.

Energy-dispersive X-ray Spectroscopy

X-rays are produced when high-energetic electrons from the beam scatter inelastically on an inner shell electron to ionize the corresponding atom. The resulting cascade of electrons from higher shells filling the lower shells' vacancies releases X-rays with energies in the order of a few keV. As the shell structure is unique for each element with discrete energy levels of each shell, the emitted photons – called the *characteristic* X-rays of an element – generate a spectrum of discreete peaks. With a database of characteristic X-ray energies, the method of *energy-dispersive X-ray spectroscopy* (EDS) is capable of identifying the elements present in the sample. Quantitative analysis of elemental composition can be performed with an appropriate software. However, the successful deconvolution of a spectrum is more difficult for materials with many components and a complex structure. Therefore, it has to be expected that the accuracy of quantitative measurements can be inadequate if such materials are not calibrated on a similar reference sample. Again, one gets a certain depth information with the measured signal. Like the secondary electrons, X-rays are produced in the whole interaction volume, but unlike them, they are far more likely to escape. Hence, the detected X-rays carry information from a depth of several µm. An exemplary X-ray signal distribution regarding depth is included in Figure 3.32.

The scanning electron beam makes it possible to record a spectrum and calculate the respective element composition not only at a single point but also along a path or for a defined area. Line scans for example (see Figure 3.34) are useful to measure diffusion profiles along a line perpendicular to the diffusion couple interface. By scanning the whole image, an EDS map (see Figure 3.35) can be created visualizing the local distribution of selected elements to identify different phase regions like precipitations.

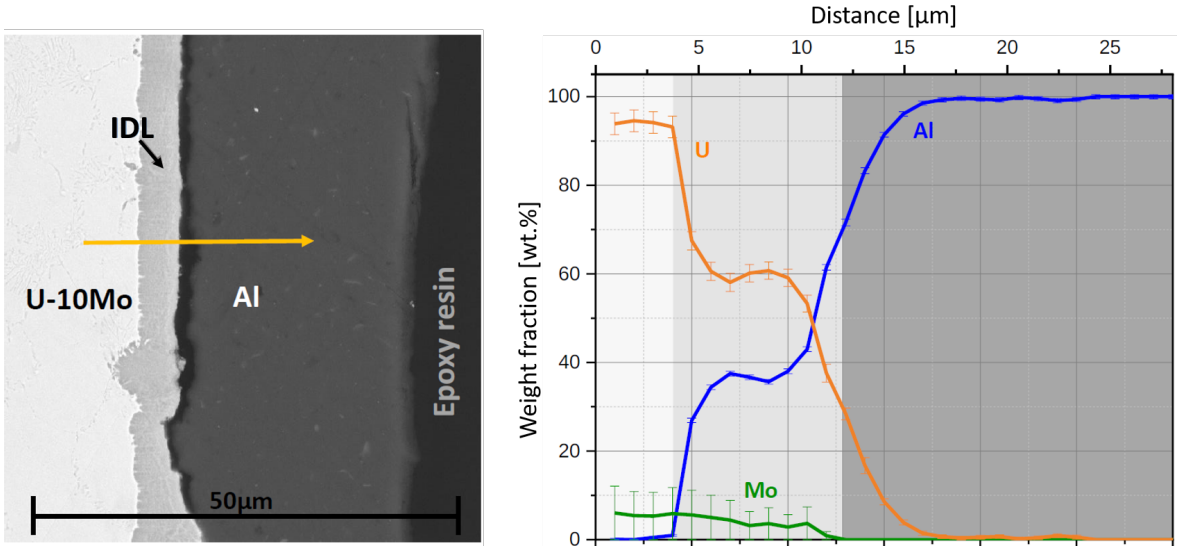

Figure 3.34: Exemplary line scan showing the elemental composition along a line (yellow arrow) of a U-Mo/Al diffusion couple with an interdiffusion layer (IDL). Based on [88].

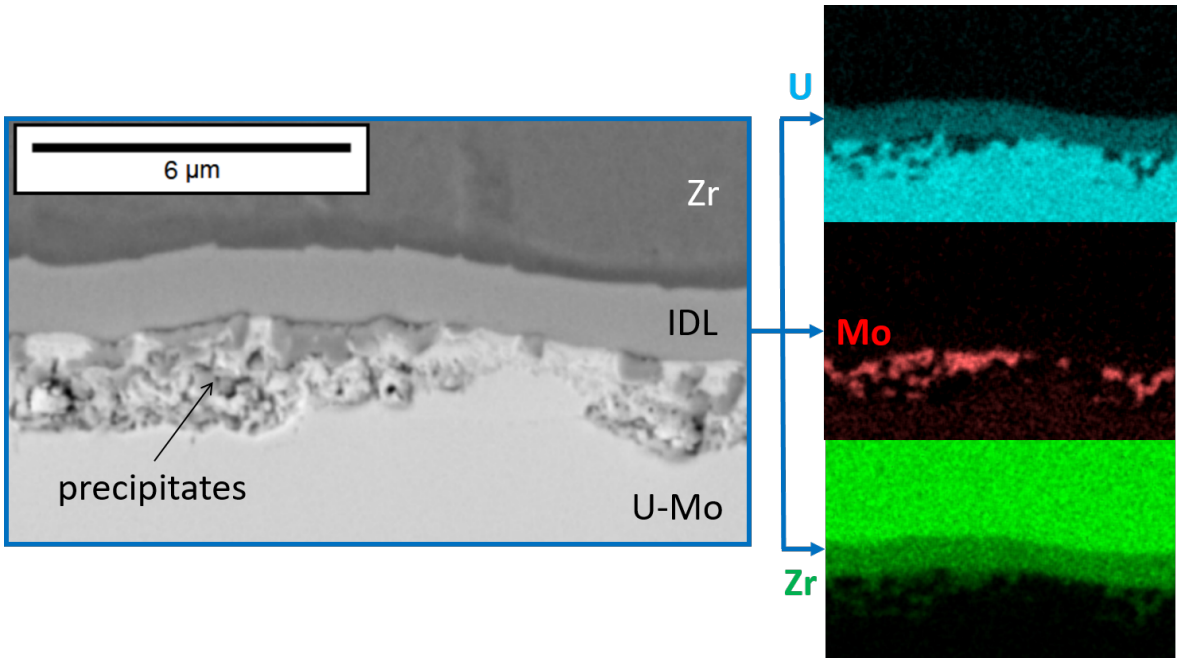

Figure 3.35: Exemplary BSE image of a U-Mo/Zr interface with significant diffusion (left). Corresponding EDS maps of the same image section illustrates the distribution of the elements U (blue), Mo (red), and Zr (green) showing their contents in the IDL and in the precipitates. Based on [23].

Chapter 4

Results

The experiments performed in the course of this thesis and the knowledge extracted from those are presented in this chapter. This includes investigations on coatings of the alternative diffusion barrier materials molybdenum and tungsten regarding layer properties and diffusion behavior when produced by PVD. The central part focuses on the work on monolithic fuel development with Zr diffusion barriers between the mini-size EMPIrE irradiation experiment and the planned full-size irradiation FUTURE-MONO-1. Destructive examinations of EMPIrE plates as well as unirradiated test plates set the foundation for further improvements that are integrated into the process of upscaling to full-size production. Several rounds of full-size plate production and subsequent characterizations are described to develop suitable plates for FUTURE-MONO-1 and a robust manufacturing process for future industrialization.

4.1 Alternative Diffusion Barriers

The strong focus on Zr as a diffusion barrier so far is rooted in its compliance with the co-rolling and hot isostatic pressing (HIP) as parts of the common fabrication process for monolithic fuel plates. However, since other materials such as Mo and W are possibly more effective at preventing diffusion between U-Mo and Al, these are examined more closely. Especially with the PVD method, a more variable technique for producing the corresponding layers is now available that features more opportunities to fine-tune the layer properties.

4.1.1 Molybdenum

Diffusion couple experiments on U-Mo/Mo interfaces using annealing [41] and heavy-ion irradiation [14] have been conducted and found a favorable behavior for Mo compared to Zr. Furthermore, Mo comes with the additional advantage that it is already present in the U-Mo, i.e. no further element is introduced, and therefore complex ternary interactions are avoided. The following studies focus on the production of Mo coatings by PVD and the resulting behavior in combination with the C2TWP process.

PVD Coating

Before a molybdenum diffusion barrier coating is tested in combination with the cladding process, the properties of the coating itself in dependence on various production parameters were investigated. For this, the mini-size PVD device (see Chapter 3.1.1) was used as it provides the necessary versatility and large parameter space for a fundamental overview. It was equipped with a molybdenum target of 99.9 % purity. Table 4.1 lists the amount of impurities in the target material. As a first step, stainless steel substrates were used to investigate the influence of techniques like plasma cleaning, substrate heating, and substrate biasing. This minimizes the use of expensive U-Mo foils and reduces radioactive waste.

Table 4.1: Impurity content of the Mo sputtering target.

Element	Fe	C	O	N	W	H	Cr	Si	Pb	Ti	Al	Ca	Cu	Mg	K
Content [ppm]	50	40	30	10	10	5	< 50	< 50	< 30	< 30	< 20	< 20	< 20	< 20	< 2

Bending tests were performed to check the integrity of the coating under mechanical deformation in foresight of the C2TWP cladding application process. This was done by bending the sample pieces to a 90° angle around an edge with a radius of about 3 mm. For preparation of cross sections, straight and bent sample pieces were mounted in epoxy resin and ultimately polished with colloidal silica (particle size: 0.04 - 0.25 µm). Figure 4.1 shows coatings produced with different biasing voltages that experienced tensile stresses from the bending. The structure exhibits the usual fine columnar grains with no significant differences noticeable between the biasing voltages. All coatings showed cracking independent of the

applied biasing voltage. However, at higher biasing voltages the trend goes to more but finer cracks, which indicates a stronger brittleness caused by the introduced damages of high-energetic particle bombardment. This corresponds with the behavior that has been already observed at Zr coatings [124]. The adhesion of the coating to the stainless steel substrate was satisfactory with no noticeable failures.

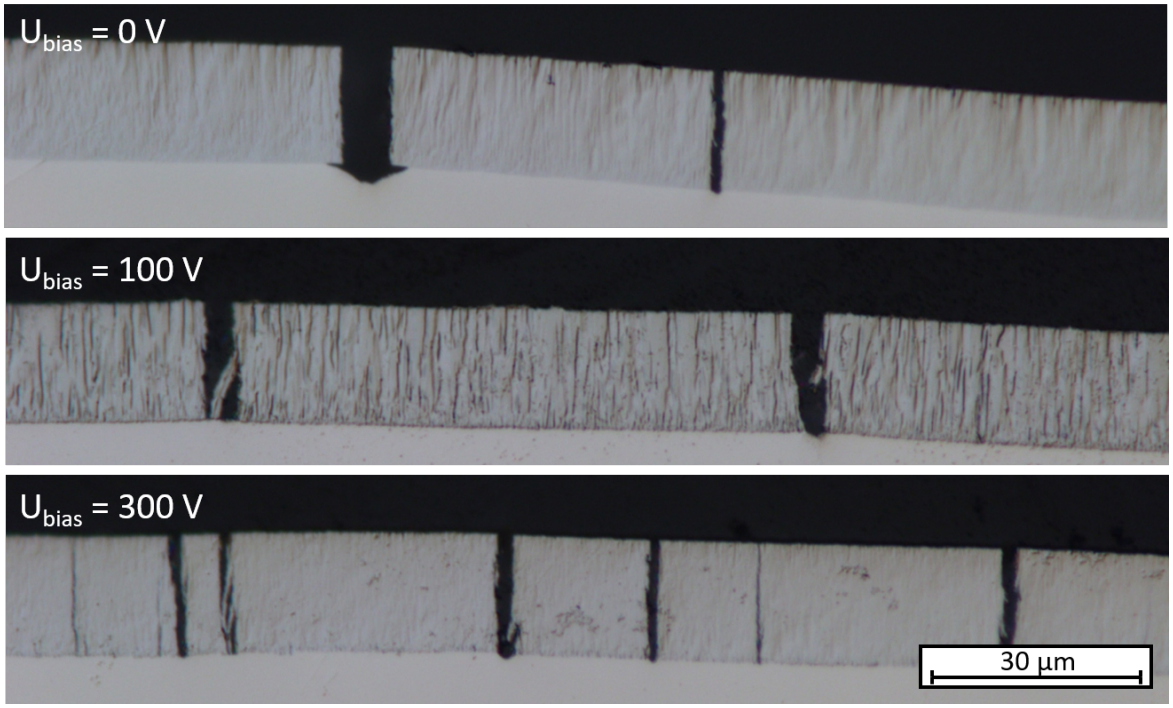

Figure 4.1: Optical microscopy images in polarized light of Mo coatings produced with different biasing voltages showing the evolution of the grain structure. Grain contrast is depending on effective polishing, which was better for the 100 V sample.

Substrate heating of 400 °C, 650 °C, 800 °C, and 950 °C was tested as a coating parameter. Cross sections of the resulting layers after bending tests are depicted in Figure 4.2. The coating produced at 400 °C shows the common structure of fine columnar grains. When comparing this to "unheated" samples, it has to be noted at this point that the coating process itself also contributes to the heating of the substrate. The average substrate temperature during a coating process without external heating was measured to be at about 350 °C, which means that the 400 °C coating is only slightly different from the sample of 0 V biasing. Hence, it is not surprising that their grain structures are indistinguishable. An increase of temperature to 650 °C already increases the grain sizes significantly. The same goes for further increases to 800 °C and 950 °C. However, starting at 800 °C this comes with the formation of a thin IDL of a maximum of 1 µm at the stainless steel interface. At 950 °C, this IDL already grew to a thickness of about 8 µm. All coatings independent of the production temperature displayed cracking when bent. The IDL that formed between Mo and the stainless steel substrate exhibited an increased brittleness with significantly more cracks than the Mo layer on top. Concave bending of the foil – synonymous with compressive stress – resulted in severe fragmentation of the IDL and complete debonding of the coating.

Apart from this, the other samples showed a good overall adhesion of the coating to the stainless steel substrate with no noticeable failures.

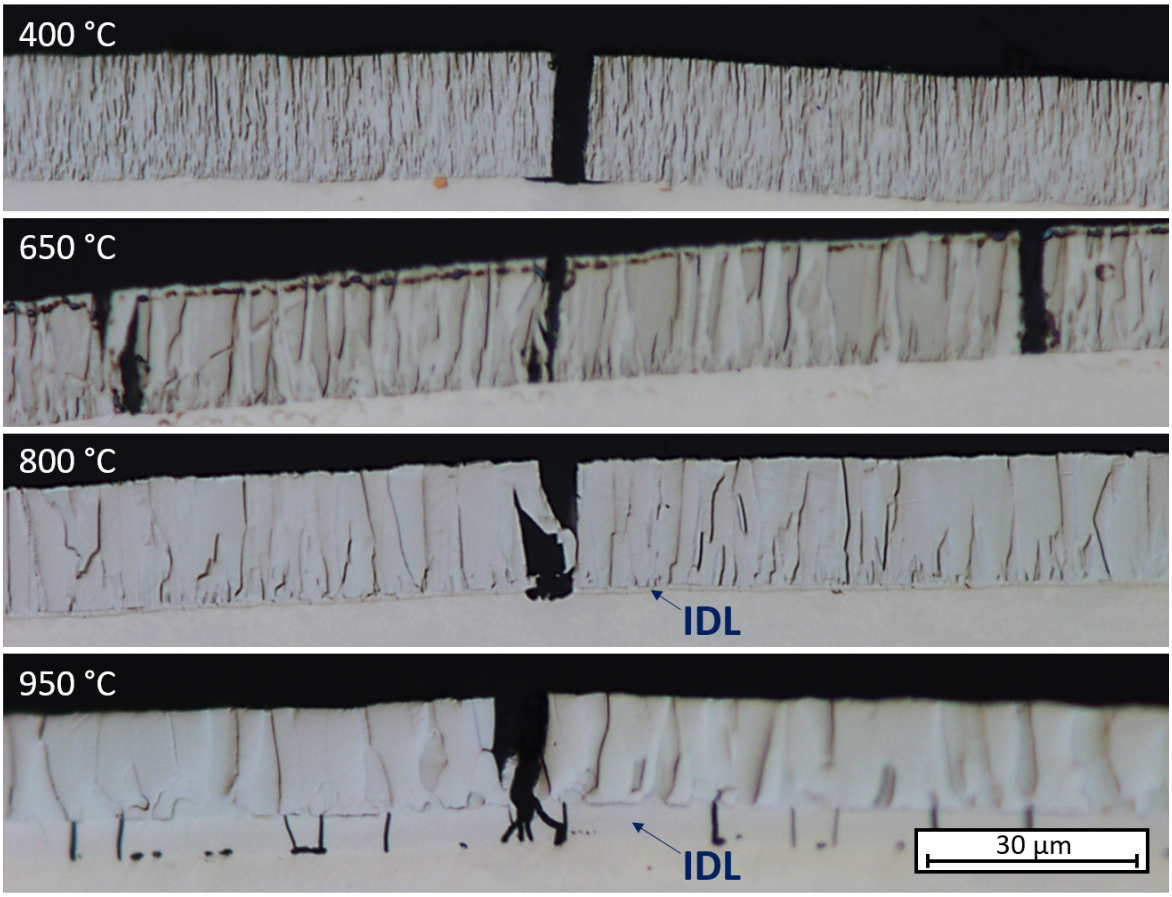

Figure 4.2: Optical microscopy images in polarized light of Mo coatings produced at different substrate temperatures showing the evolution of the grain structure.

Cladding Application

Based on the results described above, a set of six Mo-coated stainless steel substrates of mini-size geometry with about 10 µm of coating thickness were produced to investigate their behavior in combination with the C2TWP cladding process. As no significant advantage of any coating parameter regarding avoidance of cracking had been observed to this point, the parameter of 650 °C heating was chosen as it features the biggest grains without signs of interdiffusion. Plates were fabricated out of four of the six coated foils. The subsequent UT scan as depicted in Figure 4.3 indicated a complete failure of either the adhesion of coating on the substrate, the bonding of the cladding, or a combination of both. Preparation of cross sections at TUM showed a complete debonding of cladding and coating on both sides of the foil. Closer investigations revealed that the gaps are partly filled with dark powdery material of potentially oxidized molybdenum. To test this assumption, heat treatment in air was performed on a Mo coupon and showed a dark discoloration from the formation of an

oxide layer. Something similar seems to happen with the application of the cladding as the C2TWP process is not conducted in inert gas atmosphere. Thus, it is to be assumed that the brittle oxide layer forms during the cladding process and causes the debonding.

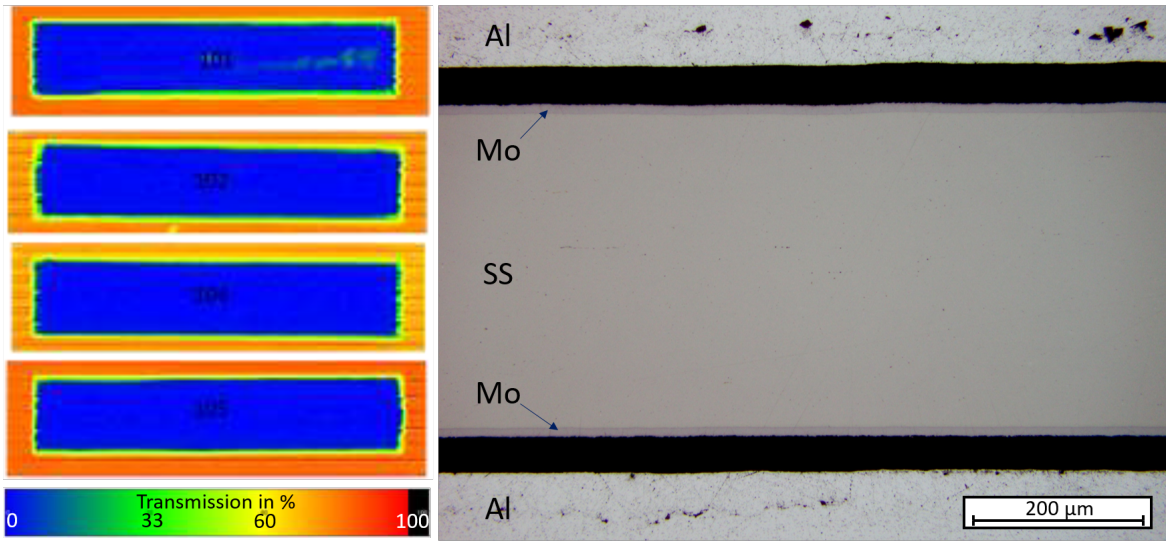

Figure 4.3: Failed set of mini-size plates with Mo coating. The UT scans (left) indicate a defect that covers the whole foils. Optical microscopy (right) identifies this as a complete debonding between Mo coating and Al cladding.

To avoid this, the coating procedure was enhanced by applying a protective layer of Al onto the Mo coating with the PVD device. Accordingly, a new set of three Mo-coated foils was produced with the same parameters as before. The target was then changed to Al and 15 µm of protective coating was applied on each side of the foil. As the adhesion of Al on the Mo coating was unknown at that point, it was decided to evaporate potential impurities off the Mo surface by preheating the foil to 600 °C in the vacuum chamber for 1 hour before the coating of each side of the foil. The three foils produced that way were again sent to Framatome for plate fabrication. Cladding was then applied with the same parameters as before. One of the unprocessed foils from the first sample set without protective coating was included in this run as a reference sample to rule out that some unknown process error created the failure in the previous production cycle.

The UT scans of the resulting plates, as seen in Figure 4.4, already confirm the success of the protective coating. No indication of debonding is seen in the scans of the three new samples, while the reference sample with the previous production scheme showed the same defective behavior as before. This is confirmed in the destructive examinations. Sufficient adhesion at the interfaces of all respective layers – stainless steel substrate, Mo coating, Al protective coating, and Al cladding – was observed. However, severe interdiffusion was detected between the Mo coating and the protective Al layer as illustrated in Figure 4.5. A remarkable feature is that the IDL differs significantly when comparing the two sides of the foil. On one side, the IDL is significantly thicker and displays many cracks, while the remaining Mo coating itself shows no cracks. This inequality between both sides is a strong

indication that the major cause of the thermal diffusion, in this case, is the coating process and not the C2TWP cladding process. Especially the preheating to 600 °C of the second side, when the protective Al layer was already applied to the first side, is expected to drive the thermal diffusion. So the second side experiences less total heat intake, which explains the thinner IDL. The cladding process, on the other hand, is unlikely to be responsible for the observed discrepancy as it treats both sides of the foil the same.

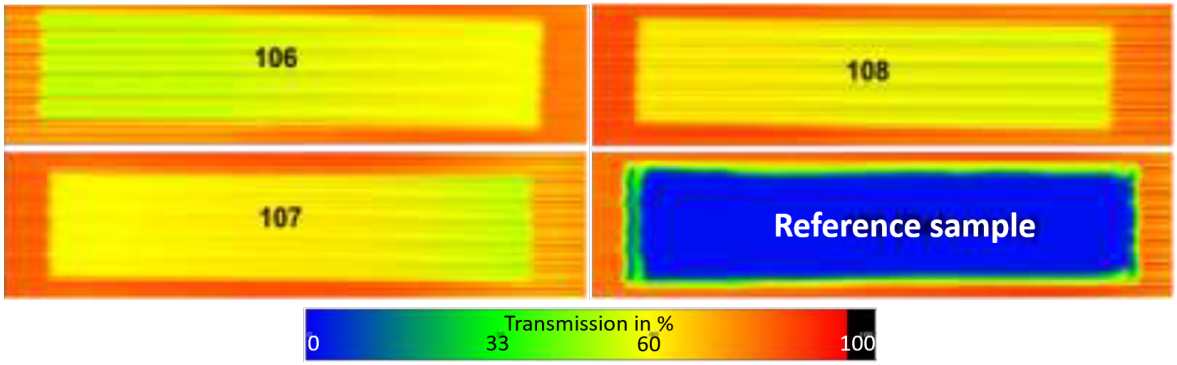

Figure 4.4: UT scans of mini-size plates with Mo coating. The reference sample failed, while the samples with protective Al coating exhibit no debonding defects.

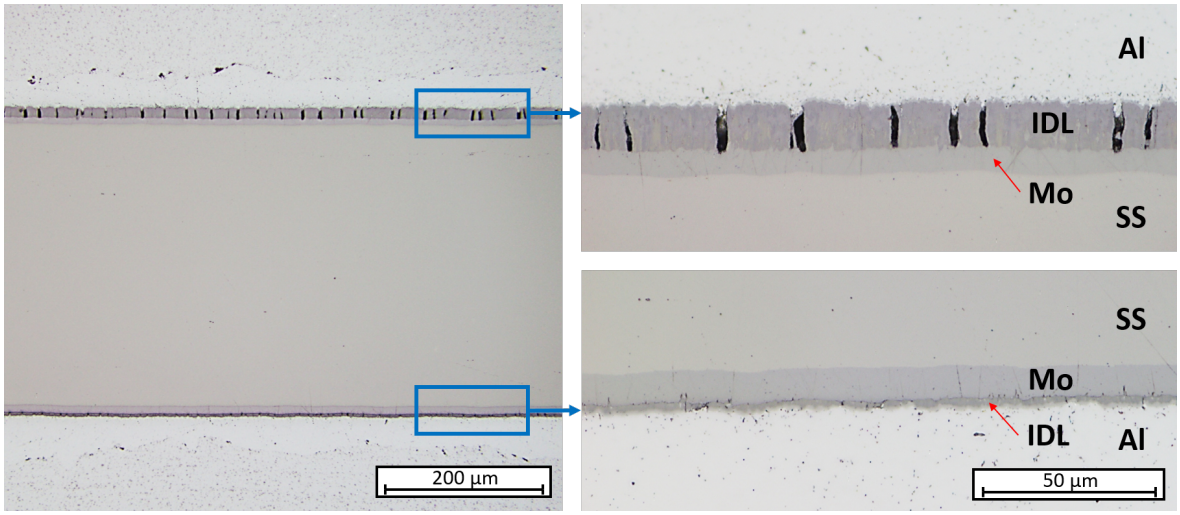

Figure 4.5: Optical micrographs of Mo-coated mini-size plates with protective Al coating showing different degrees of interdiffusion between Mo and Al on the two sides of the foil.

A closer look with the SEM reveals a more detailed view on the diffusion behavior. The foil side with the protective Al coating applied secondly exhibits an IDL of about 3 µm thickness on average. However, there are regions where the diffusion progressed at different rates as depicted in Figure 4.6. Here, intermixing phases are present as "hills" that grew to different sizes. Many of these spots display what appears to be a crack into the Mo layer, which seems to be connected with the occurring diffusion. However, the direction of causation is unknown. The cracks may be the cause for the onset of increased diffusion at this point or

created later during the cladding application at spots where mechanical properties changed due to the formation of binary phases.

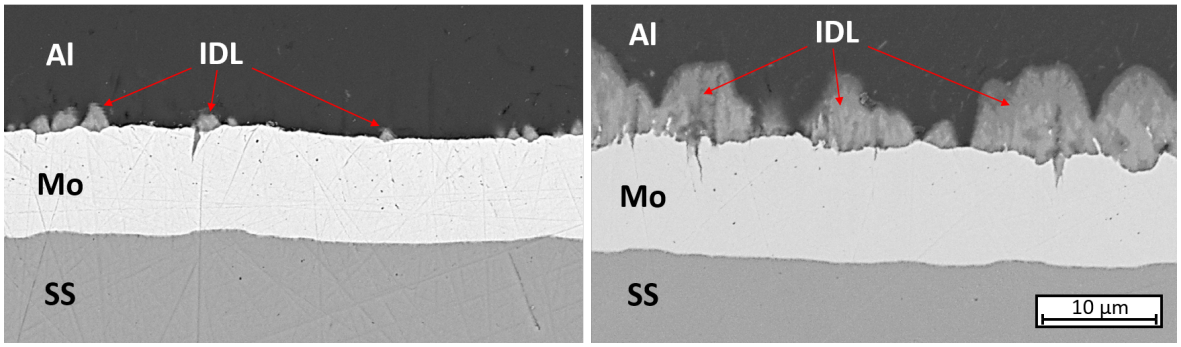

Figure 4.6: SEM BSE micrographs of Mo coating on the foil side with less heat intake. The IDL is more or less pronounced at different locations.

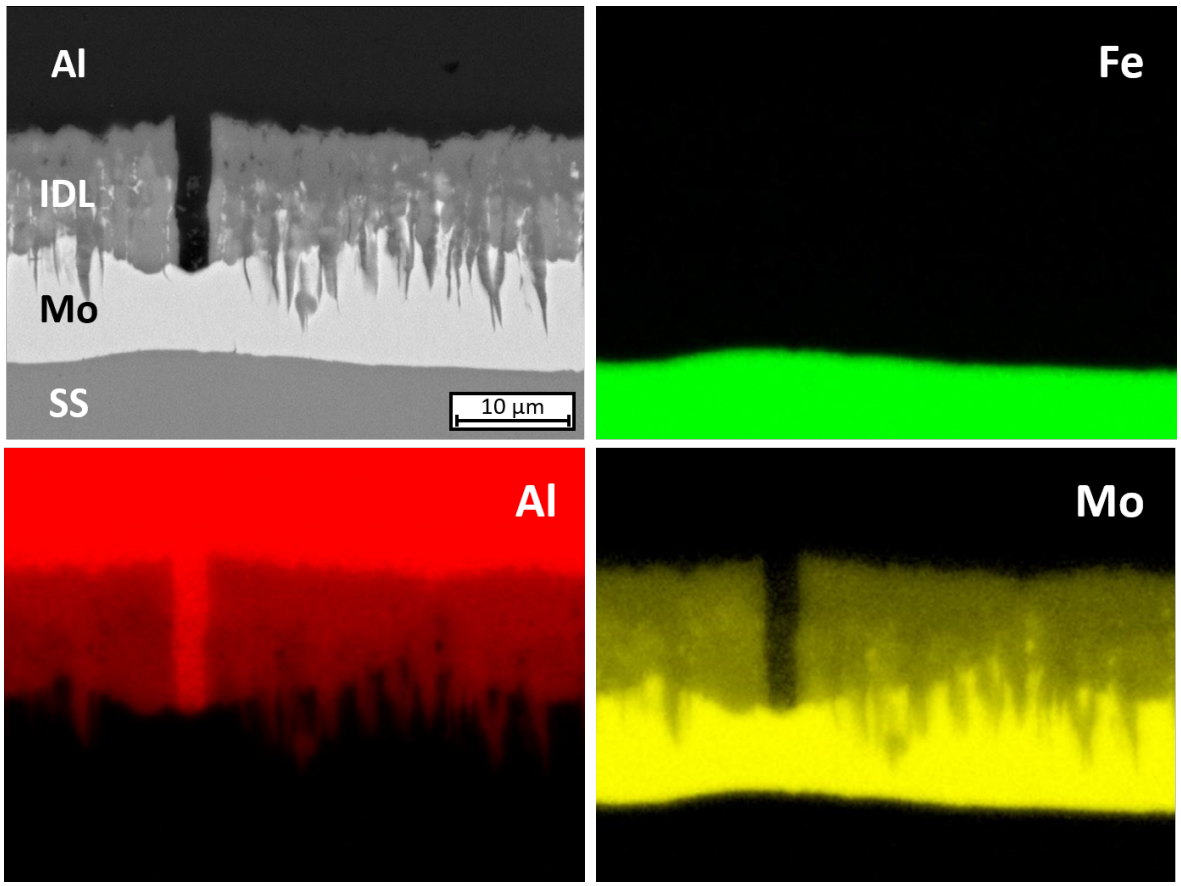

Figure 4.7: EDS maps of the SS/Mo/Al layer system with interdiffusion zone between Mo and Al. Fe as main element of stainless steel is colored in green, Al in red, and Mo in yellow.

The foil's side that has experienced the higher heat load exhibited an IDL of about 12 µm thickness, while the remaining Mo coating is still about 8 µm thick. Figure 4.7 shows a BSE image of a representative area together with EDS maps of Fe (as the main component of stainless steel), Al, and Mo to illustrate the degree of intermixing. The sharp transition at the interface of substrate and cladding confirms the observation from the preliminary PVD tests and shows that the cladding process also did not cause interdiffusion at this point.

In contrast, the Mo coating and the Al cladding are separated by an interaction zone that does not show a uniform structure. One remarkable formation are filaments rooting into the Mo coating. This may be a result of increased diffusion along the boundaries of the columnar grains in the coating, which would explain their shape. Comparison with the grain sizes of the preliminary coating tests at 650 °C (see Figure 4.2) is in good agreement with this assumption.

The IDL itself exhibits several zones distinguished by the BSE contrast; two layers of about the same thickness pervaded by bright stripes that are correlated with high Mo content. Diffusion theory does not explain this non-planar growth of intermediate phases in a binary system (see Chapter 2.2.3). However, there are exceptions where a binary intermetallic phase shows strong anisotropic diffusion that results in three-dimensional growth. A study on Al-Mo diffusion couples in the same temperature range by Mehta [74] observed a similar behavior including the Mo strings (see Figure 4.8). Here, the structure was explained with the anisotropic diffusion of the phase closer to the Mo side identified as Al_8Mo_3, while the darker phase close to the Al was identified as $Al_{22}Mo_5$.

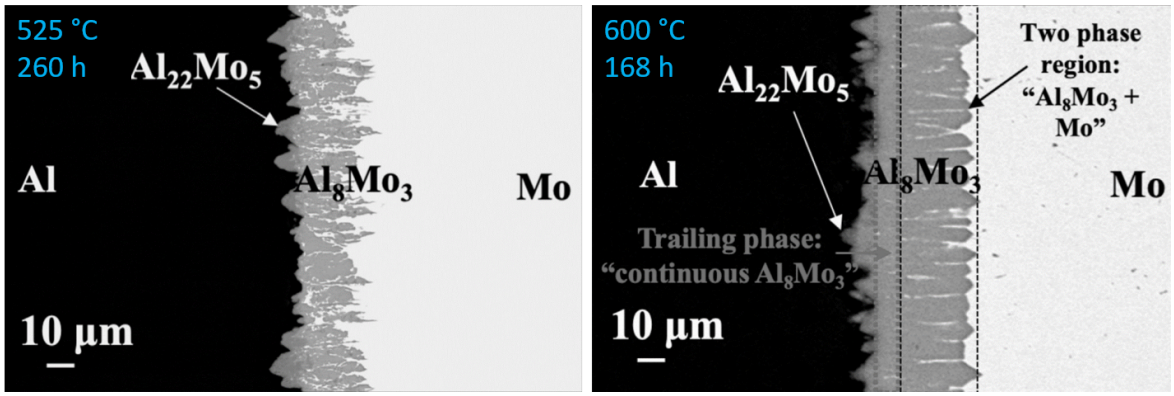

Figure 4.8: SEM BSE micrographs of Al/Mo diffusion couples isothermally annealed at 525 °C for 240 h (left), and at 600 °C for 168 h (right). Source: [74].

A more detailed investigation of the diffusion zone was carried out as shown in Figure 4.9. The EDS map confirms the Mo strings and the two zones of about equal thickness with different Al content. A performed EDS line scan shows that these two zones exhibit a constant ratio of Al and Mo. The zone closer to the Mo coating is in good agreement with the ratio of Al_8Mo_3, while the other one has a slightly higher Mo content as expected for $Al_{22}Mo_5$ (however still within the 5 % uncertainty given for the line scan results). A high-resolution image of the interface of Al and IDL revealed another layer of about 1 µm

thickness, which is too thin to be resolved in the line scan. This layer more likely resembles the $Al_{22}Mo_5$ phase as suggested by Mehta. Then, the remaining phase may be $Al_{17}Mo_4$ as described by Eumann [22].

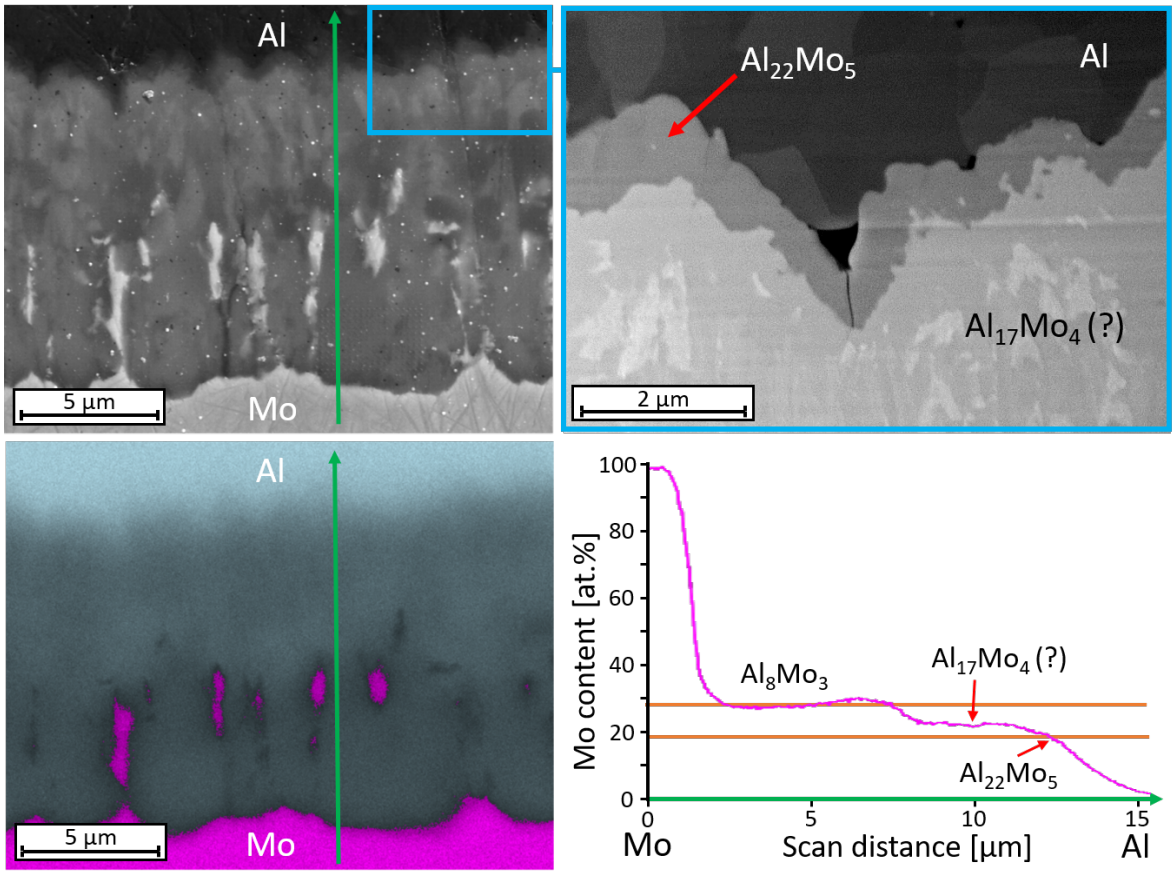

Figure 4.9: SEM micrographs and EDS analyses of the IDL between Al and Mo. The EDS map (bottom left) of the BSE image (top left) shows the zones of different Al (blue) and Mo (magenta) content with highlights the Mo stings. The EDS line scan along the green arrow (bottom right) reveals two distinct phases in the IDL, one of which fits the composition of Al_8Mo_3. A high-resolution BSE image of the Al/IDL interface displays a layer that is presumably $Al_{22}Mo_5$.

4.1.2 Tungsten

Model calculations for the mixing enthalpies of W with U and Al (see Chapter 2.2.5) show promising behavior that suggest further investigations on W as a diffusion barrier material. The following studies focus on the production of W coatings by PVD for heavy-ion irradiation experiments and the behavior of W coatings in combination with the C2TWP cladding process.

PVD Coating

Before a tungsten diffusion barrier coating is tested in combination with the cladding process or in an irradiation experiment, the properties of the coating itself in dependence on various production parameters were investigated. For this, the mini-size PVD device (see Chapter 3.1.1) was used as it provides the necessary versatility and large parameter space for a fundamental overview. It was equipped with a tungsten target of 99.95 % purity. Table 4.2 lists the amount of impurities in the target material. As a first step, stainless steel substrates were used to investigate the influence of techniques like plasma cleaning, substrate (pre-)heating, and substrate biasing. This minimizes the use of expensive U-Mo foils and reduces radioactive waste.

Table 4.2: Impurity content of the W sputtering target.

Element	Mo	C	O	N	H	Pb	Si	Sn	Ca	Cu	Ni	Ti	Mg
Content [ppm]	150	30	30	10	6	< 50	< 50	< 30	< 20	< 20	< 20	< 20	< 10

All preliminary samples were produced with a coating thickness of around 8 µm even if the finally desired thicknesses as a diffusion barrier are supposed to be much lower. This has been done to ensure a sufficient amount of material to study the mechanical properties and to reduce the uncertainty in thickness measurements. Samples produced this way are shown in Figure 4.10. By visual inspection, some samples showed partial delamination, cracks, or deformations due to stresses in the W coating. Bending tests were performed to check the integrity of the coating under mechanical deformation in foresight of the C2TWP cladding application process. This was done by bending the sample pieces to a 90° angle around an edge with a radius of about 3 mm. For the preparation of cross sections, straight and bent sample pieces were mounted in epoxy resin and ultimately polished with colloidal silica (particle size: 0.04 - 0.25 µm).

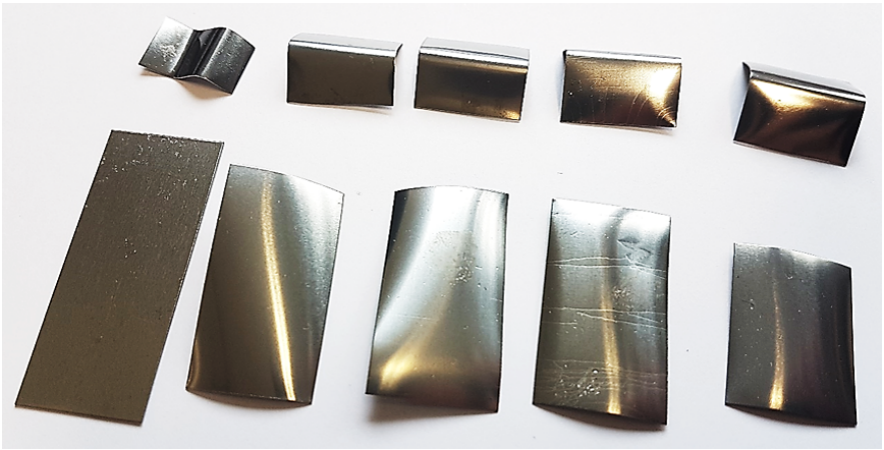

Figure 4.10: Selection of stainless steel substrates coated with W. The pieces on top were used for bending tests.

All coatings – either produced with substrate heating or biasing – exhibited more or less severe brittleness when bent, which was accompanied by delamination of individual fragments off the substrate exemplarily shown in Figure 4.11. This is not surprising, as tungsten is known for its low ductility when already containing small amounts of impurities in the order of 10 - 100 ppm [91, 106]. Purchasing a W target with a significantly higher purity to investigate this parameter was not an option at this early stage of the study. This would be an option for later if the tungsten performs well in principle but the brittleness turns out to be problematic in some way.

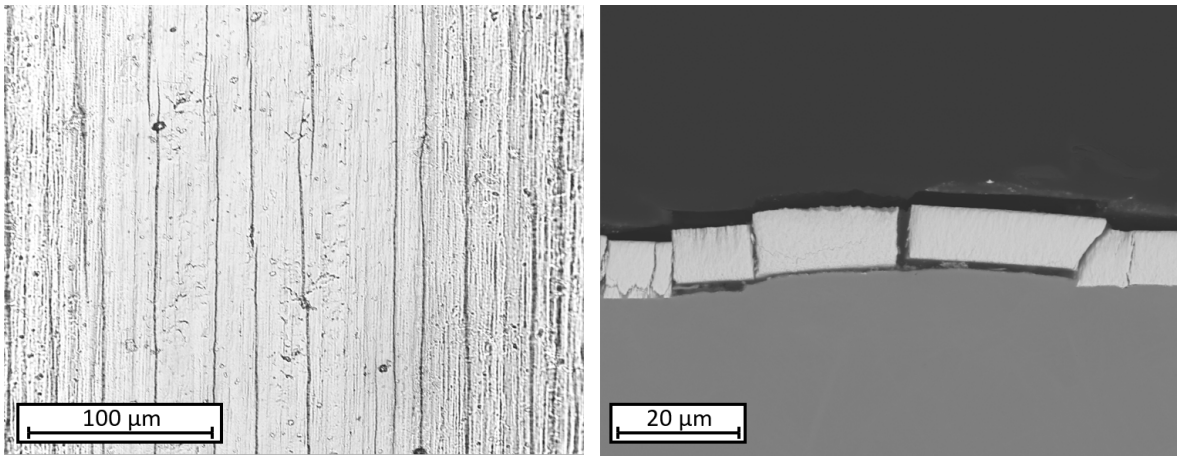

Figure 4.11: Optical microscopy images of the W coating bending tests. The bent coating surface exhibits cracks (left) and a cracked and delaminated layer is visible in the cross section (right).

Vickers hardness measurements of the W coatings were executed on the cross sections with an indentation force of 0.01 kilopond. Final values are generated by averaging 5 to 10 different measurements. As the coating thickness is just slightly larger than the size of the measurement indentations, the final values are subject to uncertainties. Therefore, this method was used more in a qualitative way to compare the influence of different coating parameters with each other. Samples that were produced without biasing showed a coating hardness of around 1200 HV with no observable influence of external heating in a temperature range of about 350 °C to 950 °C. Samples that underwent an ion bombardment with 300 V of biasing voltage showed a Vickers hardness of about 1900 HV. This general trend of increased hardness caused by high biasing voltages has already been observed at Zr coatings [8, 63]. However, typical Zr coatings are in a significantly lower hardness range in the order of 100 - 300 HV.

By weighing the substrate before and after coating, the theoretical layer thickness was calculated using the mass, the surface area of the substrate, and the bulk density of W (19.25 g/cm^3). The actual layer thicknesses were then measured in the cross sections by optical or electron microscopy, which gives the actual density of the tungsten as-sputtered. This density is usually lower than the bulk density due to porosities or Ar inclusions that form during layer growth. Zr for example is usually sputtered around 10 % below its

nominal density, but for tungsten, it is shown that bulk density is reached independently of the biasing and heating parameters within an uncertainty of ± 3 %.

The grain structure of the tungsten coatings can be observed with the SEM and turned out to consist of fine columnar grains that promote frayed cracks as depicted in Figure 4.12. A similar grain structure has already been observed at Zr layers. Zr, however, showed a significant increase in grain sizes starting at a substrate temperature of about 500 °C [63]. For tungsten, on the other hand, no significant grain enlargement was noticed up to substrate temperatures of about 950 °C, which is expectable due to the high melting point of W (3422 °C) compared to Zr (1855 °C).

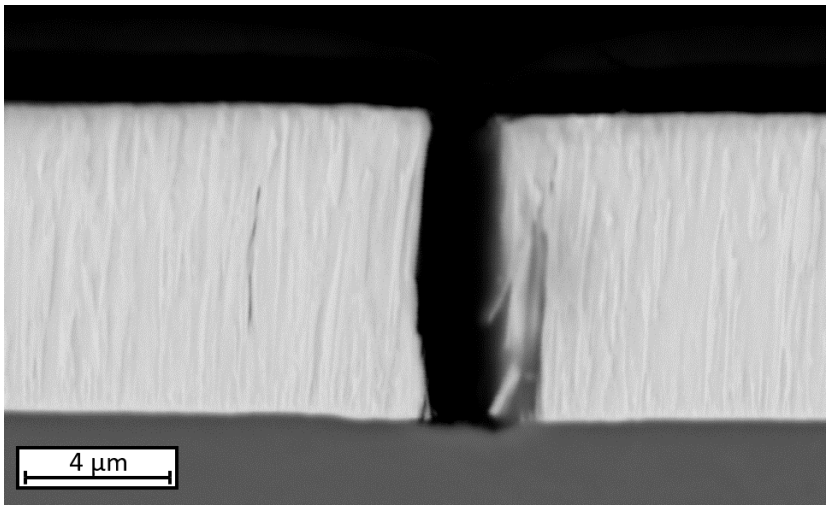

Figure 4.12: SEM BSE image of a cracked W layer produced with substrate heating of about 950 °C showing the grain structure.

Plasma cleaning, as well as substrate heating, are both valid methods to provide a good layer adhesion between substrate and coating, as far as the coated foil is not subject to severe mechanical deformation. However, due to the lower hardness of the W coating, the heating technique was chosen for further investigation steps with U-Mo substrates and ultimately for the production of the irradiated samples.

Subsequently, U-Mo substrates were used to confirm the layer adhesion and to check for potential signs of thermal diffusion at the U-Mo/W interface induced by the conditions during the sputtering process. Cross sections of the produced layer systems were then analyzed by SEM and EDS. Here, the layer adhesion of the coating was found to be sufficient, however, no bending tests were performed in U-Mo substrates to check the response on mechanical deformation. Regarding thermal diffusion, it was observed that samples produced without additional heating during the sputtering process showed no measurable IDL. The picture is different if the samples were preheated to around 600 °C for about 60 minutes. Here, the U-Mo/W interface started to show a slight IDL with a maximum thickness of 200 nm (see Figure 4.13).

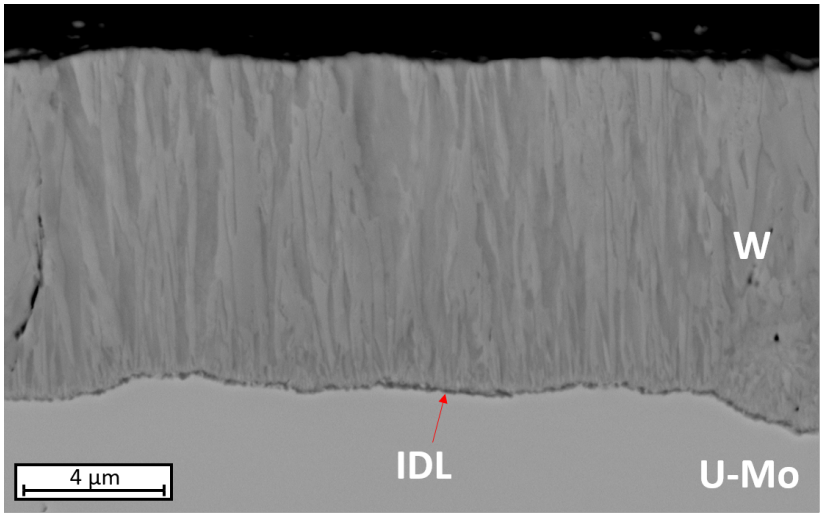

Figure 4.13: SEM BSE micrograph showing a thin IDL between W and U-Mo.

As a next step, the sputtering target was changed to aluminium to apply an additional layer of Al onto the tungsten coating in order to study the W/Al interface. Compared to the U-Mo/W interface, the W/Al interface shows a more pronounced IDL caused by thermal diffusion. An EDS line scan in Figure 4.14 illustrates the degree of intermixing, where the diffusion zone has already about the same thickness as the initial 500 nm of W layer. The composition of this layer is difficult to resolve with the line scan at such high magnifications. Possible compounds as reported by Zhang [148] are WAl_4, WAl_5, and WAl_{12}.

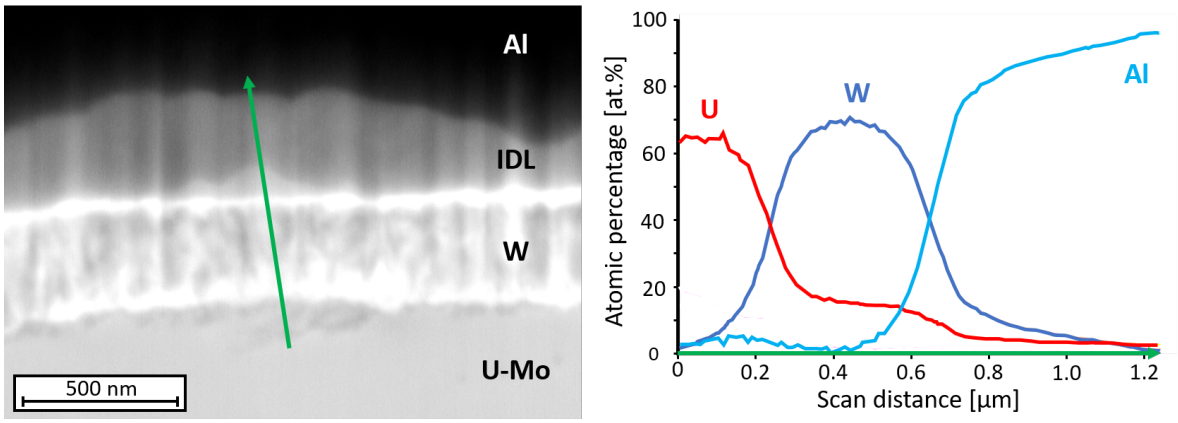

Figure 4.14: SEM BSE micrograph of 500 nm W coating that formed an IDL with Al. Composition was measured with an EDS line scan along the green arrow.

The preliminary tests were further used to optimize layer adhesion, coating homogeneity, and precise control of thickness to produce suitable samples for heavy-ion irradiation studies. These requirements were finally reached and four U-Mo samples with different W diffusion barrier thicknesses (200 nm, 500 nm, 1 µm, 2 µm) were produced. Each of these samples was coated with an Al layer of individual thickness in order to deposit the energy of the ion

beam most effectively at the U-Mo/W interface. The subsequent irradiation was performed with 80 MeV Xe ions at a constant sample temperature of 140 °C reaching a fission density equivalent of about $7.5 \cdot 10^{20}$ fissions per cm^3. The results turned out to be very promising, showing that under the given conditions, W layers of 500 nm to 1 µm already serve as suitable diffusion barriers and are therefore worth further investigation. A more detailed description of the procedure and results of this irradiation experiment can be found in [71] and [125].

Cladding Application

The mechanical properties of the sputtered W layers were of minor importance for the heavy-ion irradiation experiments but will come back into focus once W is used in actual fuel plates. To investigate the behavior of the coating in combination with the C2TWP cladding process, two stainless steel mini-size foils coated with W were produced. Regarding the PVD parameters, an approach with biasing instead of heating was chosen again, as simultaneous findings with Zr coatings suggested that biasing is beneficial for the ductility of the coating if a suitable biasing voltage is used [124]. Starting at about 150 V, the ion bombardment is too energetic and introduces too much damage into the coating, while the voltage range of 50 V - 100 V provides the best results. Accordingly, a biasing voltage of 50 V was tested for the W coatings. Regarding the layer thickness, 1 µm was chosen based on the results from the heavy-ion irradiation. The coated foils were shipped to Framatome, where the cladding was performed. Back at TUM, the finished plates were sectioned and prepared for metallographic examination. Figure 4.15 shows the cutting plan of one of the plates. Cross sections of four sample pieces were prepared; three from longitudinal cuts and one transversal cut from the center of the plate.

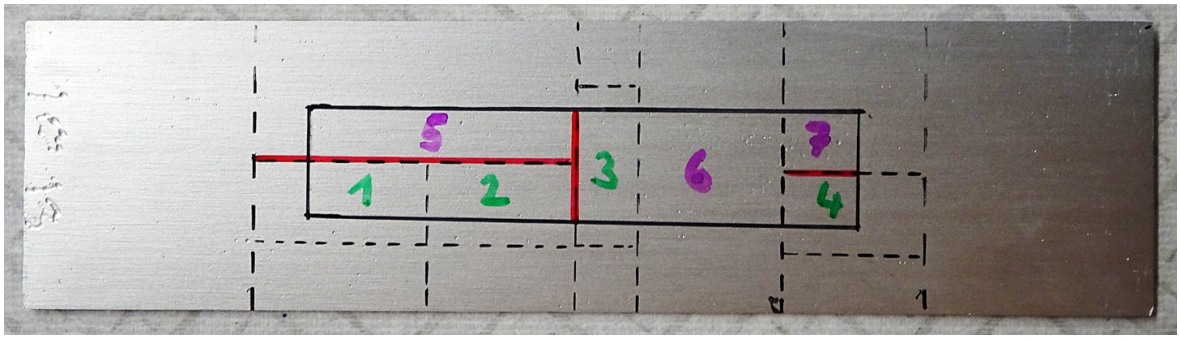

Figure 4.15: Mini-size plate consisting of a cladded stainless steel foil with W coating. The position of the foil (black line) and the sectioning scheme (dashed lines) is drawn onto the surface. Sample pieces numbered 1 – 4 are used for the cross sections (red) and the piece numbered 5 for cladding removal.

A brief inspection of the cross sections with the optical microscope showed a satisfactory adhesion of the W coating on the substrate. The interface of coating and cladding on the contrary exhibited multiple regions of debonding, which make up about 10 % of the complete interface. Following this, the SEM was used to obtain a higher resolution of the thin W layer. Figure 4.16 depicts three types of regions in which the W behaves differently.

Most commonly, the W layer shows a large number of cracks. This is not unexpected due to tungsten's brittleness which has been observed in the preliminary tests before. Regarding interdiffusion, no signs of such were found at the W/Al interface. Some regions, however, showed an increased W layer thickness without any apparent influence of interdiffusion. Especially at the Al interface, the W exhibits starting defragmentation. Other areas show even a second layer of W mainly filled with stainless steel in between. In the most severe cases, fragments of a completely disintegrated W layer with stainless steel particles fill a zone of about 30 µm between coating and cladding as depicted in Figure 4.17.

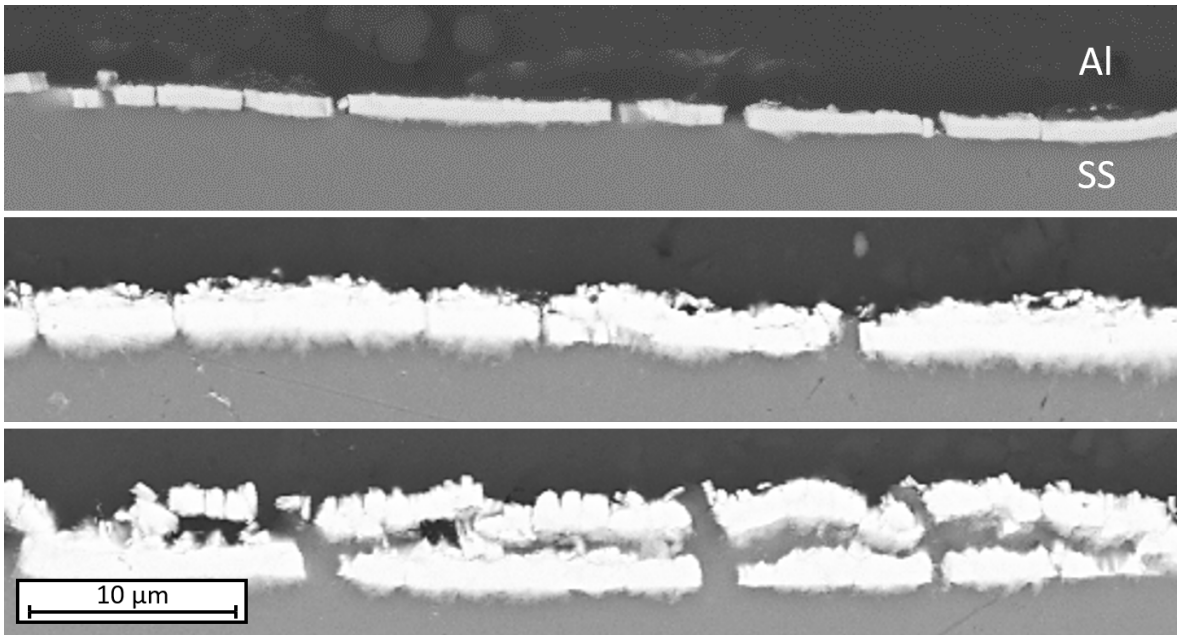

Figure 4.16: SEM BSE images of longitudinal cross sections showing different behavior of the W coating between the SS substrate and Al cladding.

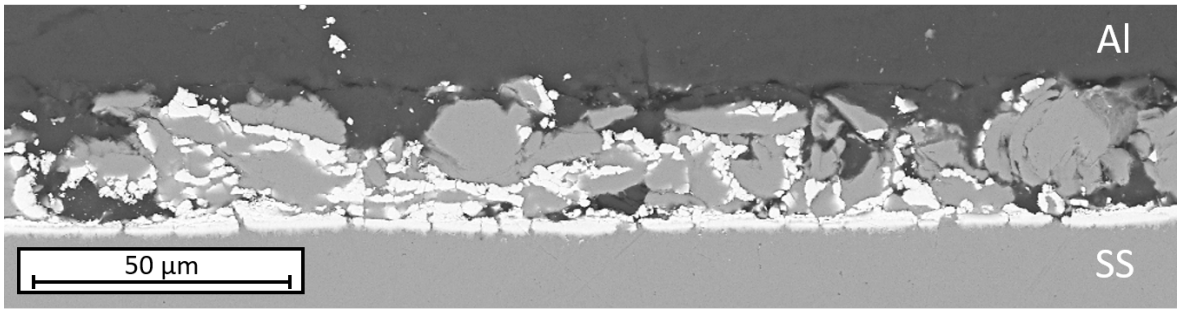

Figure 4.17: SEM BSE images of longitudinal cross sections showing disintegrated W coating between the SS substrate and Al cladding.

Transversal cross sections as seen in Figure 4.18 show mostly no cracks. Apart from this, similar features as in the longitudinal cross sections were also observed. The brittle fragments of W that separate from the surface may prevent the effective bonding of the cladding and lead to the formation of gaps in which the loose debris gathers.

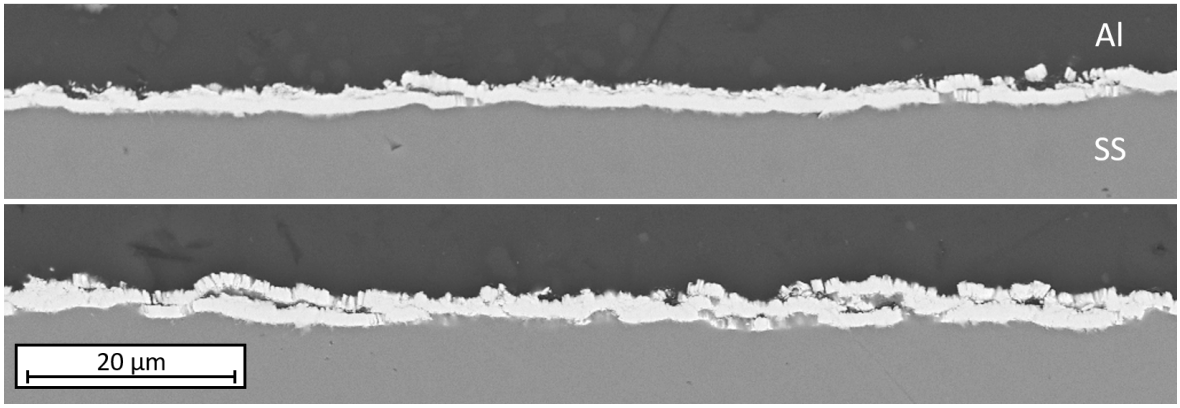

Figure 4.18: SEM BSE images of transversal cross sections showing different behavior of the W coating between the SS substrate and Al cladding.

The AlFeNi cladding of one of the sample pieces was removed with sodium hydroxide solution to investigate the surface of the coating on the stainless steel foils. This procedure most likely alters or completely removes loose structures like the one shown in Figure 4.17.

Figure 4.19 shows the uncovered sample piece and selected optical microscopy images from different positions of its surface. Within the first few millimeters from the short side of the foil, the coating is intact and shows no signs of fractures or other defects. The horizontal grooves are from the rolling pattern of the underlying stainless steel. This pattern can still be seen as the layer thickness of 1 µm W is too thin to equalize it. In the middle of the foil, the coating is severely cracked as already suggested by the cross sections. Like the Zr coatings (see Section 4.2.1), the general orientation of the cracks is parallel to the foil's short end. The amount of cracks, however, is approximately one crack every 10 µm, which is about ten times more than the amount observed in the Zr layers. A peculiar feature is seen at the long sides of the foil. Here, the density of cracks is significantly reduced within about 200 µm distance to the edge, which indicates that during the cladding process this region of the foil is subject to reduced mechanical stress.

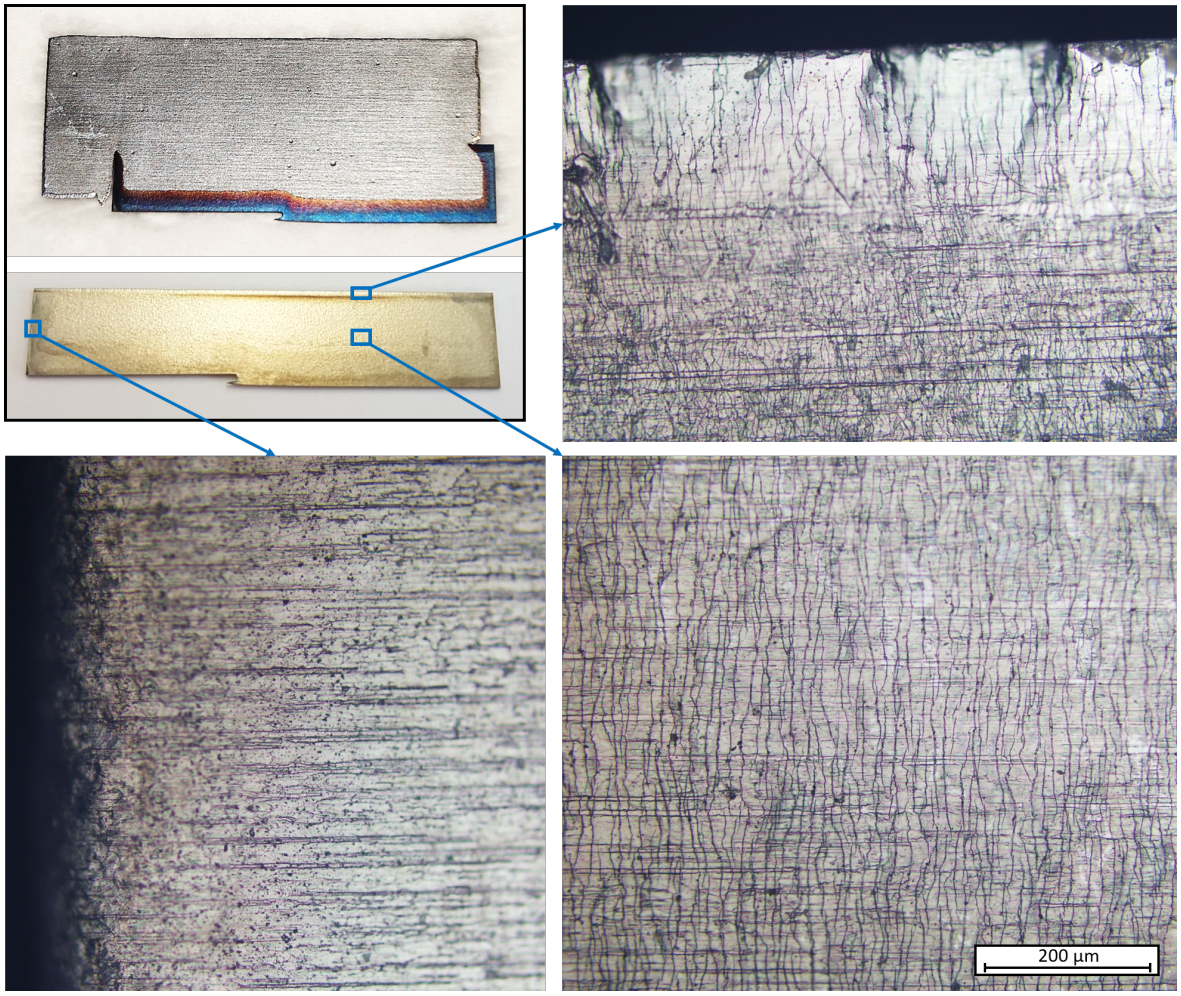

Figure 4.19: Foil piece with W coating after cladding removal. The framed box shows the chosen sample piece with partially and completely dissolved cladding. The optical microscopy images show the coated surface at the indicated positions on the foil.

4.1.3 Discussion

Properties of Mo layers produced by sputter deposition were investigated regarding the influence of biasing and substrate heating during coating. Bending tests showed that the brittleness of the coating could only be slightly modified with the given parameters and cracking could not be completely prevented. In combination with the cladding application, the problem arose that surface oxidation of the Mo coating prevented the bonding to the Al cladding. This was successfully solved by the application of a protective Al coating via PVD onto the Mo. However, this introduces a second coating step which complicates possible future industrializations. Furthermore, the parameters for this second coating process have to be adapted as the introduced heat triggered significant diffusion between the Mo coating and the protective Al layer that resulted in a brittle IDL consisting of intermetallic phases.

Tungsten as a diffusion barrier material displayed a very low ductility in first sputtering tests on stainless steel substrates. This resulted in many fine cracks when put under tensile stress, both in bending tests and during cladding application. In characterizations after the latter, regions with significant coating disintegration could be observed. Adjustment of PVD parameters within the current limits showed no significant improvement of this behavior which is possibly detrimental to in-pile fuel plate performance. A possible improvement could be to use a W material with higher purity as a sputtering target. Especially the prolific heavy-ion irradiation results affirm tungsten as a promising candidate for diffusion barriers and suggest a more detailed study.

4.2 EMPIrE - Zr Diffusion Barriers

The EMPIrE irradiation campaign included amongst others four monolithic LEU fuel plates, two of which with a PVD coated Zr diffusion barrier by TUM and the other two with Zr applied by co-rolling. All four U-Mo foils, including the co-rolled Zr, were produced at BWXT with a nominal thickness of 330 µm. For comparability of the two Zr application methods, the PVD process was performed in a way to match the nominal Zr thickness of 25 µm of the co-rolling process. For all foils, the cladding was applied similarly with the C2TWP process at Framatome. A detailed report of the EMPIrE plate production can be found in [132]. This also includes several batches of DU test plates that where produced to develop and analyze the fabrication process.

The EMPIrE plates were irradiated in two cycles at the Advanced Test Reactor (ATR) of the Idaho National Laboratory (INL). The first cycle with a calculated average U-235 burnup of 32 % included one PVD coated (Plate ID: EMPI1201) as well as one co-rolled (EMPI1103) plate each. The second cycle with the plates EMPI1207 (PVD) and EMPI1102 (co-rolled) had a calculated average burnup of 43 %.

Results from the examination of these plates as well as of unirradiated test plates is presented in the following. The main focus lies on the plates coated by PVD, which was done at TUM.

4.2.1 Examination of Unirradiated Test Plates

Several sample sets of depleted mini-size U-Mo foils with PVD coating were produced to find a suitable parameter set for the EMPIrE production of LEU foils. The main differences between the tested coating processes were the techniques of external heating and substrate biasing. Finally, the heated samples were dismissed as the interaction layer caused by thermal diffusion between fuel and coating may become a problem during irradiation. As a result, coatings produced with 300 V biasing were chosen for irradiation [132]. However, it later became apparent that the coatings produced like this were rather brittle and tend to crack in the cladding process. This could not be observed in the UT scans of the finished LEU fuel plates but was discovered subsequently in destructive examinations. These destructive examinations of the unirradiated fuel plates serve as a reference for the actual irradiation test to separate effects of irradiation from those induced by the fabrication process.

A fuel plate with the same properties as the irradiated EMPIrE samples (except for the enrichment) was sectioned as depicted in Figure 4.20. Five of the sample pieces were mounted in epoxy resin and prepared for the examination of cross sections (four longitudinal and one transversal). To obtain a more comprehensive view of the state of the coating, the cladding of another two samples has been removed. This is achieved with a sodium hydroxide solution, which dissolves the AlFeNi cladding, but leaves the U-Mo foil and the Zr coating untouched.

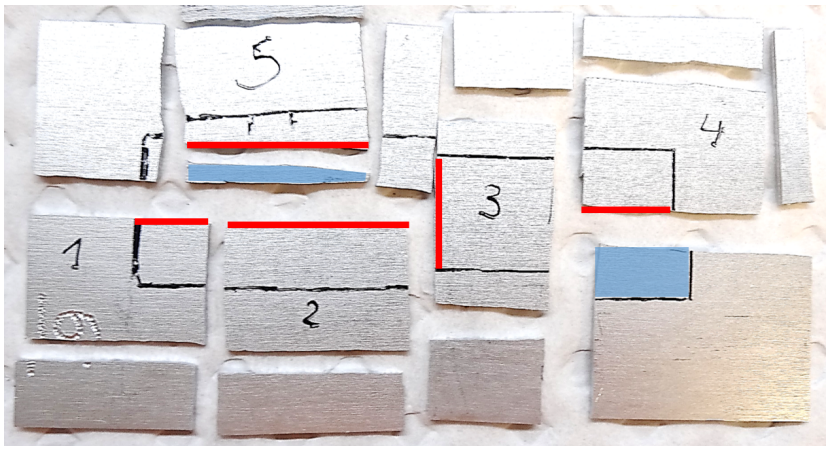

Figure 4.20: Sectioned reference fuel plate. The black line indicates the position of the U-Mo foil within the plate. Examinations include cross sections (red lines) of the numbered sample pieces as well as coating surfaces of two pieces (blue) after removal of the cladding.

The most noticeable feature are the voids surrounding the foils on the sides. These so-called *end gaps* are formed when the cladding is not completely enclosing the U-Mo foil as seen in Figure 4.21. Typically, a single void covering the whole foil's thickness is observed on the short side of the foils, while the long sides display smaller, more irregular voids. The cross sections also show that the cladding is not completely made out of AlFeNi; an interlayer consisting of pure Al is in contact with the Zr coating and can be distinguished by its lighter shade of grey.

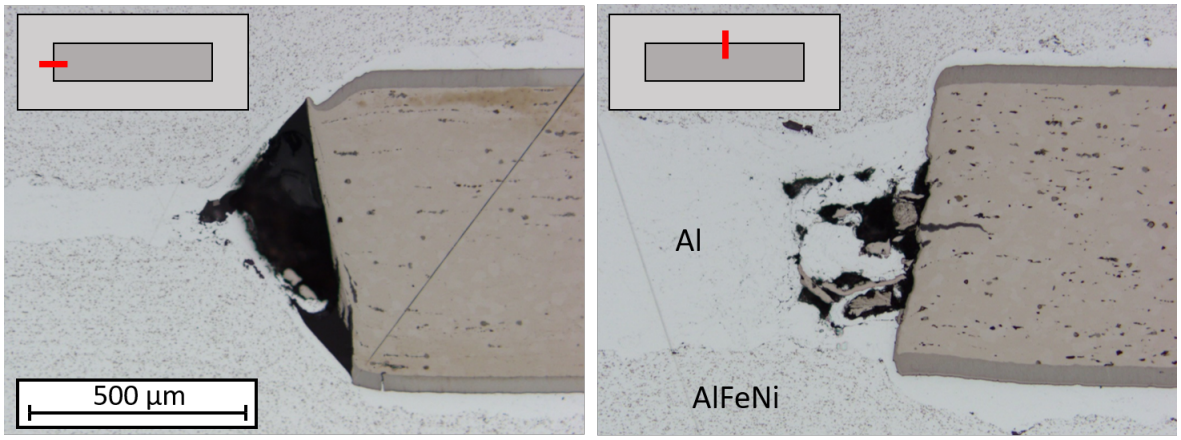

Figure 4.21: End gaps at the short sides (left) and long sides (right) of the foil.

The integrity of the coating is not given anymore as multiple cracks run through the Zr layer, which are only observed in longitudinal cross sections. Furthermore, the number and type of cracks show an inhomogeneous distribution across the length of the foil, which is illustrated in Figure 4.22. Across the first 2 millimeters after the end gap, the coating is intact and shows no signs of fractures or other defects. After that, a reduction of the foils' thickness from the initial thickness of 335 µm to about 310 µm is measured. This coincides with the beginning of cracks in the coating that are present over about the following 25 mm. Over this stretch, their number decreases from about 10 cracks per mm to about 2 cracks per mm. Simultaneously, also the morphology of the cracks changes. Wide cracks with voids that are partially penetrated by the cladding material are continuously replaced by sheared fractures towards the middle of the foil.

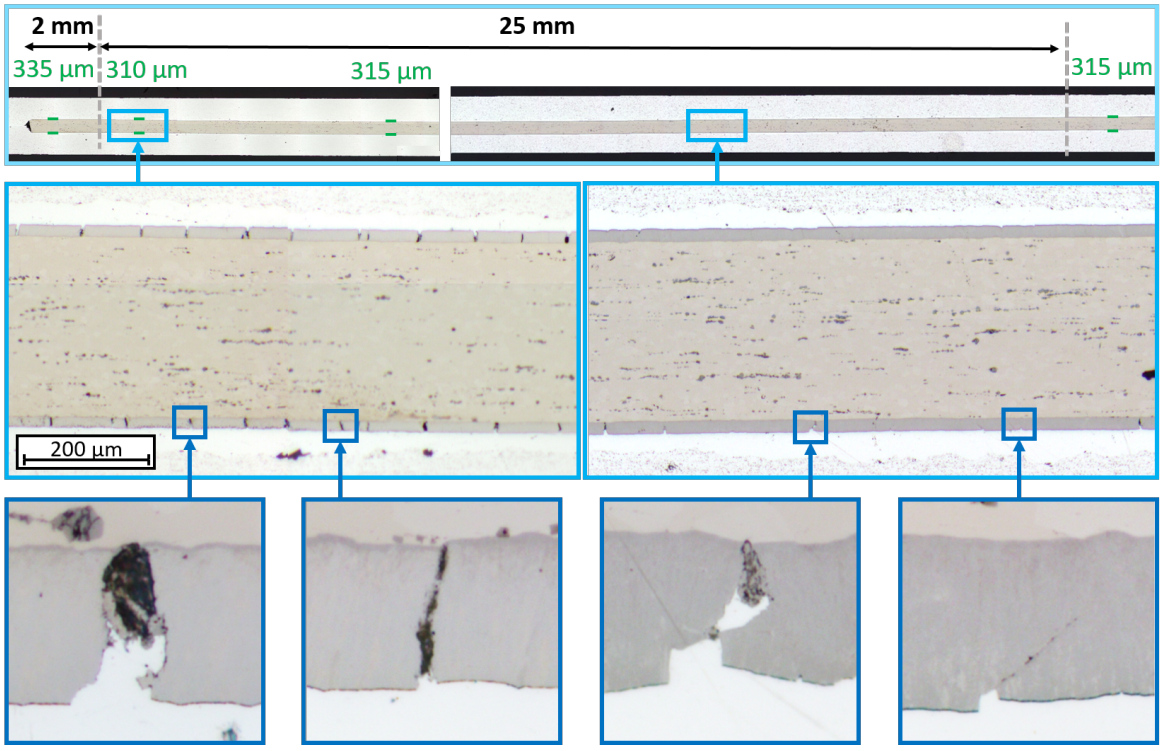

Figure 4.22: Optical microscopy images of an unirradiated DU fuel plate. Longitudinal cross sections showing different areas of coating defects. The first 2 mm after the edge, the coating is intact. The local fuel thickness is given in green. A stretch of 25 mm shows cracks and fractures that vary in number and shape from left to right.

The sample pieces with the removed cladding are utilized to get a more expanded view of the cracking behavior from the top of the coating. It confirms the location of cracking from the cross sections, where no cracks are visible close to the foil ends (see Figure 4.23). The distance between cracks of about 100 µm agrees with the observations from the cross sections. The cracks are about 1 mm long and orientated parallel to the short side of the foil. This explains why no cracks are visible in the transversal cross section; the probability to

encounter a crack is lower, and if it is the case then it would not appear as a crack but more like a stretch without coating.

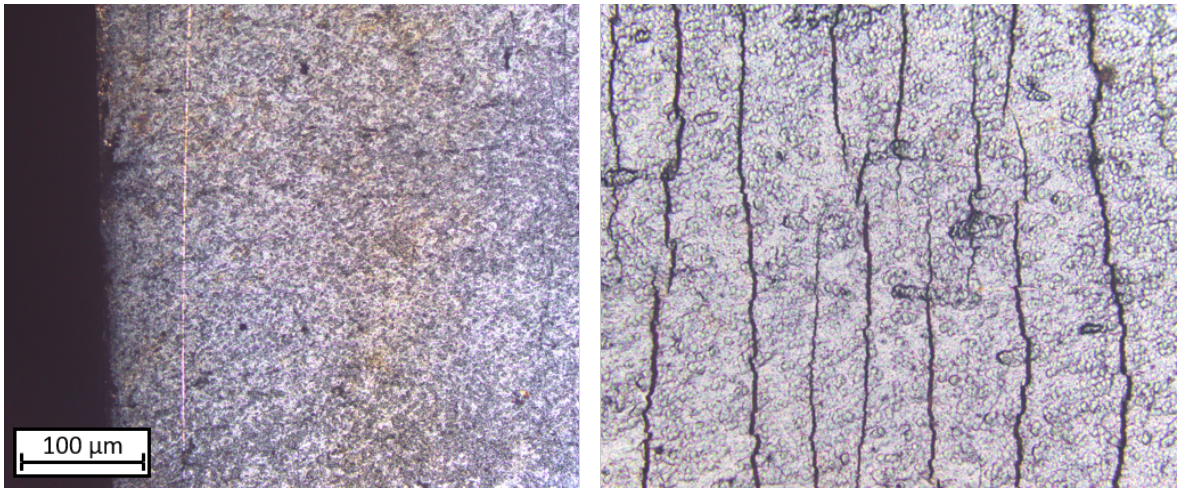

Figure 4.23: Surface of Zr-coated U-Mo foils after chemical removal of the cladding. Intact coating close to the foil's edge (left) and structure of cracks a few millimeters away from the edge (right).

Figure 4.24 visualizes the grain structure of the Zr layer using the optical microscope with polarized light as well as an electron microscope with electron backscatter diffraction (EBSD). The grains appear to be thin and long and are significantly smaller than the grains in the U-Mo fuel and Al cladding. This fine columnar structure promotes cracking along the grain boundaries.

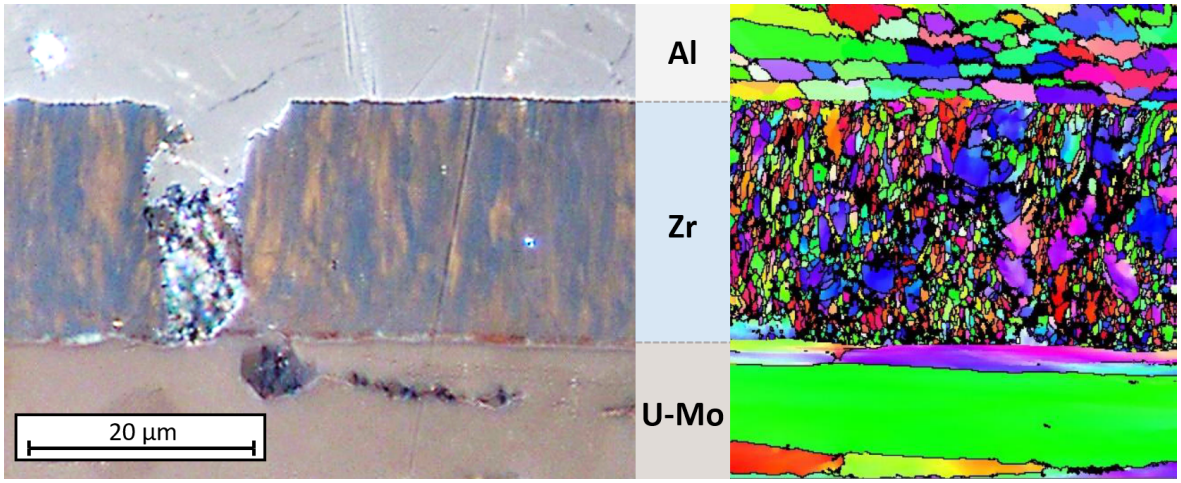

Figure 4.24: Grain structure of the Zr coating of unirradiated fuel plates. The optical image in polarized light (left) shows fine columnar grains that promote cracks. The EBSD image (right; from [44]) confirms this observation.

4.2.2 Non-destructive Post-Irradiation Examination

For PIE, the irradiated plates were shipped to the Hot Fuel Examination Facility (HFEF) at INL. *Non-destructive examinations* (NDE) performed there include visual inspection, neutron radiography, gamma scanning, profilometry, and oxide thickness measurements. The combined results demonstrated stable and predictable swelling behavior, which is in line with historical U-Mo monolithic irradiations [110]. A significant difference between plates with the two fabrication techniques was not observed. The fuel meat was intact with no signs of cracks, voids, fission product migration, or other defects and deformations. Oxide that formed on the cladding above the fuel zone was seen by visual inspection but measured to be insignificant regarding fuel swelling calculations. For more details see [37, 113].

4.2.3 Destructive Post-Irradiation Examination

Two plates from the second cycle with a higher burnup were chosen for destructive PIE. The sectioning of the plates was performed at HFEF in a way to obtain four sample pieces for cross sections of each plate as seen in Figure 4.25. Each section is designated to focus on a certain region regarding the foil's orientation and local burnup quantified by the calculated fission density:

- Sec. 1: longitudinal orientation of central fuel region
- Sec. 2: transversal orientation with end gaps on the long sides
- Sec. 3: longitudinal orientation at high-burnup ($3.0-3.5\cdot10^{21}$ fissions/cm^3) end gap
- Sec. 4: longitudinal orientation at low-burnup ($2.5-2.75\cdot10^{21}$ fissions/cm^3) end gap

These sample pieces were individually mounted with epoxy in modified SEM-stubs at the *Irradiated Materials Characterization Laboratory* (IMCL), where also the materialographic preparation, as well as the examination, was performed. The following characterization results focus on the PVD-coated plate and comparison with the corresponding samples from the preproduction with DU.

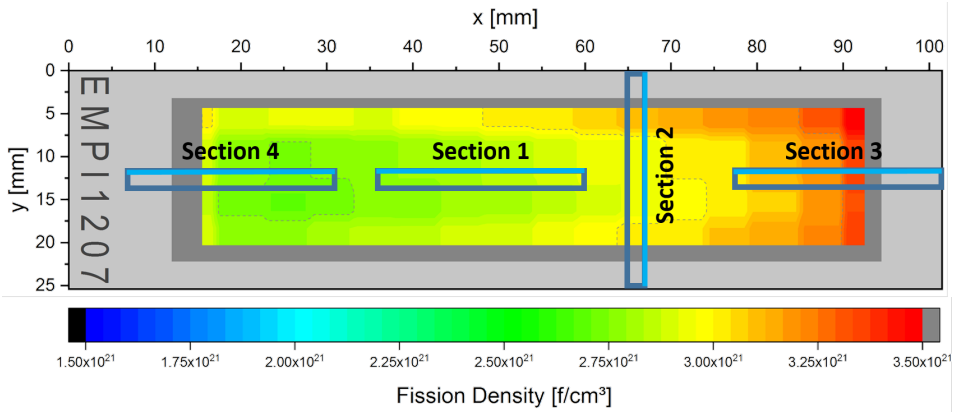

Figure 4.25: Scheme of the fuel plate EMPI1207 (PVD-coated Zr) superposed with the measured fission density. The indicated sections prepared for microscopy are true to scale. Based on [78].

As already suggested by the NDEs, the cross sections showed no general changes regarding the geometrical condition of the plates. Cladding, coating, and the U-Mo fuel meat showed the same unaltered structural features as the unirradiated reference plates. Especially the end gaps displayed no disadvantageous influence. The only difference to the as-fabricated plate is that the fuel started to creep/swell slightly into the void of the end gap, as depicted in Figure 4.26.

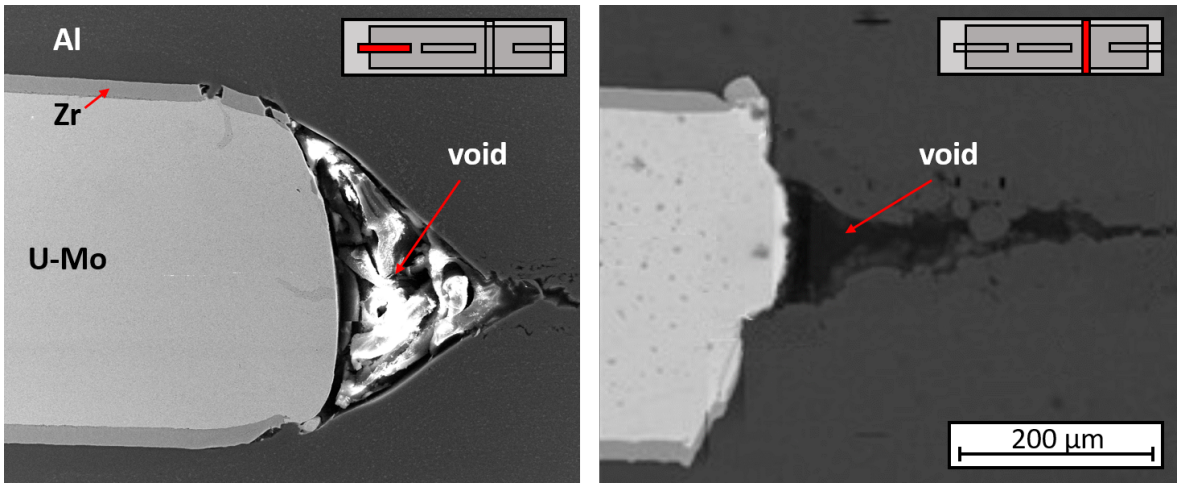

Figure 4.26: Micrographs of an irradiated fuel plate. The cross sections show slight fuel creep into the longitudinal (left) and transversal (right) end gap. The right micrograph is stitched together from mulitple smaller images, which causes some artifacs due to different brightness contrast.

Fuel Meat

The U-Mo fuel showed the characteristic microstructure expected for irradiation in the given burnup region [110]. This includes fission gas bubbles that nucleated on the grain boundaries of the U-Mo grains, which have usually the size of a few micrometers. However, there are areas of larger grains as well. Figure 4.27 shows a typical example of such a microstructure. In some areas, a higher density of fission bubbles can be observed, which likely corresponds to the beginning of mechanisms like polygonization and recrystallization that lead to the microstructures typical for high-burnup U-Mo fuel [53, 61, 109].

Uranium carbides with a size of a few micrometers are present throughout the fuel. They are observed as single precipitates, but often also appear as a group of multiple elongated pieces in a line, which is known as a carbide *stringer*. Some carbides show porosities and fractures. All these are common features coming from the fabrication process of the U-Mo foils [86]. The irradiated carbides display the same structure compared to as-fabricated fuel meat [44].

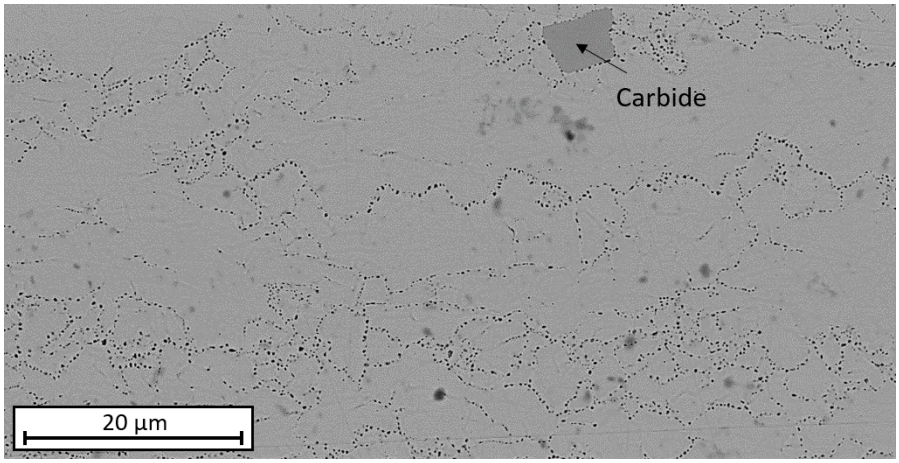

Figure 4.27: SEM BSE image of a typical irradiated U-Mo microstructure.

Cracking

Cracks were observed to display a similar distribution as the unirradiated reference samples and there is no indication that the cracks were altered in size and structure by the irradiation. Again, no cracks were present directly at the edges, then started to appear after about 2 mm and gradually turned into more sheared fractures (without a preferred direction) towards the middle. Figure 4.28 shows two such cracks as an example of the different types. In the transversal cross section, no cracks were observed.

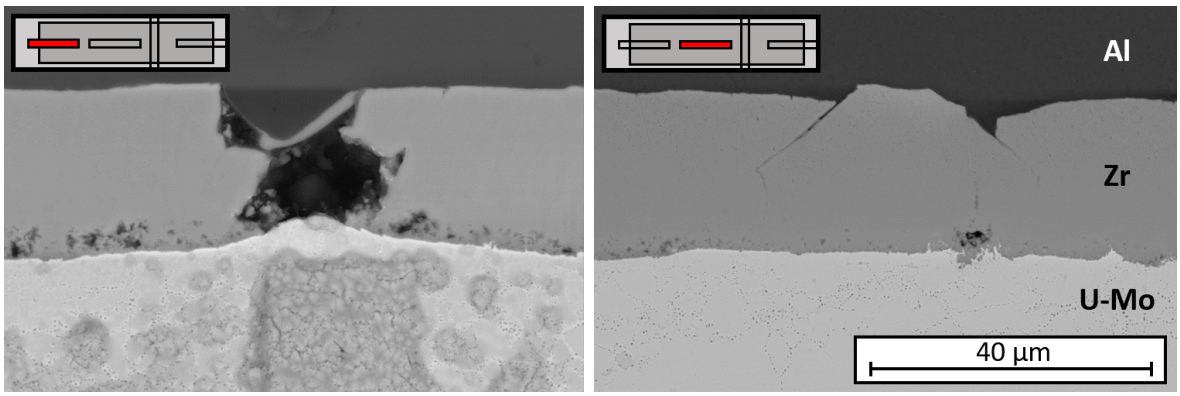

Figure 4.28: SEM BSE images of cracks in the Zr coating. Wide cracks are more present closer to the foil's end (left), while sheared fractures are common towards the middle. The rectangular shape below the left image is not a feature in the fuel but can be attributed to debris from the polishing.

In the vast majority of cases of cracks with a completely separated Zr layer, the cladding is not in contact with the fuel. Cladding material usually penetrates the cracks but reaches halfway through the Zr layer at best. This is similar to the as-fabricated plates. The only observable difference is a slight fuel creep into the voids of the cracks, which is similar to the behavior detected at the end gaps (see Figure 4.26).

The case that fuel and cladding come in contact through the barrier layer was found only a few times, and exclusively at singular cracks very close to the end gaps, where otherwise no cracks are present as reported above. The longitudinal end gap shown before in Figure 4.26 (left) exhibits the described behavior. A magnified view of this feature together with another example from a transverse cross section is depicted in Figure 4.29. Most noticeable consequence of the two materials touching is the formation of elongated interaction zones, which can expand more than 50 µm into the fuel. Their form appears to be caused by a macroscopic material flow and less by diffusive material transport. The composition of these areas remains currently unknown. Something roughly similar has been already observed at cracks in the zirconium nitride (ZrN) coating of irradiated disperse U-Mo fuel. However, here the resulting features – so-called *volcanos* – show more of an interdiffusion behavior as intermixing is present on both sides of the barrier layer [59, 77]. A compositional analysis of the interaction zone by EDS is not feasible as the detector can not efficiently operate with the high dose of background radiation from the sample.

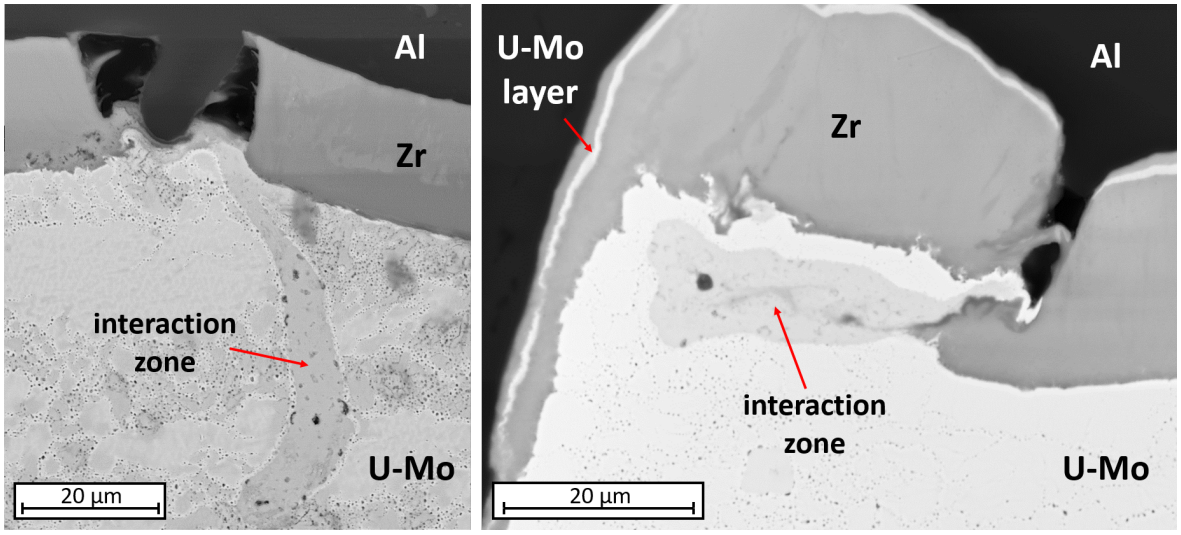

Figure 4.29: SEM BSE images of fuel-cladding interaction at cracked coating in the proximity of the longitudinal (left; sample section 4 with $\approx 2.75 \cdot 10^{21}$ fissions/cm^3) and transversal (right; sample section 2 with $\approx 3.0 \cdot 10^{21}$ fissions/cm^3) end gaps.

Further worth mentioning is the thin bright layer noticeable in Figure 4.29(right). This feature is only visible close to the foils' ends and just on one side. It can be explained with the course of the PVD coating process. When one side of the coating is finished, the foils get turned around and then undergo the plasma cleaning and the coating step. Some of the removed U-Mo from the plasma cleaning redeposits on the already coated backside, which is visible as a bright line with the BSE detector. The subsequent sputtering process coats this again slightly as some Zr particles reach the backside by diffusion. No disadvantageous effect of this feature was observed after irradiation.

Fuel/Zr Interface

Interdiffusion between fuel and diffusion barrier barely occurred, but a thin interaction layer $< 100\,\text{nm}$ is visible at high magnifications of the SEM. The exact nature of this layer has to be investigated with other analytical methods.

The most dominant feature at the fuel/Zr interface of the irradiated plate is a layer of porosities that extends about 5 µm exclusively into the zirconium as shown in Figure 4.30. This was observed throughout the plate and is independent of the position or orientation of the examined sample piece, which indicates that the pores come from the accumulation of fission gas. However, the variation of fission density across the plate is not big enough to distinguish a significant difference between low-burnup ($2.5 \cdot 10^{21}$ fissions per cm^3) and high-burnup ($3.5 \cdot 10^{21}$ fissions per cm^3) regions. This thickness of the porous layer roughly coincides with the reported recoil range of fission fragments in Zr [126].

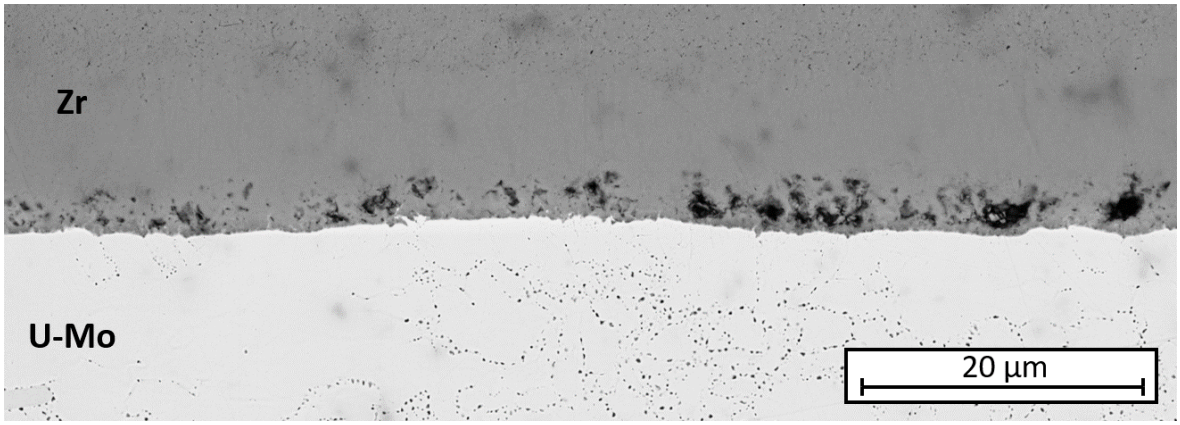

Figure 4.30: SEM BSE image of the fuel/Zr interface at about $2.8 \cdot 10^{21}$ fissions per cm^3 with a porous layer in the Zr.

The density of pores seems to be varying across the interface. Some areas display many big pores with multiple microns in size, while others are scarce of them. There even appear short stretches of several 10 µm that are completely devoid of porosities. These different regions are contrasted in Figure 4.31. To better understand the morphology and distribution of these pores, a cube of about 40 µm was extracted from the porous interface region using the focused ion beam (FIB) of the SEM. The cube was then milled with the FIB in 50 nm increments, creating multiple images of the process that can be played as a movie. A selection of micrographs from this process is shown in Figure 4.32. It turned out that after removal of a few micrometers of material areas with large porosities show lower porosities and vice versa. This indicates that the porosities are randomly distributed throughout the plate and not affected on a large scale by a specific feature in the as-fabricated microstructure.

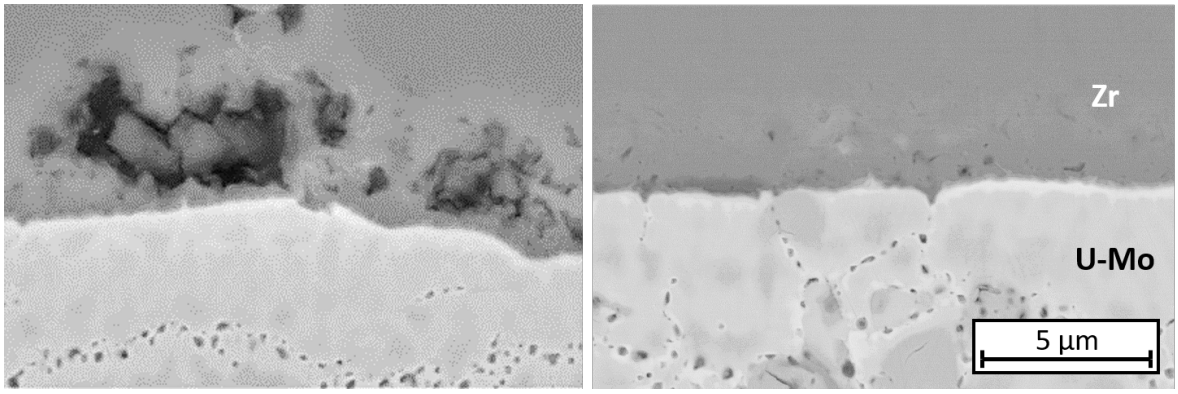

Figure 4.31: SEM BSE image of the fuel/Zr interface showing region of high porosity (left) and low porosity (right) in the Zr layer.

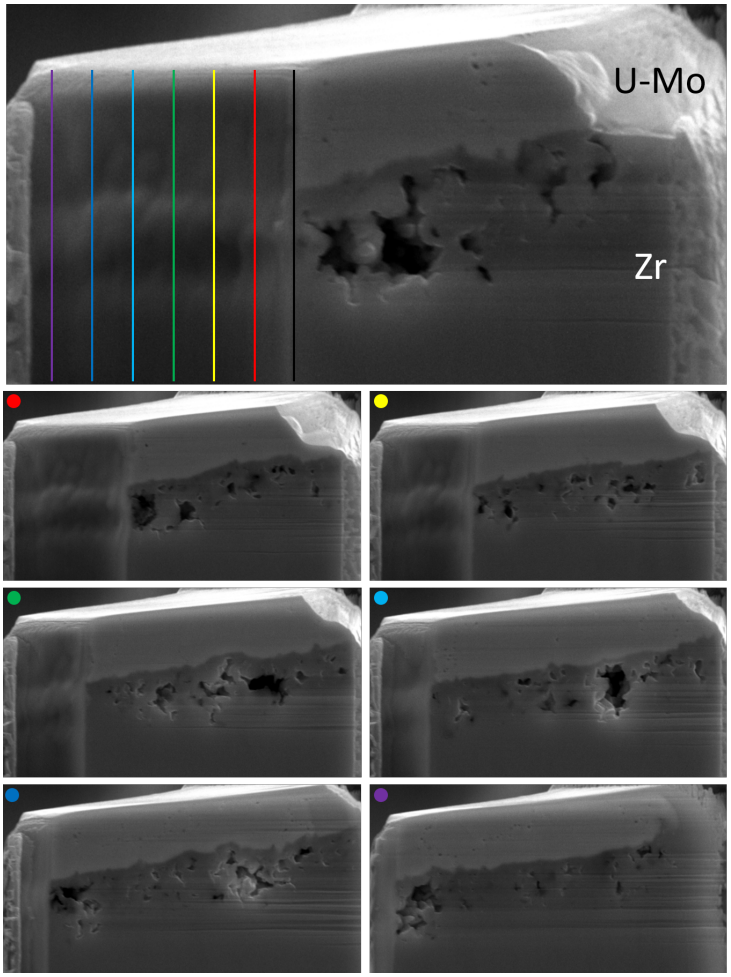

Figure 4.32: SEM BSE micrographs showing the sectioning of a cube from the fuel/Zr interface with the progression of the porosities. Each slice corresponds to the removal of about 1 µm of material. It should be noted that scales are distorted in this view of the cube, i.e. cutting depth as well as x and y coordinates of the cut area are not the same scale.

Surface-near carbides, however, have an effect as they block the diffusion of fission gases into the Zr layer as depicted in Figure 4.33. This example suggests an increased accumulation of fission gases left and right to the carbide as a result. The occurrence of such spots is rare though and therefore does not affect the overall behavior.

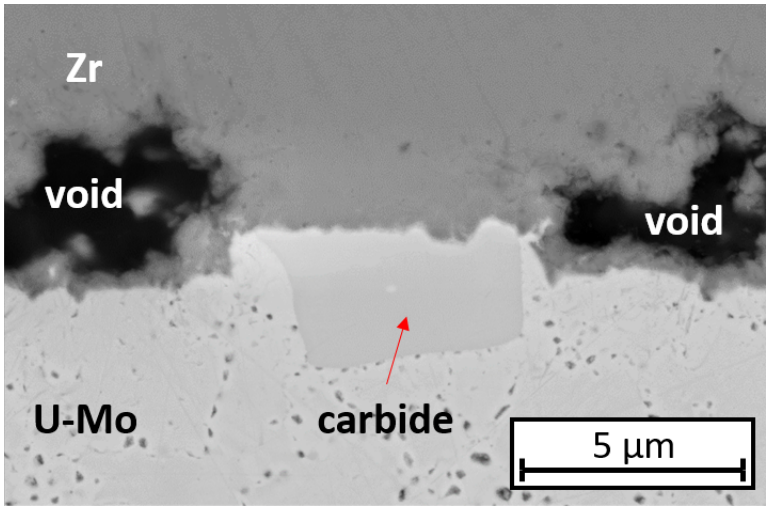

Figure 4.33: BSE SEM image of the fuel/Zr interface with a surface-near carbide.

Zr/Cladding Interface

A thin layer of about 200 nm thickness can be observed at the Zr/cladding interface (see Figure 4.34). This is already known from the as-fabricated fuel plates and was identified by [44] as α-ZrO_2. This layer seems to be a starting point for cracks but in most cases, they do not penetrate much further into the Zr layer. This behavior has been already observed in the unirradiated plate. So, to sum up, no defects or modifications of features at the Zr/cladding interface could be attributed to irradiation.

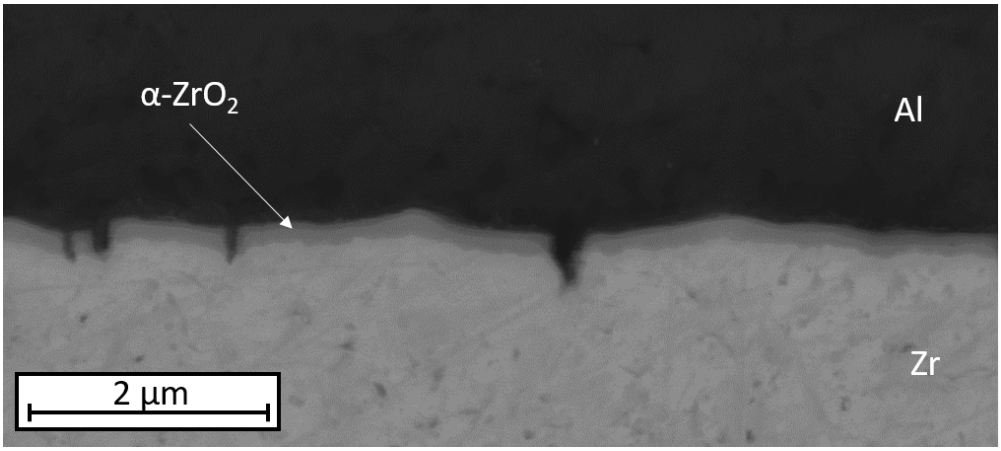

Figure 4.34: SEM BSE image of the Zr/cladding interface showing a thin oxide layer and small cracks.

Cladding Oxidation

As already observed by the visual inspection of the plates, the cladding is covered by an oxide layer. However, no compositional characterizations have been carried out. The cross sections show a continuous layer thickness of about 3 - 5 µm with occasional cracks that extend down to the AlFeNi, as seen in Figure 4.35.

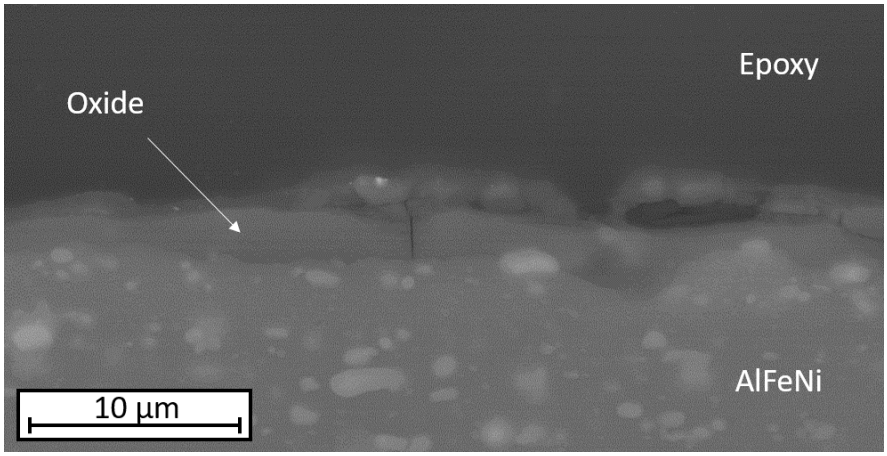

Figure 4.35: SEM BSE micrograph of a typical oxide layer on the AlFeNi cladding.

4.2.4 Co-Rolled Plates

Monolithic U-Mo fuel plates with a Zr diffusion barrier applied by co-rolling have been irradiated before in the RERTR-12 test [110]. For the co-rolled plates in the EMPIrE test, however, the cladding was applied by the C2TWP process instead of HIP.

Unirradiated plates already show a pronounced interaction zone at the U-Mo/Zr interface (see Figure 4.36), which has been observed and thoroughly investigated before [49, 93, 97]. This zone is fully developed after the co-rolling step, which is performed at 650 °C with a total exposition time of about 130 minutes. It consists of a layer of UZr_2 of about 2 µm thickness adjacent to the Zr coating, followed by a zone of about 3 µm that includes Mo_2Zr precipitates surrounded by a Mo-depleted fuel zone, which promoted the formation of α-U. Cladding application by HIP (560 °C for up to 345 minutes) does not significantly alter this zone [93]. The same is observed for plates that underwent the C2TWP cladding method.

The irradiated plate EMPI1102 was chosen for PIE. Is has a fission density profile similar to the one of the PVD coated plate (see Figure 4.25) in the order of $(3 \pm 0.5) \cdot 10^{21}$ fissions/cm^3.

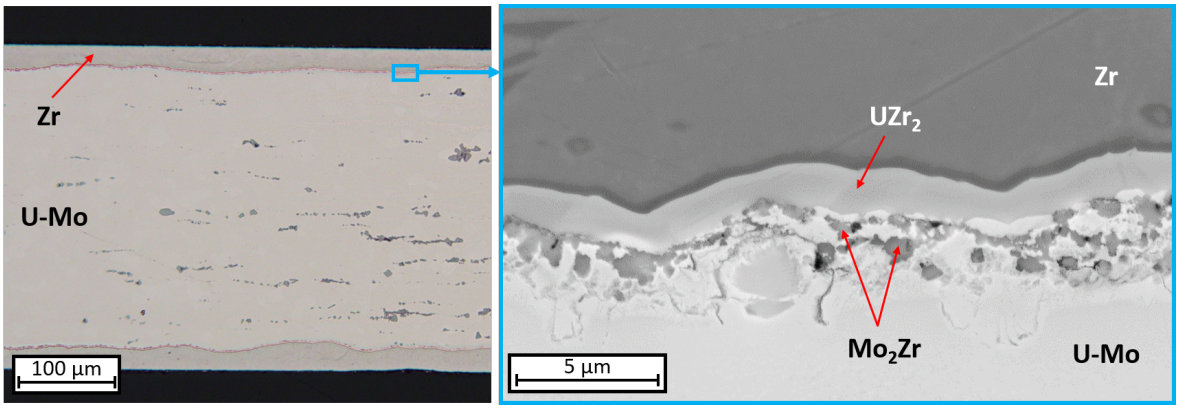

Figure 4.36: Optical micrograph of co-rolled Zr coating on a monolithic U-Mo foil before irradiation (left). SEM BSE micrograph of the U-Mo/Zr interface (right) shows a pronounced interaction zone.

Figure 4.37 displays the U-Mo/Zr interface, which has not significantly changed when compared to the as-fabricated plate. Fission gas bubbles have almost exclusively formed along the grain boundaries inside the layer of α-U. The grain sizes of about 1 µm and less are an indication that recrystallization has occurred. The Mo_2Zr precipitates in the α-U layer are believed to turn amorphous and therefore appear more diffuse when compared to an unirradiated plate. The layer of UZr_2, on the other hand, shows no detrimental behavior under irradiation. It retains its crystal form and displays only a small amount of fission gas bubbles. All this is consistent with observations that have been reported for previous irradiations of monolithic U-Mo plates in this fission density range [51, 110]. Again, a chemical composition analysis by EDS could not be performed because of the high radiation background.

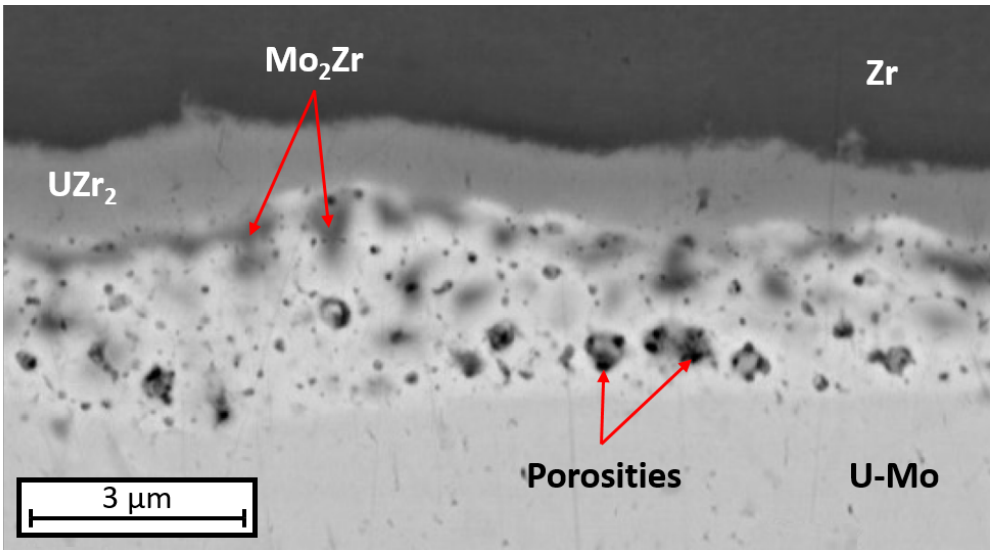

Figure 4.37: SEM BSE micrograph of the interaction zone at the U-Mo/Zr interface after irradiation.

The Zr/Al interface is similar to the one observed at the PVD coated plate (see Figure 4.34) except that the supposed ZrO_2 layer is just about 100 nm thick and displays no cracks. Apart from this, no interaction zone can be observed. This significantly differs from plates with cladding applied by HIP, where a $(Al,Si)_3Zr$ layer of a few µm is observed before and after irradiation [110]. However, these plates used the Al alloy AA6061 (containing Mg and Si in the order of about 1 %) as the cladding material, while the EMPIrE plates consist of AlFeNi cladding with a thin interlayer of pure Al, which is in contact with the Zr. A comparison of the described behavior is shown in Figure 4.38.

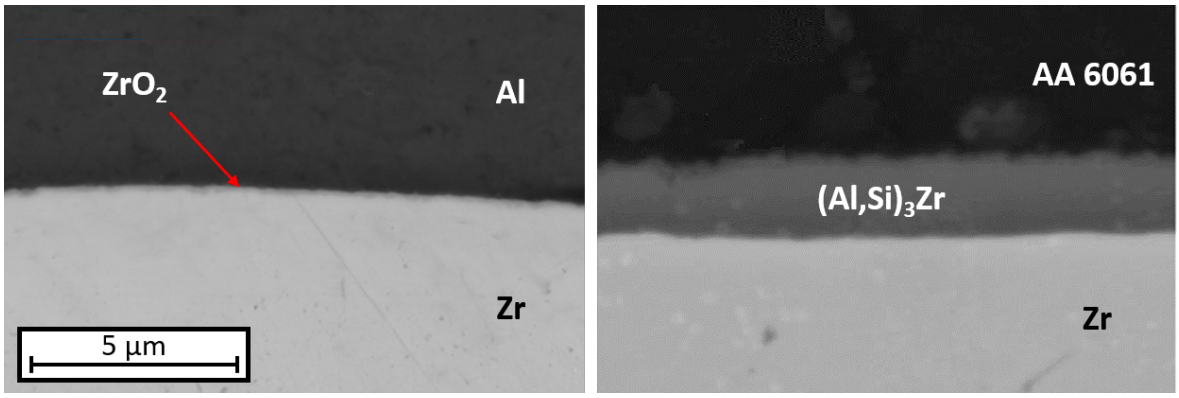

Figure 4.38: SEM BSE micrographs of the Zr/cladding interface of co-rolled fuel plates after irradiation. The EMPIrE plate (left) only shows a thin ZrO_2 layer, while plates with AA6061 cladding applied by HIP (right) form a more pronounced interaction zone. Right image based on [110].

4.2.5 Discussion

The EMPIrE irradiation experiment, together with the various test plates that were produced beforehand in preparation for the actual irradiation, provided valuable data regarding the behavior of mini-size fuel plates consisting of a monolithic U-Mo fuel meat, AlFeNi cladding, and the Zr diffusion barrier applied by PVD.

Destructive examinations on unirradiated plates produced with the same PVD parameters as the final plates for EMPIrE showed an spatially inhomogeneous – but for multiple plates similar – distribution of cracks in the Zr coating after application of the cladding with the C2TWP process. All cracks are basically parallel to the short side of the plate and start to appear 2 mm in distance from the foil's edge with about one crack every 100 µm. Over the following 25 mm towards the middle of the foil, the frequency of the cracks slowly decreases until they disappear again. Simultaneously, their morphology changes from straight wide cracks to narrower sheared ones. This has to be related to the type and distribution of mechanical stresses applied by the cladding process. However, the cracks displayed no detrimental influence on the fuel plate up to the tested fission density of $3.5 \cdot 10^{21}$ fissions/cm^3.

Post-irradiation examinations of the EMPIrE plates showed stable and predictable swelling behavior comparable to previous irradiation experiments of similar monolithic fuel plates. This includes the structure of the fuel meat that shows first signs of recrystallization and accumulation of fission gas bubbles around the grain boundaries. Furthermore, corrosion of the AlFeNi cladding is observed to be at an extent comparable to previous irradiation tests.

Except for some fuel creep, the end gaps display no observable change after irradiation. However, they do raise concern as they might serve as possible origins of plate failures when more and more fission gases accumulate in the voids at higher fission densities.

The diffusion barrier served its purpose for the most part. Only a few spots are observed where intermixture of Al and U-Mo has occurred, which resulted in the formation of a few fission gas bubbles larger than the ones commonly found around grain boundaries. The composition of this intermixing zone is to be determined and excluded that it has a disadvantageous influence. At the interface to the fuel, the Zr showed very little interaction, just a thin layer $< 100\,\text{nm}$ is visible. Inside the Zr, however, a layer of pores formed that indicates the accumulation of fission gas. These pores seem to be homogeneously distributed throughout the plate, with variations in density only on a small scale. Single stretches of a few $10\,\mu\text{m}$ can be devoid of pores, while other regions display bigger pores that start to interlink. At the given fission density this behavior has no negative impact on the fuel performance. Diffusion between Zr and AlFeNi cladding was not observed, which is possibly suppressed by a thin layer of α-ZrO_2 that was already present before irradiation.

Comparisons with Zr coatings applied by co-rolling show diffusion behavior especially at the U-Mo/Zr interface. The co-rolled plates display a much more pronounced interaction zone that includes multiple phases like UZr_2 and Mo_2Zr. However, this interaction zone barely changes under irradiation up to the investigated fission densities. At the Zr/cladding interface, the C2TWP process in combination with an Al interlayer seems to be more gentle compared to the application of AA6061 cladding by HIP.

These results will serve as a starting point for further improvements of the PVD process. Especially regarding the ductility of the Zr coating. Although the cracks in the diffusion barrier layer showed no significant negative effects on fuel performance in the EMPIrE test, the risk has to be minimized that this becomes a problem in full-size irradiations at higher fission density.

TEM lamellae of various regions across the fuel plate have been prepared and shipped to SCK CEN and CEA for investigation with transmission electron microscopy. This is supposed to achieve a higher resolution of intermixing areas and a determination of their composition to identify possible adverse phases.

4.3 Fabrication Studies for FUTURE-MONO-1

Similar to the plate production for the mini-size irradiation test EMPIrE [132], the process of finding suitable production parameters for the corresponding full-size test FUTURE-MONO-1 cycles through multiple stages. Basic parametrization of the full-size sputtering device (see Chapter 3.1.2) has been performed first, followed by characterization of the produced coatings [28, 103]. Subsequently, coated half-size stainless steel foils have been used in combination with the C2TWP process to fabricate plates for characterization [8, 143]. Now, the next step was to process foils of depleted U-Mo instead of stainless steel substrates to investigate the interaction of fuel and coating. The following describes the production and findings of three batches of plates produced to study the influence of biasing voltage, Zr purity, coating thickness, and foil quality.

4.3.1 Batch 1 – Biasing Voltage

Plate Production

The first set of four half-size plates was based on the previous tests with stainless steel substrates, which exhibited good coating properties with almost no cracking when using biasing voltages of 100 V. However, two plates were decided to be coated without biasing voltage as a comparison. The half-size geometry ($\approx 380\,\text{mm} \times 45\,\text{mm}$) was chosen to economize the scarce supply of full-size foils. Accordingly, two full size foils procured from BWXT were cut and trimmed as described in Chapter 3.2, where also the subsequent steps of drilling and chemical cleaning are explained. For the coating process, the second-generation substrate holder (see Chapter 3.1.3) of the full-size device was used, which features the foil tensioning mechanism to prevent bending. Further conditions of the PVD device and process parameters regarding the plasma cleaning and coating step are listed in Table 4.3.

Table 4.3: PVD process parameters for batch 1.

Process parameter		Operation point
Device conditions	Sputtering target	Industrial-grade Zr 702
	Magnetron configuration	SRM80 (balanced)
	Substrate holder	Generation 2
	Target-substrate distance	30 mm
Plasma cleaning	Process pressure	$6 \cdot 10^{-2}$ mbar
	Process time	300 s
	Substrate voltage	800 V
Coating	Process pressure	$6 \cdot 10^{-3}$ mbar
	Sputtering power	5000 W
	Biasing voltage	0 V / 100 V
	Targeted coating thickness	8 µm

The coated foils, of which one is exemplarily depicted in Figure 4.39, were transferred out of the glovebox and cut with the workshop guillotine to a length of 350 mm. After that, one of the foils showed a slight delamination of coating in one corner the size of a few millimeters. This resulted from a less effective plasma cleaning step at the end of the foil, where the grounded parts of the substrate holder disturb the uniform particle bombardment. After packaging, the foils were shipped to Framatome, where they underwent the C2TWP process to produce the finished fuel plates.

Figure 4.39: Coated half-size U-Mo foil before removal of the drilled and uncoated end pieces.

Plate Characterization

UT scans performed at Framatome, as seen in Figure 4.40, confirm the good overall quality of the plates. The stripe at the right side of each foil is an artifact of the cladding process that does not affect the quality of a plate. Only one plate shows a small defect at the top left corner, which could be traced back to the observed delamination of the Zr coating mentioned above.

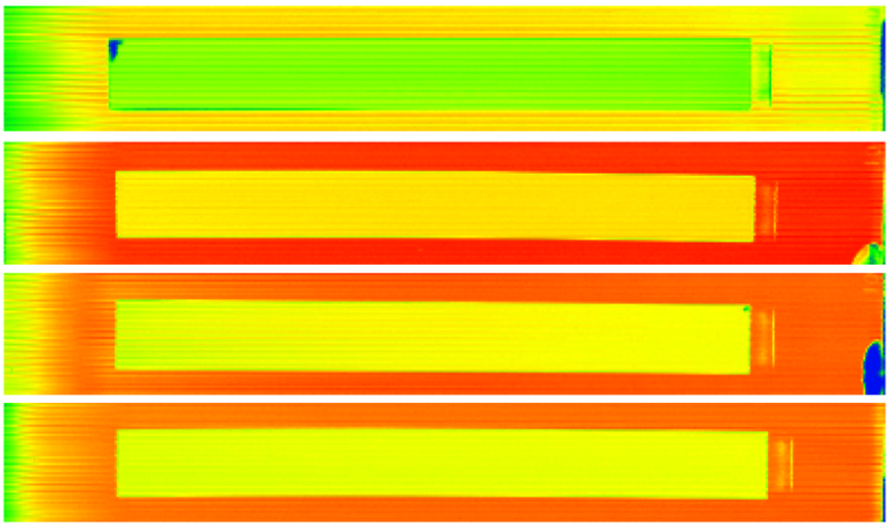

Figure 4.40: UT scans of the first batch of half-size plates with Zr coating. The first plate has a slightly shifted color coding and shows a small defect in the top left corner.

Three of the foils were shipped back to TUM and prepared for destructive examination as described in Chapter 3.3. Figure 4.41 shows a scheme that illustrates the basic idea of which kind of sample sections were chosen for investigation. The focus is clearly on the areas close to the U-Mo foil edges where usually the most interesting features – including the end gaps – appear. Furthermore, it is important to know how the coating behaves in longitudinal and

transversal directions as the cladding process creates different mechanical stress in those directions. To account for this, 5 of the cross sections are orientated in a way that shows the longitudinal direction and 4 show the transversal direction.

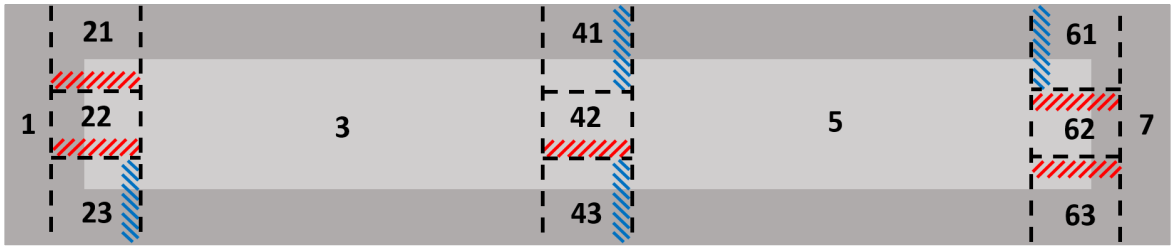

Figure 4.41: Sectioning scheme for the half-size plates with the U-Mo foil inside in light grey. The dashed line indicates the sections that are to be investigated. The corresponding cross sections are marked in red (longitudinal) and blue (transversal).

The end gaps are not discussed here in detail as the main focus is on improving the coating process, while the end gaps are a result of the cladding application. In general, it can be said that the end gaps (see Figure 4.42) showed the same structure and distribution around the foil edges as already known from the EMPIrE plates and preliminary tests with half-size stainless steel substrates [8].

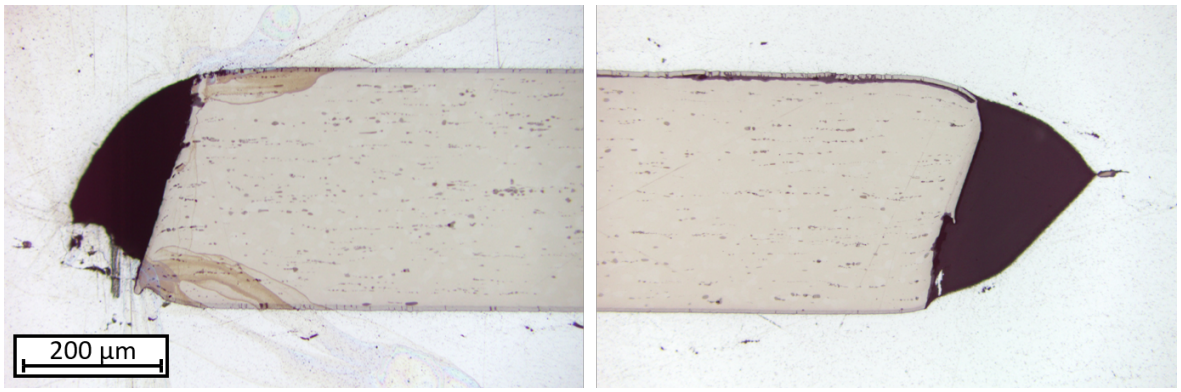

Figure 4.42: Exemplary cross sections of longitudinal end gaps.

The most remarkable observation in the cross sections at the optical microscope was dark structures of what seemed to be oxide on uranium surfaces. Figure 4.43 shows a selection of different forms of this phenomenon. It can appear as a layer of constant thickness under an intact coating, as a more irregular layer with many cracks in the coating, or as "bubbles" that bulge the coating. An EDS line scan (see Figure 4.44) on such a bubble confirmed that it contains mostly uranium oxides.

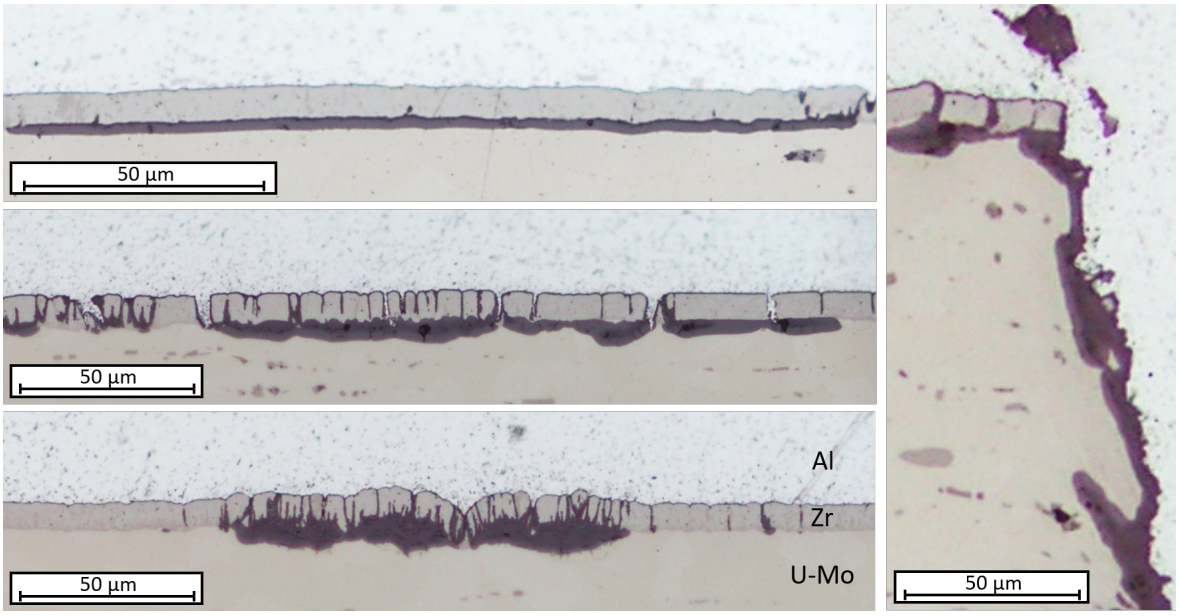

Figure 4.43: Examples of U-Mo oxidation of the first fuel plate batch showing different oxide structures between fuel and coating (left) and on the uncoated foil's end (right).

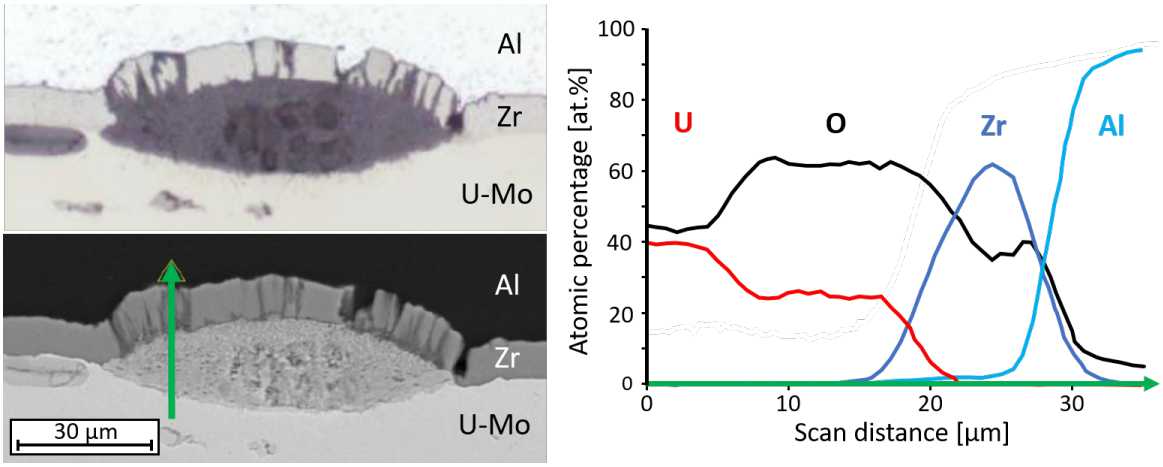

Figure 4.44: Optical (top left) and SEM (bottom left) micrograph of a coating defect. The EDS line scan along the green arrow confirms that the bubble is uranium oxide.

In contrast to the characterization of previous plates, no significant difference between longitudinal and transversal cross sections was observed. Regarding the different PVD parameters of the plates, it was concluded that the coatings produced with 100 V biasing performed better as fewer spots of oxidation, which were also less severe on average, were observed. Furthermore, the unbiased foil showed significantly more cracks in the coating. Representative sections of plates with the different parameters are compared in Figure 4.45 to illustrate the different behavior. However, at this point, it is not certain yet that the coating parameters caused this difference. In any case, a higher carbide content in the unbiased sample was conspicuous, which may also be a cause for the observed behavior.

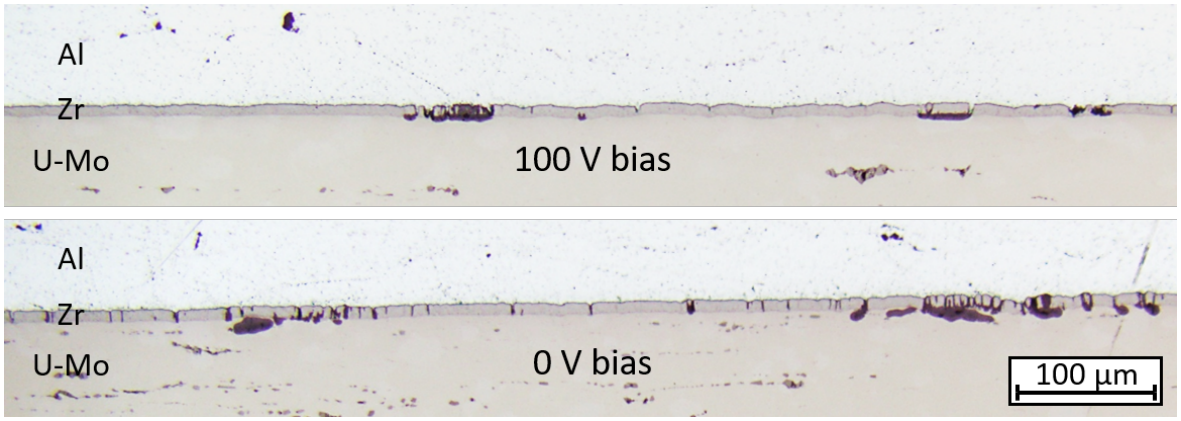

Figure 4.45: Comparison of the coating produced with different biasing parameters.

For investigation of the unbiased coating surface, the cladding of a sample piece from about the center of the plate is dissolved in sodium hydroxide solution. This process caused the Zr coating to peel off at one side, which may be due to the thermal stresses from the generated reaction heat and aided by the oxidized U-Mo surface. Figure 4.46 shows both sides of the remaining sample piece together with optical micrographs of the corresponding surfaces.

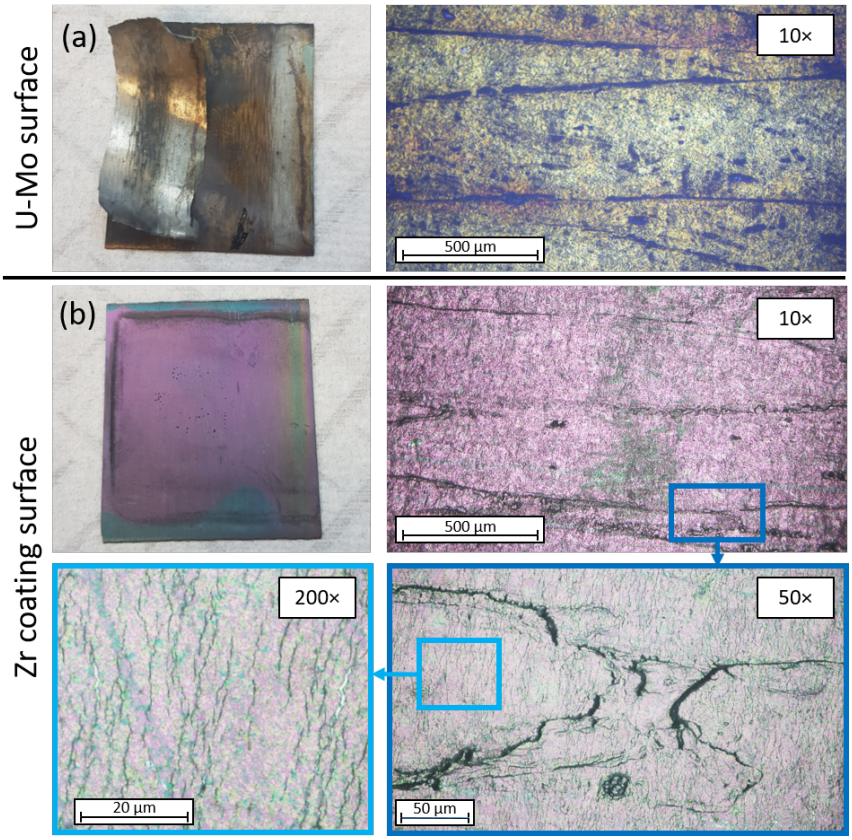

Figure 4.46: Sample piece with removed cladding. The side with detached Zr coating shows the U-Mo surface (a) and the side with adhering coating the Zr surface (b) with cracks.

The surface texture of the U-Mo with long grooves looked the same as before the coating. Black spots may be due to the oxidation observed in the cross sections. However, any conclusions regarding the oxidation have to be viewed with caution as the dissolution process of the cladding probably altered or removed structures. The coating surface still shows the grooves in the underlying U-Mo as the coating is not thick enough to cover them completely. Surface irregularities like this are a possible source of defects that cause oxidation. Higher magnification reveals the structure of the cracks in the coating. They are very fine and in general orientated longitudinally but slightly wavy, which is why they also appear in longitudinal cross sections.

The large-scale occurrence of oxides remains unexplained at this point. Except for oxidation of uncoated U-Mo at end gaps, this behavior has not been observed before in any of the mini-size plates that were produced in the course of the EMPIrE experiment [23, 132], which raises the question of its origin. Possible sources are:

- The U-Mo foils

The procured full-size foils may have a different quality compared to previous mini-size tests. This can include a higher content of oxygen-rich impurities that redistribute at the interface through enhanced thermal diffusion during certain process steps [70]. Also, surface-near carbides may directly cause the oxide bubbles, this however has not been observed before in other coated foils that also included carbides. Furthermore, a different surface texture after the chemical cleaning can be an issue as it may promote the formation of cracks through which oxygen can penetrate.

- The coating process

The full-size PVD device is conceptually different compared to the previously used mini-size device and was operated for the first time with U-Mo foils. The significantly larger vacuum chamber is more difficult to evacuate, so the achieved base pressure before coating (about 10^{-6} mbar) is about an order of magnitude worse. However, other unknown factors of the device can also influence the observed behavior.

- The cladding process

Framatome stated that the C2TWP process is indeed not performed in an inert gas atmosphere, which makes it possible that this is the source of the oxygen that oxidizes the uranium by penetrating the cracks. However, as stated above, no such extent of oxidation has been observed in previous cladding tests with U-Mo foils and, except for the size of the foils, the C2TWP process has not been altered since then.

It is also possible that the oxidation is caused by a combination of the above-mentioned sources. In order to resolve this issue, a deeper analysis of the material and processes was necessary. As a first measure, the end pieces of the foils, which were cut off before the cladding process, were examined. Figure 4.47 depicts such a pair of foil ends together with corresponding micrographs of the surface and of cross sections. The uneven surface of the U-Mo seems to promote that the coating does not properly cover the complete surface as gaps are observed that cannot be caused by mechanical stress yet. Brittle surface-near carbides were also found and may contribute to this. Furthermore, cracks that reach into the U-Mo foil serve as potential channels for oxygen penetrating the coating. However, the examined sample pieces in the given state of the fabrication process exhibited no signs of oxidation. This eliminates the coating process as the direct primary source of the oxidation.

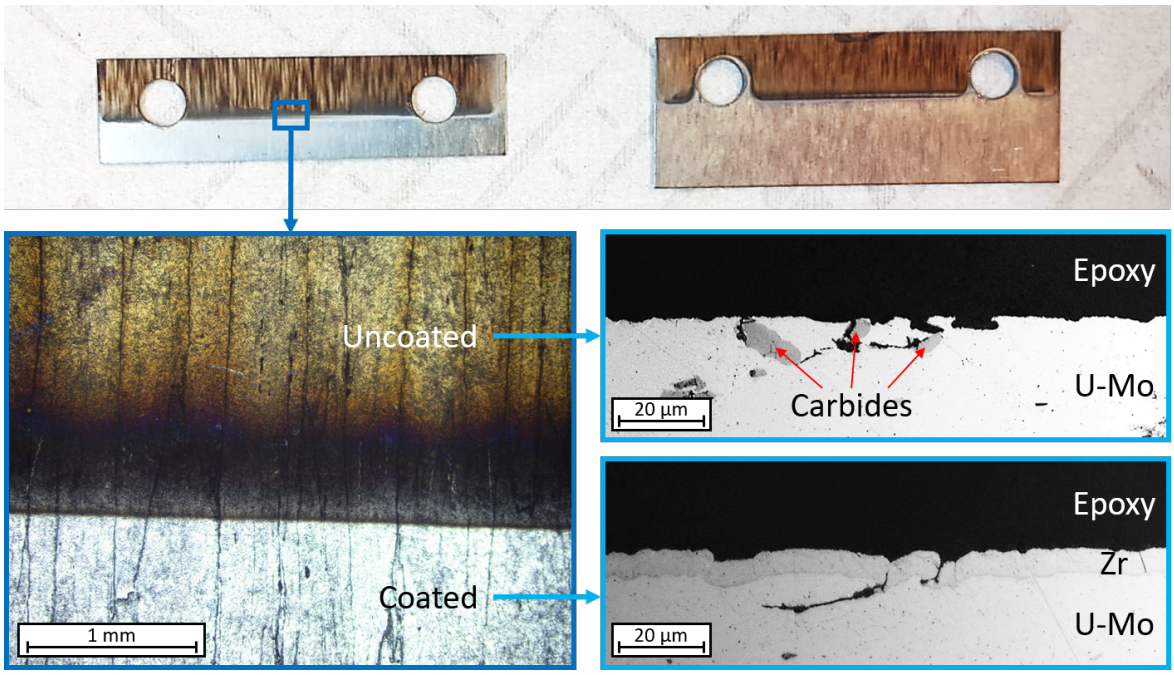

Figure 4.47: Foil end pieces remaining after coating and cutting (top) with optical micrographs of the surface (left) and of cross sections from uncoated and coated areas (right).

A follow-up experiment was set up using U-Mo foils pieces with the same origin as the full-size foils. These were coated with Zr the same way as before. Artificial cracks were introduced by bending and then the foils were put into a furnace at 480 °C for one hour. At the same time, the vacuum was deliberately poorly maintained at about 10^{-2} mbar to provide for a small source of oxygen. These parameters served as a best guess as the ones of the cladding process are proprietary to Framatome. Cross sections of the samples (see Figure 4.48) showed that this procedure was able to at least rudimentary reproduce the observed oxidation features.

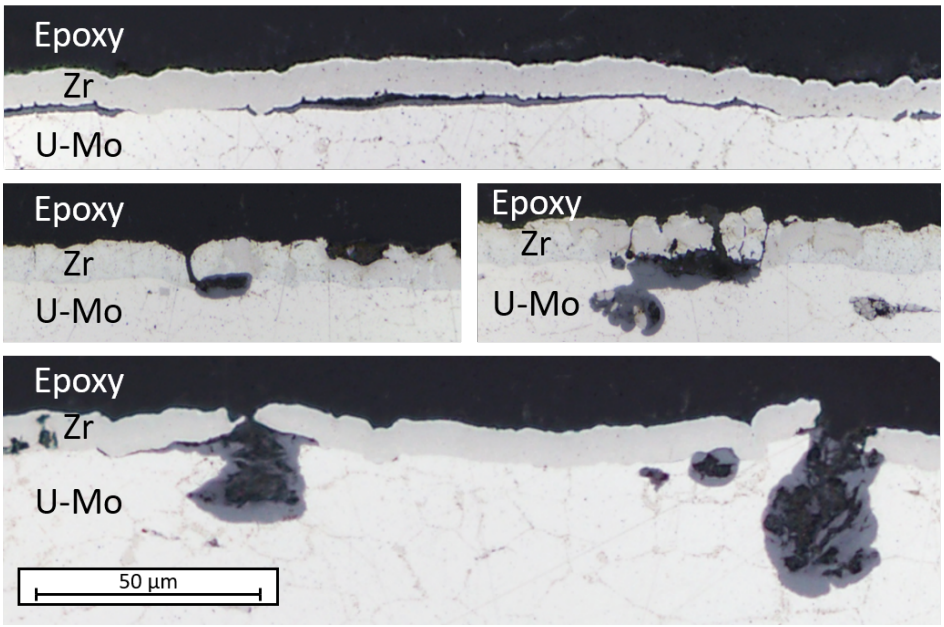

Figure 4.48: Foil end pieces remaining after coating and cutting (top) with optical micrographs of the surface (left) and of cross sections from uncoated and coated areas (right).

4.3.2 Batch 2 – Reactor-grade Zr

Plate Production

Before the production of the second sample set, the target was changed to one made out of reactor-grade Zr, which has significantly fewer impurities than the one made out of Zr 702 (see Tables 3.1 and 3.2 in Chapter 3.1.2). Based on preliminary tests at the mini-size device with Zr targets of different purities, it is expected that this increases the ductility of the Zr coating and therefore reduces the cracks [121, 122]. As a result, oxidation may be reduced, in case the oxide is introduced from outside by the cladding process. In the course of the target replacement, the magnet bar is also exchanged for the one with the unbalanced magnetic field configuration, which is supposed to deliver a higher particle bombardment to improve the coating properties. A side effect of the altered magnetic field is that the plasma ignition characteristics are slightly different, which was used to tone down the plasma cleaning step by using a lower process pressure of $4 \cdot 10^{-2}$ mbar. This reduces the contamination of the vacuum chamber with sputtered uranium.

Apart from the changes mentioned above, the procedure was the same as for the first batch using two full-size foils from BWXT again to get four half-size foils. The PVD device conditions and coating parameters are summarized in Table 4.4.

Table 4.4: PVD process parameters for batch 2 with the changes to the previous batch marked in red.

Process parameter		Operation point
Device conditions	Sputtering target	Reactor-grade Zr
	Magnetron configuration	uTRM80 (unbalanced)
	Substrate holder	Generation 2
	Target-substrate distance	30 mm
Plasma cleaning	Process pressure	$4 \cdot 10^{-2}$ mbar
	Process time	300 s
	Substrate voltage	800 V
Coating	Process pressure	$6 \cdot 10^{-3}$ mbar
	Sputtering power	5000 W
	Biasing voltage	0 V /100 V
	Targeted coating thickness	8 µm

An irregularity occurred during the plasma cleaning step before the coating of the first side of one foil. The clamping block of the substrate holder (see Chapter 3.1.3) got stuck on the guiding rods, which resulted in down-bending of the foil that expanded with the rising temperature and ultimately caused a short circuit as the energized foil came too close to the grounded shielding plates. The discharge created a visible spot on the surface of the U-Mo foil. To mitigate the influence of the altered surface, it was decided to double the process time of the plasma cleaning step for this side of the foil. However, this strategy turned out to be insufficient, as the coating adhesion on this spot was clearly affected as seen in Figure 4.49.

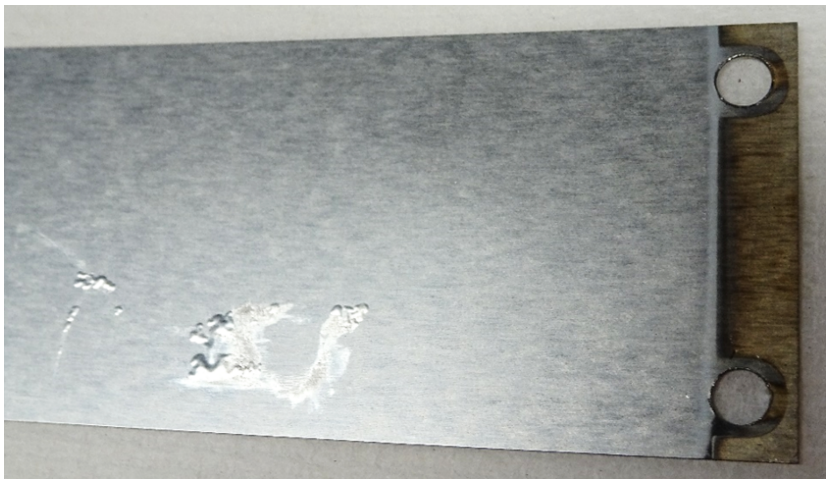

Figure 4.49: Coating defect caused by a short circuit during plasma cleaning.

Apart from this, no defects were visible on the foils. As with the first batch, they were transferred out of the glovebox and cut with the workshop guillotine to a length of 350 mm. After packaging, the foils were shipped to Framatome, where they underwent the C2TWP process to produce the finished fuel plates.

Plate Characterization

UT scans performed at Framatome, as seen in Figure 4.50, confirm the good overall quality of the plates. The stripe at the right side of two of the foils is an artifact of the cladding process that does not affect the quality of a plate. One plate shows a defective spot, which is related to the previously described coating error.

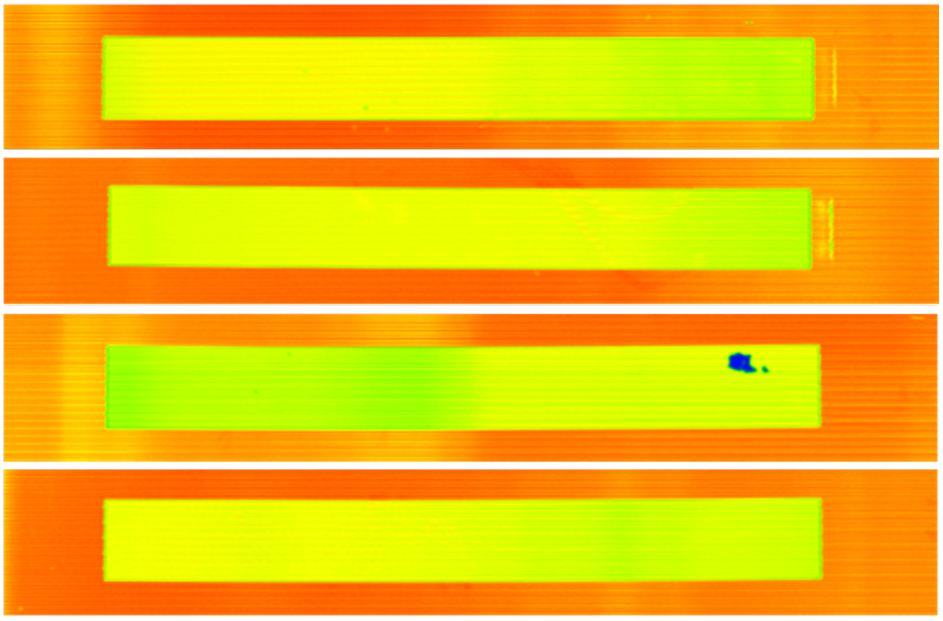

Figure 4.50: UT scans of the second batch of half-size plates with Zr coating. The third plate shows a defect, which is related to a coating failure.

For destructive examinations, the same sectioning scheme as for the first batch was used (see Figure 4.41). However, this time the sectioning was performed by laser cutting at Framatome. The sample pieces were then shipped to TUM, where the final metallographic preparation was executed as before.

Investigation of the cross sections showed that oxides are still present but rarer than in the first batch of plates. There are stretches of several millimeters where no defects are visible at all. However, oxidation spots that caused the debonding of the coating are seemingly more common. Cracks, on the other hand, are almost eliminated; even at oxidation spots, they are rarely found. Figure 4.51 shows some representative spots of the described behavior. Regarding the coating parameters, the biased coating exhibits a slightly better resilience. The greater impact, however, has the higher purity of the Zr when compared to the previous plate batch.

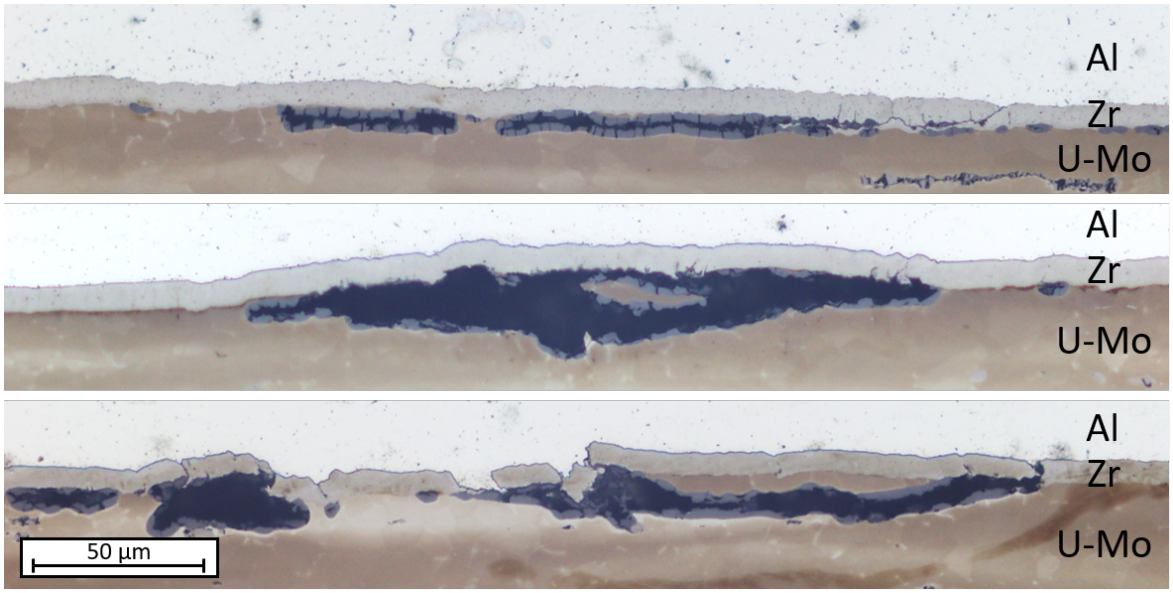

Figure 4.51: Examples of U-Mo oxidation of the second fuel plate batch showing brittle oxide structures that cause delamination of the coating (top and middle) without cracking. The example at the bottom shows oxidation inside the U-Mo.

Again, follow-up tests were carried out on the foil ends that were cut off after coating. Cross sections, as exemplarily depicted in Figure 4.52, confirm the general observation from the first batch that, despite the occurrence of defects in the fuel as well as in the coating, no resulting oxidation can be found. Coating defects seem to be related to uneven surface texture.

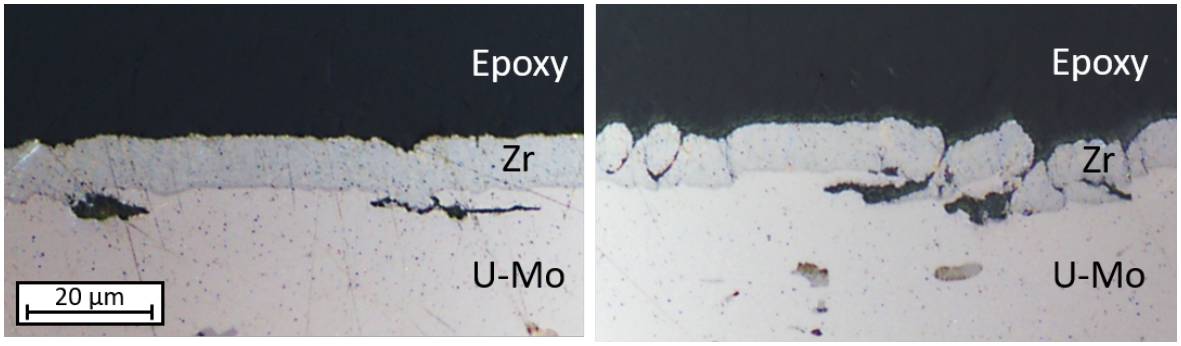

Figure 4.52: Cross section of the uncladded end pieces of the second sample batch showing defects inside the U-Mo (left) as well as coating defects (right) without oxidation.

4.3.3 Batch 3 – Coating Thickness & Foil Quality

Plate Production

Based on the findings of the first two sample sets, the conditions of the third batch were adjusted with the purpose of further investigating the causes of the oxidation defects. The focus hereby is on the quality of the U-Mo foils and the coating thickness. This was done by choosing two foils from BWXT as before and two foil that were produced at LANL to compare the influence of the surface finish, which is depicted in Figures 4.53 and 4.54.

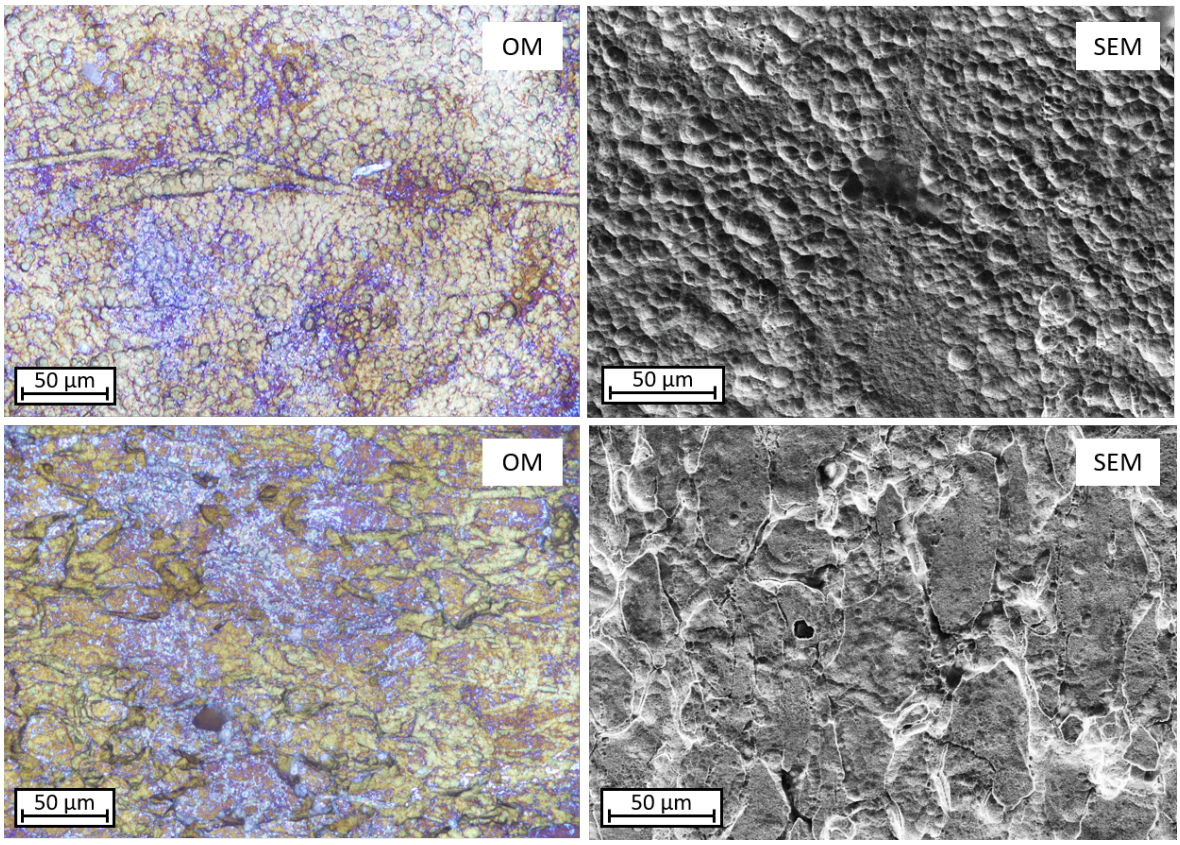

Figure 4.53: Optical (left) and SEM SE (right) micrographs of surface textures of LANL U-Mo foils showing areas of conchoidal craters (top) and areas of scaly plates between distinct valleys (bottom).

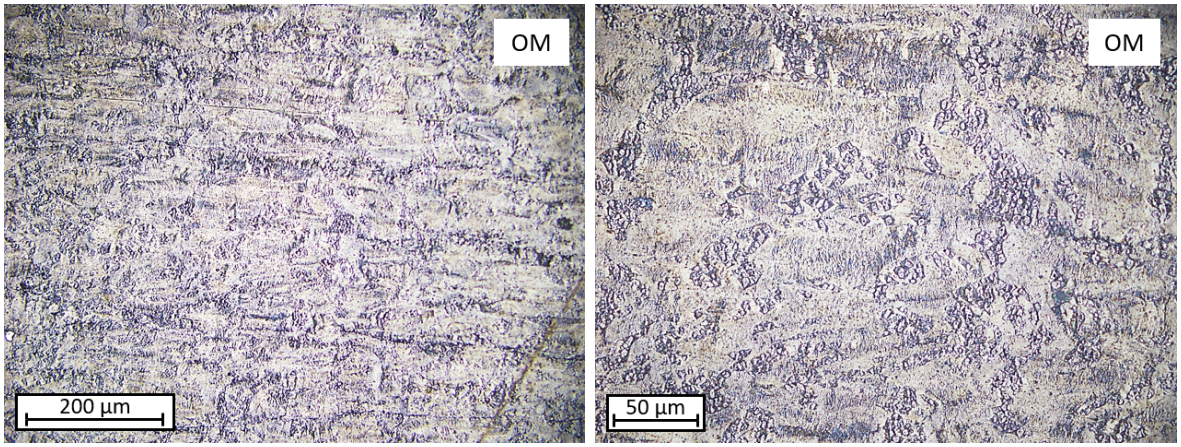

Figure 4.54: Optical micrographs of surface textures of BWXT U-Mo foils.

Figure 4.55 shows a comparison of the foils from different suppliers before and after cleaning. BWXT foils have a higher degree of initial oxidation and are almost black, while the LANL foils are of an orange-brown color. After the chemical cleaning, however, both foils showed the almost same metallic shine of pure U-Mo alloy. Nevertheless, the surface texture is still visibly different. The two foils from each supplier were then coated with Zr of thickness 8 µm and 20 µm respectively to check if this changes the oxidation behavior during the cladding process. For the first time, the full-size geometry of the foils was retained before the coating. Hence, no cutting was performed before drilling and chemical cleaning of the foils.

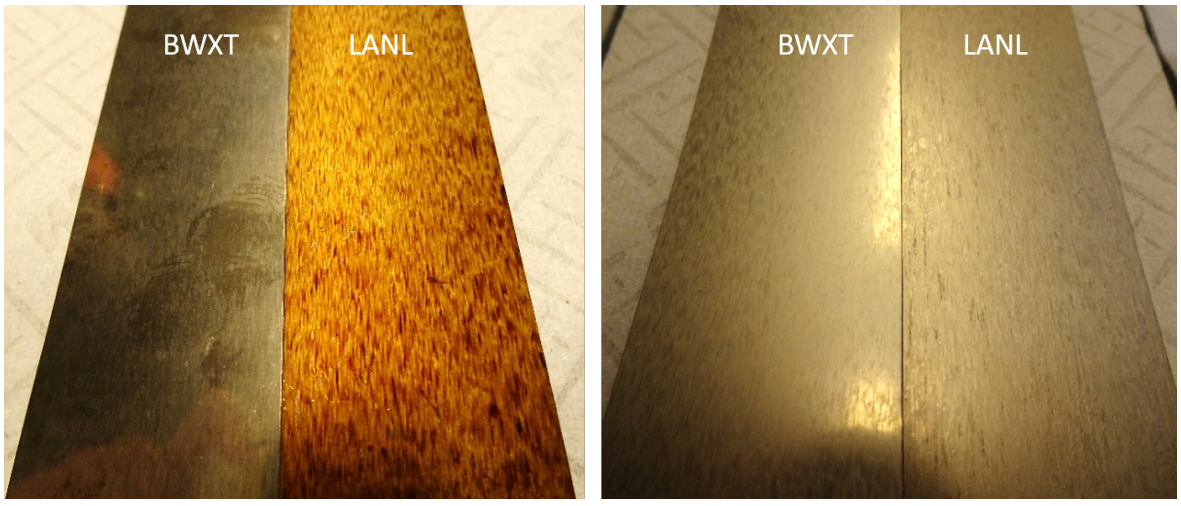

Figure 4.55: Two foils of different quality before (left) and after the chemical cleaning (right).

The third generation of the substrate holder (see Chapter 3.1.3) was ready to use on this batch to avoid the failures that occurred before. However, its installation in the vacuum chamber was accompanied by an increase of the target-to-substrate distance from 30 mm to 40 mm due to geometrical reasons of the final assembly. The PVD device conditions and coating parameters are summarized in Table 4.5.

Table 4.5: PVD process parameters for batch 3 with the changes to the previous batch marked in red.

Process parameter		Operation point
Device conditions	Sputtering target	Reactor-grade Zr
	Magnetron configuration	uTRM80 (unbalanced)
	Substrate holder	Generation 3
	Target-substrate distance	40 mm
Plasma cleaning	Process pressure	$4 \cdot 10^{-2}$ mbar
	Process time	300 s
	Substrate voltage	800 V
Coating	Process pressure	$6 \cdot 10^{-3}$ mbar
	Sputtering power	5000 W
	Biasing voltage	100 V
	Targeted coating thickness	8 µm / 20 µm

One of the LANL foils showed a surface defect where a U-Mo flake is about to peel off. It was decided not to remove this defect and to coat on top of it as depicted in Figure 4.56. This way, its influence on the finished plate can be investigated.

Figure 4.56: Surface defect on a coated LANL foil, where a flake of U-Mo is about to peel off.

The foils were directly packaged inside the glovebox after the coating and shipped to Framatome, where this time the final cropping of the uncoated end pieces was performed with the laser cutting equipment. Subsequently, the foils underwent the cladding process to produce the final full-size plates.

To obtain some insight regarding the condition of the foils between the processes of coating and cladding, slices of about 5 mm have been cut from each foil after the chemical cleaning procedure. These foil pieces were then coated separately with 8 µm of Zr to investigate their resulting surface texture and cross sections. Figure 4.57 shows a comparison of coated

surfaces of a BWXT and LANL foil. While the surface of the BWXT foil is comparatively even with occasional grooves, the LANL foil's surface is much more rugged. This uneven surface that includes holes and steps deeper than 10 µm can cause disrupted coating (as depicted in Figure 4.58) even before any mechanical stress is applied in the cladding process. Ultimately, such coating failures serve as a starting point for external oxidation. A thicker coating layer may be able to avoid some of the defects of this kind.

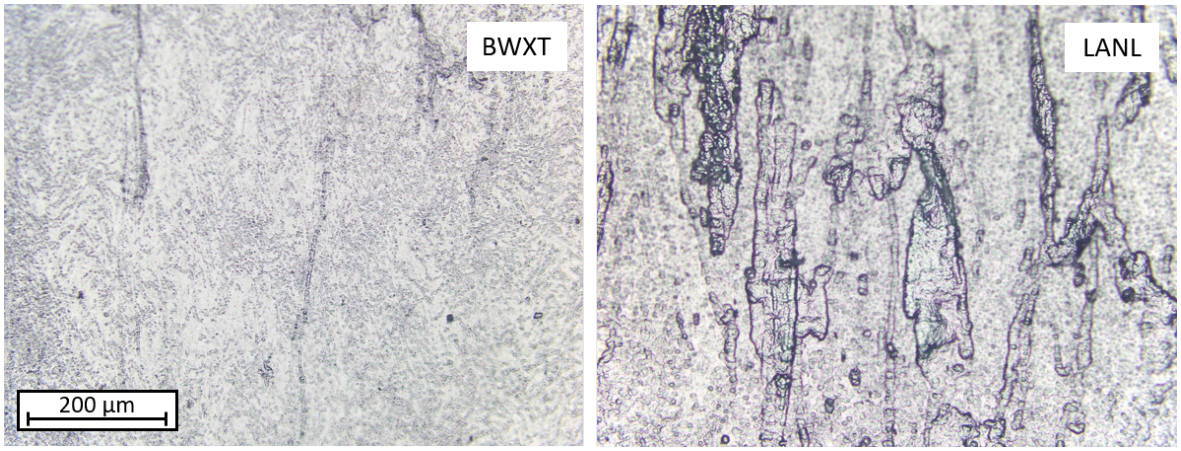

Figure 4.57: Optical micrographs of the foil surfaces after coating. The BWXT foils (left) display a much more even surface than the LANL foils (right).

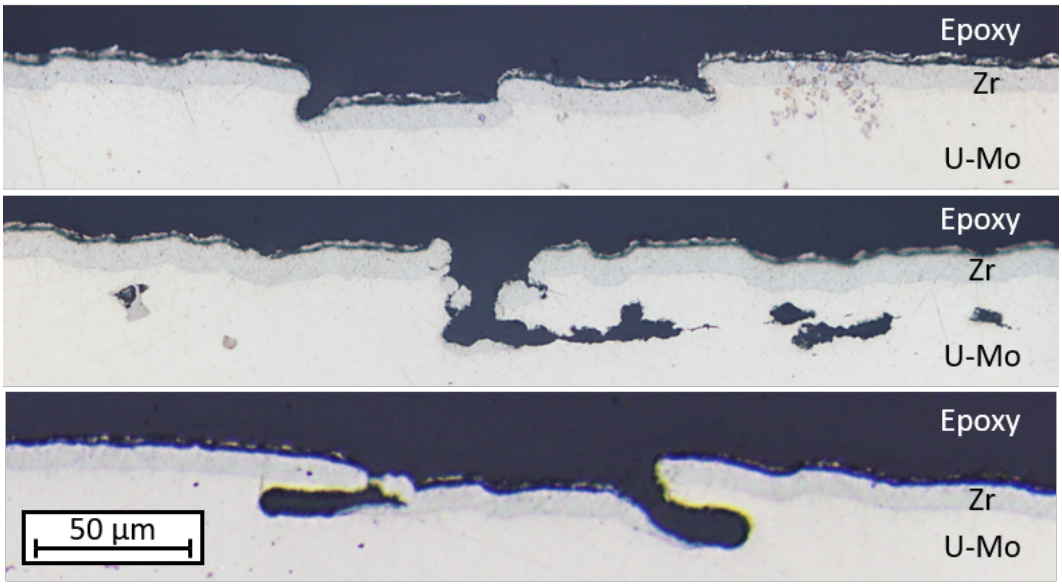

Figure 4.58: Cross sections of LANL foils after coating showing areas of high surface roughness that cause coating defects.

Plate Characterization

UT scans performed at Framatome, as seen in Figure 4.59, confirm the good overall quality of the plates regarding the bonding of U-Mo, coating, and cladding interfaces. Small spots are visible on the plates fabricated with LANL foils, which are ascribed to surface defects as described above (see Figure 4.56). A significant difference between the two foil types is the low transmission around the LANL foils which indicates larger end gaps. However, a finding like this was expected as it turned out that the LANL foils were slightly distorted after that coating. This was caused by the release of mechanical stresses in the foils by the elevated temperatures during the coating process. These distortions then affected the cladding process.

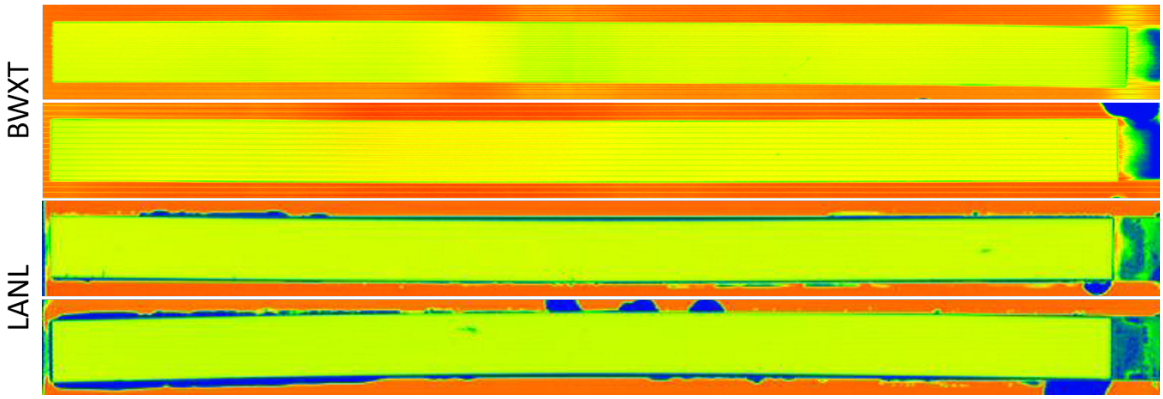

Figure 4.59: UT scans of the full-size plates with Zr coating. The two plates on top are produced with U-Mo foils from BWXT and the ones below with LANL foils. The LANL foils were slightly distorted after the coating, which was an issue for the cladding process and caused bigger end gaps around the foils.

For destructive examinations of the full-size plates, the sectioning scheme was modified, as illustrated in Figure 4.60. Again, the sectioning was performed by laser cutting at Framatome. However, a failure during the handling of the BWXT plate with 20 µm Zr coating prevented further processing. The sample pieces of the other three plates, as exemplarily depicted in Figure 4.61, were then shipped to TUM, where the final metallographic preparation was executed as before.

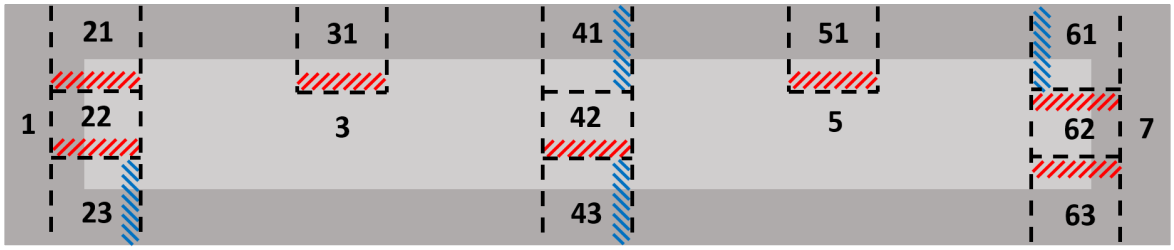

Figure 4.60: Sectioning scheme for the full-size plates (not to scale) with the U-Mo foil inside in light grey. The dashed line indicates the sections that are to be investigated. The corresponding cross sections are marked in red (longitudinal) and blue (transversal).

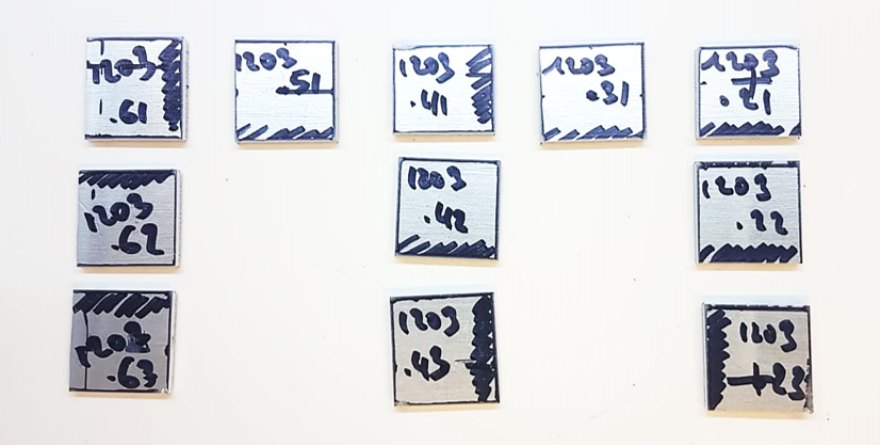

Figure 4.61: Sample pieces of a full-size plate produced by laser cutting.

The short ends of the foil are of special interest in this sample set, as the uncoated end pieces of the U-Mo foils were removed by laser cutting for the first time instead of the mechanical cutting performed before. Figure 4.62 shows an exemplary laser-cut foil's end after application of the cladding. On the side where the laser beam enters the material, it creates a spherical void of about 10 – 20 µm in diameter right after the Zr coating. Furthermore, some intermixing of Zr and U-Mo can be observed at this position. The other side of the foil, where the beam exits, showed an edge burr consisting of U-Mo on top of the coating. On the cutting edge, a mostly homogeneous oxide layer of about 2 µm thickness can be observed.

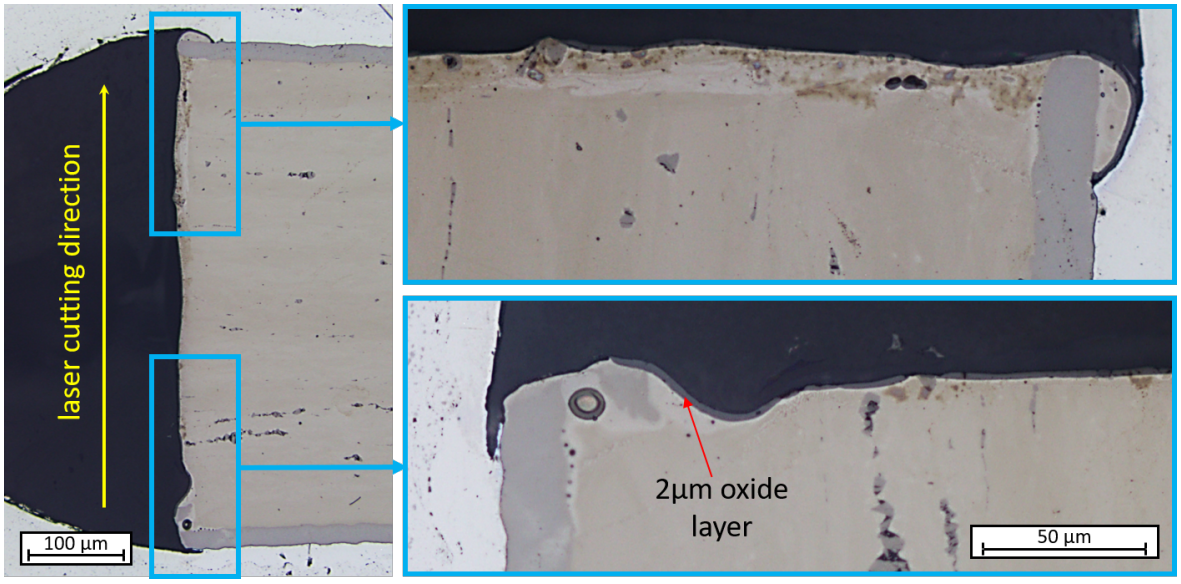

Figure 4.62: Cross section of laser-cut foil's end after cladding.

The degree of intermixing caused by the laser is investigated further with the SEM by generating an EDS map shown in Figure 4.63. It can be observed that some Zr enters the U-Mo fuel but the two materials are still separated for the most part. Only some areas around the spherical void display intermixing. The oxide layer is also clearly visible and some of the oxide seems to accumulate in the void, which may be caused by the laser or during sample preparation.

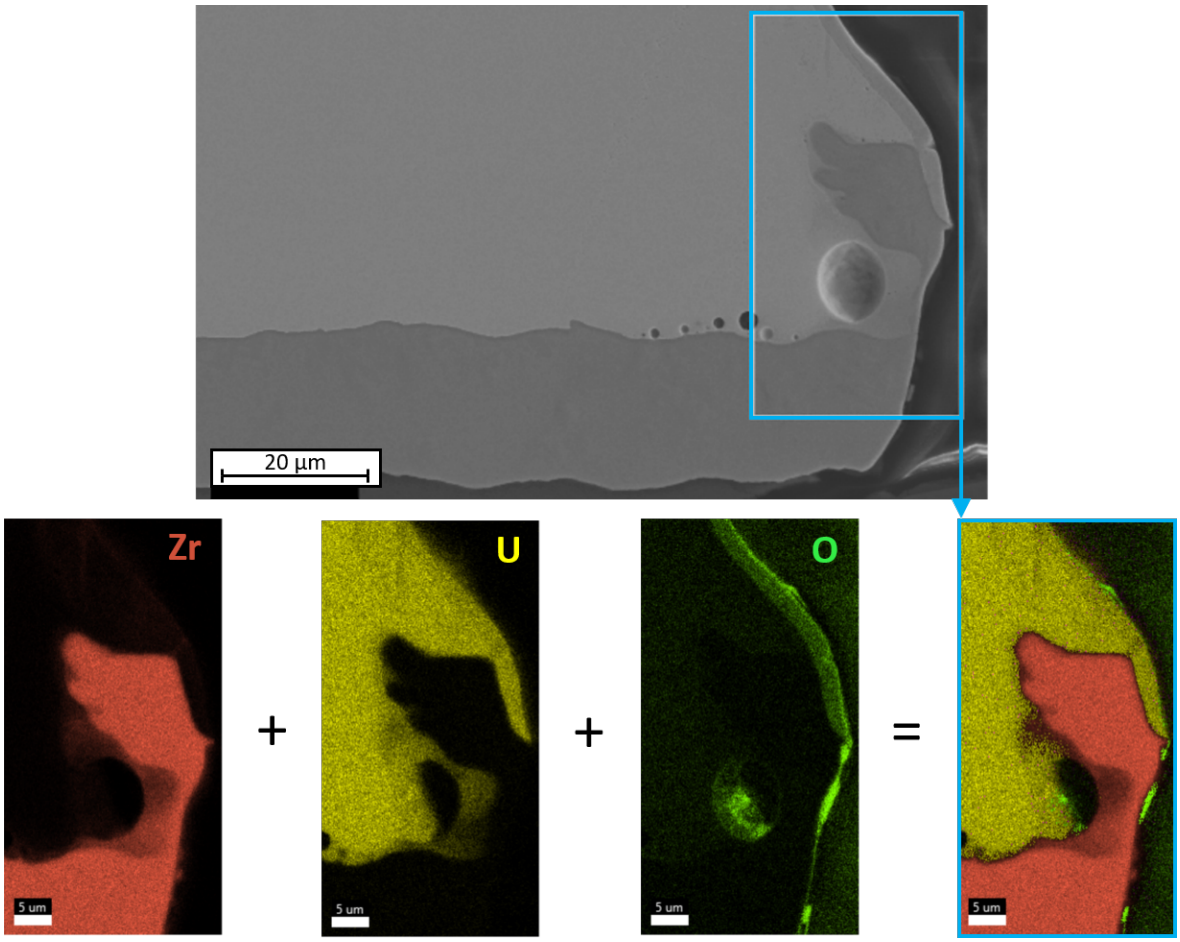

Figure 4.63: SEM micrograph of laser-cut foil's end (top) and corresponding EDS maps of the elements Zr (red), U (yellow) and O (green).

The surface roughness of the LANL foils in the samples after coating (see Figure 4.58) was already observed to be potentially problematic. This conjecture is confirmed in cross sections of the final plates produced with LANL U-Mo foils (see Figure 4.64). The coating defects caused by the surface texture act as starting points for oxidation. However, the oxidation at the defect sites often penetrates the U-Mo in channels parallel to the surface that extend several 100 µm. This indicates a disadvantageous structure in the surface-near region of the U-Mo foil itself, which also manifested in the flaking of the surface observed before (see Figure 4.56). Surface-near carbon stringers may be an explanation for this behavior, however, BWXT foils with similar carbon content rarely show this type of defects. Hence, it

has to be attributed to the final cold-rolling steps of the LANL foil fabrication or potential post-production processes like annealing of the foils.

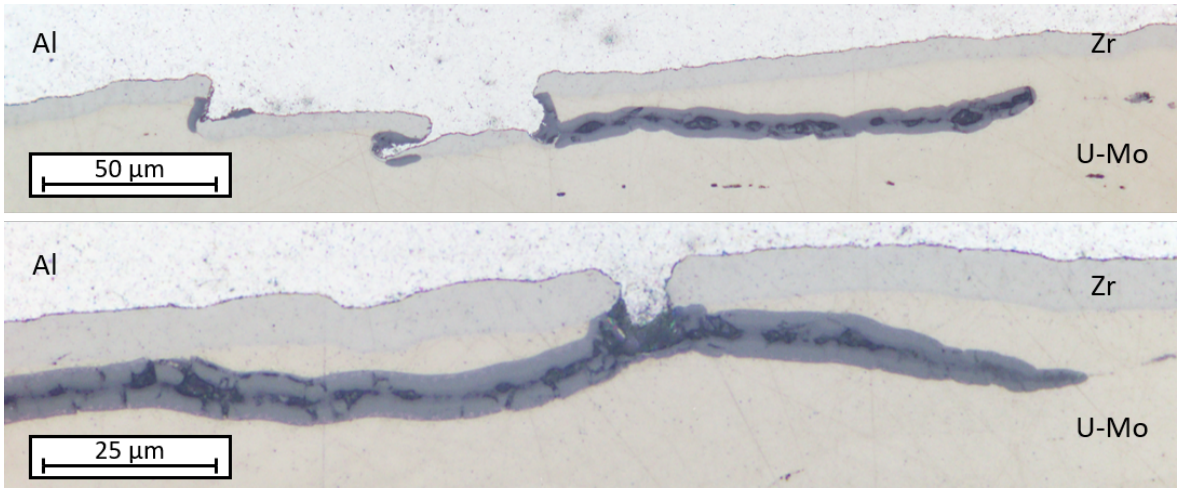

Figure 4.64: Coating defects of LANL foils causing oxide channels into the U-Mo.

Regarding the coating thickness, 20 µm appeared to be slightly more beneficial, which is illustrated by examples in Figure 4.65. The thicker coating better levels rugged surface textures and is less prone to defects, which ultimately causes smaller oxidation spots.

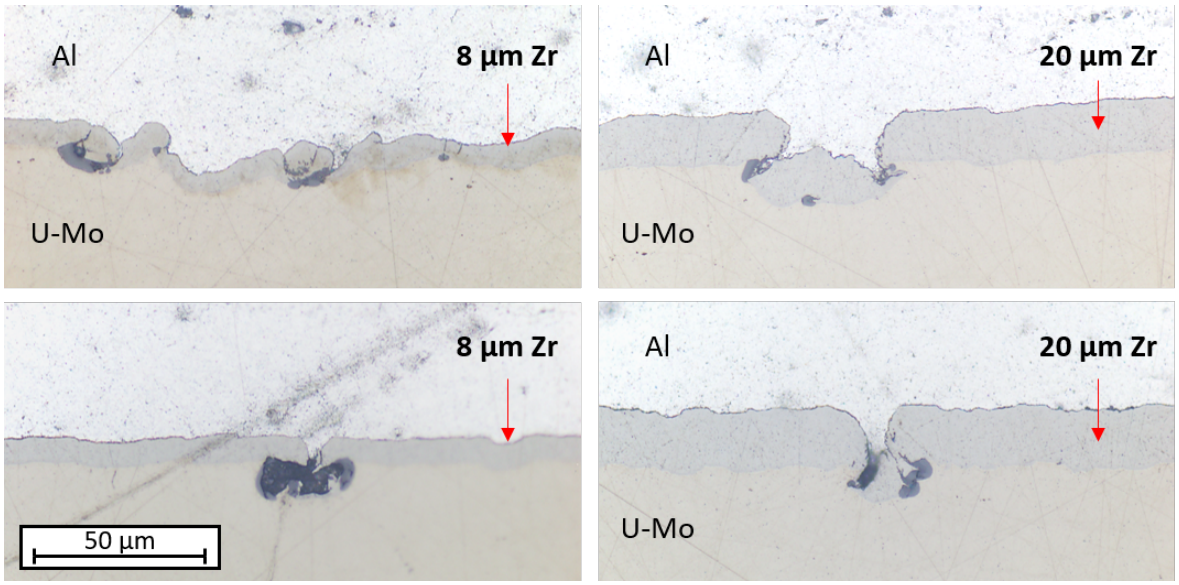

Figure 4.65: Comparison of exemplary oxidation defects in fuel plates with coating thicknesses of 8 µm (left) and 20 µm (right).

4.3.4 Discussion

The produced sample batches show a clear progression in quality. On one hand, this includes the reduction of occasional coating defects introduced during the PVD process, which was accomplished by the improvement of the substrate holder. However, the main improvement was achieved regarding the initial strong oxidation of the U-Mo after the application of coating and cladding, which was steadily reduced by adjustment of the PVD parameters. Here, a combination of substrate biasing at 100 V with a reactor-grade Zr target and an unbalanced magnetic field configuration resulted in a good ductility of the coatings to reduce cracks to a minimum, while a thicker coating was able to better smoothen irregularities on the foil surfaces.

Characterizations of samples after coating showed that the cause of U-Mo oxidation is not related to the PVD process. On the other hand, U-Mo foil quality, especially the surface texture, has a serious impact on the introduction of defects during the cladding process. This issue needs to be tackled. However, U-Mo foils for the FUTURE-MONO-1 irradiation test will be manufactured at Framatome with a new production line that is currently being set up. The surface texture of these foils has then to be investigated and re-evaluated if the current chemical cleaning is the right method for deoxidation. Furthermore, to reduce the oxide content in the finished fuel plates in the long run, Framatome might consider performing critical steps of the C2TWP process in an inert gas atmosphere if technically feasible.

Laser-cutting of the coated foils was shown to introduce some intermixing of Zr coating and fuel meat along the cut. It remains to be investigated how these areas behave under irradiation.

Regarding the coating process, the optimization can be considered as completed at this stage of plate production for irradiation experiments. The successful pilot device can now serve as a basic blueprint for an industrial device. The main optimization for this will be on the time efficiency of the process to increase the throughput of foils. This includes faster coating steps, better handling, but also easier maintenance, which will be necessary for more prolonged continuous operation times.

Chapter 5

Conclusion & Outlook

This final chapter concludes the work performed within this PhD thesis on destructive examinations of the EMPIrE plates, development of full-size plate fabrication, and investigations on the alternative diffusion barrier materials molybdenum and tungsten. Furthermore, an outlook is given on subsequent steps as well as on new opportunities that open up based on the acquired knowledge.

5.1 Conclusion

Alternative Diffusion Barriers

The versatility of the mini-size PVD device at TUM allows it to easily produce coatings of various materials and subsequently test them regarding their ability to act as a diffusion barrier for monolithic U-Mo fuels. In this work, certain aspects of molybdenum and tungsten were investigated concerning their layer properties with regard to different coating parameters and the subsequent compatibility of such coatings with the C2TWP cladding process.

The layer structure of Mo sputtered on stainless steel substrates showed no significantly improved ductility in bending tests with variation of the substrate temperature, although growth of bigger grains was observable towards higher temperatures. Additionally, interaction with the stainless steel formed a brittle IDL at the interface starting at temperatures of 800 °C. The technique of substrate biasing was also not able to inhibit cracking. Accordingly, coated mini-size foils were produced at 600 °C to generate comparatively big grains without formation of an IDL. These foils were cladded with the C2TWP process but displayed complete bonding failure when examined with UT scans. It turns out that oxidation of the Mo coating between the processes of coating and cladding is severe enough to inhibit adequate adhesion of Mo and Al cladding. This issue was successfully solved by applying a protective Al coating onto the Mo layer with the PVD device. However, sputtering parameters turned out to be disadvantageous as the temperature triggered thermal diffusion between Al and Mo that formed a complex IDL of several interaction products. This behavior was in line with other published observations on Al/Mo diffusion couples. The IDL was found to be very brittle, however, the residual Mo coating resisted the mechanical stresses of the cladding process and was discovered to be intact. Concluding from these findings there seems to be no obvious advantage of Mo coating compared to the Zr coating.

Similar investigations were performed on tungsten layers. Though, the severe brittleness of the W quickly became apparent in bending tests as well as in destructive examinations of W-coated foils after cladding application. This resulted in extensive cracking and even complete disintegration of the coating in some spots. A significant improvement by variation of the PVD parameters substrate heating and biasing within the accessible parameter space could not be observed. The structure of the sputtered layers remained in the form of fine columnar grains. If intact, however, the W coating displayed very promising behavior as a diffusion barrier between U-Mo and Al. This was verified with heavy-ion irradiations of U-Mo/W/Al layer systems. It demonstrated that W is able to effectively inhibit interdiffusion already with thin coating thicknesses of 500 nm to 1 µm. While some interdiffusion with the Al was observed, intermixing at the U-Mo interface was hardly detectable. In conclusion, W shows excellent diffusion barrier behavior. However, the promising results from ion irradiation need confirmation by in-pile tests.

EMPIrE

The characterization of the plates irradiated in the EMPIrE test provided first insights on the performance of the monolithic U-Mo fuel with PVD-coated Zr diffusion barrier and cladding application by the C2TWP process. This serves as the starting point for further optimization of the fabrication process. The characterization includes the unirradiated plates that were produced in preparation for the irradiation test, which serve as a comparison to separate the effects that occur in-pile. The most noticeable observation regarding the coating was that it displayed defects in the form of cracks introduced by the cladding process. Destructive examinations showed a pattern of aligned cracks parallel to the short side of the foil. Their inhomogeneous distribution – many wide ones close to the short ends of the foils and fewer but sheared ones towards the middle – is similar for every produced plate and therefore suggests a non-uniform distribution of mechanical force in the cladding process. However, the cracks showed no adverse effect on a large scale for the irradiated plates up to the tested fission density of about $3.5{\cdot}10^{21}$ fissions per cm^3. Fuel-cladding interaction was scarce as the cracks contain considerable voids with no contact of U-Mo and Al. The few observable interaction zones yet display some fission gas bubbles bigger than the ones that commonly appear within the fuel meat. The most distinctive change in the fuel plate after irradiation is a layer of voids inside the Zr coating on the interface of the fuel meat. These porosities are present throughout the fuel plate and almost equally distributed with local variations on the scale of a few 10 µm. Other regions of the fuel plates showed expected behavior based on previous irradiation tests. In the fuel meat, fission gas bubbles accumulated around the grain boundaries to a degree common for the given burnup. Corrosion of the AlFeNi cladding also showed the usual extent, while observed oxidation of the Zr coating on the interface to the cladding was already present before irradiation and did not change in-pile.

Fabrication Studies for FUTURE-MONO-1

The fabrication process for monolithic U-Mo fuel plates with Zr diffusion barrier was successfully scaled up to full-size dimensions in preparation for the planned FUTURE-MONO-1 irradiation test. Correspondingly, the processes of bare foil preparation, Zr coating, and cladding were adapted for the larger geometry. First fabrication tests and subsequent characterizations, however, showed large-scale cracking of the 8 µm Zr coating and oxidation of the U-Mo below, which was slightly less severe if the coatings were produced with 100 V substrate biasing. Follow-up experiments on small coated foil pieces could verify that the oxidation was not resulting from the PVD process. In a second batch of plates, the PVD device was altered by using an unbalanced magnetic field and a target of reactor-grade Zr. These changes created a more ductile Zr layer which resulted in less cracking during application of the cladding. Still, oxidation was present due to coating defects caused by the surface texture of the bare foils. This influence of foil quality was investigated with a final batch of fabricated plates that used bare foils from two different sources. Furthermore, a thicker coating of 20 µm was tested. It showed again that a rough surface texture with many steps induces coating defects that result in oxidation. A thicker coating is able to mitigate this effect to some extent by smoothening of these steps.

Enhancement of the PVD Device

Apart from the analysis of sputtering parameters, the advancement of the full-size PVD device itself is also particularly noteworthy. This includes especially the newly designed substrate holder based on the experience gained from multiple coating campaigns. It has been achieved that the current version is less prone to short circuits and more robust regarding long-term operation, which is particularly important for the future industrialization of the process. Furthermore, the handling has been simplified, which makes it more time-efficient. The implemented tensioning mechanism for the substrate foil reliably suppresses foil bending and therefore improves coating thickness homogeneity.

5.2 Outlook

Alternative Diffusion Barriers

The investigations on possible materials for diffusion barriers are still ongoing. This is not exclusively done for monolithic U-Mo fuels but also for dispersion fuel particles for which the PVD method is the most viable coating option.

Especially the tungsten is worth a deeper investigation as the heavy-ion irradiation showed comparatively small interaction with the U-Mo fuel and the Al cladding. Currently, new experiments are planned to analyze the behavior of U-Mo/W/Al layer systems regarding thermal diffusion plus dose effects in subsequent heavy-ion irradiations. Furthermore, the fabrication process has to be improved to reduce the cracking of the W coating. This may include:

- Adjustment of PVD parameters for more ductile coating
- W target of higher purity
- Adjustment of C2TWP cladding parameters
- Alternative cladding technique (HIP,...)
- Investigation on the influence of cracks under heavy-ion irradiation

The Mo coating, on the other hand, is still an option, even after observation of the complex interaction zone at the Mo/Al interface. The intermetallic phases are not necessarily detrimental under irradiation but can be even beneficial as shown for $Al_{12}Mo$, which prevented further intermixing [14]. Whether the supposed phases of Al_8Mo_3 and $Al_{22}Mo_5$ have a similar effect is still to be investigated. Either way, the PVD parameters have to be adjusted especially for the application of the Al protective layer as too much formation of the brittle intermetallic phases during the PVD process results in cracking. This includes a significantly reduced introduction of external heat while reassuring that the bonding of Mo and protective layer is still given under the new parameters.

EMPIrE

The EMPIrE samples still contain information that has not yet been extracted. Most importantly, this includes compositional analyses of interaction zones, which could not be performed on the sample piece because of the high radiation background. Therefore, FIB lamellae were also cut and extracted from multiple zones of the fuel plate during the PIE. These were sent to SCK CEN and CEA for more detailed analysis by transmission electron microscopy (TEM) to obtain a better understanding of the basic mechanisms that lead to defects like the porosity formation in the Zr layer and fission gas bubbles in interaction zones.

Fabrication Studies for FUTURE-MONO-1

Until the final LEU plates for the FUTURE-MONO-1 irradiation test can be manufactured, several more batches of test plates are needed to improve the coating quality, subsequently establish confidence in a chosen set of production parameters and verify reproducibility.

Currently, experiments are performed to improve the surface quality of the U-Mo bare foils by appropriate preparation techniques. This includes lapping of the foil surfaces, a more intense plasma cleaning step, and different chemical cleaning parameters using the current alkaline cleaning solution as well as nitric acid. Electropolishing also showed to be a particularly promising candidate to obtain a suitable surface texture for the U-Mo foils. A new batch of full-size foils was already coated after the foils have been prepared with several of the mentioned techniques. After the cladding application, characterizations will show which method is worth pursuing further as a final fabrication procedure.

As a prerequesite for the planned FUTURE-MONO-1 test, Framatome recently established its capabilities to produce U-Mo bare foils. The DU foils that will be made beforehand have to be first examined regarding their quality and then a new batch of plates produced with them. Depending on the results from the following characterization, the final parameters for foil preparation, coating, and cladding have then to be adjusted.

The end gaps as a phenomenon resulting from the C2TWP cladding process also still remain an issue that raises concern with regard to the planned FUTURE-MONO-1 irradiation. They may pose a risk for plate failures during irradiation, as fission gas accumulation can create a pressure that tears the plate open along the bond line. This issue can be resolved either by adjusting the C2TWP process in a way to get rid of the end gaps or by proving with tensile testing that the fuel plate can withstand a reasonable amount of force. Furthermore, it is to be evaluated whether the intermixing of U-Mo and Zr caused by laser cutting of the foil ends has a detrimental influence on the fuel's performance.

Although it is currently agreed upon that the parameter space of the full-size PVD device is sufficient to grow Zr layers with suitable properties, the option of resistive substrate heating is soon to be implemented and tested. If unforeseen results make this technique necessary in the future, a fast adaption can be executed with the preparatory work already done.

Industrialization of the PVD Process

The current pilot PVD device successfully served its purpose of producing diffusion barrier coatings in the frame of the fuel qualification process. However, the PVD process has to be industrialized at Framatome. While still retaining the parameters found to be crucial for the coating quality, this new device needs to be conceptually different in order to achieve the increased throughput necessary for series manufacturing of fuel plates. For a designated production of more than 500 specification-conform fuel plates per year, the current process needs to be more efficient. The most time-consuming process steps include venting and re-evacuation of the vacuum chamber for foil exchange, heat dissipation after coating, and manual turning of the foils for coating of the other side, which again needs venting and re-evacuation. Techniques to skip or combine these steps for multiple foils may include:

- In-line production with an inventory of bare foils
- Automated turning of the foils during coating
- Second target for simultaneous coating of both sides
- Load-lock transfer systems for input and output of foils

Appendix

List of Abbreviations

ATR	Advanced Test Reactor
bcc	body-centered cubic
BR2	Belgian Reactor 2; nuclear test reactor in Mol, Belgium
BSE	Backscattered Electrons
BWXT	BWX Technologies, Inc.; commercial supplier of nuclear components
C2TWP	Term for a fuel cladding process developed by Framatome
CEA	Commissariat à l'énergie atomique et aux énergies alternatives; French research organization
CERCA	Compagnie pour l'Etude et la Réalisation de Combustibles Atomiques; fuel business unit of Framatome
DC	Direct Current
DOE	United States Department of Energy
DU	Depleted Uranium (usually < 0.3 at.% ^{235}U)
EMPIrE	European MiniPlate Irradiation Experiment
fcc	face-centered cubic
FIB	Focused Ion Beam
FRM	Forschungsreaktor München
FRM II	Forschungs-Neutronenquelle Heinz Maier-Leibnitz
hcp	hexagonal close-packed
HEU	High Enriched Uranium (≥ 20 at.% ^{235}U)
HFEF	Hot Fuel Examination Facility at the Idaho National Laboratory
HFIR	High Flux Isotope Reactor at the Oak Right National Laboratory
HFR	High Flux Reactor at the Institut Laue-Langevin in Grenoble, France

HIP	Hot Isostatic Pressing
HPRR	High-Performance Research Reactor
IAEA	International Atomic Energy Agency
IDL	Interdiffusion Layer
ILL	Institut Laue-Langevin in Grenoble, France
IMCL	Irradiated Materials Characterization Laboratory at the Idaho National Laboratory
INL	Idaho National Laboratory
LEU	Low Enriched Uranium (> 0.7 at.% ^{235}U and < 20 at.% ^{235}U)
NDE	Non-Destructive Examination
NRC	Nuclear Regulatory Commission
NU	Natural Uranium
ORNL	Oak Ridge National Laboratory
PVD	Physical Vapor Deposition
PIE	Post-Irradiation Examination
RERTR	Reduced Enrichment for Research and Test Reactors
RF	Radio Frequency
SCK CEN	Belgian Nuclear Research Centre in Mol, Belgium
SE	Secondary Electrons
SEM	Scanning Electron Microscopy
SS	Stainless Steel
SZD	Structure Zone Diagram
TSK	Terrace Step Kink model for crystal growth
TTT	Time-Temperature-Transformation diagram for phase transformations in alloys
TUM	Technische Universität München
U-Mo	Uranium-Molybdenum alloy
US	United States
UT	Ultrasound Transmission

Bibliography

[1] S. Alvarez. "A cartography of the van der Waals territories." In: *Dalton transactions (Cambridge, England : 2003)* 42.24 (2013), pp. 8617–8636. DOI: 10.1039/c3dt50599e.

[2] A. Anders. "A structure zone diagram including plasma-based deposition and ion etching." In: *Thin Solid Films* 518.15 (2010), pp. 4087–4090. ISSN: 00406090. DOI: 10.1016/j.tsf.2009.10.145.

[3] A. Anders. "Physics of arcing, and implications to sputter deposition." In: *Thin Solid Films* 502.1-2 (2006), pp. 22–28. ISSN: 00406090. DOI: 10.1016/j.tsf.2005.07.228.

[4] A. Axmann and K. Boening. *The safety concept of the FRM-II*. 2003. DOI: 10.5170/CERN-2003-004.26.

[5] M. M. Baker, L. N. Less, and S. Orman. "Uranium + water reaction. Part 2. – Effect of oxygen and other gases." In: *Transactions of the Faraday Society* 62.0 (1966), pp. 2525–2530. ISSN: 0014-7672. DOI: 10.1039/TF9666202525.

[6] P. Barna and M. Adamik. "Fundamental structure forming phenomena of polycrystalline films and the structure zone models." In: *Thin Solid Films* 317.1-2 (1998), pp. 27–33. ISSN: 00406090. DOI: 10.1016/S0040-6090(97)00503-8.

[7] F. H. Baumann, D. L. Chopp, T. D. de la Rubia, G. H. Gilmer, J. E. Greene, H. Huang, S. Kodambaka, P. O'Sullivan, and I. Petrov. "Multiscale Modeling of Thin-Film Deposition: Applications to Si Device Processing." In: *MRS Bulletin* 26.3 (2001), pp. 182–189. ISSN: 0883-7694. DOI: 10.1557/mrs2001.40.

[8] B. Baumeister. "Advancements in Monolithic U-Mo Fabrication: Demonstration of Gradient Foil Fabrication and Development of a Pilot Physical Vapor Deposition Process for Full-Size U-Mo Foils." Dissertation. München: Technische Universität München, 2022.

[9] B. Baumeister. "Reinigungsverfahren für metallische Uran-Molybdän-Kernbrennstoffe." Bachelor's thesis. München: Technische Universität München, 2011.

[10] H. Breitkreutz, T. Huber, T. Zweifel, A. Röhrmoser, W. Petry, S. van den Berghe, A. Leenaers, M. Delpech, H. Palancher, Y. Calzavara, H. Guyon, B. Stepnik, C. Jarousse, and D. Geslin. *HERACLES-CP: Towards the Conversion of High Performance Research Reactors in Europe*. 2015. DOI: 10.3030/661935.

[11] Buehler Ldt. *Isomet 1000 Brochure*. https://www.buehler.com/products/sectioning/precision-cutters/isomet-1000-precision-cutter. Lake Bluff, IL.

[12] T. Chemnitz. "Inbetriebnahme und Parametrisierung einer Sputteranlage in der Kernbrennstoffentwicklung." Bachelor's thesis. München: Technische Universität München, 2014.

[13] H.-Y. Chiang. "Material Selection of UMo Fuel for Research Reactors: Swift Heavy Ion Irradiation Studies." Dissertation. München: Technische Universität München, 2014.

[14] H.-Y. Chiang, S.-H. Park, M. Mayer, K. Schmid, M. Balden, U. Boesenberg, R. Jungwirth, G. Falkenberg, T. Zweifel, and W. Petry. "Swift heavy ion irradiation induced interactions in the UMo/X/Al trilayer system (X=Ti, Zr, Nb, and Mo): RBS and m-XRD studies." In: *Journal of Alloys and Compounds* 626 (2015), pp. 381–390. ISSN: 09258388. DOI: 10.1016/j.jallcom.2014.12.041.

[15] C. D. Child. "Discharge From Hot CaO." In: *Physical Review (Series I)* 32.5 (1911), pp. 492–511. DOI: 10.1103/PhysRevSeriesI.32.492.

[16] Committee on the Current Status of and Progress Toward Eliminating Highly Enriched Uranium Use in Fuel for Civilian Research and Test Reactors. *Reducing the Use of Highly Enriched Uranium in Civilian Research Reactors*. Washington, D.C: National Academies Press, 2016. ISBN: 978-0-309-37918-2. DOI: 10.17226/21818.

[17] K. Daum, C. Miller, B. Durtschi, and J. Cole. *U-10Mo Monolithic Fuel Qualification Plan*. Idaho Falls, 2021.

[18] D. Depla and S. Mahieu, eds. *Reactive Sputter Deposition*. 1st ed. 2008. Vol. 109. Springer series in materials science. Berlin, Heidelberg: Springer Berlin Heidelberg and Imprint: Springer, 2008. ISBN: 9783540766643. DOI: 10.1007/978-3-540-76664-3.

[19] J. P. Durand, B. Duban, Y. Lavastre, and S. de Perthuis. *CERCA's 25 Years Experience in U_3Si_2 Fuel Manufacturing*. Ed. by International Atomic Energy Agency. 2003.

[20] A. Einstein. "Über die von der molekularkinetischen Theorie der Wärme geforderte Bewegung von in ruhenden Flüssigkeiten suspendierten Teilchen." In: *Annalen der Physik* 322.8 (1905), pp. 549–560. ISSN: 00033804. DOI: 10.1002/andp.19053220806.

[21] N. Eriksson. "Phase Transformations and Microstructural Evolution in the U-10wt.% Mo Alloy with Various Zr Additions at 900 °C and 650 °C." Master's Thesis. Orlando, Florida: University of Central Florida, 2015.

[22] M. Eumann, G. Sauthoff, and M. Palm. "Re-evaluation of phase equilibria in the Al–Mo system." In: *International Journal of Materials Research* 97.11 (2006), pp. 1502–1511. ISSN: 1862-5282. DOI: 10.3139/146.101412.

[23] P. Felbinger. "Präparation und Charakterisierung von monolithischen Uran-Molybdän-Brennstoffen mit Zr-Diffusionsbarriere und AlFeNi-Cladding." Bachelor's thesis. München: Hochschule für angewandte Wissenschaften München, 2018.

[24] J. C. Fisher. "Calculation of Diffusion Penetration Curves for Surface and Grain Boundary Diffusion." In: *Journal of Applied Physics* 22.1 (1951), pp. 74–77. ISSN: 0021-8979. DOI: 10.1063/1.1699825.

[25] L. Fisher-Skipper. "Development, Construction and Commissioning of an Improved Substrate Holder for the Sputter Coating of Uranium-Molybdenum Nuclear Fuels." Bachelor's thesis. München: Technische Universität München, 2021.

[26] G. Franz. *Oberflächentechnologie mit Niederdruckplasmen: Beschichten und Strukturieren in der Mikrotechnik*. Zweite, völlig neubearbeitete Auflage. Berlin, Heidelberg: Springer Berlin Heidelberg, Imprint, and Springer, 1994. ISBN: 9783662089798.

[27] A. Fridman and L. A. Kennedy. *Plasma Physics and Engineering*. CRC Press, 2016. ISBN: 9780429190759. DOI: 10.1201/b11728.

[28] E. Fuchs. "Vergleich zweier PVD-Anlagen über die Charakterisierung von hergestellten Zirkonium-Schichten." Bachelor's thesis. München: Technische Universität München, 2021.

[29] K. H. Gayer and L. C. Thompson. "The Solubility of Uranium Peroxide in Acidic and Basic Media at 25 °C." In: *Canadian Journal of Chemistry* 36.12 (1958), pp. 1649–1652. ISSN: 0008-4042. DOI: 10.1139/v58-239.

[30] H. Gerstenberg and I. Neuhaus. "A brief overview of the research reactor FRM II." In: *International Journal of Nuclear Energy Science and Technology* 4.4 (2009), p. 265. ISSN: 1741-6361. DOI: 10.1504/IJNEST.2009.028587.

[31] P. Ghekiere. "Structure Evolution of Biaxially Aligned Thin Films Deposited by Sputtering." Dissertation. Gent: Universiteit Gent, 2007.

[32] J. I. Goldstein, D. C. Joy, J. R. Michael, N. W. M. Ritchie, and J. H. J. Scott. *Scanning Electron Microscopy and X-Ray Microanalysis*. 4th ed. Springer eBook Collection Chemistry and Materials Science. New York, NY: Springer, 2018. ISBN: 9781493966769. DOI: 10.1007/978-1-4939-6676-9.

[33] *Good Practices for Qualification of High Density Low Enriched Uranium Research Reactor Fuels*. Vol. no. NF-T-5.2. IAEA Nuclear energy series. Vienna: International Atomic Energy Agency, 2009. ISBN: 9789201043092.

[34] A. Grimm. "Untersuchung von Verbesserungsmethoden für einen Sputterprozeß in der Kernbrennstoffentwicklung und Entwicklung eines dafür geeigneten Meßprobenhalters." Master's Thesis. München: Technische Universität München, 2016.

[35] R. de Gryse, J. Haemers, W. P. Leroy, and D. Depla. "Thirty years of rotatable magnetrons." In: *Thin Solid Films* 520.18 (2012), pp. 5833–5845. ISSN: 00406090. DOI: 10.1016/j.tsf.2012.04.065.

[36] J. T. Gudmundsson. "Physics and technology of magnetron sputtering discharges." In: *Plasma Sources Science and Technology* 29.11 (2020), p. 113001. ISSN: 0963-0252. DOI: 10.1088/1361-6595/abb7bd.

[37] W. A. Hanson, A. B. Robinson, N. J. Lybeck, J. W. Nielsen, B. Ye, Z.-G. Mai, D. D. Keiser, L. M. Jamison, G. L. Hofman, A. M. Yacout, A. Leenaers, B. Stepnik, and I. Y. Glagolenko. "Non-destructive analysis of swelling in the EMPIrE fuel test." In: *Journal of Nuclear Materials* 564 (2022). ISSN: 00223115. DOI: 10.1016/j.jnucmat.2022.153683.

[38] L. G. Harrison. "Influence of dislocations on diffusion kinetics in solids with particular reference to the alkali halides." In: *Transactions of the Faraday Society* 57 (1961), p. 1191. ISSN: 0014-7672. DOI: 10.1039/tf9615701191.

[39] HERACLES Consortium. *Homepage*. https://heracles-consortium.eu/.

[40] K. Huang, C. C. Kammerer, D. D. Keiser, and Y. H. Sohn. "Diffusion Barrier Selection from Refractory Metals (Zr, Mo and Nb) Via Interdiffusion Investigation for U-Mo RERTR Fuel Alloy." In: *Journal of Phase Equilibria and Diffusion* 35.2 (2014), pp. 146–156. ISSN: 1547-7037. DOI: 10.1007/s11669-013-0270-x.

[41] K. Huang, Y. Park, D. D. Keiser, and Y. H. Sohn. "Interdiffusion Between Potential Diffusion Barrier Mo and U-Mo Metallic Fuel Alloy for RERTR Applications." In: *Journal of Phase Equilibria and Diffusion* 34.4 (2013), pp. 307–312. ISSN: 1547-7037. DOI: 10.1007/s11669-013-0236-z.

[42] L. Hubbard, C. Arendt, D. Dye, C. Clayton, M. Lerchen, N. Lombardo, C. Lavender, and A. Zacher. *U-10Mo Baseline Fuel Fabrication Process Description*. 2017. DOI: 10.13140/RG.2.2.28508.54400.

[43] IAEA. *Material Properties of Unirradiated Uranium–Molybdenum (U–Mo) Fuel for Research Reactors*. Vol. v.1923. IAEA TECDOC Series. Vienna: IAEA, 2020. ISBN: 9789201158208.

[44] X. Iltis, D. Drouan, T. Blay, I. Zacharie, C. Sabathier, C. Onofri, C. Steyer, C. Schwarz, B. Baumeister, J. Allenou, B. Stepnik, and W. Petry. "Microstructural characteristics of a fresh U(Mo) monolithic mini-plate: Focus on the Zr coating deposited by PVD." In: *Nuclear Engineering and Technology* 53.8 (2021), pp. 2629–2639. ISSN: 17385733. DOI: 10.1016/j.net.2021.02.026.

[45] *INFCE summary volume*. Vol. 534. STI/PUB. Vienna: International Atomic Energy Agency, 1980. ISBN: 9201599803.

[46] A. L. Izhutov, V. V. Iakovlev, A. E. Novoselov, V. A. Starkov, A. A. Sheldyakov, V. Y. Shishin, V. M. Kosenkov, A. V. Vatulin, I. V. Dobrikova, V. B. Suprun, and G. V. Kulakov. "Comparative Analysis of Structural Changes in U-Mo Dispersed Fuel of Full-size Fuel Elements and Mini-rods Irradiated in the MIR Reactor." In: *Nuclear Engineering and Technology* 45.7 (2013), pp. 859–870. ISSN: 17385733. DOI: 10.5516/NET.07.2013.716.

[47] S. Jana, A. L. Schemer-Kohrn, N. R. Overman, L. E. Sweet, E. J. Kautz, C. A. Lavender, and Joshi V. V. *Eutectoid Transformation in U10Mo Alloy: Effect of Deformation History and Homogenization Heat Treatment*. 2019.

[48] L. Jollay, H. A. Longmire, A. Moore, M. Gambrell, J. Gooch, and A. DeMint. "Low Enriched Uranium-Molybdenum Coupon Fabrication at the Y-12 National Security Complex." In: *34th International Meeting on Reduced Enrichment for Research and Test Reactors*. Warsaw, 2012.

[49] J.-F. Jue, D. D. Keiser, C. R. Breckenridge, G. A. Moore, and M. K. Meyer. "Microstructural characteristics of HIP-bonded monolithic nuclear fuels with a diffusion barrier." In: *Journal of Nuclear Materials* 448.1-3 (2014), pp. 250–258. ISSN: 00223115. DOI: 10.1016/j.jnucmat.2014.02.004.

[50] D. D. Keiser, J. F. Jue, and D. E. Burkes. *Characterization and Testing of Monolithic RERTR Fuel Plates*. Idaho Falls, 2007.

[51] D. D. Keiser, J.-F. Jue, B. B. Miller, J. Gan, A. B. Robinson, and J. Madden. "Observed Changes in As-Fabricated U-10Mo Monolithic Fuel Microstructures After Irradiation in the Advanced Test Reactor." In: *JOM* 69.12 (2017), pp. 2538–2545. ISSN: 1047-4838. DOI: 10.1007/s11837-017-2564-7.

[52] P. J. Kelly and R. D. Arnell. "Magnetron sputtering: a review of recent developments and applications." In: *Vacuum* 56.3 (2000), pp. 159–172. ISSN: 0042207X. DOI: 10.1016/S0042-207X(99)00189-X.

[53] Y. S. Kim, G. L. Hofman, and J. S. Cheon. "Recrystallization and fission-gas-bubble swelling of U–Mo fuel." In: *Journal of Nuclear Materials* 436.1-3 (2013), pp. 14–22. ISSN: 00223115. DOI: 10.1016/j.jnucmat.2013.01.291.

[54] K. M. Kjølerbakken, W. J. Miloch, and K. Røed. "The influence of probe spacing and probe bias in a double Langmuir probe setup." In: *AIP Advances* 11.8 (2021), p. 085007. DOI: 10.1063/5.0058540.

[55] R. Koenig. "Reactor project presses ahead despite protests." In: *Science* 269.5224 (1995), pp. 628–629. ISSN: 0036-8075. DOI: 10.1126/science.269.5224.628.

[56] N. Laegreid and G. K. Wehner. "Sputtering Yields of Metals for Ar^+ and Ne^+ Ions with Energies from 50 to 600 eV." In: *Journal of Applied Physics* 32.3 (1961), pp. 365–369. ISSN: 0021-8979. DOI: 10.1063/1.1736012.

[57] I. Langmuir. "The Adsorption of Gases on Plane Surfaces of Glass, Mica and Platinum." In: *Journal of the American Chemical Society* 40.9 (1918), pp. 1361–1403. ISSN: 0002-7863. DOI: 10.1021/ja02242a004.

[58] A. D. Le Claire and I. J. Bear. "The interdiffusion of uranium and aluminium." In: *Journal of Nuclear Energy (1954)* 2.3-4 (1956), pp. 229–242. ISSN: 08913919. DOI: 10.1016/0891-3919(55)90039-5.

[59] A. Leenaers, B. Ye, J. van Eyken, and S. van den Berghe. "ZrN coating as diffusion barrier in U(Mo) dispersion fuel systems." In: *Journal of Nuclear Materials* 552 (2021), p. 153000. ISSN: 00223115. DOI: 10.1016/j.jnucmat.2021.153000.

[60] Leonid Guzei and Materials Science International Team, MSIT. *The Al-Zr System: Datasheet from MSI Eureka in SpringerMaterials (https://materials.springer.com/msi/phase-diagram/docs/sm_msi_r_10_024007_01_full_LnkDia0)*. Ed. by G. Effenberg.

[61] L. Liang, Z.-G. Mei, and A. M. Yacout. "Fission-induced recrystallization effect on intergranular bubble-driven swelling in U-Mo fuel." In: *Computational Materials Science* 138 (2017), pp. 16–26. ISSN: 09270256. DOI: 10.1016/j.commatsci.2017.06.013.

[62] M. A. Lieberman and A. J. Lichtenberg. *Principles of Plasma Discharges and Materials Processing*. Hoboken, NJ, USA: John Wiley & Sons, Inc, 2005. ISBN: 9780471724254. DOI: 10.1002/0471724254.

[63] S. Lo Muzio. "Property Studies of Sputtered Zr Layers on Monolithic Uranium-Molybdenum Nuclear Fuels." Bachelor's thesis. München: Technische Universität München, 2018.

[64] L. B. Loeb. *Fundamental Processes of Electrical Discharges in Gases*. New York: John Wiley & Sons, Inc, 1939.

[65] Long Life for Art. *Technical Datasheet Aluminium barrier film A30 T*. Eichstetten, 2020.

[66] J. M. López and J. A. Alonso. "Semiempirical Theory of Solid Solubility in Transition Metal Alloys." In: *Zeitschrift für Naturforschung A* 40.12 (1985), pp. 1199–1205. ISSN: 0932-0784. DOI: 10.1515/zna-1985-1204.

[67] L. I. Maissel and P. M. Schaible. "Thin Films Deposited by Bias Sputtering." In: *Journal of Applied Physics* 36.1 (1965), pp. 237–242. ISSN: 0021-8979. DOI: 10.1063/1.1713883.

[68] A. Martínez-Torrents, S. Meca, N. Baumann, V. Martí, J. Giménez, J. de Pablo, and I. Casas. "Uranium speciation studies at alkaline pH and in the presence of hydrogen peroxide using time-resolved laser-induced fluorescence spectroscopy." In: *Polyhedron* 55 (2013), pp. 92–101. ISSN: 02775387. DOI: 10.1016/j.poly.2013.02.075.

[69] N. Matsunami, Y. Yamamura, Y. Itikawa, N. Itoh, Y. Kazumata, S. Miyagawa, K. Morita, R. Shimizu, and H. Tawara. "Energy dependence of the ion-induced sputtering yields of monatomic solids." In: *Atomic Data and Nuclear Data Tables* 31.1 (1984), pp. 1–80. ISSN: 0092640X. DOI: 10.1016/0092-640X(84)90016-0.

[70] D. M. Mattox. *Handbook of physical vapor deposition (PVD) processing: Includes index*. 2nd ed. Amsterdam: Elsevier, 2010. ISBN: 9780815520382.

[71] S. Matuschik. "Production and Heavy-Ion Irradiation of Tungsten Coatings as Diffusion Barrier in the U-Mo/Al Fuel System." Bachelor's thesis. Technische Universität München, 2020.

[72] E. W. McDaniel. *Collision phenomena in ionized gases*. New York: Wiley, 1964. ISBN: 978-0471583851.

[73] H. Mehrer, ed. *Diffusion in solids: Fundamentals, methods, materials, diffusion controlled processes ; with 27 tables*. Vol. 155. Springer Series in Solid-State Sciences. Berlin and Heidelberg: Springer, 2007. ISBN: 9783540714866.

[74] A. Mehta, Le Zhou, D. D. Keiser, and Y. Sohn. "Anomalous growth of Al_8Mo_3 phase during interdiffusion and reaction between Al and Mo." In: *Journal of Nuclear Materials* 539 (2020), p. 152337. ISSN: 00223115. DOI: 10.1016/j.jnucmat.2020.152337.

[75] M. K. Meyer, J. Gan, J. F. Jue, D. D. Keiser, E. Perez, A. B. Robinson, D. M. Wachs, N. E. Woolstenhulme, G. L. Hofman, and Y. S. Kim. "Irradiation Performance of U-Mo Monolithic Fuel." In: *Nuclear Engineering and Technology* 46.2 (2014), pp. 169–182. ISSN: 17385733. DOI: 10.5516/NET.07.2014.706.

[76] A. R. Miedema. "On the heat of formation of solid alloys. II." In: *Journal of the Less Common Metals* 46.1 (1976), pp. 67–83. ISSN: 00225088. DOI: 10.1016/0022-5088(76)90180-6.

[77] B. D. Miller, D. D. Keiser, A. Aitkaliyeva, B. J. Hernandez, and A. J. Winston. *3D reconstruction of M11A2 from the SELENIUM Experiment*. 2017. DOI: 10.2172/1483618.

[78] B. D. Miller, C. Schwarz, B. Baumeister, C. Reiter, A. B. Robinson, and D. D. Keiser. *EMPIRE Destructive Characterization of Irradiated Monolithic Fuel*. Idaho Falls, 2022.

[79] M. Moisan and J. Pelletier. *Physics of Collisional Plasmas: Introduction to High-Frequency Discharges*. improved version of the original book "Physiques des plasmas collisionnels", EDP sciences - Grenoble sciences' coll., 2006, ISBN 978 2 86883 822 3. Grenoble sciences. Dordrecht: Springer Netherlands, 2012. ISBN: 9789400745575. DOI: 10.1007/978-94-007-4558-2.

[80] G. A. Moore and M. C. Marshall. *Co-Rolled U10Mo/Zirconium-Barrier-Layer Monolithic Fuel Foil Fabrication Process*. 2010. DOI: 10.2172/978364.

[81] B. A. Movchan and A. V. Demchishin. "Study of the structure and properties of thick vacuum condesates of nickel, titanium, tungsten, aluminum oxide and zirconium oxide." In: *Physics of Metals and Metallography* 28 (1969), pp. 653–662.

[82] J. Musil and M. Jaroš. "Plasma and floating potentials in magnetron discharges." In: *Journal of Vacuum Science & Technology A: Vacuum, Surfaces, and Films* 35.6 (2017), p. 060605. ISSN: 0734-2101. DOI: 10.1116/1.4992054.

[83] Nuclear Regulatory Commission. *Safety evaluation report related to the evaluation of low-enriched uranium silicide-aluminum dispersion fuel for use in non-power reactors*. 1988. DOI: 10.2172/6830338.

[84] Nucleonica GmbH and Marktdienste Haberbeck GmbH. *Karlsruher Nuklidkarte*. 10. Auflage. Karlsruhe, 2018. ISBN: 9783943868500.

[85] M. Nuding, M. Rottmann, A. Axmann, and K. Böning. "FRM-II Project Status and Safety of its Compact Fuel Element." In: *European Nuclear Society (Hg.) 2000 – RRFM 2000 transactions*, pp. 42–47.

[86] E. A. Nyberg, V. V. Joshi, D. Burkes, and C. A. Lavender. *The Microstructure of Rolled Plates from Cast Billets of U-10Mo Alloys*. 2015. DOI: 10.2172/1177710.

[87] O. Fabrichnaya and Materials Science International Team, MSIT. *Phase diagram of the U-Zr system: Datasheet from MSI Eureka in SpringerMaterials (https://materials.springer.com/msi/phase-diagram/docs/sm_msi_r_10_016877_01_full_LnkDia0)*. Ed. by G. Effenberg.

[88] A. Oberbauer. "Diffusion Behavior of Ternary U-Mo-X Alloys with Al Cladding." Master's Thesis. München: Technische Universität München, 2022.

[89] H. Okamoto. "Al-U (Aluminum-Uranium)." In: *Journal of Phase Equilibria and Diffusion* 33.6 (2012), pp. 489–490. ISSN: 1547-7037. DOI: 10.1007/s11669-012-0089-x.

[90] K. Oura, V. G. Lifšic, A. A. Saranin, A. V. Zotov, and M. Katayama. *Surface science: An introduction*. Advanced texts in physics. Berlin, Heidelberg, and New York: Springer, 2003. ISBN: 3540005455.

[91] Z. Pan, L. J. Kecskes, and Q. Wei. "The nature behind the preferentially embrittling effect of impurities on the ductility of tungsten." In: *Computational Materials Science* 93 (2014), pp. 104–111. ISSN: 09270256. DOI: 10.1016/j.commatsci.2014.06.036.

[92] Y. Park, N. Eriksson, R. Newell, D. D. Keiser, and Y. H. Sohn. "Phase decomposition of γ-U (bcc) in U-10 wt% Mo fuel alloy during hot isostatic pressing of monolithic fuel plate." In: *Journal of Nuclear Materials* 480 (2016), pp. 271–280. ISSN: 00223115. DOI: 10.1016/j.jnucmat.2016.08.022.

[93] Y. Park, J. Yoo, K. Huang, D. D. Keiser, J. F. Jue, B. Rabin, G. Moore, and Y. H. Sohn. "Growth kinetics and microstructural evolution during hot isostatic pressing of U-10wt.% Mo monolithic fuel plate in AA6061 cladding with Zr diffusion barrier." In: *Journal of Nuclear Materials* 447.1-3 (2014), pp. 215–224. ISSN: 00223115. DOI: 10.1016/j.jnucmat.2014.01.018.

[94] A. Paul. *Thermodynamics, Diffusion and the Kirkendall Effect in Solids*. Aufl. 2014. SpringerLink Bücher. Cham, Switzerland: Springer International Publishing, 2014. ISBN: 9783319074610. DOI: 10.1007/978-3-319-07461-0.

[95] A. Paul and S. Divinski, eds. *Handbook of Solid State Diffusion: Diffusion Analysis in Material Applications*. Vol. 2. Amsterdam, Netherlands: Elsevier, 2017. ISBN: 9780128045787.

[96] A. Paul and S. Divinski, eds. *Handbook of solid state diffusion: Diffusion Fundamentals and Techniques*. Vol. 1. Amsterdam, Netherlands: Elsevier, 2017. ISBN: 9780128042878.

[97] E. Perez, B. Yao, D. D. Keiser, and Y. H. Sohn. "Microstructural analysis of as-processed U–10wt.%Mo monolithic fuel plate in AA6061 matrix with Zr diffusion barrier." In: *Journal of Nuclear Materials* 402.1 (2010), pp. 8–14. ISSN: 00223115. DOI: 10.1016/j.jnucmat.2010.04.016.

[98] E. Perez. "Interdiffusion Behavior of U-Mo Alloys in Contact with Al and Al-Si Alloys." Dissertation. Orlando, Florida: University of Central Florida, 2011.

[99] C. A. W. Peterson, W. J. Steele, and S. L. DiGiallonardo. *Isothermal Transformation Study of some Uranium-Base Alloys*. 1964. DOI: 10.2172/4672623.

[100] I. Petrov, F. Adibi, J. E. Greene, L. Hultman, and J. E. Sundgren. "Average energy deposited per atom: A universal parameter for describing ion–assisted film growth?" In: *Applied Physics Letters* 63.1 (1993), pp. 36–38. ISSN: 0003-6951. DOI: 10.1063/1.109742.

[101] A. Pflug, M. Siemers, C. Schwanke, B. Febty Kurnia, V. Sittinger, and B. Szyszka. "Simulation of plasma potential and ion energies in magnetron sputtering." In: *Materials Technology* 26.1 (2011), pp. 10–14. DOI: 10.1179/175355511X12941605982028.

[102] A. M. Phillips, G. S. Mickum, and D. E. Burkes. *Thermophysical Properties of U-10Mo Alloy*. 2010. DOI: 10.2172/1000547.

[103] N. Plößner. "Inbetriebnahme und Parametrisierung einer hochskalierten Sputteranlage für die Kernbrennstoffentwicklung." Bachelor's thesis. München: Technische Universität München, 2019.

[104] U. W. Pohl, ed. *Epitaxy of Semiconductors*. Graduate Texts in Physics. Cham: Springer International Publishing, 2020. ISBN: 978-3-030-43868-5. DOI: 10.1007/978-3-030-43869-2.

[105] C. Reiter, A. Bergeron, D. Bonete-Wiese, M. Kirst, J. Mercz, R. Schönecker, K. Shehu, B. Ozar, F. Puig, J. Licht, W. Petry, and P. Müller-Buschbaum. "A Low-Enriched Uranium (LEU) option for the conversion of FRM II." In: *Annals of Nuclear Energy* (accepted for publication) (2022).

[106] C. Ren, Z. Z. Fang, M. Koopman, B. Butler, J. Paramore, and S. Middlemas. "Methods for Improving Ductility of Tungsten - A review." In: *International Journal of Refractory Metals and Hard Materials* 75 (2018), pp. 170–183. ISSN: 02634368. DOI: 10.1016/j.ijrmhm.2018.04.012.

[107] P. E. Repas, R. H. Goodenow, and R. F. Hehemann. "Transformation Characteristics of U-Mo an U-Mo-Ti Alloys." In: *Trans. Am. Soc. Metals* 57 (1964), pp. 150–163.

[108] *RERTR Homepage*. https://www.rertr.anl.gov/. 18.05.2020.

[109] J. Rest. "Evolution of Fission-Gas-Bubble-Size Distribution in Recrystallized U–10Mo Nuclear Fuel." In: *Journal of Nuclear Materials* 407.1 (2010), pp. 55–58. ISSN: 00223115. DOI: 10.1016/j.jnucmat.2010.07.009.

[110] F. J. Rice, W. Williams, A. B. Robinson, J. Harp, M. K. Meyer, and B. H. Rabin. *RERTR-12 Post-irradiation Examination Summary Report*. 2015. DOI: 10.2172/1173078.

[111] Riverhawk Company. *Data sheet on flexural pivots*. www.flexpivots.com. New Hartfort, NY.

[112] A. B. Robinson, G. S. Chang, D. D. Keiser, D. M. Wachs, and D. L. Porter. *Irradiation Performance of U-Mo Alloy Based Monolithic Plate-Type Fuel - Design Selection*. 2009. DOI: 10.2172/968567.

[113] A. B. Robinson, W. A. Hanson, I. Glagolenko, and J. W. Nielsen. *EMPIRE Monolithic Plates NDE Results*. Idaho Falls, 2019.

[114] A. B. Robinson, D. M. Wachs, D. E. Burkes, and D. D. Keiser. *US RERTR Fuel Development Post Irradiation Examination Results*. Idaho Falls, 2008.

[115] A. Röhrmoser, W. Petry, K. Böning, and N. Wieschalla. "Reduced Enrichment Program for the FRM-II, Status 2004." In: *RERTR 2004*. Vienna, 2004.

[116] J. R. Roth. *Industrial plasma engineering*. Repr. Vol. 1. Bristol: Inst. of Physics Publ, 2000. ISBN: 0750303174.

[117] A. M. Saliba-Silva, M. Durazzo, E. F. Urano de Carvalho, and H. G. Riella. "Fabrication of U_3Si_2 Powder for Fuels Used in IEA-R1 Nuclear Research Reactor." In: *Materials Science Forum* 591-593 (2008), pp. 194–199. DOI: 10.4028/www.scientific.net/MSF.591-593.194.

[118] N. Saunders. "The Al-Mo system (aluminum-molybdenum)." In: *Journal of Phase Equilibria* 18.4 (1997), pp. 370–378. ISSN: 1054-9714. DOI: 10.1007/s11669-997-0063-1.

[119] W. Schmid. "Construction of a sputtering reactor for the coating and processing of monolithic U-Mo nuclear fuel." Dissertation. München: Technische Universität München, 2011.

[120] J. C. Schuster and Materials Science International Team, MSIT. *Al-rich region of the critically evaluated phase diagram: Datasheet from MSI Eureka in SpringerMaterials (https://materials.springer.com/msi/phase-diagram/docs/sm_msi_r_20_012123_02_full_LnkDia1)*. Ed. by G. Effenberg.

[121] C. Schwarz and B. Baumeister. *Optimization of PVD Coating*. Ed. by European Commission. 2022. DOI: 10.3030/754378.

[122] C. Schwarz, B. Baumeister, E. Fuchs, L. Fisher-Skipper, W. Petry, S. Lorand, K. Buducan, and B. Stepnik. "Production of Full-size Monolithic U-Mo Fuel Plates." In: *European Nuclear Society (Hg.) 2022 – RRFM 2022*. Budapest, 2022.

[123] C. Schwarz, T. Dirks, B. Baumeister, C. Steyer, and W. Petry. "All-in-one chemical cleaning and deoxidation process for monolithic Uranium-Molybdenum foils." In: *RRFM 2016*. Ed. by European Nuclear Society. 2016.

[124] C. Schwarz, N. Plößner, J. Mercz, C. Steyer, B. Baumeister, and W. Petry. "Scale-up of the TUM PVD Zr Coating Process for Monolithic U-Mo Fuel Foils." In: *RRFM 2020*. Ed. by European Nuclear Society. 2020.

[125] J. Shi. "Qualification of U-Mo fuel for research reactors: Characterisation of the interfaces between U-Mo kernel, diffusion barrier and Al matrix under heavy ion irradiation." Dissertation. München: Technische Universität München, 2021.

[126] E. R. Smith and P. W. Frank. *Recoil Range of Fission Fragments in Zirconium*. Pittsburgh, 1959. DOI: 10.2172/4205534.

[127] M. von Smoluchowski. "Zur kinetischen Theorie der Brownschen Molekularbewegung und der Suspensionen." In: *Annalen der Physik* 326.14 (1906), pp. 756–780. ISSN: 00033804. DOI: 10.1002/andp.19063261405.

[128] T. Smy, L. Tan, S. S. Winterton, S. K. Dew, and M. J. Brett. "Simulation of sputter deposition at high pressures." In: *Journal of Vacuum Science & Technology A: Vacuum, Surfaces, and Films* 15.6 (1997), pp. 2847–2853. ISSN: 0734-2101. DOI: 10.1116/1.580838.

[129] M. Stepanova and S. Dew. "Anisotropic energies of sputtered atoms under oblique ion incidence." In: *Nuclear Instruments and Methods in Physics Research Section B: Beam Interactions with Materials and Atoms* 215.3-4 (2004), pp. 357–365. ISSN: 0168583X. DOI: 10.1016/j.nimb.2003.09.013.

[130] B. Stepnik, M. Grasse, C. Moyroud, and C. Jarousse. "Method for Manufacturing a Nuclear Fuel Element, and Nuclear Fuel Element." WO2023280897A1. 06.07.2022.

[131] C. Steyer, B. Baumeister, H. Breitkreutz, W. Petry, B. Stepnik, M. Grasse, C. Moyroud, R. Johnson, R. Mayfield, and G. Argon. "Production results of monolithic UMo plates for the EMPIrE irradiation experiment." In: *RRFM 2017*. Ed. by European Nuclear Society. 2017.

[132] C. Steyer. "Plasma- und festkörperphysikalische Optimierung eines Beschichtungsverfahrens für monolithische UMo-Kernbrennstoffe." Dissertation. München: Technische Universität München, 2019.

[133] SurTec International GmbH. *Technical Data Sheet SurTec 138*.

[134] J. A. Thornton. "Influence of apparatus geometry and deposition conditions on the structure and topography of thick sputtered coatings." In: *Journal of Vacuum Science and Technology* 11.4 (1974), pp. 666–670. ISSN: 0022-5355. DOI: 10.1116/1.1312732.

[135] A. Travelli. "The RERTR program." In: *ENS RRFM '97 Transactions* (1997), pp. 29–34.

[136] S. Valance, B. Baumeister, W. Petry, and J. Höglund. "Innovative and safe supply of fuels for reactors." In: *EPJ Nuclear Sciences & Technologies* 6 (2020), p. 40. DOI: 10.1051/epjn/2019013.

[137] S. van den Berghe, A. Leenaers, E. Koonen, and L. Sannen. "From High to Low Enriched Uranium Fuel in Research Reactors." In: *5th FORUM ON NEW MATERIALS PART B*. Advances in Science and Technology. Trans Tech Publications Ltd Switzerland, 2010, pp. 78–90. DOI: 10.4028/www.scientific.net/AST.73.78.

[138] P. Villars and H. Okamoto, eds. *Al-W Binary Phase Diagram 0-100 at.% W: Datasheet from "PAULING FILE Multinaries Edition – 2012" in SpringerMaterials (https://materials.springer.com/isp/phase-diagram/docs/c_0900141)*.

[139] P. Villars and H. Okamoto, eds. *Mo-U Binary Phase Diagram 40-100 at.% U: Datasheet from "PAULING FILE Multinaries Edition – 2012" in SpringerMaterials (https://materials.springer.com/isp/phase-diagram/docs/c_0904591)*.

[140] P. Villars and H. Okamoto, eds. *Mo-U-Zr Isothermal Section of Ternary Phase Diagram: Datasheet from "PAULING FILE Multinaries Edition – 2012" in SpringerMaterials (https://materials.springer.com/isp/phase-diagram/docs/c_0952031)*.

[141] P. Villars and H. Okamoto, eds. *Mo-Zr Binary Phase Diagram 0-100 at.% Zr: Datasheet from "PAULING FILE Multinaries Edition – 2012" in SpringerMaterials (https://materials.springer.com/isp/phase-diagram/docs/c_1600351)*.

[142] P. Villars and H. Okamoto, eds. *U-W Binary Phase Diagram 0-100 at.% W: Datasheet from "PAULING FILE Multinaries Edition – 2012" in SpringerMaterials (https://materials.springer.com/isp/phase-diagram/docs/c_0108201)*.

[143] M. Voithenleitner. "Präparation und Charakterisierung von Edelstahl-Surrogaten mit AlFeNi-Cladding für die Kernbrennstoffentwicklung." Bachelor's thesis. München: Hochschule für angewandte Wissenschaften München, 2020.

[144] D. Wachs. *RERTR Fuel Developmemt and Qualification Plan*. 2007. DOI: 10.2172/911912.

[145] G. Wehner. "Influence of the Angle of Incidence on Sputtering Yields." In: *Journal of Applied Physics* 30.11 (1959), pp. 1762–1765. ISSN: 0021-8979. DOI: 10.1063/1.1735051.

[146] B. Window and N. Savvides. "Charged particle fluxes from planar magnetron sputtering sources." In: *Journal of Vacuum Science & Technology A: Vacuum, Surfaces, and Films* 4.2 (1986), pp. 196–202. ISSN: 0734-2101. DOI: 10.1116/1.573470.

[147] Y. Yamamura, T. Takiguchi, and M. Ishida. "Energy and angular distributions of sputtered atoms at normal incidence." In: *Radiation Effects and Defects in Solids* 118.3 (1991), pp. 237–261. ISSN: 1042-0150. DOI: 10.1080/10420159108221362.

[148] H. Zhang, P. Feng, and F. Akhtar. "Aluminium matrix tungsten aluminide and tungsten reinforced composites by solid-state diffusion mechanism." In: *Scientific Reports* 7.1 (2017), p. 12391. ISSN: 2045-2322. DOI: 10.1038/s41598-017-12302-w.

[149] R. F. Zhang, S. H. Zhang, Z. J. He, J. Jing, and S. H. Sheng. "Miedema Calculator: A thermodynamic platform for predicting formation enthalpies of alloys within framework of Miedema's Theory." In: *Computer Physics Communications* 209 (2016), pp. 58–69. ISSN: 00104655. DOI: 10.1016/j.cpc.2016.08.013.

[150] V. Zutić and M. Branica. "Redox processes of uranium(IV) peroxo complexes in alkaline hydroxide solutions." In: *Journal of Electroanalytical Chemistry and Interfacial Electrochemistry* 52.2 (1974), pp. 217–228. ISSN: 00220728. DOI: 10.1016/S0022-0728(74)80363-3.

Scientific Contributions

Supervised Theses

P. Felbinger, *Präparation und Charakterisierung von monolithischen Uran-Molybdän-Brenn-stoffen mit Zr-Diffusionsbarriere und AlFeNi-Cladding*, B.Sc. thesis, München, 2018.

N. Plößner, *Commissioning and Parametrization of an Upscaled Sputtering Device for Nuclear Fuel Development*, B.Sc. thesis, München, 2019.

M. Voithenleitner, *Präparation und Charakterisierung von Edelstahl-Surrogaten mit AlFeNi-Cladding für die Kernbrennstoffentwicklung*, B.Sc. thesis, München, 2019.

E. Fuchs, *Vergleich zweier PVD-Anlagen über die Charakterisierung von hergestellten Zirko-nium-Schichten*, B.Sc. thesis, München, 2021.

L. Fisher-Skipper, *Development, Construction and Commissioning of an Improved Substrate Holder for the Sputter Coating of Uranium-Molybdenum Nuclear Fuels*, B.Sc. thesis, München, 2021.

A. Oberbauer, *Diffusion Behavior of Ternary U-Mo-X Alloys with Al Cladding*, M.Sc. thesis, München, 2022.

List of Publications

C. Schwarz, T. Dirks, B. Baumeister, C. Steyer, W. Petry, *All-in-one Chemical Cleaning and Deoxidation Process for Monolithic Uranium-Molybdenum Foils*, European Research Reactor Conference (RRFM), Berlin, 2016.

C. Schwarz, N. Plößner, J. Mercz, C. Steyer, B. Baumeister, W. Petry, *Scale-up of the TUM PVD Zr Coating Process for Monolithic U-Mo Fuel Foils*, European Research Reactor Conference (RRFM), 2020.

C. Schwarz, B. Baumeister, C. Reiter, W. Petry, *The TUM Nuclear Fuel Laboratory: Current Developments and Planned Expansion*, International Meeting on Reduced Enrichment for Research and Test Reactors (RERTR), 2021.

C. Schwarz, B. Baumeister, E. Fuchs, L. Fisher-Skipper, W. Petry, J. Allenou, S. Lorand, B. Stepnik, *PVD and C2TWP for the Fabrication of Monolithic U-Mo Fuel Plates - A Status Update*, European Research Reactor Conference (RRFM), Helsinki, 2021.

C. Schwarz, B. Baumeister, E. Fuchs, L. Fisher-Skipper, W. Petry, J. Allenou, S. Lorand, B. Stepnik, *Production of Full-size Monolithic U-Mo Fuel Plates*, European Research Reactor Conference (RRFM), Budapest, 2022.

X. Iltis, D. Drouan, T. Blay, I. Zacharie, C. Sabathier, C. Onofri, C. Steyer, **C. Schwarz**, B. Baumeister, J. Allenou, B. Stepnik, W. Petry, *Microstructural characteristics of a fresh U(Mo) monolithic mini-plate: Focus on the Zr coating deposited by PVD*, Nuclear Engineering and Technology 53 (2021) 2629–2639. https://doi.org/10.1016/j.net.2021.02.026.

D. Salvato, J. Shi, H. Breitkreutz, W. van Renterghem, B. Baumeister, **C. Schwarz**, A. Leenaers, S. van den Berghe, C. Detavernier, W. Petry, *U(Mo) grain refinement induced by irradiation with high energy iodine*, Journal of Nuclear Materials 548 (2021) 152850. https://doi.org/10.1016/j.jnucmat.2021.152850.

Danksagung / Acknowledgments

Trotz intensiver Beschäftigung mit langen Tagen im Labor und vorm PC füllen sich die Seiten dieses Werkes doch nicht ausschließlich von mir allein. Im Folgenden möchte ich mich bei allen bedanken, die ebenfalls zum guten Gelingen beigetragen haben:

Allen voran ist **Prof. Dr. Winfried Petry** zu danken, der mir die Möglichkeit gegeben hat die vorliegende Arbeit durchzuführen. Ihre bewundernswerte Energie Dinge anzugehen hat selbst in Rente nicht nachgelassen.

An **Prof. Dr. Bastian Märkisch** geht besonderer Dank für das Zweitgutachten dieser Arbeit.

Herzlicher Dank gilt meinen Kollegen und Vorgängern **Bruno Baumeister** und **Christian Steyer**, auf derern Leistungen meine Arbeit aufbaut. Die Zusammenarbeit war stets geprägt von gegenseitiger Unterstützung um dieses gemeinsame Projekt voranzubringen.

Die **Arbeitsgruppe für Hochdichte Kernbrennstoffe** am FRM II mit all seinen aktuellen und ehemaligen Kollegen, die mich über die letzten Jahre begleitet haben:
Harald Breitkreutz, **Tobias Chemnitz**, **Christian Reiter**, **Jingyi Shi**, **Kaltrina Shehu**.
Die Studenten, die ich betreuen durfte und mir zugearbeitet haben: **Peter Felbinger**, **Leon Fisher-Skipper**, **Eric Fuchs**, **Julius Mercz**, **Anna Oberbauer**, **Nikolas Plößner**, **Michael Voithenleitner**.
Unser technisches Team um **Thomas Kerschl**, **Serhat Polat**, **Nicholas Rehms** und **Viktor Schweigert**, die sich mit allerlei Tücken der Technik und Bürokratie herumschlagen, um den Laborbetrieb aufrecht zu erhalten.

Our partners at **Framatome-CERCA** in France, **Jérôme Allenou**, **Kevin Buducan**, **Sylvain Lorand**, and **Bertrand Stepnik**, who processed many of our coated foils over the past years to fabricate finished fuel plates. Merci beaucoup!

The people at **Idaho National Laboratory**, who helped me with the PIE of the EMPIrE samples. Especially **Brandon Miller**, who even offered me accommodation at his home if I had not made it out of the country in time before the borders closed due to covid-19.

Dem **Hochschulhaus Garching**, welches mir seit nun 12 Jahren durch Studium und Promotion eine Heimat ist in der viele Freundschaften entstanden sind.

Meiner Familie, einerseits für die aktive finanzielle Unterstützung während des gesamten Studiums, aber im Besonderen auch für die passive Unterstützung, dass ich diesen für uns ungewöhnlichen Weg beschreiten konnte.

Julia Mausz - das Boon ♡

Hey **Claudi**, ich krieg jetzt so ein "Dr."... verrückt!